

Dissertation
submitted to the
Combined Faculty of Mathematics, Engineering and Natural Sciences
of Heidelberg University, Germany
for the degree of
Doctor of Natural Sciences

Put forward by
Jan Henneco
born in: Leuven, Belgium
Oral examination: February 6th, 2025

The Progenitors and Products of Stellar Mergers

by

Jan Henneco

SUPERVISORS

Dr. Fabian Schneider
Prof. dr. ir. Saskia Hekker

EXAMINATION COMMITTEE

Dr. Fabian Schneider (referee)
Prof. Dr. Laura Kreidberg (referee)
Prof. dr. ir. Saskia Hekker
Prof. Dr. Jim Hinton

Summary

A considerable fraction of stars live in binary systems and may exchange mass with each other. One of the outcomes of this mass transfer is a contact phase in which the two stars share a common envelope. If this contact phase is unstable, the binary components will merge and leave behind a merger product. In the first part of this thesis, we evolve several thousand binary systems with varying initial parameters and assumptions regarding the efficiency of mass transfer to trace which binaries evolve into a contact phase and which of these may merge. We identify the mechanisms leading to contact and stellar mergers, assess the influence of our assumptions, and compare our population of contact binaries to observations.

In the second part of this thesis, we predict the pulsations of stellar merger products to investigate whether they differ significantly from those of genuine single stars. We find that the peculiar internal structure of these merger products affects their predicted asteroseismic signatures, both for merger products on the main sequence and more evolved merger products. With these predictions, we demonstrate the potential of asteroseismology to distinguish merger products from genuine single stars.

Zusammenfassung

Ein beträchtlicher Teil der Sterne lebt in Doppelsternsystemen. Neben der gravitativen Wechselwirkung können diese Sterne auch Masse austauschen. Ein mögliches Ergebnis dieses Massenaustauschs ist eine Kontaktphase, in der die beiden Sterne eine gemeinsame Hülle teilen. Wenn diese Kontaktphase instabil ist, verschmelzen die Komponenten zu einem Stern. Im ersten Teil dieser Arbeit entwickeln wir mehrere tausend Doppelsysteme mit variierenden Anfangsparametern und Annahmen zur Effizienz des Massentransfers, um zu untersuchen, welche Systeme eine Kontaktphase erreichen und welche davon vermutlich verschmelzen. Wir identifizieren die Mechanismen, die zu Kontaktphasen und stellaren Verschmelzungen führen, bewerten den Einfluss unserer Annahmen und vergleichen unsere Population von Kontakt-Doppelsternen mit Beobachtungen.

Im zweiten Teil dieser Arbeit sagen wir die Pulsationseigenschaften von Verschmelzungsprodukten vorher und untersuchen dann, ob sie sich signifikant von echten Einzelsternen unterscheiden. Wir stellen fest, dass die besondere innere Struktur dieser Verschmelzungsprodukte ihre vorhergesagten asteroseismischen Eigenschaften beeinflusst, sowohl für Verschmelzungsprodukte auf der Hauptreihe als auch für weiter entwickelte Sterne. Mit diesen Vorhersagen zeigen wir das Potenzial der Asteroseismologie, Verschmelzungsprodukte von echten Einzelsternen zu unterscheiden.

List of abbreviations

AGB	Asymptotic giant branch
BV	Brunt-Väisälä
CE	Common envelope
CM	Centre of mass
HG	Hertzsprung gap
HRD	Hertzsprung-Russell diagram
LHS	Left-hand-side
MHD	Magnetohydrodynamic
MS	Main sequence
ND	N dimension(s), N-dimensional
PSP	Period spacing pattern
RHS	Right-hand-side
RG	Red giant
RL	Roche lobe
RLOF	Roche lobe overflow
SN	Supernova
SPH	Smoothed particle hydrodynamic

List of physical constants

symbol	name	value in SI units
M_{\odot}	Solar mass	$1.988410 \times 10^{30} \text{ kg}$
L_{\odot}	Solar luminosity	$3.828 \times 10^{26} \text{ W}$
R_{\odot}	Solar radius	$6.957 \times 10^8 \text{ m}$
σ	Stefan-Boltzmann constant	$5.6703744191844314 \times 10^{-8} \text{ W m}^{-2} \text{ K}^{-4}$
c	Speed of light in vacuum	$2.99792458 \times 10^8 \text{ m s}^{-1}$
G	Gravitational constant	$6.6743 \times 10^{-11} \text{ m}^3 \text{ kg}^{-1} \text{ s}^{-2}$

Contents

Summary	v
Zusammenfassung	v
List of abbreviations	vii
List of physical constants	ix
1 Context and theoretical background	1
1.1 Binary star evolution: the basics	2
1.1.1 Timescales	2
1.1.2 The Roche potential	3
1.1.3 Tides in binary systems	5
1.1.4 Mass transfer	7
1.1.5 Contact phases and stellar mergers	12
1.2 Asteroseismology: going beyond the stellar surface	14
1.2.1 Describing stellar oscillations	15
1.2.2 Asteroseismic diagnostics	19
1.2.3 Driving and damping mechanisms	21
1.2.4 The space revolution	24
1.3 Numerical methods	27
1.3.1 Stellar and binary evolution	27
1.3.2 Stellar oscillations	29
1.4 Overview of this thesis	29
2 Contact tracing of binary stars: Pathways to stellar mergers	33
2.1 Introduction	34
2.2 Methods	36
2.2.1 Adopted stellar physics	36
2.2.2 Adopted binary physics	38
2.2.3 Binary-star grid	39
2.2.4 Stopping conditions	40
2.2.5 Birth probabilities	40
2.3 Physical mechanisms leading to contact	41
2.3.1 Expansion of accretor	42
2.3.2 Non-conservative mass transfer	43
2.3.3 Outflow from second Lagrange point	44
2.3.4 Tidally driven contact	46
2.3.5 Unstable mass transfer and CE phases	48

2.4	Occurrence of contact phases	49
2.4.1	Contact phases for different initial primary masses	50
2.4.2	Stable Case-BI and -C mass transfer	56
2.4.3	Population properties	58
2.4.4	Stellar merger and classical CE incidence	60
2.4.5	Comparison with observed contact binaries	61
2.5	Discussion	64
2.5.1	The role of mass-transfer efficiency	64
2.5.2	The stability of Case-B and -C mass transfer	66
2.5.3	The fate of binaries with non-ejected matter	66
2.5.4	The onset of contact through runaway mass transfer and L_2 -overflow	67
2.6	Summary and conclusions	67
3	Contact tracing of binary stars with fully conservative mass transfer	69
3.1	Introduction	69
3.2	Methods	70
3.3	Results and discussion	70
3.4	Conclusions	76
4	Merger seismology: Distinguishing massive merger products from genuine single stars using asteroseismology	79
4.1	Introduction	80
4.2	Methods	82
4.2.1	Stellar model computations with MESA	83
4.2.2	Stellar oscillation calculations with GYRE	85
4.3	Results	86
4.3.1	Detailed comparison between Case-Be merger products and genuine single HG stars	86
4.3.2	Deep dips in pure g-mode PSPs	92
4.3.3	Effect of the added mass fraction, f_{add}	96
4.3.4	Comparison for oscillation equations including rotation	99
4.3.5	Observability	99
4.4	Discussion and conclusions	104
5	Asteroseismic predictions for a massive main-sequence merger product	107
5.1	Introduction	108
5.2	Methods	109
5.2.1	Stellar evolution computations with MESA	109
5.2.2	Merger models and prescriptions	110
5.2.3	Oscillation mode predictions with GYRE	113
5.3	Results	114
5.3.1	Asteroseismic comparison	115
5.3.2	Comparison with and between 1D merger methods	126
5.4	Discussion and conclusions	138

6	Conclusions and outlook	141
6.1	Binary evolution and contact tracing	141
6.2	Merger seismology	142
A	Appendices for Chapter 2: ‘Contact tracing of binary stars: Pathways to stellar mergers’	145
A.1	Nuclear timescale expansion of the accretor	145
A.2	Contact tracing results for other $M_{1,i}$	145
A.3	Evolutionary states at contact or termination of models	145
A.4	Expansion timescales for Case-A contact systems	146
A.5	Assignment criteria for evolutionary outcomes of models with numerical issues	146
A.6	Mass-transfer efficiency	155
A.7	Table with contact tracing results	156
B	Appendices for Chapter 3: ‘Contact tracing of binary stars with fully conservative mass transfer’	159
B.1	Contact tracing results for other $M_{1,i}$	159
C	Appendices for Chapter 4: ‘Merger seismology: Distinguishing massive merger products from genuine single stars using asteroseismology’	163
C.1	Inclusion of slow rotation: TAR versus perturbative inclusion of the Coriolis acceleration	163
C.2	Propagation diagrams as a function of radial coordinate	165
C.3	Effect of semi-convection efficiency on ICZs	165
C.4	Disentangling of dip structures in genuine single stars with an ICZ	166
C.5	Wave displacements and differential mode inertia for a selection of modes	168
D	Appendices for Chapter 5: ‘Asteroseismic predictions for a massive main-sequence merger product’	173
D.1	Period spacing patterns for $\ell = 2$ modes of 3D MHD merger product	173
D.2	Mean envelope density and sound speed comparison	173
D.3	Comparison of p modes with rotation	173
D.4	Composition profiles and propagation diagrams for 1D merger methods	175
	List of publications	185
	Bibliography	187
	Acknowledgments	223

“A few years ago the city council of Monza, Italy, barred pet owners from keeping goldfish in curved bowls. The measure’s sponsor explained the measure in part by saying that it is cruel to keep a fish in a bowl with curved sides because, gazing out, the fish would have a distorted view of reality. But how do we know we have the true, undistorted picture of reality?”

– Stephen Hawking (1942–2018), *The Grand Design* (2010)

Context and theoretical background

Living together can complicate the lives of stars, but, just as for people, it definitely makes them considerably more interesting and exciting. It just happens that most stars, especially the ones more massive than our Sun, do not live alone. Observations have firmly established this for over a decade now (Sana et al., 2012). In fact, approximately half of the stars as massive as our Sun (one solar mass, $1 M_{\odot}$) are part of what we call a *multiple system*. Such a multiple system can be a binary system (two stars), triple system (three stars), quadruple system (four stars) and so on. For stars more massive than our Sun, this multiplicity factor increases, and for masses around $10 M_{\odot}$, the fraction of triple systems even overtakes the fraction of binary systems (Moe and Di Stefano, 2017; Offner et al., 2023). Thus, if we want to correctly interpret the ever-growing collection of data from ground- and space-based instruments, we ought to realise that single stellar structure and evolution theory alone does not suffice. For the remainder of this thesis, we focus specifically on binary systems.

The first mention of ‘double stars’ (that we know of) dates back to the 2nd century of the Common Era, when the Alexandrian astronomer Claudius Ptolemy described ‘the nebulous and double star at the eye’ of the Sagittarius constellation. Later, with the invention of telescopes, many more binary stars could be discovered by astronomers such as Benedetto Castelli, John Mitchel, and William Herschel. During these early days of binary detections, astronomers were restricted to detecting *visual binaries*, stars that are positioned closely in the sky, but that can still be distinguished. The difficulty back then was that some of these visual binaries were not *physical binaries*, orbiting around the components’ common centre of mass, but rather *optical binaries*. The latter are nothing more than chance alignments of two stars, which may in reality be separated by lightyears. For more information on the first detections of binary stars, we refer the reader to Tauris and van den Heuvel (2023).

In the 1950s, observations of the inner binary of the Algol¹ triple system showed that the more evolved star was the less massive one. Assuming that both stars were born together, this went against the basic theory that more massive stars evolve faster than less massive stars. This *Algol paradox* was eventually solved by Crawford (1955), who realised that significant amounts of mass transfer (see Sect. 1.1.4) must have occurred between the two stars.

¹The variability of the Algol system was realised already in ancient times. This prompted Arabic astronomers to call the system *ra’s al-ghūl* (رأس الغول) or *head of the ogre*. It was only in 1881 that Edward Charles Pickering confirmed that the system contained an eclipsing binary, hence finding the cause for the variability.

With this, the realisation was born that the evolution of binary stars can severely impact the binary components.

One of the more extreme ways in which binary evolution can impact the binary components is when it leads to a situation in which they merge into one star. Such *stellar mergers* are predicted to be common; de Mink et al. (2014) estimate that $\sim 8\%$ of early-type stars in their simulated sample are *stellar merger products*, while Sana et al. (2012) infer from the comparison between observations of massive stars and simulations that 20–30% of binary systems will likely merge. In the first part of this thesis, we focus on the evolution of binary systems (*binary star systems* or *binary stars*) and how this evolution can lead to contact phases, which are the phases that precede stellar mergers. Stellar merger products are predicted to have peculiar properties, and based on these properties, several merger product candidates have been found. Examples of these candidates include τ Sco (Schneider et al., 2016, 2020) and one of the components of the binary system HD 148937 (Frost et al., 2024, in this case, the merger happened between two components of a triple system). It is, however, not straightforward and sometimes even impossible to identify merger products from their potentially peculiar surface properties alone. Therefore, in the second part of this thesis, we use asteroseismology, the study of stellar interiors through stellar pulsations. We predict how peculiarities in the internal structure of merger products might lead to signatures in their pulsations that could help us to distinguish them from ‘normal’ single stars.

The following sections are meant to introduce the worlds of binary evolution (Sect. 1.1) and asteroseismology (Sect. 1.2). Since this is a theoretical work, we also introduce the computational tools we use to predict the evolution of stars and their asteroseismic characteristics in this thesis (Sect. 1.3). In Sect. 1.4, we further highlight the importance of stellar mergers in astrophysics and discuss the idea of using asteroseismology to identify their products.

1.1. Binary star evolution: the basics

1.1.1. Timescales

In stellar evolution, we typically consider three timescales. From the theoretical side, these timescales serve as diagnostics for understanding the evolution of stars. When we see that a certain process, for example, the expansion of the star, occurs on a timescale similar to one of these three timescales, we get an idea of what physics is likely driving this process. The first timescale estimates the time a star, a binary component in this case, will spend in a phase of central nuclear burning, such as on the main sequence (MS) when it burns hydrogen (H) in its core. This timescale, the *nuclear timescale* τ_{nuc} , is typically the longest and is on the order of 10^7 years for a $10 M_{\odot}$ MS star. The nuclear timescale of a star is usually estimated by the available nuclear energy in its core E_{nuc} and its luminosity L_{\star} , as given in Kippenhahn et al. (2013)

$$\tau_{\text{nuc}} = \frac{E_{\text{nuc}}}{L_{\star}} \approx 10^{10} \frac{M_{\star} L_{\odot}}{M_{\odot} L_{\star}} \text{yr}, \quad (1.1)$$

where M_{\star} is the mass of the star. The *Kelvin-Helmholtz timescale* τ_{KH} , also referred to as the *thermal timescale*, essentially tells us how long it would take for a star with a certain luminosity to radiate away all of its internal energy. In other words, it is the survival time of

a star without nuclear burning to generate counterpressure, and it is on the order of 10^4 years for a $10 M_\odot$ MS star. When a star is out of thermal equilibrium, for example, because it loses or gains mass (see Sect. 1.1.4), the thermal timescale is the time it takes to regain this thermal equilibrium. Its explicit expression is (Kippenhahn et al., 2013)

$$\tau_{\text{KH}} = \frac{GM_\star^2}{2R_\star L_\star} \approx 1.5 \times 10^7 \left(\frac{M_\star}{M_\odot} \right)^2 \frac{R_\odot L_\odot}{R_\star L_\star} \text{yr}, \quad (1.2)$$

where R_\star is the stellar radius and G the gravitational constant. The *dynamical timescale* τ_{dyn} is on the order of 10^{-3} years or half a day for a $10 M_\odot$ MS star and is thus the shortest of the three timescales. It is the time a star needs to regain hydrostatic equilibrium after experiencing a perturbation. We typically estimate it as the sound-crossing time, that is, the time it takes a sound wave, which is a pressure disturbance, with a global average sound speed $\langle c_s \rangle$ to traverse the stellar radius R_\star (Kippenhahn et al., 2013; Tauris and van den Heuvel, 2023):

$$\tau_{\text{dyn}} = \int_0^{R_\star} \frac{dr}{c_s} \approx \frac{R_\star}{\langle c_s \rangle} \approx 0.04 \left(\frac{M_\odot}{M_\star} \right)^{1/2} \left(\frac{R_\star}{R_\odot} \right)^{3/2} \text{day}, \quad (1.3)$$

where $c_s = c_s(r)$ is the local sound speed and r the radial coordinate.

1.1.2. The Roche potential

The Roche potential is an approximation of the effective gravitational potential felt by a particle, be it a blob of stellar matter, material flowing between the two stars, or a planet. This approximation, introduced by Édouard Roche (1820–1883), assumes that both stars are co-rotating with the binary orbit, treats the stars as point masses, and assumes a circular orbit, that is, the eccentricity $e = 0$. Putting the origin of the coordinate system, which we take to co-rotate with the binary system, in the centre of mass (CM), we can write down the Roche potential $\Phi(\vec{r})$ as follows (Tauris and van den Heuvel, 2023):

$$\Phi(\vec{r}) = -\frac{GM_1}{|\vec{r} - \vec{r}_1|} - \frac{GM_2}{|\vec{r} - \vec{r}_2|} - \frac{1}{2} \left(\vec{\Omega}_{\text{bin}} \times \vec{r} \right)^2. \quad (1.4)$$

In this expression, \vec{r} is the position vector of a particle in the Roche geometry, \vec{r}_1 and \vec{r}_2 are the positions of the centres of the primary and secondary star, respectively, and M_1 and M_2 are the masses of the primary and secondary star, respectively. ‘Primary’ usually refers to the more massive star in the binary, and ‘secondary’ to the less massive star. It is important to realise that some authors will use this terminology for the *currently* more and less massive stars, for example, in an observed binary system. In this thesis, as emphasised in Sect. 2.2.2, we call the *initially* more massive star the primary and the initially less massive star the secondary. The force a test particle feels is retrieved by taking the negative of the gradient of the Roche potential: $\vec{f}_{\text{Roche}} = -\vec{\nabla}\Phi$.

The last term on the right-hand-side (RHS) of Eq. (1.4) is the centrifugal potential, with $|\vec{\Omega}_{\text{bin}}| = \Omega_{\text{bin}} = 2\pi/P_{\text{orb}} = \sqrt{G(M_1 + M_2)/a_{\text{orb}}^3}$ the angular orbital frequency, and P_{orb} and a_{orb} the orbital period and separation, respectively. A stationary particle in the Roche geometry will thus feel the combined effect of the gravitational force from both stars and the centrifugal force. If a particle moves with respect to the co-rotating coordinate system, it will, in addition, be influenced by the Coriolis force.

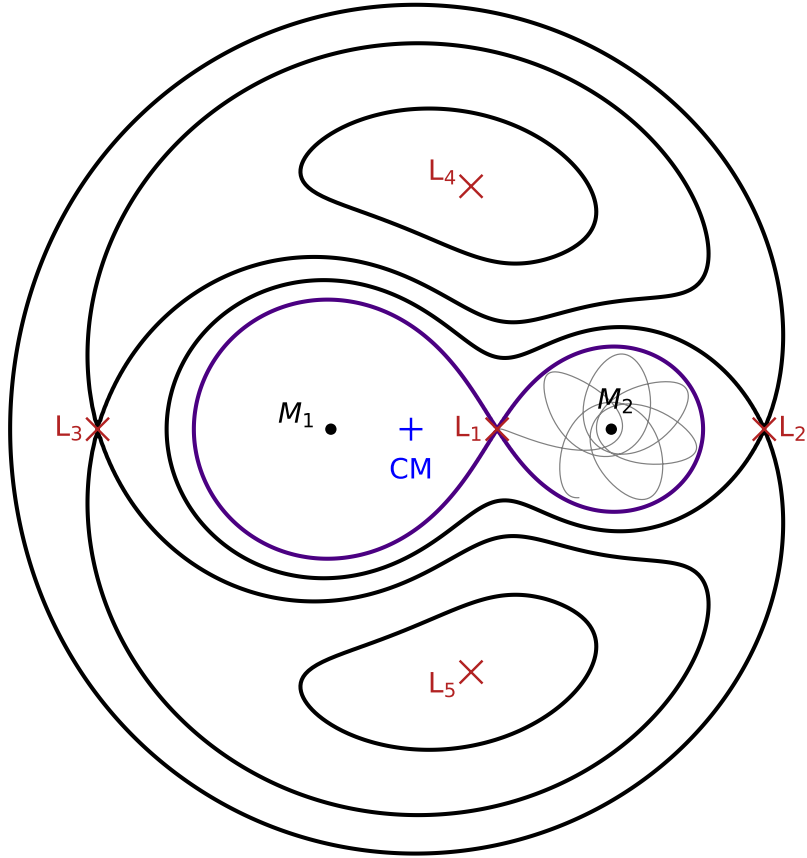


Figure 1.1: Roche equipotential lines (indigo and black) through the Lagrange points L_1 , L_2 , and L_3 , indicated by red crosses, in the orbital (xy) plane for a binary system with $M_1 = 10 M_\odot$, $M_2 = 4 M_\odot$ and $P_{\text{orb}} = 20$ days. The Roche lobe is highlighted in indigo, and the centre of mass with a blue plus symbol. Around the L_4 and L_5 points, which themselves are indicated by red crosses, equipotential lines between $\Phi(L_3)$ and $\Phi(L_4)$, and $\Phi(L_3)$ and $\Phi(L_5)$ are shown, respectively. The thin grey line in the secondary star's Roche lobe shows the trajectory (for one orbital period) of a particle travelling through L_1 with a small initial velocity in the x - and y -directions. The script to produce this figure is a combination of adapted scripts originally by V. Bronner (Roche equipotentials) and F. Schneider (particle trajectories).

The Roche potential has a total of five saddle points, commonly referred to as the Lagrange points and shown in Fig. 1.1. The first three Lagrange points lie on the line connecting the centres of the two stars. The first Lagrange point, L_1 , is the point in between the two stars. The second and third Lagrange points, L_2 and L_3 , lie on the outside of the binary system, at the side of the less massive and more massive star, respectively. These points are also referred to as the *outer Lagrange points*. The L_4 and L_5 points lie in the orbital plane on a line orthogonal to the line connecting the two stars. Figure 1.1 shows equipotential lines of the Roche potential through the L_1 , L_2 , and L_3 points and around the L_4 and L_5 points. The two sides of the eight-shaped equipotential through L_1 are called the *Roche lobes*. A star filling its Roche lobe will thus no longer be spherical but more tear-shaped. When both binary components are well within their Roche lobes, we call the binary *detached*. If one of the binary components fills or overfills its Roche lobe, it is called *semi-detached*, and when both stars (over)fill their Roche lobes, we say that the stars are in a *contact* phase. A more detailed classification scheme for the different kinds of contact phases is given in Sect. 1.1.5. As discussed in Sect. 1.3.1, we often need to make further approximations because we want to model binary systems in one dimension (1D). To know if a star, which is necessarily spherically symmetric in 1D, fills or overfills its Roche lobe, we need to compare its radius to the so-called Roche-lobe radius R_{RL} . This Roche-lobe radius is a volume-equivalent radius of the star's Roche lobe, that is, the radius of a sphere with the same volume as the Roche lobe. Different approximations for R_{RL} exist (see, e.g. Paczyński 1971), but the one from Eggleton (1983) is most often used and is given by

$$\frac{R_{\text{RL}}}{a_{\text{orb}}} = \frac{0.49q^{-2/3}}{0.6q^{-2/3} + \ln(1 + q^{-1/3})}. \quad (1.5)$$

It is important to realise that $R_{\text{RL}} = R_{\text{RL}}(a_{\text{orb}}, q)$ only depends on the orbital separation a_{orb} and the mass ratio² $q = M_2/M_1$, not on the total mass of the binary system.

1.1.3. Tides in binary systems

One of the main approximations in the Roche potential is that the binary components are treated as point masses, which they obviously are not. Since stars are extended objects, the different parts of the star feel different amounts of gravitational attraction from their companion in a binary system. As a result, the star is squeezed at its poles and stretched at its equator along the line between the binary components. This is referred to as *tidal deformation*. A simple way to see this is if we look at the problem in the orbital xy -plane (in 2D) and start from the expression of the gravitational potential at position \vec{r} caused by the companion with mass M_{comp} at position \vec{a}_{orb} (with the origin in the centre of the tidally deformed star), which is

$$\Phi_{\text{grav}}(\vec{r}) = -\frac{GM_{\text{comp}}}{|\vec{r} - \vec{a}_{\text{orb}}|}. \quad (1.6)$$

By taking θ as the angle between \vec{r} and \vec{a}_{orb} , we can rewrite the denominator on the RHS as

²Throughout this thesis, we define q to always be the ratio of the mass of the less massive over the mass of the more massive star. So, assuming that at a given time $M_1 > M_2$, we use $q = M_2/M_1$ in Eq. (1.5) to get the Roche-lobe radius of the more massive star. To get R_{RL} for the less massive star, we use the inverse mass ratio $q_{\text{inv}} = M_1/M_2$ in Eq. (1.5).

$$\begin{aligned} \frac{1}{|\vec{r} - \vec{a}_{\text{orb}}|} &= \frac{1}{\sqrt{(\vec{r} - \vec{a}_{\text{orb}}) \cdot (\vec{r} - \vec{a}_{\text{orb}})}} = \frac{1}{\sqrt{r^2 - 2ra_{\text{orb}} \cos \theta + a_{\text{orb}}^2}} \\ &= \frac{1}{a_{\text{orb}}} \frac{1}{\sqrt{\left(\frac{r}{a_{\text{orb}}}\right)^2 - 2\left(\frac{r}{a_{\text{orb}}}\right) \cos \theta + 1}}. \end{aligned} \quad (1.7)$$

Realising that the second fraction on the RHS of Eq. (1.7) is the generating function of the Legendre polynomials $P_\ell^{m=0}(\cos \theta)$, we can write Φ_{grav} as

$$\Phi_{\text{grav}} = -\frac{GM_{\text{comp}}}{a_{\text{orb}}} \sum_{\ell=0}^{\infty} P_\ell^0(\cos \theta) \left(\frac{r}{a_{\text{orb}}}\right)^\ell. \quad (1.8)$$

Writing this out up to the second degree ($\ell = 2$), we find

$$\Phi_{\text{grav}} \simeq -\frac{GM_{\text{comp}}}{a_{\text{orb}}} \left[1 + \left(\frac{r}{a_{\text{orb}}}\right) \cos \theta + \frac{1}{2} \left(\frac{r}{a_{\text{orb}}}\right)^2 (3 \cos^2 \theta - 1) \right], \quad (1.9)$$

where we have used that $P_0^0(\cos \theta) = 1$, $P_1^0(\cos \theta) = \cos \theta$, and $P_2^0(\cos \theta) = (1/2)(3 \cos^2 \theta - 1)$. The first term in Eq. (1.9) is a constant. From the second term, we recover the gravitational attraction in the x -direction, $-GM_{\text{comp}}/a_{\text{orb}}^2$, with $x = r \cos \theta$. The third term is the one responsible for the stretching and squeezing. It reaches its minimum and is negative in the y -direction ($\theta = \pi/2$ and $\theta = 3\pi/2$), and has its maximum and is positive in the x -direction ($\theta = 0$ and $\theta = \pi$). Assuming the tidally deformed star is otherwise spherical (i.e. not rotationally deformed), the deformation, which we now derived in a specific 2D plane, is independent of the orientation of this plane. Hence, we see how the third term on the RHS of Eq. (1.9) deforms the star into a ‘rugby ball’ shape.

In a binary where the rotation of the tidally deformed component is synchronised with the binary orbit, the tidal bulges align with the line connecting the centres of the two stars, as recovered from Eq. (1.9). When a star rotates non-synchronously, various dissipative forces in the stellar interior, which convert the kinetic energy of the large-scale fluid motions in the tidal bulge into heat, cause a misalignment of the tidal bulge with this connecting line (see, e.g. Zahn 2008 for an overview of these dissipation mechanisms). When the tidally deformed star has a rotation period that is longer than the orbital period, the bulge lags behind because of this friction, while the bulge gets dragged ahead when a star’s rotation period is shorter than the orbital period. This misalignment causes a torque on the tidally deformed star, which serves as a mechanism to transfer angular momentum between the binary orbit and the deformed star. If, for example, a tidally deformed star has a longer rotation period than the orbital period, this torque and conservation of angular momentum cause a spin-up of the star and a shrinking of the binary orbit. This transfer of angular momentum between the orbit and the components is often referred to as *L-S-coupling* or *spin-orbit-coupling*, where $L = L_{\text{orb}}$ stands for the orbital angular momentum and S for the spin-angular momentum. Through this *L-S-coupling*, tides influence the evolution of binary systems.

Assuming no angular momentum is lost, a binary system strives to be in a minimal energy state. In this state, called the state of *equilibrium tides*, the binary components are synchronised ($P_1 = P_2 = P_{\text{orb}}$, with P_1 and P_2 the rotation periods of the primary and

secondary, respectively), the orbit is circularised (eccentricity $e = 0$), and the spins of the components are aligned (Hut, 1981). The synchronisation, circularisation, and spin-alignment timescales τ_{sync} , τ_{circ} , and τ_{align} , respectively, can be estimated and depend on the structure of the binary components (see Hut 1981 and Hurley et al. 2002). In general, it is found that $\tau_{\text{circ}} \gg \tau_{\text{sync}}, \tau_{\text{align}}$. It is also important to realise that $\tau_{\text{sync}} \propto (a_{\text{orb}}/R_{\star})^6$ and $\tau_{\text{circ}} \propto (a_{\text{orb}}/R_{\star})^8$, meaning that the effect of tides become relevant only in relatively close binary systems or systems in which one or both components is/are near Roche-lobe filling. For example, Lennon et al. (2024) find that systems with primary masses of 5–20 M_{\odot} and orbital periods below 3 days in the 30 Doradus region of the Large Magellanic Cloud (LMC) are synchronised, while those with orbital periods of more than 10 days are not. Giuricin et al. (1984) find that systems in a similar mass range have circular orbits if their orbital period is roughly below 2 days. Lastly, this state of equilibrium tides can, in certain cases, become unstable, resulting in contact phases and potentially stellar mergers. We dive deeper into this possibility in Sect. 2.3.4.

1.1.4. Mass transfer

When a component of a binary system (over)fills its Roche lobe, that is, $R_{\star} \geq R_{\text{RL}}$, some of its mass is transferred to its companion. The more massive a star, the quicker it evolves through the MS and, consequently, the more rapidly it expands (be it on the MS or by the fact that it reaches the post-MS expansion phases earlier). Therefore, the more massive binary component fills its Roche lobe first and initiates mass transfer.

Mass transfer occurs through the L_1 -point, which acts as a nozzle. To estimate the mass-transfer rate \dot{M}_{trans} (usually expressed in units of $M_{\odot} \text{ yr}^{-1}$) we need to know the density ρ of stellar material, the local sound speed c_s , and the effective cross-section of the mass flow Q at L_1 (Kippenhahn and Weigert, 1967; Savonije, 1979; Meyer and Meyer-Hofmeister, 1983; Ritter, 1988):

$$\dot{M}_{\text{trans}} \simeq \rho c_s Q. \quad (1.10)$$

Estimating these three quantities is not straightforward, especially in 1D approximations, and is part of ongoing research (Pavlovskii and Ivanova, 2015; Marchant et al., 2021; Cechula and Pejcha, 2023; Ivanova et al., 2024). See also Tauris and van den Heuvel (2023) for some commonly used approximations. An important realisation was made by Kolb and Ritter (1990) about the onset of mass transfer. They found that mass transfer must start gradually instead of suddenly when $R_{\star} = R_{\text{RL}}$. The reason for this is that the radius R_{\star} is often defined as the photospheric radius, meaning that there is a non-negligible optically thin part of the stellar atmosphere above R_{\star} . In other words, mass transfer starts gradually and before the star is formally filling its Roche lobe, that is, when $R_{\star} < R_{\text{RL}}$. This is the *optically thin* regime in the scheme of Kolb and Ritter (1990), and when $R_{\star} \geq R_{\text{RL}}$, mass transfer occurs in the *optically thick* regime.

The star that loses mass in a mass-transfer phase is commonly referred to as the *donor* star (subscript ‘d’ in the following chapters), and the mass gainer is called the *accretor* star (subscript ‘a’). Although the accretor is often overlooked in binary evolution studies, its response to mass gaining can alter the evolution of the binary system tremendously (see Chapters 2 and 3).

Mass-transfer phases are typically classified in *cases* based on the evolutionary stage of the donor star. More specifically, these cases are based on the main expansion phases of a star, as shown in Fig. 1.2. *Case-A* mass transfer refers to mass transfer that occurs when the donor star is on the MS. The donor star is, in this case, initially driven to fill its Roche lobe by the nuclear-timescale expansion during its core-H burning phase. When mass transfer sets in while the donor star has left the MS and before it has ignited helium (He) in its core, that is, when the star is on the Hertzsprung gap (HG), we refer to it as *Case-B* mass transfer. In these cases, the donor star is out of thermal equilibrium, which leads to a thermal-timescale expansion phase. We subdivide *Case-B* mass transfer further into *early* (*Case Be*) and *late* (*Case Bl*) phases. This distinction is based on the state of the donor star’s envelope. *Case-Be* mass transfer occurs when the donor star still has a mostly radiative envelope, while *Case-Bl* mass transfer occurs when this envelope is mostly convective. Lastly, mass transfer is classified as *Case-C* when the donor star is post-core-He ignition. Technically, a massive star such as the one shown in Fig. 1.2 contracts upon core-He ignition and only expands again close to core-He exhaustion. For this reason, some authors put the line between *Case-B* and *Case-C* mass transfer at core-He exhaustion.

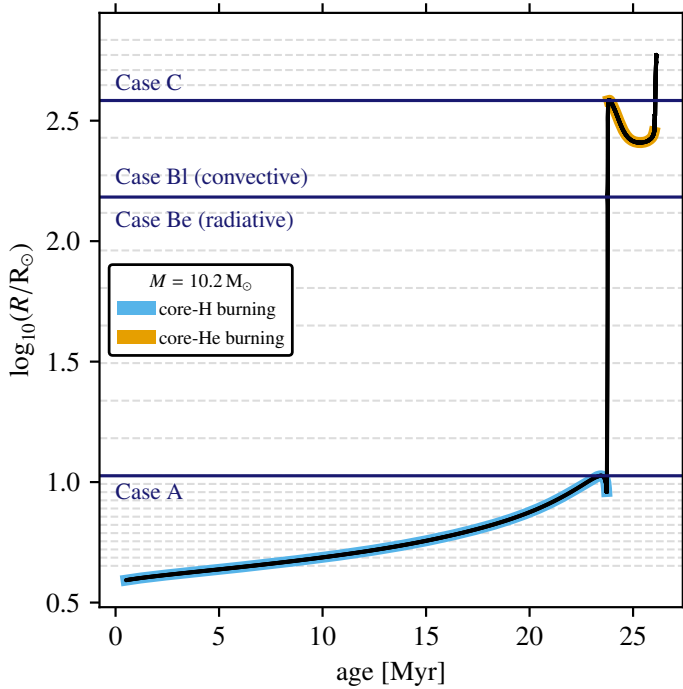


Figure 1.2: Radial expansion of a $10.2 M_{\odot}$ star (solid black line). The radial evolution is divided into different cases based on the main phases of expansion (solid horizontal lines). The dashed horizontal lines are the sampling points at which we put $R = R_{\text{RL}}$, as described in Sect. 2.2.3. This figure is taken from Henneco et al. (2024b).

1.1.4.1 Mass-transfer efficiency

Since accretors do not only accrete mass but also angular momentum (either by direct impact or through an accretion disk), they tend to spin up to higher rotation rates. Once the critical rotation rate is reached, which is the rotation rate at which the centrifugal force balances out the gravitational force (hence the often used name *breakup* rotation rate), mass accretion is quenched. This creates a situation where the accretor does not accrete all the mass

transferred into its Roche lobe through L_1 . Mass transfer is then said to be *non-conservative* and has a *mass-transfer efficiency*, defined as the fraction of accreted mass over the transferred mass, smaller than one. However, this is a simplified picture. Interactions between the inner rim of the accretion disk and the surface of the accretor combined with various angular momentum transport processes in the accretion disk can allow for higher accretion efficiencies than what we predict from the spin-up of the accretor alone (Paczynski, 1991; Popham and Narayan, 1991). Both from the observational and theoretical side, the mass-transfer efficiency is ill-constrained (see discussion in Sect. 2.5.1). It remains one of the main uncertainties in binary evolution. However, there is hope now that the first populations of stripped stars, stars that have lost (part of) their envelope in a mass-transfer event, are being observed and detected (Schootemeijer et al. 2018; Wang et al. 2021; El-Badry and Quataert 2021; Irrgang et al. 2022; El-Badry and Burdge 2022; El-Badry et al. 2022; Frost et al. 2022; Gilkis and Shenar 2023; Ramachandran et al. 2023; Drout et al. 2023; Götberg et al. 2023). Comparing, for example, the mass ratio and orbital period distributions of observed populations of these post-mass-transfer binaries to those from simulated populations could help us constrain the mass-transfer efficiency.

During conservative mass transfer, when both the total mass (ignoring mass loss through stellar winds) and angular momentum are conserved, we can easily estimate the binary orbit's response by differentiating the expression of the total angular momentum in a binary system and equating it to zero (Tauris and van den Heuvel, 2023). Under these assumptions, the change in accretor mass with time, \dot{M}_a , is exactly the opposite of the change in donor mass with time, \dot{M}_d , namely $\dot{M}_a = -\dot{M}_d$. Using this together with the assumption that the orbit is circular, one finds that

$$\frac{\dot{a}_{\text{orb}}}{a_{\text{orb}}} = 2 \left(\frac{M_d}{M_a} - 1 \right) \frac{\dot{M}_d}{M_d}, \quad (1.11)$$

with \dot{a}_{orb} the time derivative of the orbital separation, and M_a and M_d the accretor and donor mass, respectively. What comes out of this is that, as long as the donor star is more massive than the accretor, the orbit will shrink ($\dot{a}_{\text{orb}} < 0$). At the point where $M_a = M_d$, the sign of \dot{a}_{orb} reverses and the orbit widens. For non-conservative mass transfer, the expression for the orbital evolution becomes more complicated and depends on the mass-transfer efficiency and the uncertain amount of specific angular momentum taken away by the non-accreted matter:

$$\frac{\dot{a}_{\text{orb}}}{a_{\text{orb}}} = -2 \left[1 - \beta_{\text{th}} \frac{M_d}{M_a} - (1 - \beta_{\text{th}})(\gamma + 1/2) \frac{M_d}{M_d + M_a} \right] \frac{\dot{M}_d}{M_d}. \quad (1.12)$$

Here, $\beta_{\text{th}} = -\dot{M}_a/\dot{M}_d$ is the mass-transfer efficiency³ and γ the fraction of the binary system's total specific angular momentum that is taken away by the non-accreted matter. Figure 1.3 shows the evolution of $q = M_a/M_d$ and the sign of \dot{a}_{orb} for different mass-transfer efficiencies. We set $\gamma = M_d/M_a$, which is appropriate for the case in which the non-accreted matter is isotropically re-emitted from the vicinity of the accretor (Soberman et al., 1997). The plots in Fig. 1.3 show that in the case of isotropic re-emission, systems with non-conservative mass transfer widen before the accretor mass exceeds the donor mass.

³Note the 'th' = 'theoretical' subscript added to differentiate this definition of the mass-transfer efficiency from the more practical definition introduced in Sect. 2.2.2.1 and used in Chapter 2.

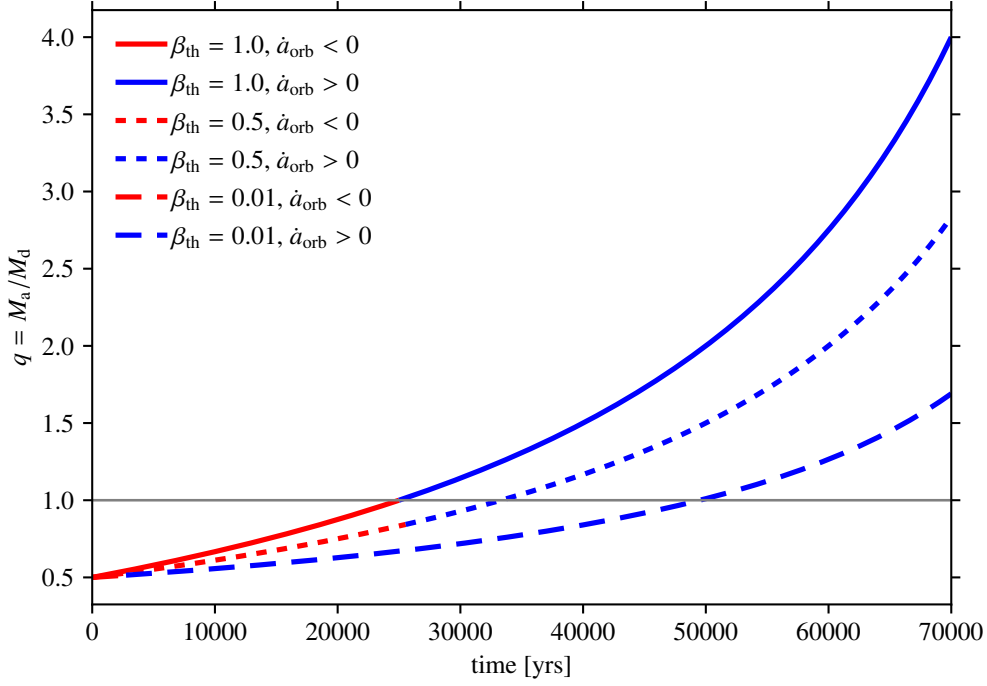


Figure 1.3: Evolution of $q = M_a/M_d$ for different values of β_{th} and a fixed value of $|\dot{M}_d| = 10^{-4} M_{\odot} \text{yr}^{-1}$. The colour of the lines indicates the sign of \dot{a}_{orb} , determined with Eq. (1.12). The horizontal grey line indicates the point where $q = 1$.

1.1.4.2 Mass-transfer stability

A second key aspect of mass transfer is its *stability*. It is also one of its most ill-defined aspects. Mass transfer is said to be unstable if the mass-transferring binary system finds itself in a runaway situation with ever-increasing mass-transfer rates. However, defining what exactly is a runaway situation is ambiguous and often not straightforward (e.g. Temmink et al., 2023). As shown at the beginning of this section, the mass-transfer rate depends on the density ρ at L_1 . The more the donor star overfills its Roche lobe, the higher this density and the higher \dot{M}_{trans} . Therefore, to assess the stability of mass transfer in simulations, we ought to see how the donor star’s radius and Roche lobe radius respond to mass loss (Soberman et al., 1997). This is made quantitative by Webbink (1984) in so-called *mass-radius exponents*, defined as

$$\zeta_{\star} = \frac{d \ln R}{d \ln M} \quad \text{and} \quad \zeta_{\text{RL}} = \frac{d \ln R_{\text{RL}}}{d \ln M}, \quad (1.13)$$

where ζ_{\star} and ζ_{RL} are the mass-radius exponents of the donor star and its Roche lobe, respectively. These mass-radius exponents are simply the slopes of the mass-radius relation. When the donor star loses mass, it is out of hydrostatic and thermal equilibrium. To find out the response of the donor star to mass loss, one should look at its dynamic and thermal responses. However, it is often assumed that the dynamic response of the star happens adiabatically, hence, the classical criteria for mass-transfer stability are based on the adiabatic and thermal responses, ζ_{ad} and ζ_{th} , respectively. These mass-radius exponents determine the radius of the donor after regaining hydrostatic and thermal equilibrium. The mass transfer stability criteria then become a matter of comparing ζ_{ad} , ζ_{th} , and ζ_{RL} :

Stable mass transfer: $\zeta_{\text{RL}} \leq \zeta_{\text{th}}$ **and** $\zeta_{\text{RL}} \leq \zeta_{\text{ad}}$ — The donor star remains in thermal and hydrostatic equilibrium, and is at all times contained within its Roche lobe. Stable mass transfer is typical when the mass transfer is driven by the star’s expansion during central nuclear-burning stages such as the MS (nuclear-timescale mass transfer, Case-A mass transfer). Alternatively, the orbital shrinkage caused by angular momentum loss can also drive stable mass-transfer phases.

Thermal timescale (stable) mass transfer: $\zeta_{\text{th}} \leq \zeta_{\text{RL}} < \zeta_{\text{ad}}$ — In this case, the donor star is in hydrostatic but not in thermal equilibrium. This kind of mass-transfer phase lasts until the donor star has regained thermal equilibrium and is characterised by higher mass-transfer rates than stable mass-transfer.

Unstable mass transfer: $\zeta_{\text{RL}} > \zeta_{\text{th}}$ **and** $\zeta_{\text{RL}} > \zeta_{\text{ad}}$ — This is a runaway situation in which the Roche lobe fails to contain the donor star. As a result, the more mass is lost, the more Roche-lobe overflow there is, and the more the mass-transfer rate increases.

In general, stars with convective envelopes (Case-BI and -C mass transfer) tend to expand upon mass loss, while those with radiative envelopes (Case-A and -Be mass transfer) shrink. From the definitions above, it is clear that a situation in which the donor star expands upon mass loss can quickly become unstable if its Roche lobe does not expand at least at the same rate. Although this is a convenient rule of thumb for estimating what will happen to a binary system when mass transfer sets in, detailed mass-transfer calculations show that a more nuanced approach is appropriate (see, e.g. [Temminck et al. 2023](#)).

Since most binary evolution codes operate on evolutionary timescales, the dynamic and adiabatic responses of donor stars to mass loss cannot be captured. However, detailed computations for the adiabatic response of donor stars exist (e.g. [Hjellming, 1989a,b](#); [Deloye and Taam, 2010](#); [Ge et al., 2010a,b](#); [Ge et al., 2015, 2020](#); [Ge et al., 2023, 2024](#)) and can be incorporated through fitting formulae and/or tables. A drawback of these studies is that they do not always account for the evolution of the binary system as a whole in their stability assessment. Additionally, despite looking at the adiabatic response of the donor star, they still assume the star to be in hydrostatic equilibrium, that is, the fluid velocities are neglected ([Ge et al., 2010a](#)). This assumption only breaks down in the vicinity of L_1 , yet it causes us to potentially miss physical processes influencing the stability of mass transfer. To alleviate this shortcoming, other works do not look at the adiabatic response of the donor star but instead include hydrodynamic terms in the stellar structure equations solved in stellar evolution codes to find the response of the donor star to mass loss (e.g. [Woods and Ivanova, 2011](#); [Ivanova et al., 2024](#)). In yet another way, works such as [Pavlovskii and Ivanova \(2015\)](#) and [Temminck et al. \(2023\)](#), do not consider the hydrodynamic or adiabatic response of the donor star but take into account the fact that the sub-surface layers of certain types of stars are super-adiabatic when determining the stability of mass transfer. Furthermore, it is also important to realise that the onset of mass transfer can be stable and become unstable later on (*delayed instability*), or vice versa; what seems like a runaway behaviour in the mass-transfer rate can stabilise ([Temminck et al., 2023](#)). In Sect. 2.3.5, we come back to this issue of predicting the onset of unstable mass transfer in the light of our own models.

Unstable mass transfer results in the onset of a contact phase, which can be catastrophic for the binary system’s survival. The next section focuses on such and other contact phases.

1.1.5. Contact phases and stellar mergers

Two things can happen during a mass-transfer phase between ‘living’⁴ stars: either the donor star settles back into its Roche lobe and the binary becomes detached again, or the two stars enter a contact phase. Once a binary reaches such a contact phase, the stars are said to share a *common envelope* (CE). Depending on the physical driving mechanism and relative sizes of the binary components, such common envelope systems can be subdivided into several categories (Röpke and De Marco, 2023). We discuss the physical driving mechanisms for contact phases at length in Sect. 2.3, so we only briefly mention them here.

1.1.5.1 Contact binaries

Under the term ‘contact binaries’ (also referred to as *overcontact binaries*), we typically count systems in which both components are MS or hot post-MS stars, that is, when contact is reached during Case-A or -Be mass transfer. The latter stars have evolved off the MS but have not yet evolved to (super)giant proportions. When such stars initially come into contact, there is no loss of co-rotation, and they form peanut-shaped objects. Within their peanut-shaped common envelope, the components exchange energy, as theorised by Lucy (1968) and modelled by Lucy (1976), Flannery (1976), Hazlehurst (1985), Kaehler (1989), Shu et al. (1976, 1979), and Lubow and Shu (1977, 1979). More recently, Fabry et al. (2023) implemented the model from Shu et al. (1976, 1979) and Lubow and Shu (1977, 1979) in the modern-day stellar evolution code MESA (see Sect. 1.3.1 for more info about MESA). The models for contact binaries given above resolved *Kuiper’s paradox* (Kuiper, 1941), which stated that unequal-mass contact binaries should be unstable. In fact, stable contact binary configurations must exist, since on the order of 10^5 contact binary candidates, with equal *and* unequal masses, have been observed with the Optical Gravitational Lensing Experiment (OGLE, Pietrukowicz et al., 2013; Pawlak et al., 2016; Soszyński et al., 2016, and references therein), the All Sky Automated Survey (ASAS, Paczyński et al., 2006; Rucinski, 2007), *Kepler* (Prša et al., 2011), the Transiting Exoplanet Survey Satellite (TESS Ricker et al., 2015), and *Gaia* (Gaia Collaboration et al., 2016, 2023b). The majority of these observations are of low-mass contact binaries. Only on the order of 10 high-mass (initial primary mass $\geq 8 M_{\odot}$) contact binaries have been detected so far (Abdul-Masih et al., 2022). We know that both stable and unstable contact binaries exist from the theoretical side (see, e.g. Fabry et al. 2022, 2023 and references therein).

To understand the stability of contact binaries, we need to consider the mechanisms that drive them. Contact binaries form when the accretor star fills its Roche lobe during a mass-transfer phase (see Sect. 2.3.1). If it does this on its nuclear timescale (i.e. the accretor has regained thermal equilibrium), the resulting contact phase is initially likely stable. If the expansion happens on the accretor’s thermal timescale, two things can happen. If the thermal expansion of the accretor continues, the contact binary will be unstable and likely merge. If the thermal expansion halts upon reaching contact, the contact phase tends to be relatively short-lived since the accretor typically shrinks again after regaining thermal equilibrium. During unstable mass transfer, the accretor’s expansion timescale typically approaches its dynamical timescale, leading to an unstable contact binary (see Sect. 2.3.5). Tides, more specifically tidal instabilities, can lead to the formation of unstable contact binaries (see Sect. 2.3.4) or destabilise previously stable contact binaries. The luminous red

⁴In this thesis, we focus on stars before they turn into compact objects. We use the term ‘living’ as an antonym for the way compact objects tend to be referred to as ‘dead’ stars (see, e.g. Longair, 2011)

nova V1309 Sco, the transient phenomenon linked to a stellar merger, has been shown by Tylenda et al. (2011) and Stępień (2011) to be likely caused by a tidal instability.

When the common envelope of a (stable) contact binary increasingly overfills the Roche lobe (e.g. because of the expansion of the components or orbital shrinkage), it can fill the L_2 -lobe (see Fig. 1.1). Expansion beyond this point leads to mass loss through the L_2 -point (L_2 -overflow). Matter lost through L_2 carries a substantial amount of angular momentum (depending on the assumed expulsion velocity, see Marchant et al. 2021), causing the binary orbit to shrink. This is yet another way in which contact binaries can become unstable and result in stellar mergers.

1.1.5.2 Classical common envelopes

A *classical CE* is a contact phase in which one of the components is of (super)giant proportions (Case-BI or -C mass transfer). Its more compact companion, for example, an MS star, hot post-MS star, or compact object (white dwarf, neutron star, or black hole), is engulfed by the (super)giant star and spirals in together with the (super)giant’s core under the influence of drag forces (Röpke and De Marco, 2023). The classical CE phase, first hypothesised explicitly by Paczynski (1976), is a necessary phase of binary evolution to explain the formation of the close, compact object binaries, which are the progenitors of gravitational wave sources. This is because, from binary evolution calculations, we know that this particular kind of binary system must have been initially in significantly wider orbits. In general, classical common envelopes have two outcomes (these are often referred to as ‘failed’ and ‘successful’ classical CEs, but this naming scheme is rather subjective in the sense that whether the classical CE ‘fails’ depends on which aspect of classical CE evolution one is interested in). In the first scenario, the common envelope is fully ejected, and a binary with a closer orbit than the one at the onset of the classical CE is left behind. One of the mechanisms fuelling this envelope ejection is the conversion of orbital energy into kinetic energy through dynamical friction (Röpke and De Marco, 2023). Together with the transfer of angular momentum from the orbit to the envelope material, this creates spiral arms and shock fronts, which can additionally heat the envelope material, causing it to expand. During the later stages of the classical CE phase, the colder envelope material recombines and can be further accelerated by radiation pressure. Furthermore, magnetohydrodynamic instabilities can occur and, for example, lead to magnetised outflows (Ondratschek et al., 2022; Vetter et al., 2024). In the second classical CE scenario, the envelope cannot be fully ejected, and the continuous gravitational drag forces lead to a stellar merger. The onset of classical CE phases can be caused by the expansion of the (super)giant donor star, possibly even beyond the outer Lagrange points (see Sect. 2.3.3). This is often accompanied by the onset of unstable mass transfer (see Sect. 2.3.5). Tidal instabilities (see Sect. 2.3.4) can also cause the onset of classical CE phases. Next to their importance for the formation of gravitational wave progenitors, their ejected common envelopes are responsible for a significant fraction of observed planetary nebulae (Boffin and Jones, 2019).

1.1.5.3 Double-core common envelopes

The last category of common envelopes is that of the *double-core CEs*. This contact phase sets in when two stars of (super)giant proportion come into contact. The difference with classical CEs is that the extended CE now consists of material from both stars. Although double-core CEs are often overlooked, they have been shown by Vigna-Gómez et al. (2018)

to be essential in explaining the population of double neutron stars. Like the classical CEs, double-core CEs can also result in stellar mergers (Röpke and De Marco, 2023).

1.1.5.4 Stellar mergers

As made clear in the preceding sections, one of the principal outcomes of a contact phase is a stellar merger. We note that binary evolution is not the only pathway to stellar mergers. In dense stellar environments such as clusters, dynamical interactions have been shown to lead to stellar mergers (Hills and Day, 1976; Portegies Zwart et al., 1997, 1999, 2004). These dynamically driven mergers are usually more energetic than evolution-driven ones since the components have higher kinetic energy upon contact. Such a merger event can be viewed as a *collision*, whereas an evolution-driven merger is a *coalescence* between stars. Regardless of their nature, stellar mergers are violent events linked to various types of transients such as luminous red novae⁵ (Tylenda et al., 2005; Soker and Tylenda, 2007; Tylenda et al., 2011; Stępień, 2011) and the great eruption of η Carinae (Frew, 2004; Gallagher, 1989; Iben, 1999; Podsiadlowski et al., 2006; Morris and Podsiadlowski, 2006; Podsiadlowski, 2010; Fitzpatrick, 2012; Portegies Zwart and van den Heuvel, 2016; Smith et al., 2018; Owocki et al., 2019; Hirai et al., 2021). During the merger, material is turbulently mixed, and shocks change the overall thermal structure. Moreover, seed magnetic fields can be amplified and produce highly magnetic stars (Schneider et al., 2019; Ryu et al., 2024). Depending on the initial conditions and nature of the stellar merger, it results in a merger product with a peculiar internal structure and surface diagnostics (see, e.g. Gaburov et al., 2008b; Glebbeek et al., 2013; Menon et al., 2024).

In this section, we have given an overview of the physical mechanisms and evolutionary phases that allow us to describe and predict the progenitor systems of stellar mergers. As can be inferred from the title of this thesis, its second part focuses on the objects left behind after stellar mergers, namely the merger products. We have gone beyond classical surface diagnostics and used asteroseismology, the study of the internal structures of stars through their stellar pulsations, to characterise these potentially peculiar stars and make predictions which could one day be used to identify them among populations of ‘regular’ or ‘genuinely single’ stars.

1.2. Asteroseismology: going beyond the stellar surface

In the 20th century, seismologists such as Richard Dixon Oldham (e.g. Oldham, 1906), Andrija Mohorovičić (e.g. Mohorovičić, 1910), Inge Lehmann (e.g. Lehmann, 1930), and Beno Gutenberg (e.g. Gutenberg and Richter, 1941) successfully used the waves sent out by earthquakes to characterise the interior structure of the Earth. Decades later, Christensen-Dalsgaard and Gough (1976) realised that they could use solar pulsations, which cause periodic variations in the Sun’s intensity, to study its interior. This realisation and the subsequent years of work triggered by it gave rise to the field of *helioseismology*. From helioseismology, *asteroseismology* was eventually born when the same principle was applied to stars other than the Sun. Although both fields are based on the same physical principles, they

⁵It should be noted that according to some authors, these novae are neither red nor luminous. Since this concerns an observational classification, we do not address this further in this thesis and keep referring to transients linked to stellar mergers as luminous red novae.

employ different methods due to the enormous difference in the data quality for the Sun and the more distant other stars (Aerts et al., 2010a).

Asteroseismology uses the fact that stellar *pulsations* (or *oscillations*) cause the star to expand and contract locally. As a result, the star’s brightness varies, and these variations can be captured in photometric time series. The local expansion and contraction of the stellar surface can also be detected via the Doppler shifts they introduce in spectral lines with spectroscopic time series (*radial velocity measurements* and *line profile variability*, Aerts et al., 2010a). These time-series data, that is, the star’s variability in terms of the time, can be converted into a frequency or *Fourier spectrum* through a Fourier transform. In such a Fourier spectrum, the individual *oscillation modes* appear as peaks (given that the observational baseline is long enough to resolve them) with a certain amplitude. From these spectra, the stellar pulsations can then be further analysed. For more info on the analysis of asteroseismic measurements, we refer the reader to, for example, Aerts et al. (2010a), Hekker and Christensen-Dalsgaard (2017), and Aerts (2021).

Various processes within the star can create waves in the stellar interior. If these waves are reflected between two turning points, they form standing waves and thus correspond to the eigenmodes of the star. The eigenmodes’ frequencies, amplitudes, and whether there is something amplifying and sustaining small perturbations at the right frequency all depend on the star’s size, internal structure, and the physical processes that take place within. More generally, the properties of these stellar oscillations are extremely sensitive to the stellar interior, which is why asteroseismology is such a powerful tool for the characterisation of stellar interiors.

In this section, we give an overview of the basic concepts of asteroseismology and the asteroseismic diagnostics used in Chapter 4 and 5. Parts of Sect. 1.2.1 and 1.2.2 are based on the original Sect. 2 (‘Asteroseismic diagnostics’) of Henneco et al. (2024a), which has consequently been omitted from the reproduction of this work in Chapter 4.

1.2.1. Describing stellar oscillations

In the simplest case, that of a spherically symmetric star, stellar oscillations can be described by using *spherical harmonics* Y_ℓ^m . The spherical harmonics are defined as (Aerts et al., 2010a)

$$Y_\ell^m(\theta, \phi) = (-1)^m \sqrt{\frac{(2\ell + 1)(\ell - m)!}{4\pi(\ell + m)!}} P_\ell^m(\cos \theta) \exp(im\phi). \quad (1.14)$$

Here, the $P_\ell^m(\cos \theta)$ are the Legendre polynomials encountered already in Sect. 1.1.3, ℓ is the *spherical degree*, and m is the *azimuthal order*. The variables θ and ϕ are the co-latitude (measured from the pole) and the longitude, respectively, and are shown in Fig. 1.4. In this figure, we show the morphology of a spherical harmonic with $\ell = 7$ and $m = 4$ on the surface of a unit sphere. The spherical degree gives the total number of nodal lines (lines at which there is no displacement) on the surface, and the azimuthal order gives the number of these lines that cross the equator, hence $|m| \leq \ell$. In practice, we cannot observe modes with high spherical degrees because the brightness measured for a star is the integrated value over the whole stellar surface. With a high ℓ value, the stellar surface is divided into many smaller regions with nodal lines in between them. This leads to the so-called *partial cancellation* of the signal of such a mode (Aerts et al., 2010a). The line of sight at which a star is observed also matters for the detectability of a mode. In the example shown in

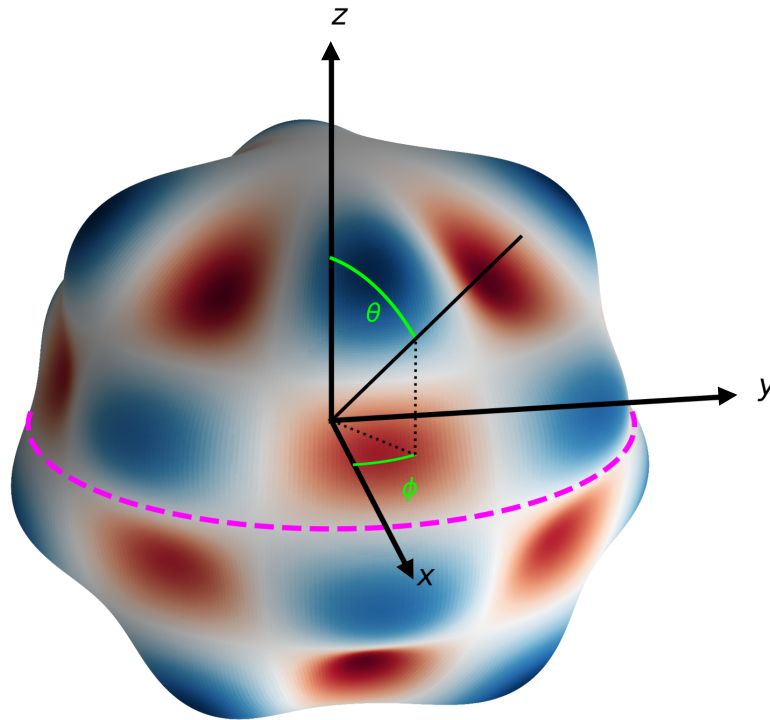


Figure 1.4: Illustration of the deformation of the spherical stellar surface because of a spherical harmonic $Y_{\ell=7}^{m=4}$. The spherical harmonic has been added to a unit sphere to produce this illustration. The blue regions (hills) are moving outwards, the red regions (depressions) are moving inwards, and the white lines indicate the positions with no displacement with respect to the unit sphere (nodal lines). The dashed magenta line shows the equator of the spherical harmonic. The amplitude of the displacement with respect to the unit sphere is exaggerated compared to the amplitudes of real stellar non-radial oscillations.

Fig. 1.4, the $(\ell, m) = (7, 4)$ mode will be harder to detect pole-on than when the star's equator is pointed at us. We focus on oscillations with $\ell > 0$ in this thesis, which are called *non-radial* oscillations. Each mode needs one additional quantum number to describe its morphology, namely the *radial order* or *overtone* n . The radial order gives us the number of nodal surfaces within the star. Modes with $n = 0$, the fundamental modes, only have nodes at the centre and surface of the star.

Knowing the morphology and frequency ν of a mode, we can write down its *wave displacement* $\xi(r, \theta, \phi, t)$ in 3D. This wave displacement is a function of the radial coordinate r and the time t , and its components are (Aerts et al., 2010a)

$$\xi_r(r, \theta, \phi, t) = A(r)Y_\ell^m(\theta, \phi) \exp(-2\pi i\nu t), \quad (1.15)$$

$$\xi_\theta(r, \theta, \phi, t) = B(r) \frac{\partial Y_\ell^m(\theta, \phi)}{\partial \theta} \exp(-2\pi i\nu t), \quad \text{and} \quad (1.16)$$

$$\xi_\phi(r, \theta, \phi, t) = \frac{B(r)}{\sin \theta} \frac{\partial Y_\ell^m(\theta, \phi)}{\partial \phi} \exp(-2\pi i\nu t). \quad (1.17)$$

The amplitudes $A(r)$ and $B(r)$ depend on the driving and damping mechanisms present in the star. Since these mechanisms play a role in Chapter 4, we discuss them shortly in Section 1.2.3 below.

Stellar oscillations can be characterised in another way, namely by their *restoring force*. For a stellar oscillation mode to propagate, there needs to be a force that pushes it towards its original position. For *pressure modes* or *p modes*, this restoring force is the pressure gradient of the stellar material (Aerts et al., 2010a). These p modes are essentially sound or acoustic waves propagating through the star, are most sensitive to the outer layers of stars, and can propagate in both radiative and convective regions. *Gravity modes* or *g modes* are restored by the buoyancy force, so, in other words, they propagate following Archimedes' principle (Aerts et al., 2010a). Hence, in convective regions, the buoyancy force cannot act as a restoring force, and g modes cannot propagate.

More formally, the regions in which p and g modes can propagate, their *mode cavities*, are determined by the Lamb frequency \tilde{S}_ℓ and Brunt-Väisälä (BV) or buoyancy frequency \tilde{N} , defined as⁶ (Aerts et al., 2010a)

$$\tilde{S}_\ell^2 = \frac{\ell(\ell + 1)c_s^2}{4\pi^2 r^2} \quad (1.18)$$

and

$$\tilde{N}^2 = \frac{g}{4\pi^2} \left(\frac{1}{\Gamma_{1,0}} \frac{d \ln P}{dr} - \frac{d \ln \rho}{dr} \right). \quad (1.19)$$

In the expressions above, g is the local gravitational acceleration, $\Gamma_{1,0}$ the first adiabatic exponent and P the pressure. Assuming a fully ionised ideal gas, we can rewrite the expression for the BV frequency \tilde{N} in terms of the temperature gradient ∇ , adiabatic temperature gradient ∇_{ad} , and chemical gradient ∇_μ within the star as

⁶Throughout this thesis, we use *linear* frequencies (as opposed to *angular* frequencies) unless stated otherwise. Therefore, we use the linear definitions of the Lamb and Brunt-Väisälä frequency, indicated by a tilde. The linear definitions of these frequencies are related to their angular definitions N and S_ℓ by $N = 2\pi\tilde{N}$ and $S_\ell = 2\pi\tilde{S}_\ell$, respectively.

$$\tilde{N}^2 \simeq \frac{g^2 \rho}{4\pi^2 P} (\nabla_{\text{ad}} - \nabla + \nabla_{\mu}), \quad (1.20)$$

with

$$\nabla = \frac{d \ln T}{d \ln P}, \quad \nabla_{\text{ad}} = \left(\frac{d \ln T}{d \ln P} \right)_{\text{ad}}, \quad \nabla_{\mu} = \frac{d \ln \mu}{d \ln P}. \quad (1.21)$$

Here, T is the temperature, and μ is the mean molecular weight. This approximate expression shows how a chemical gradient, for example, in the near-core region of an MS star with a receding convective core, can stabilise the stellar matter against convection, which is what happens when $\tilde{N}^2 < 0$. Gravity modes with a linear frequency ν (see Footnote 6) can propagate when $|\nu| < \tilde{S}_{\ell}$ and $|\nu| < |\tilde{N}|$, while pressure modes can propagate when their frequency obeys $|\nu| > \tilde{S}_{\ell}$ and $|\nu| > |\tilde{N}|$. Outside of these mode cavities, the amplitudes of the modes decay exponentially and they are said to be *evanescent*.

In some stars, such as evolved MS stars with convective cores (Unno et al., 1989) and red giant stars (Cunha et al., 2015), the p- and g-mode cavities can overlap in terms of frequency. Provided that the oscillation modes can tunnel through the evanescent zone separating the two cavities, the p and g modes can interact and will have a dual p-g character. These *p-g mixed modes*⁷ thus carry information about the stellar structure in both the p- and g-mode cavity. For example, g modes propagate in the radiative core of red giant stars and cannot propagate in the extended convective envelope of these stars. Thanks to their coupling with the p modes propagating in this convective envelope, asteroseismologists can nevertheless characterise the cores of such stars (Hekker and Christensen-Dalsgaard, 2017). Since p-g mixed modes have radial nodes in both the g-mode and p-mode cavity⁸, extra care is required to describe them in a unique way. To this end, we define n_g as the number of radial nodes in the g-mode character regime, and n_p as the number of radial nodes in the p-mode character regime. The radial order n_{pg} of the p-g mixed mode as a whole is then, following the Eckart-Scuflaire-Osaki-Takata scheme (Takata, 2006, 2012)

$$n_{\text{pg}} = \begin{cases} n_p - n_g & \text{for a } g_{n_p - n_g} \text{ mode} \\ n_p - n_g + 1 & \text{for a } p_{n_p - n_g + 1} \text{ mode} \end{cases}. \quad (1.22)$$

In this scheme, a pure (not mixed) g mode has $n_{\text{pg}} = -n_g$ and a pure p mode has $n_{\text{pg}} = n_p + 1$.

Before we look into how these oscillation modes can be used as diagnostics for the interior structure of stars, we mention some other types of oscillation modes that are observed in stars. *Inertial modes* have the Coriolis force as their main restoring force and can propagate in convective regions. In the near-core region of rotating stars with convective cores, for example, g modes have both the buoyancy and Coriolis force as a restoring force. Such modes are called *gravito-inertial waves* (GIWs) or *gravito-inertial modes*. *Rossby* or *r* modes are a specific subset of the inertial modes. These are toroidal modes (as opposed to the spheroidal modes discussed so far), which can only propagate against the rotation of a star (Aerts, 2021). In stars with magnetic fields, the Lorentz force can also act as an additional restoring force for gravity, inertial, and gravito-inertial modes (Aerts et al., 2019).

⁷In literature, these modes are usually simply referred to as ‘mixed’ modes, but we explicitly refer to them as ‘p-g mixed’ modes to avoid confusion with other types of mode mixing treated in Chapter 4.

⁸As detailed in Takata (2006), the distinction between p and g nodes is based on whether the spatial derivative of the phase angle φ , $d\varphi/dr$, is positive or negative at the node location, respectively.

1.2.2. Asteroseismic diagnostics

The asymptotic theory for non-radial oscillations (Tassoul, 1980) holds for oscillation modes with a high radial order, $n \gg 1$, also called high-order modes. Within this asymptotic regime, several asteroseismic diagnostics can be derived, each of which can be linked to the physical conditions in the mode cavity.

Assuming that we have a chemically homogeneous, non-rotating, non-magnetic star, the asymptotic theory tells us that high-order g modes ($n_g \gg 1$) with the same spherical degree ℓ are equally spaced in period. In other words, the difference in period between two g modes of consecutive radial order,

$$\Delta P_n = P_n - P_{n-1}, \quad (1.23)$$

is constant, with P_n the period⁹ of an oscillation mode with radial order n . For a given degree ℓ , this constant value of the period spacing is the *asymptotic period spacing* Π_ℓ , that is, $\Delta P_n = \Pi_\ell$ with

$$\Pi_\ell = \frac{\Pi_0}{\sqrt{\ell(\ell+1)}} \quad (1.24)$$

and

$$\Pi_0 = \pi \left(\int_{r_i}^{r_o} \frac{\tilde{N}}{r} dr \right)^{-1}. \quad (1.25)$$

The quantity Π_0 is the *characteristic period* or *buoyancy travel time* for high-order g modes (Aerts et al., 2010a) and relates the period spacing to the size of the g-mode cavity, bounded by its inner and outer turning points r_i and r_o . From the definition of the g-mode cavity given in the previous section, we see that these turning points are the points when the star becomes convective, that is, when \tilde{N}^2 becomes negative.

From the observed g modes of a g-mode pulsator, we can construct so-called *period spacing patterns* (PSPs), but only if these modes can be identified, that is, assign an n , ℓ , and m value to each mode. These PSPs are plots of the period spacing between g modes of consecutive radial order ΔP_n as a function of the mode period P_n or the radial order n . For MS stars with convective cores and radiative envelopes, the mean value of an observed PSP is directly related to the extent of their convective core. The mean value of observed PSPs can, therefore, be used to estimate convective core radii and sizes of such stars (Moravveji et al., 2015, 2016; Pedersen et al., 2018, 2021; Mombarg et al., 2019, 2021; Michielsen et al., 2019, 2021; Wu and Li, 2019; Wu et al., 2020b).

In general, stars are not chemically homogeneous, rotate, and can have magnetic fields. As a result, observed PSPs and PSPs constructed for less idealised stellar models will deviate from this constant value Π_ℓ . These deviations hold a wealth of information about the structure and chemical composition of the mode cavities in which these g modes propagate. Structural and chemical gradients and glitches (sudden changes) influence the BV frequency \tilde{N} and, hence, change the shape of the g-mode cavity. For example, the chemical gradient left behind by the receding convective core of an intermediate- or high-mass MS star causes a large peak to form in the \tilde{N} -profile. Glitches in the chemical composition cause spike features to appear in the \tilde{N} -profile. When the spatial extent of such peak and spike features is smaller than or of the same order as the local wavelength of a g-mode pulsation, the mode

⁹We use the more general symbol n instead of n_g in the expression for the period spacing ΔP_n for legibility.

can become trapped. This *mode trapping* leads to quasi-periodic variation away from the mean value Π_ℓ in the star's PSP and has been theoretically predicted (Miglio et al., 2008; Cunha et al., 2015, 2019, 2024) and observed (Degroote et al., 2010) for g-mode pulsators. This effect on the PSPs is shown in Fig. 1.5a. Stellar models with more envelope mixing have weaker chemical gradients and weaker deviations from the constant value Π_ℓ , which is apparent from the PSPs shown in this figure. The interaction or *coupling* between modes of different mode cavities, such as the coupling between p and g modes in p-g mixed modes or between the inertial modes from the convective core of a star with the GIWs in the near-core region can cause dips in the PSP (i.e. locations in the PSP where $\Delta P_n < \Pi_\ell$, Mosser et al., 2012; Cunha et al., 2015; Saio et al., 2018; Tokuno and Takata, 2022; Aerts and Mathis, 2023).

Another deviation from the constant value of a star's PSP is caused by rotation, more specifically, by the Coriolis force. However, theoretically predicting the effect of the Coriolis force on the stellar pulsations is not straightforward. When the Coriolis term is no longer neglected, the stellar oscillation equations become a set of infinitely coupled equations (Aerts and Tkachenko, 2023). For modes with angular frequencies $\omega = 2\pi\nu$ much larger than twice the angular rotation frequency Ω of the star, that is, $\omega \gg 2\Omega$, we can treat the Coriolis force as a perturbation to the original, non-rotating oscillation equations. Such modes are a subset of what we call *super-inertial* modes, which are modes with $\omega > 2\Omega$. For modes with $\omega \lesssim 2\Omega$, called *sub-inertial* modes, the Coriolis force acts as an additional restoring force. Hence, these are the GIWs mentioned in Sect. 1.2.1. For GIWs, the Coriolis force can no longer be treated as a perturbation. High-order g-modes, which have $n_g \gg 1$, typically have frequencies low enough such that $\nu \ll \tilde{S}_\ell$ and $\nu \ll \tilde{N}$. For such modes, we can assume that the vertical wave motions (in the radial direction) are inhibited by the strong chemical and entropy stratification inside the radiative regions of stars with convective cores. We can, therefore, neglect these vertical motions and thus also the horizontal components (the θ and ϕ components) of the rotation vector. As a result, the vertical component of the Coriolis force can be neglected. With this approximation, referred to as the *traditional approximation of rotation* (TAR, Eckart, 1960; Berthomieu et al., 1978; Lee and Saio, 1987; Townsend, 2003; Mathis, 2009), the stellar oscillation equations decouple and can be written in the form of the *Laplace tidal equation* (Laplace, 1799). By solving the Laplace tidal equation, we recover for each mode its corresponding eigenvalue $\Lambda_{s,\ell,m}$, with $s = 2\Omega/\omega$ the *spin parameter*. With these eigenvalues, it is possible to construct a theoretical PSP for gravito-inertial modes in the frame co-rotating with the star,

$$(\Pi_s)_{\text{co}} \simeq \frac{\Pi_0}{\sqrt{\Lambda_{s,\ell,m}} \left(1 + \frac{1}{2} \frac{d \ln \Lambda_{s,\ell,m}}{d \ln s} \right)}. \quad (1.26)$$

Because of the frequency dependence of the period spacing $(\Pi_s)_{\text{co}}$, through the spin parameter s , each mode is affected by the Coriolis force to a different extent. The PSPs for GIWs are not uniform (ignoring the effect of chemical inhomogeneities and mode coupling described above) but have slopes (Bouabid et al., 2013). The sign of these slopes (with respect to the increasing mode period or radial order) depends on the sign of the azimuthal order m of the modes, while their magnitude depends on the value of m and the rotation rate Ω . In the co-rotating frame, *prograde* modes, which have $m > 0$ and travel with the rotation of the star, have PSPs with negative slopes, while *retrograde* modes, which have $m < 0$ and

travel against the star’s rotation, have PSPs with positive slopes. This effect is demonstrated in Fig. 1.5b and 1.5c. Thanks to the theoretical framework of the TAR and observed GIW PSPs, it has been possible to constrain the internal rotation profiles of hundreds of MS stars with convective cores (Van Reeth et al., 2015a,b, 2016; Ouazzani et al., 2017; Van Reeth et al., 2018; Li et al., 2019, 2020; Van Reeth et al., 2022).

Before such comparisons between predicted and observed PSPs of gravito-inertial modes can be made, we need to convert our theoretically predicted mode periods in the co-rotating frame, P_{co} , to periods in the *inertial* or *observer’s frame*, P_{in} . To do this, the Doppler shift needs to be taken into account, which is done as

$$P_{\text{in}} = \frac{P_{\text{co}}}{1 + m \frac{P_{\text{co}}}{P_{\text{rot}}}}, \quad (1.27)$$

with $P_{\text{rot}} = 2\pi/\Omega$ the rotation period of the star.

Just as for high-order g modes, several asteroseismic diagnostics for high-order p modes can be derived within the framework of the asymptotic theory. Going back to our idealised chemically homogeneous, non-rotating, non-magnetic star, the asymptotic theory predicts that high-order p modes of consecutive radial order n_p are equally spaced in frequency (Aerts et al., 2010a). This constant frequency difference is called the *large frequency spacing* $\Delta\nu$ and is an often-used diagnostic (Hekker and Christensen-Dalsgaard, 2017). Analogue to the period spacing for high-order g modes, $\Delta\nu$ is sensitive to small- and large-scale variations in the stellar structure, rotation, and magnetic fields, which cause deviations from a constant large frequency spacing value. The *small frequency spacing* $\delta\nu$, or more precisely the small frequency spacing $\delta\nu_{02}$ between radial ($\ell = 0$) and quadrupole ($\ell = 2$) modes of consecutive radial order n_p , is sensitive to the chemical composition inside the p-mode cavity and is, therefore, a proxy for the star’s age. We will not dive deeper into these asteroseismic diagnostics for high-order p modes since this thesis, more specifically Chapter 5, only focuses on low-order p modes.

1.2.3. Driving and damping mechanisms

This section gives a brief overview of the main driving and damping mechanisms for stellar oscillations. For more details, we refer the reader to Aerts (2021), Aerts et al. (2010a, Chapter 3.7), and Unno et al. (1989, Chapter V). An oscillation mode is said to be *unstable* or *excited* when it has a positive growth rate and *stable* or *damped* when this growth rate is negative. A star usually has tons of eigenmodes, but the stability of the modes tells us which of these, when they start off as a small perturbation, are amplified and sustained enough to still have a non-negligible amplitude at the stellar surface, causing the brightness variations and Doppler shifts we measure. This growth rate varies throughout the star; a mode may be excited (positive growth rate) in some regions and damped (negative growth rate) in others. Operating in a similar way as a classical heat engine, the growth rate of an oscillation mode is positive when the heating of the stellar material is in phase with its compression. Depending on the source of this heating, we generally distinguish between three different heat-engine mechanisms. To make this more concrete, take the energy equation of stellar interiors (Aerts, 2021),

$$\rho T \frac{\partial S}{\partial t} + \rho T \vec{v} \cdot \nabla S = \rho \epsilon - \nabla \vec{F}, \quad (1.28)$$

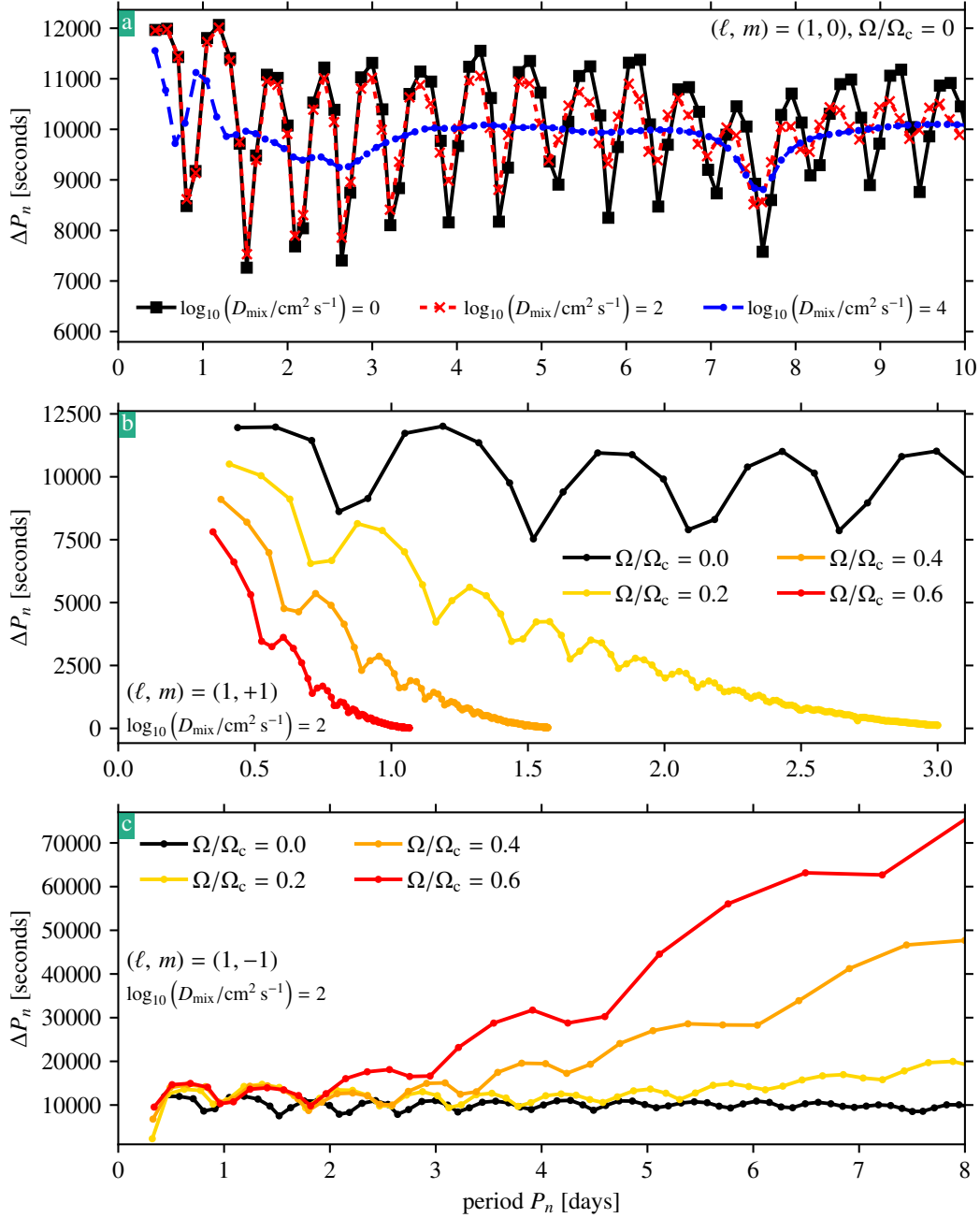


Figure 1.5: Period spacing patterns for g modes in a $7.0 M_{\odot}$ MS star with a central hydrogen mass fraction of $X_c = 0.50$. Panel (a) shows the effect of envelope mixing through the minimal envelope mixing parameter D_{mix} on the period spacing patterns. Panel (b) and (c) show the effect of the Coriolis force, computed with the TAR, on the period spacing patterns for prograde dipole $(\ell, m = 1, +1)$ and retrograde dipole $(\ell, m = 1, -1)$ modes, respectively. This effect is shown for the model with $\log_{10}(D_{\text{mix}}/\text{cm}^2 \text{s}^{-1}) = 2$ for no rotation, 20% of the Roche critical angular rotation rate $\Omega_c = \sqrt{8GM_{\star}/27R_{\star}^3}$, 40% of Ω_c , and 60% of Ω_c .

where S is the specific (i.e. per unit mass) entropy, \vec{v} the velocity of the gas, ϵ the energy generation per unit mass (with energy loss through neutrinos taken into account), and $\vec{F} = \vec{F}_{\text{rad}} + \vec{F}_{\text{conv}}$ the sum of the radiative and convective energy flux.

When the main heat supplier to the stellar gas upon compression is the (nuclear) energy generation, we say that the modes are excited by the ϵ -mechanism. This mechanism is responsible for mode excitation in the inner stellar regions, where nuclear energy generation occurs.

In the outer regions of the star, where we typically find regions of increased opacity because of partial ionisation zones and the iron opacity bump, the radiative energy flux \vec{F}_{rad} is responsible for heating the gas during its compression. Due to its relation to the opacity, this mechanism is often called the κ -mechanism. Because of the increased opacity in certain layers of the star, the radiation essentially pushes on this layer, converting radiative energy into mechanical energy and driving the oscillation mode.

Things become more complicated in the cases where the convective energy flux \vec{F}_{conv} is the main heat source. If a star has a convective outer envelope, for example, when it is a Solar-like oscillator, the convective flux does not lead to a heat-engine mechanism in this envelope. Instead, perturbations to the convective flux and turbulent pressure damp the modes, rendering them stable. However, another form of mode excitation occurs in these situations, namely *stochastic forcing*. In these convective envelopes, convection has a more turbulent, chaotic nature, leading to the creation of random, acoustic noise. Global eigenmodes of the star with frequencies within this range are subsequently excited yet simultaneously strongly damped by the aforementioned processes in convective regions. These modes must be continuously driven by the acoustic noise, and these stochastically forced modes usually span a wide frequency range. Convective motions are more structured (as opposed to turbulent) in the inner convective regions of stars, such as convective cores and near-core convective shells. If the turn-over timescales of the convective motions are similar to those of the star's eigenmodes, convection can also excite modes this way. This mechanism is called *convective forcing*. Predictions for stochastic and convective forcing are plagued by our current simplified descriptions of convection, especially in 1D models. However, 3D simulations are quite valuable in this regard (see references in Aerts 2021 Sect. III.A).

The last excitation mechanism related to convection that we discuss concerns a mode that reaches the boundary of a convective region with convective turn-over timescales several orders of magnitude longer than the period of the mode. In such cases, the convective flux is unaffected by the mode, which is blocked and ‘pushes’ on this boundary (similar to the κ -mechanism). This mechanism is often referred to as *convective flux blocking*.

Apart from stochastic forcing, there are other excitation mechanisms unrelated to the general heat-engine mechanism. *Non-linear resonant mode excitation* is a mechanism in which combinations of ‘parent’ modes, driven by other mechanisms and interacting non-linearly, excite other ‘daughter’ modes. Although the theories behind non-linear mode excitation are not new, their practical exploitation is currently still under development (Aerts, 2021). Given the right orbital period and eccentricity, eigenmodes can also be excited by tides in a close binary system. Such modes are said to be *tidally excited*.

An important point to make here is that our current theoretical mode excitation predictions are lagging behind on the observations (Aerts, 2021). In stars which are known to pulsate, mode instability predictions with the heat-engine mechanism tend to under-predict

the number of excited modes compared to the observed modes (see, e.g. Rehm et al., 2024). Recently, Hey and Aerts (2024) and Mombarg et al. (2024a) showed that even outside of the so-called *instability strips*, regions in the Hertzsprung-Russell diagram (HRD) in which stars are predicted to have excited modes, a significant number of pulsating stars can be found.

1.2.4. The space revolution

In the early years of asteroseismology, asteroseismologists could only rely on ground-based observations of stars to detect and characterise pulsating stars. Although it is possible with time and dedication to get high-quality time-series data from the ground, see, for example, the results from the 21-year-long observational campaign of the hybrid pulsator (pulsating in both p and g modes) HD 129929 by Aerts et al. (2003), the process of getting ground-based time series for asteroseismic purposes has several disadvantages. The frequency resolution of time series data is the inverse of the total observation time. Especially for g modes, which have longer periods than p modes, long observational baselines are required to get sufficient frequency resolution. Getting these long observational baselines from the ground, where the day-night cycle, weather conditions, observational schedules, and the time certain targets are observable from a specific location all play a role, is challenging. The day-night cycle leads to another difficulty in time-series data in the form of *aliasing*. If one observes a star every night for a certain number of days, the Fourier spectrum of these observations will be contaminated by a series of peaks at multiples of 1/day, which is especially problematic for stars exhibiting pulsations with periods on the order of a day. For a concise overview of the challenges and pitfalls of ground-based asteroseismic observations, we refer the reader to Aerts et al. (2010a), which was published on the advent of the space revolution of asteroseismology. Asteroseismic measurements based on spectroscopy do benefit from being ground-based. For example, the Stellar Oscillations Network Group (SONG, Grundahl et al., 2006; Andersen et al., 2016) is a project that set up a network of telescopes around the globe with the aim of providing high-resolution spectroscopic time series. Such time series are required for radial velocity measurements and detecting line profile variability. Even though space-based spectroscopy is possible, getting high-quality spectroscopy from the ground is often more efficient.

Going to space alleviates many of the problems plaguing ground-based photometric time-series observations. Observations can go on (nearly) uninterrupted, independent of the weather and the day-night cycle, atmospheric effects are no longer contributing to the overall noise budget, and observational baselines of years are possible for more than one target simultaneously. What we have been referring to as the ‘space revolution’ (a term borrowed from the review of Bowman et al. 2020) started with two cases of ‘piggyback riding’ (Buzasi, 2000). Using data from the European Space Agency’s (ESA) *Hipparcos* mission (van Leeuwen et al., 1997), a telescope intended for astrometry and a predecessor of the *Gaia* space mission, Waelkens et al. (1998), Koen and Eyer (2002), Aerts et al. (2006), and Lefèvre et al. (2009) were able to detect and characterise hundredths of pulsating stars (Bowman et al., 2020). Around the same time, Buzasi (2000) proposed repurposing NASA’s Wide-field InfraRed Explorer (WIRE) mission for asteroseismic measurements. The primary science instrument, built to study galaxies, was damaged beyond repair because of problems during the spacecraft’s deployment in orbit. However, its star guiding camera, as Buzasi (2000) realised, could be used to measure the brightness variations of

stars. These two endeavours, in which asteroseismic studies were conducted using instruments and spacecraft intended for other purposes (hence ‘piggyback riding’), showcased the potential of space-based asteroseismic observations to the astronomy community.

These proof-of-concept studies undertaken using the WIRE and *Hipporacos* spacecrafts prompted the first dedicated asteroseismic space mission called Microvariability and Oscillations of STars (MOST¹⁰) by the Canadian Space Agency (CSA), launched in 2003. Despite its limitations (compared to the specifications of today’s space missions), MOST was a successful mission, revealing pulsations in stars across many classes of pulsators, which are shown on the asteroseismic HRD in Fig. 1.6, and proved to be a definite improvement for detecting pulsation modes compared to ground-based observations (Aerts, 2021).

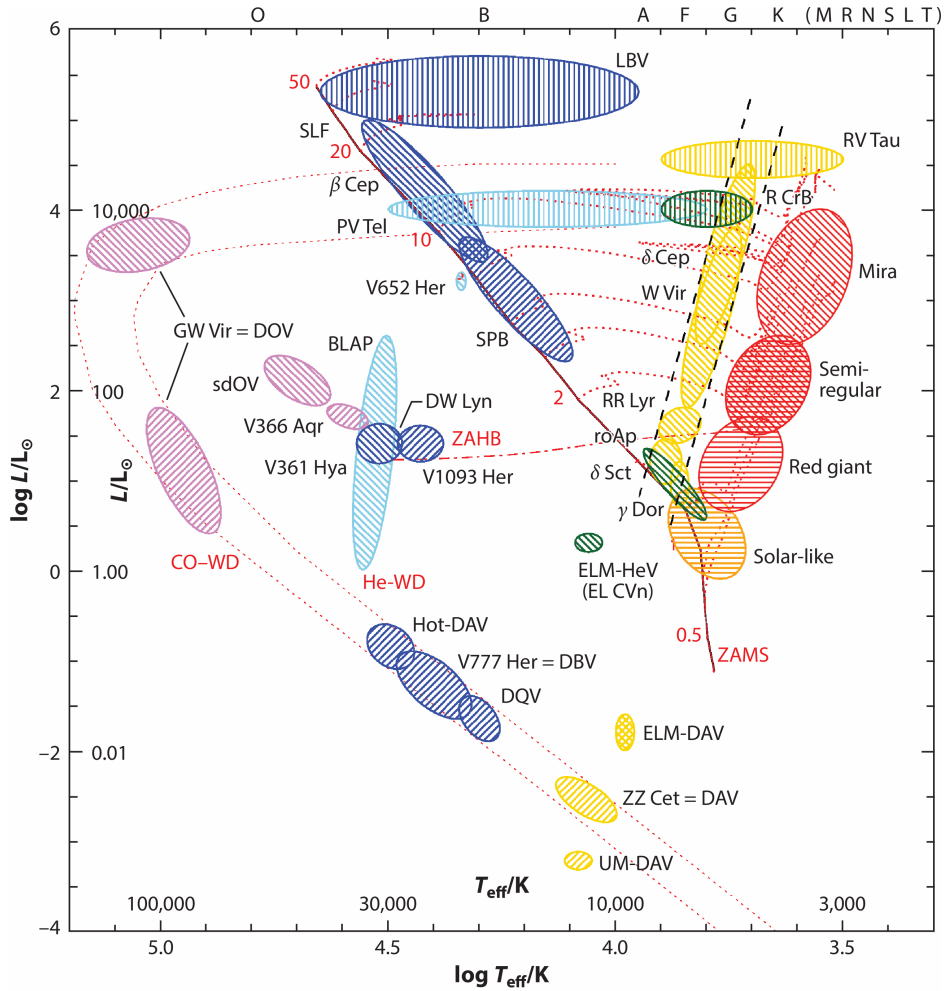
After MOST came the Convection, Rotation & planetary Transits (CoRoT, Auvergne et al., 2009) mission, which started operating in 2007. CoRoT was a hybrid mission dedicated not only to asteroseismology but also to detecting exoplanets via the transit method. Like the MOST mission, CoRoT detected pulsations in many different classes of pulsators, from low- to high-mass stars (for an overview, see Aerts 2021). One of the many highlights of the CoRoT science output is the proper asteroseismic characterisations of Sun-like stars and red giants.

The BRiGht Target Explorer (BRITE) mission, launched in 2013 and born out of a collaboration between Austria, Poland, and Canada, consisted of a constellation of nanosatellites that obtained long-term photometric time series of the brightest stars in the sky (Bowman et al., 2020). These bright stars are excluded from the CoRoT and *Kepler* (see next paragraph) missions, making BRITE a key mission in the asteroseismic studies of massive stars. Furthermore, BRITE collected photometric time series in two wavelength passbands (red and blue) simultaneously, which allowed the data to be used for mode identification (Weiss et al., 2014).

The *Kepler* (Koch et al., 2010, launched in 2009) and Transiting Exoplanet Survey Satellite (TESS, Ricker et al., 2016, launched in 2018) missions’ primary goal is the detection of exoplanets (in the case of *Kepler*, the focus was on Earth-sized planets specifically). However, in the process of finding these exoplanets, valuable data for asteroseismic purposes were/are collected. Whereas *Kepler*’s target list contained mostly low-mass stars, TESS has also been observing massive (intermediate- and high-mass) stars. Both missions can provide photometric time series with observational baselines on the order of years, which lead to extremely small uncertainties on the derived oscillation mode frequencies (see Table 1 in Aerts et al. 2019 for an overview of these uncertainties). After four years of observing, *Kepler* lost an essential reaction wheel and could not observe its intended field of view any longer. The spacecraft was then repurposed to observe patches of the sky containing more massive stars for periods of 80 days (Howell et al., 2014). This new mission was dubbed K2 and is another example of space-based recycling. The upcoming PLAnetary Transits and Oscillations of stars (PLATO, Rauer et al., 2024) mission, again primarily an exoplanet mission suited for asteroseismology, will continue to observe a plethora of pulsators and is *planned* to be launched in 2026.

These space missions have not only lifted the quality of asteroseismic data (at least two orders of magnitude improvement in precision, Bowman et al. 2020) to higher levels but also the quantity of detected pulsating stars. The *Kepler* mission alone provided four-year long

¹⁰Given that this is a Canadian mission, we also provide the acronym in French: Microvariabilité et Oscillations STellaire.



 Kurtz DW, 2022
Annu. Rev. Astron. Astrophys. 60:31–71

Figure 1.6: Asteroseismic HRD from Kurtz (2022). The dashed red lines show single-star evolution tracks for different initial masses in units of M_{\odot} . The classical Cepheid instability strip is indicated by the two dashed black lines. The instability strips for other pulsator classes are indicated by the hatched ellipses. The κ -mechanism instability strips for the g and p modes are shown with // and \\ hatching, respectively. Stochastically excited pulsators are shown with ≡ hatching, and strange-mode pulsators (see Kurtz 2022 for more details about strange modes) with ||| hatching. See Aerts et al. (2010a, Chapter 2) and Kurtz (2022) for the definitions of the different classes shown in the figure with their abbreviated names.

photometric time series for upwards of 200 000 stars. As recent works by Hey and Aerts (2024), Fritzewski et al. (2024b), and Mombarg et al. (2024a) show, the asteroseismic space revolution and the steady development of sophisticated software tools have brought us from being able to characterise and model individual pulsators to the advent of population-based studies of pulsating stars.

1.3. Numerical methods

The works presented in this thesis are all of a theoretical nature. Using the theories of single and binary star evolution, stellar structure, and asteroseismology, parts of which are presented in the preceding sections, we computed evolutionary models of binary systems and merger products, and predicted stellar oscillations. To do so, we used a set of often-used numerical codes. Since these codes are only mentioned but not explained in the method sections of the upcoming chapters, we give a brief overview of the workings and assumptions of the stellar/binary evolution and pulsation codes used in this thesis.

1.3.1. Stellar and binary evolution

Stars, especially those in binary systems, are typically not spherically symmetric objects. We have seen in the preceding sections how the Roche geometry (even though it is derived for point-mass stars) and tides deform stars. The centrifugal force in a rotating star turns the star into an oblate spheroid. Internal processes such as convection, with its large-scale boiling motions, are evidently not well described in a spherically symmetric setting.

Despite these fundamental departures from spherical symmetry, we are, to this day, still forced to resort to 1D (i.e. spherically symmetric) approximation of stars to be able to evolve them over evolutionary timescales within a reasonable amount of time. 3D processes such as convection can be simulated in specific regions of a star for a time on the order of a few dynamical timescales only, although this requires some clever tricks (see, e.g. [Andrassy et al. 2024](#)). Even though important steps forward have been taken recently for stellar evolution in 2D ([Mombarg et al., 2023, 2024b](#)), it is not yet in a mature enough stage to evolve a wide variety of stars, let alone stars in binary systems. In other words, the standard for stellar evolution computations is still 1D.

To compute a star's structure and evolution, a 1D stellar structure and evolution (SSE) code needs to solve the set of non-linear coupled differential equations of stellar structure. [Iben and Ehrman \(1962\)](#), [Henyey et al. \(1964\)](#), [Hofmeister et al. \(1964\)](#), and [Kippenhahn et al. \(1967\)](#) were the first to use the recently made available electronic computers to solve the set of stellar structure equations. In this thesis, we have used the open-source and community-driven SSE code Modules for Experiments in Stellar Astrophysics (MESA, [Paxton et al., 2011, 2013, 2015, 2018, 2019](#); [Jermyn et al., 2023](#)). MESA is based on Peter Eggleton's stellar structure and evolution code ([Eggleton, 1971, 1972, 1973](#); [Eggleton et al., 1973](#)), which became to be known as the Cambridge STARS code ([Pols et al., 1995](#)). The STARS code was rewritten by [Paxton \(2004\)](#) and eventually transformed into its modular (i.e. each of the modules, such as the opacity and equation of state modules, can be used independently) form by [Paxton et al. \(2011\)](#). Other SSE codes exist, such as the PAdova TRIeste Stellar Evolutionary Code (PARSEC, [Bressan et al., 2012](#)), the Geneva Code (GENEC, [Eggenberger et al., 2008](#)), the STAREVOL code ([Forestini et al., 1991](#); [Siess et al., 2000](#); [Siess, 2006](#)), the STERN code ([Yoon and Langer, 2003](#)), and the Garching Stellar Evolution Code

(GARSTEC, Weiss and Schlattl, 2008). Even though MESA, thanks to its open-source nature and large community, seems to dominate SSE calculations in recent years, it is important to remember that it, like the other codes, has its strengths and weaknesses. As a community, we should, therefore, keep comparing these codes, use them in a complementary fashion, and avoid a situation in which all SSE predictions are made with one single code.

MESA solves the set of stellar structure equations using a *Newton-Raphson scheme*. This scheme is an iterative root-finding algorithm. In the simplest case, for finding the root of a 1D function $f(x)$, it uses the function value and derivative $f'(x)$ at the previous estimate of the root, x_n , to find a better estimate of the root, x_{n+1} (Scherer, 2017):

$$x_{n+1} = x_n - \frac{f(x_n)}{f'(x_n)}. \quad (1.29)$$

This scheme works well if the function $f(x)$ is at least two times differentiable around the root and the initial guess for the root, x_0 , is chosen sufficiently close to the actual one. In MESA, which has to solve a system of non-linear coupled differential equations, the update rule to find an acceptable solution for the stellar structure has the following form (Paxton et al., 2011):

$$\vec{F}(\vec{y}) = \vec{F}(\vec{y}_i + \delta\vec{y}_i) = \vec{F}(\vec{y}_i) + \left[\frac{d\vec{F}}{d\vec{y}} \right]_i \delta\vec{y}_i + \mathcal{O}(\delta\vec{y}_i^2) = 0. \quad (1.30)$$

Here, \vec{y}_i is the vector containing the trial solution for the physical quantities, \vec{F} the set of differential equations, $\vec{F}(\vec{y}_i)$ the residual, $\delta\vec{y}_i$ the correction, and $[d\vec{F}/d\vec{y}]_i$ the Jacobian matrix (i.e. the matrix containing the partial derivatives). Over the course of multiple iterations, MESA attempts to minimise the residual and correction to a point where they satisfy a set (which can be set, to an extent, by the user) of convergence criteria. Solving the stellar structure equation is one step in the scheme MESA follows to evolve a stellar model over one timestep:

1. Remesh the model's spatial grid based on a specific set of criteria.
2. Take into account any changes to the total mass of the star (e.g. because of stellar winds), adjust its chemical structure based on the diffusion and changes because of nuclear burning, compute the convective diffusion coefficients (to go from 3D to 1D, convection is treated as a diffusive process), and solve the stellar structure equations using the Newton-Raphson scheme.
3. Estimate the next timestep based on a set of specific criteria.
4. Write out the output files.

To evolve a binary star, MESA evolves two single stars (MESA has the option to treat the accretor star as a point mass, but we do not make use of this in this thesis) within the same timestep. It computes the mass transfer rate following a 1D prescription, as mentioned in Sect. 1.1.4, and changes the masses of the two stars accordingly in the second step of the evolution scheme above. After going through the evolution step for the two components, MESA takes into account the changes in angular momentum of the orbit and the components. The binary module of MESA was introduced in Paxton et al. (2015), and is a continuation of the works of Madhusudhan et al. (2006) and Lin et al. (2011). These works, along with other parts of the code, were implemented in MESA by Pablo Marchant (Marchant, 2017).

1.3.2. Stellar oscillations

To predict the eigenmodes and eigenfrequencies for a specific stellar structure profile, which we call the *equilibrium model*, we need to solve the linearised stellar oscillation equations (see, e.g. Smeyers and van Hoolst, 2010). This is a set of differential equations governing small perturbations to the equilibrium structure with boundary values at the surface and in the model’s centre that needs to be solved numerically (Townsend and Teitler, 2013).

Traditionally, there have been two types of numerical schemes to solve this boundary-value problem (BVP): *relaxation schemes*, such as the Newton-Raphson scheme described above, and *shooting schemes*. In the latter, the BVP is split up into two initial value problems (IVPs), each starting from one of the boundaries. The solutions (i.e. the eigenfrequencies) are recovered by matching the solutions of the two IVPs at a certain interior point where they meet (Townsend and Teitler, 2013).

In this thesis, we use the stellar oscillation code GYRE (Townsend and Teitler, 2013; Townsend et al., 2018), which uses the ‘Magnus Multiple Shooting’ scheme. This scheme, described in Townsend and Teitler (2013), alleviates some typical problems with simpler shooting schemes. Stellar oscillation codes using relaxation schemes are the BOOJUM code (Townsend, 2005), the Nice Oscillation code (NOC, Provost, 2008), the Granada Oscillation code (GRACO, Moya and Garrido, 2008), and the Linear NonAdiabatic NonRadial (LNAWENR, Suran, 2008) code. Codes using some sort of shooting scheme are the Aarhus adiabatic oscillation package (ADIPLS, this code can use both a relaxation and a shooting scheme, Christensen-Dalsgaard, 2008), the Porto Oscillation Code (posc, Monteiro, 2008), and the OSCROX code (Roxburgh, 2008).

Generally speaking, GYRE has two modes, the adiabatic one and the non-adiabatic one. In the adiabatic mode, GYRE computes the eigenfrequencies and eigenmodes for an equilibrium model ignoring the change in energy of the oscillations. Hence, as seen in Sect. 1.2.3, it does not take into account the driving and damping of modes. In the non-adiabatic mode, this energy exchange is taken into account, albeit only in the form of the κ -mechanism. Although it is often sufficient to use the adiabatic form of the oscillation equations if one is not interested in mode excitation and damping, there are situations in which the non-adiabatic mode is warranted. For example, in the outer regions of massive stars, the thermal timescale becomes relatively short and the p modes can no longer be assumed to propagate adiabatically.

1.4. Overview of this thesis

With the stellar astrophysics community having warmed up to the idea that the products of binary evolution are not merely an afterthought but rather play a critical role in stellar populations (Marchant and Bodensteiner, 2024), stellar mergers and their products have emerged as a potential explanation for a wealth of peculiar observations. The progenitor of the core-collapse supernova SN 1987A, which was a blue supergiant and not a red supergiant as expected from single stellar evolution, has been shown to likely have been a merger product (e.g. Podsiadlowski et al., 1990; Podsiadlowski, 1992; Morris and Podsiadlowski, 2007). More generally, the products of post-MS stellar mergers can stay in the blue part of the HG for millions of years, appearing and even ending their evolution as blue supergiants (Bellinger et al., 2024; Schneider et al., 2024). Therefore, these merger products serve as a

natural explanation for the *blue supergiant problem*¹¹ (Castro et al., 2014, 2018; de Burgos et al., 2023; Bernini-Peron et al., 2023). As mentioned in Sect. 1.1.5.4, various transients, such as the luminous red novae (or *gap transients*) V1309 Sco (Tylenda et al., 2011; Stępień, 2011), V838 Mon (Soker and Tylenda, 2007) and V4332 Sgr (Tylenda et al., 2005), and the great eruption of η Carina (Frew, 2004; Gallagher, 1989; Iben, 1999; Podsiadlowski et al., 2006; Morris and Podsiadlowski, 2006; Podsiadlowski, 2010; Fitzpatrick, 2012; Portegies Zwart and van den Heuvel, 2016; Smith et al., 2018; Owocki et al., 2019; Hirai et al., 2021), can be linked to the dynamical merger phase itself. When two MS stars merge, the mass of the merger product can be higher than the MS turn-off mass in a cluster, that is, the mass of the most massive MS stars that have not yet evolved off the MS. Such merger products appear as *blue stragglers* (e.g. Rasio, 1995; Sills et al., 1997, 2001; Mapelli et al., 2006; Glebbeek et al., 2008; Ferraro et al., 2012; Schneider et al., 2015). Moreover, MS merger products can *rejuvenate* (injection of fresh hydrogen into the hydrogen-burning core, see, e.g. Braun and Langer 1995) and evolve as seemingly normal, younger MS stars, leading to age discrepancies when they are analysed. Merger products may be rotating relatively slowly (Schneider et al., 2019), forming the blue main sequence in cluster observations (Wang et al., 2022). As shown by Menon et al. (2024), the luminosity, effective temperature, surface gravity, and surface abundances of merger products can differ significantly from those of *genuine* single stars (i.e. stars born as single stars). The peculiar surface abundances of merger products have also been used as a potential explanation for α -rich young stars (e.g. Chiappini et al., 2015; Martig et al., 2015; Izzard et al., 2018; Hekker and Johnson, 2019). The turbulent and shearing flows during the stellar merger phase of low-mass (Ryu et al., 2024) and massive (Schneider et al., 2019) stars have been demonstrated to amplify seed magnetic fields. This leads to the formation of merger products with strong, large-scale magnetic fields observable at the stellar surface. The presence of such fields in stars such as τ Sco (Schneider et al., 2016, 2020) and one of the binary components of HD 148937 (Frost et al., 2024) thus provides compelling evidence for their merger origin. Furthermore, these magnetic merger products are likely the progenitors of highly-magnetic white dwarfs and magnetars (e.g. Tout et al., 2004; Ferrario and Wickramasinghe, 2005; Wickramasinghe and Ferrario, 2005; Wickramasinghe et al., 2014; Shenar et al., 2023). Lastly, some of the most massive stars in the Universe are predicted to have been formed through stellar mergers (e.g. Portegies Zwart et al., 1999; Banerjee et al., 2012; Schneider et al., 2014; Boekholt et al., 2018).

It is, however, important to have a solid base when invoking the stellar merger scenario in the explanations for the transient phenomena and peculiar stellar properties given above. Thus, it is essential to know which binary systems are likely progenitors of stellar mergers. Furthermore, we want to characterise these progenitor binary and contact systems to provide satisfactory explanations for the mass-ratio distributions of contact binaries (Kobulnicky et al., 2022), especially the massive ones (Abdul-Masih et al., 2022). Even though they are considered essential in forming gravitational wave sources, the progenitor systems and onset of classical common envelope phases have not been characterised and mapped consistently. Modern 3D simulations of binary-evolution-driven stellar merger (Schneider et al., 2019) and classical common envelope (Moreno et al., 2022; Lau et al., 2022a,b; Morán-Fraile et al., 2023; Röpke and De Marco, 2023; Vetter et al., 2024) can benefit from more realistic input models too. More generally, predictions for the outcomes of binary evolu-

¹¹The blue supergiant problem arises from the fact that blue supergiant stars are abundant in the Hertzsprung gap, despite single-stellar evolution theory predicting that stars rapidly evolve through this part of the HRD.

tion are valuable for binary and compact object population studies. Lastly, fast population synthesis models predict that between 50% to 95% of mass-transferring binaries (depending on the initial primary mass) experience a *dynamical interaction*, that is, a stellar merger of classical/double-core CE phase (Schneider et al., 2015). These challenges form the basis for the first part of this thesis. In Chapter 2 and 3, we present two grids of several thousand detailed 1D binary evolution models with different assumptions regarding the mass-transfer efficiency. These two grids have been computed with the lowest (Chapter 2) and highest (Chapter 3) physically possible mass-transfer efficiency. The actual mass-transfer efficiency of binary systems is expected to lie in between these two extremes. With these grids, we conduct a ‘contact tracing’ exercise to determine which binary systems evolve towards contact binaries and classical/double-core common envelope phases. We predict which contact binaries will likely merge, synthesise our population of binary evolution models to provide statistics that can serve as input in future work, and compare the predicted contact binaries with observed systems.

So far, the peculiar properties attributed to stellar merger products concern so-called surface diagnostics. At the same time, stellar merger simulations show that the interior structures of merger products can be considerably different from genuine single stars (e.g. Glebbeek et al., 2013; Schneider et al., 2019). As discussed in the preceding sections, with asteroseismology, we can probe these stellar interiors. Asteroseismology can thus, potentially, give us an additional, less ambiguous set of diagnostics for distinguishing merger products from genuine single stars by exploiting their internal differences. Moreover, if a star’s merger origin imprints a detectable signature in its stellar pulsations, this signature could help confirm that some of the aforementioned peculiarities in surface properties are indeed related to this merger origin. Therefore, in the second part of this thesis, we make asteroseismic predictions for merger products and genuine single stars. By comparing these predictions for stars that otherwise have similar surface diagnostics, we assess the potential of asteroseismology to distinguish merger products from genuine single stars. In Chapter 4, we focus on merger products formed after one of the binary components has left the main sequence (Case-Be mergers). As mentioned above, these types of merger products are of special interest because they remain in the blue part of the HRD for millions of years and are, therefore, a potential explanation of the blue supergiant problem. In Chapter 5, we use similar tools as in Chapter 4 to assess whether products of the merger between two MS stars (Case-A mergers) can be identified based on their asteroseismic characteristics. Lastly, in Chapter 6, we list all of our conclusions for the work presented in this thesis and look at how this work can serve as a basis for future research in the fields of binary evolution, asteroseismology, and their rapidly expanding interface.

Contact tracing of binary stars: Pathways to stellar mergers

AUTHORS Jan Henneco, Fabian R. N. Schneider, and Eva Laplace

CHAPTER INFO This chapter is a reproduction of the first paper I published as part of my doctoral studies, Henneco et al. (2024b), A&A, vol. 682, A169. It covers the search and characterisation of the progenitors of contact systems and stellar mergers through a grid of one-dimensional binary star evolution models. I was the main author of this work, and I computed, analysed, and interpreted the models. Fabian Schneider was my doctoral supervisor during this work. He was instrumental in shaping this project. Both Fabian Schneider and Eva Laplace assisted me in the interpretation of the results and provided helpful comments and suggestions for the main text and figures.

ABSTRACT Stellar mergers are responsible for a wide variety of phenomena such as rejuvenated blue stragglers, highly magnetised stars, spectacular transients, iconic nebulae, and stars with peculiar surface chemical abundances and rotation rates. Before stars merge, they enter a contact phase. Here, we investigate which initial binary-star configurations lead to contact and classical common-envelope (CE) phases and assess the likelihood of a subsequent merger. To this end, we computed a grid of about 6000 detailed 1D binary evolution models with initial component masses of $0.5\text{--}20.0 M_{\odot}$ at solar metallicity. Both components were evolved, and rotation and tides were taken into account. We identified five mechanisms that lead to contact and mergers: runaway mass transfer, mass loss through the outer Lagrange point L_2 , expansion of the accretor, orbital decay because of tides, and non-conservative mass transfer. At least 40% of mass-transferring binaries with initial primary-star masses of $5\text{--}20 M_{\odot}$ evolve into a contact phase; $> 12\%$ and $> 19\%$ likely merge and evolve into a CE phase, respectively. Because of the non-conservative mass transfer in our models, classical CE evolution from late Case-B and Case-C binaries is only found for initial mass ratios $q_i < 0.15\text{--}0.35$. For larger mass ratios, we find stable mass transfer. In early Case-B binaries, contact occurs for initial mass ratios $q_i < 0.15\text{--}0.35$, while in Case-A mass transfer, this is the case for all q_i in binaries with the initially closest orbits and $q_i < 0.35$ for initially wider binaries. Our models predict that most Case-A binaries with mass ratios of

$q < 0.5$ upon contact mainly get into contact because of runaway mass transfer and accretor expansion on a thermal timescale, with subsequent L_2 -overflow in more than half of the cases. Thus, these binaries likely merge quickly after establishing contact or remain in contact only for a thermal timescale. On the contrary, Case-A contact binaries with higher mass ratios form through accretor expansion on a nuclear timescale and can thus give rise to long-lived contact phases before a possible merger. Observationally, massive contact binaries are almost exclusively found with mass ratios $q > 0.5$, confirming our model expectations. Because of non-conservative mass transfer with mass transfer efficiencies of 15–65%, 5–25%, and 25–50% in Case-A, -B, and -C mass transfer, respectively (for primary-star masses above $3 M_{\odot}$), our contact, merger, and classical CE incidence rates are conservative lower limits. With more conservative mass transfer, these incidences would increase. Moreover, in most binaries, the non-accreted mass cannot be ejected, raising the question of the further evolution of such systems. The non-accreted mass may settle into circumstellar and circumbinary disks, but could also lead to further contact systems and mergers. Overall, contact binaries are a frequent and fascinating result of binary mass transfer of which the exact outcomes still remain to be understood and explored further.

2.1. Introduction

Mergers of non-compact stars frequently occur in the Universe (Podsiadlowski et al., 1992; Sana et al., 2012; de Mink et al., 2014). They can be caused by the evolution of the components in a binary system, during which the stars come into contact because of their radial expansion or orbital decay. Such orbital decay is not necessarily a result of the binary evolution itself, but can also be induced by von Zeipel-Kozai-Lidov oscillations (von Zeipel, 1910; Lidov, 1962; Kozai, 1962; Naoz, 2016) caused by a third component or a circumbinary disk (e.g. Lubow and Artymowicz, 2000; Perets and Fabrycky, 2009; Toonen et al., 2020, 2022). A third option is dynamically driven mergers, which occur during close encounters between stars in dense stellar environments (e.g. Hills and Day, 1976; Portegies Zwart et al., 1997, 1999, 2004).

The products of stellar mergers can explain a multitude of objects. Examples include blue stragglers (e.g. Rasio, 1995; Sills et al., 1997, 2001; Mapelli et al., 2006; Glebbeek et al., 2008; Ferraro et al., 2012; Schneider et al., 2015), some of the most massive stars observed in the Universe (e.g. Portegies Zwart et al., 1999; Banerjee et al., 2012; Schneider et al., 2014; Boekholt et al., 2018), B[e] supergiants (e.g. Podsiadlowski et al., 2006; Wu et al., 2020a), OBA stars with large-scale surface magnetic fields (Schneider et al., 2019), highly-magnetic white dwarfs and magnetars (e.g. Tout et al., 2004; Ferrario and Wickramasinghe, 2005; Wickramasinghe and Ferrario, 2005; Wickramasinghe et al., 2014; Shenar et al., 2023), and α -rich young stars (e.g. Chiappini et al., 2015; Martig et al., 2015; Izzard et al., 2018; Hekker and Johnson, 2019). Transients linked to stellar mergers include supernovae such as the core-collapse supernova SN 1987A (e.g. Podsiadlowski et al., 1990; Podsiadlowski, 1992; Morris and Podsiadlowski, 2007), the great eruption of η Car (Frew, 2004; Gallagher, 1989; Iben, 1999; Podsiadlowski et al., 2006; Morris and Podsiadlowski, 2006; Podsiadlowski, 2010; Fitzpatrick, 2012; Portegies Zwart and van den Heuvel, 2016; Smith et al., 2018; Owocki et al., 2019; Hirai et al., 2021), and luminous red novae such as V1309 Sco (Tylenda et al., 2011; Stępień, 2011), V838 Mon (Soker and Tylenda, 2007), and V4332 Sgr (Tylenda et al., 2005).

Three-dimensional simulations of stellar mergers with magnetohydrodynamic (MHD, Schneider et al., 2019) and smoothed particle hydrodynamic (SPH, Sills et al., 1997, 2001; Freitag and Benz, 2005; Dale and Davies, 2006; Suzuki et al., 2007; Gaburov et al., 2008a; Antonini et al., 2011; Glebbeek et al., 2013; Ballone et al., 2023) codes provide useful insights into the merger events and merger products (Schneider et al., 2020; Costa et al., 2022). However, to obtain realistic initial conditions for these computationally expensive simulations, it is crucial to understand in which binary configurations stellar mergers are most commonly expected to occur. Moreover, it is important to characterise the interior structures of stars directly before they enter a merger phase, as these largely determine the merger outcome.

Before stars in a binary system merge, they go through a phase of contact (e.g. Langer, 2012). Yet, not every contact phase necessarily leads to a merger. These contact phases can be (over-)contact binaries in which both stars (over-)fill their Roche lobe¹, or classical common-envelope (CE) phases, in which one star is engulfed by the envelope of the other star (e.g. Ivanova et al., 2013). Hence, as a first step towards predicting the occurrence of mergers, it is important to determine in which binary configurations contact phases occur and what the outcomes of these phases are. Mapping the occurrence of contact binaries using detailed 1D binary evolution simulations has been carried out, for example, by Pols (1994), Wellstein et al. (2001), de Mink et al. (2007), Claeys et al. (2011), and Mennekens and Vanbeveren (2017) for massive stars. Marchant et al. (2016) and Menon et al. (2021) additionally computed through contact binary phases, which yields information on their lifetime and stability (i.e. likelihood to merge). More recently, three extended grids of detailed binary evolution models, spanning masses of 0.5-300 M_{\odot} , have been computed as part of the binary population synthesis code POSYDON (Fragos et al., 2023). These contain valuable information about the onset of contact phases. Using rapid binary population synthesis codes, de Mink et al. (2014) and Schneider et al. (2014) evolved entire populations of binary systems and mapped the occurrence of contact phases.

In this work, we use a grid of low-mass and massive binary evolution models with component masses between 0.5 and 20.0 M_{\odot} at solar metallicity ($Z = 0.0142$, Asplund et al. 2009) to trace the occurrence of contact phases over the complete range of initial mass ratios² and orbital separations. We evolve both components and include physical processes such as stellar winds, rotation, and tidal interactions. It is known that binary systems can evolve towards tidal instabilities, which lead to rapid orbital decay and subsequent mergers (Darwin, 1879). These instabilities have been proposed to be responsible for the lack of observations of W UMa type contact binaries at low mass ratios (Rasio, 1995) and the final spiral-in of the progenitor system of V1309 Sco (Stępień, 2011).

Including these physical processes allows us to arrive at a picture of the physical mechanisms leading to contact and their likelihood to lead to stellar mergers that is as complete as possible. Moreover, it illustrates the relative importance of, for example, tides, wind-mass loss, and mass-transfer efficiency on the evolution of binaries. We allow for non-conservative mass transfer and expect differences in the occurrence rate of contact binaries compared to works that assume conservative mass transfer (e.g. Pols, 1994; Wellstein et al., 2001; Menon et al., 2021) or that use fixed mass-transfer efficiencies (e.g. de Mink et al.,

¹For simplicity, we use ‘contact’ to refer to both contact and ‘overcontact’ systems.

²In this work, the mass ratio q is always defined as the mass of the less massive star over the mass of the more massive star.

2007; Claeys et al., 2011). Lastly, by including low-mass and massive binaries in our grid, we can compare the onset of contact over a wide mass range.

This chapter is structured as follows. In Sect. 2.2, we describe the computational setup of the grid of binary evolution models. Section 2.3 covers the physical mechanisms that have been identified to lead to contact phases, their likelihood to result in a merger, and the way in which they are traced throughout the evolution of the binary models. Our findings of the occurrence of contact phases and mergers over the whole mass range, as well as some notable cases, are given in Sect. 2.4. Our results are discussed in Sect. 2.5, and summary and conclusions can be found in Sect. 2.6.

2.2. Methods

We computed a grid of 5957 1D binary evolution models using the binary module of MESA (release 12778; Paxton et al., 2011, 2013, 2015, 2018, 2019). First, we describe the adopted single-star physics used in the stellar models in Sect. 2.2.1 before describing the binary star physics in Sect. 2.2.2. We briefly outline the setup of the grid in Sect. 2.2.3 and list the stopping conditions of our binary evolution models in Sect. 2.2.4. In Sect. 2.2.5, we describe how we compute the birth probabilities for the binaries in our grid, which we use for population studies.

2.2.1. Adopted stellar physics

Each binary component was initialised from a precomputed zero-age main-sequence (ZAMS) model at solar metallicity, that is, $Z = 0.0142$ and $Y = 0.2703$ (Asplund et al., 2009). We used a blend of the OPAL (Iglesias and Rogers, 1993, 1996) and Ferguson et al. (2005) opacity tables appropriate for the chemical composition of Asplund et al. (2009). We allowed the stars to rotate using the shellular approximation as implemented in MESA, with a limit on the rotation rate at 97% of the Roche critical rotation rate $\Omega_c = \sqrt{GM/R_{\text{eq}}^3} \approx \sqrt{8GM/27R^3}$ (Maeder, 2009). In this expression, M and R are the mass and radius of the star, respectively, G is the gravitational constant and R_{eq} is the equatorial radius of a rotationally deformed star. All models were hydrostatic, meaning that MESA’s implicit hydrodynamic solver was disabled. We used the approx21 nuclear network.

2.2.1.1 Mixing

Convective mixing was handled via the mixing length theory (Böhm-Vitense, 1958; Cox and Giuli, 1968) and a mixing length parameter of $\alpha_{\text{mlt}} = 2.0$ (Paxton et al., 2013). We used the Ledoux criterion to identify regions in the star that were unstable to convection. The efficiency of semi-convective mixing was set to $\alpha_{\text{sc}} = 10.0$ (Schootemeijer et al., 2019). Thermohaline mixing was also included with an efficiency of $\alpha_{\text{th}} = 1.0$ (Marchant et al., 2021).

Convective boundary mixing (CBM) was included via the step-overshoot scheme, in which we allowed the convective hydrogen-burning core to extend by $0.20 H_P$ beyond the core boundary set by the Ledoux criterion, with H_P the pressure scale height (Martinet et al., 2021). At the bottom of nonburning convective envelopes, we used step overshoot with a $0.05 H_P$ extension of the convective region towards the centre. This corresponds to one-half

of the upper limit typically inferred for the Sun (Angelou et al., 2020). For convectively burning cores beyond the main sequence (MS), overshooting is not yet understood properly and is known to have a large effect on the final fate of stars (Herwig, 2000; Temaj et al., 2024). Because of this, we followed Marchant et al. (2021) and used exponential overshoot extending only $0.005 H_P$ beyond the edge of the convective region set by the Ledoux criterion.

To account for the rotational mixing of chemical elements and diffusion of angular momentum, the Goldreich-Schubert-Fricke instability, Eddington-Sweet circulation, and the secular and dynamic shear instabilities were included (see for example Heger et al. 2000 for a detailed description). Additional diffusion of angular momentum was taken care of by the Spruit-Tayler dynamo. We scaled the strength of the mixing of chemical elements by a factor $f_c = 1/30$ as in Heger et al. (2000). The sensitivity of the rotational instabilities to stabilising composition gradients, which is incorporated in the factor f_μ , was set to $f_\mu = 0.1$ (see also Pinsonneault et al., 1989).

2.2.1.2 Wind mass-loss prescription

Our binary models contain low-, intermediate-, and high-mass stars, and the masses can change significantly over the star’s evolution. Therefore, we employed a wind mass-loss prescription that covered this large mass range and all evolutionary stages.

We considered two distinct regimes, the hot-wind regime with surface temperature³ $T_{\text{surf}} \geq 11 \text{ kK}$ and the cool-wind regime for stars with $T_{\text{surf}} \leq 10 \text{ kK}$. We used linear interpolation to determine the mass-loss rate in the temperature region between those two values.

Within the hot-wind regime, the mass-loss rate for stars with hydrogen envelopes (surface hydrogen mass fraction $X_{\text{surf}} > 0.5$) was computed via the Vink et al. (2000) prescription. When X_{surf} dropped below 0.4, either the prescription for Wolf-Rayet (WR) stars from Sander and Vink (2020) or the prescription for low-mass helium stars from Vink (2017) was used, depending on whether the star’s luminosity L was higher or lower than a certain luminosity L_0 respectively. As described in Sander and Vink (2020), L_0 is the asymptotic limit below which no WR-like wind mass-loss is expected to occur. Its value is metallicity-dependent and obtained from stellar atmosphere models. In the regime where $L > L_0$, we computed the mass-loss rate with both prescriptions and took the maximum value as the adopted wind mass-loss rate (J. Vink, 2021, priv. comm.). All of the aforementioned prescriptions had a scaling factor of 1.0. For $0.4 \leq X_{\text{surf}} \leq 0.5$, the mass-loss rate was determined via linear interpolation between the mass-loss rates from both regimes.

When a model reached the cool-wind regime, the distinction between stars expected to become giants or supergiants was made. The cut was made at $\log_{10}(\mathcal{L}/\mathcal{L}_\odot) = 3.15$, where \mathcal{L} is defined as in Langer and Kudritzki (2014),

$$\mathcal{L} = \frac{1}{4\pi\sigma G} \frac{L}{M} \quad . \quad (2.1)$$

Here, σ is the Stefan-Boltzmann constant. This cut corresponds roughly to a mass of $10 M_\odot$ at the base of the (super-)giant branch. Models below the cut used the Reimers (1975) wind prescription on the red giant branch (RGB) and the Bloeker (1995) wind prescription

³In these wind mass-loss rate computations, the surface temperature T_{surf} is that of the outermost cell of the model.

on the asymptotic giant branch (AGB). Following Choi et al. (2016), we used a scaling factor of 0.1 for the former and 0.2 for the latter. Models above the cut in \mathcal{L} used the Nieuwenhuijzen and de Jager (1990) prescription with a scaling factor of 1.0.

We increased the scaling factor for the Bloeker (1995) wind to 3.0 at the onset of thermal pulses (TP) during the AGB phase following Choi et al. (2016). This increase aimed to ease the computations through this phase by mimicking the enhanced mass loss during the TP-AGB phase while simultaneously avoiding the TPs themselves (by removing the envelope). Additionally, by removing part of the envelope, we aimed to avoid the Hydrogen Recombination Instability (HRI) and the Fe-Peak Instability (FePI). These instabilities, which lead to envelope inflation over multiple orders of magnitude, can occur when the cold, expanded envelopes of AGB stars are modelled with a hydrostatic code (Rees et al., in prep.). The HRI is caused by the increased dynamical instability of the envelope because of hydrogen recombination (Wagenhuber and Weiss, 1994), and the FePI occurs when luminosity at the base of the convective envelope exceeds the Eddington luminosity because of a local iron opacity bump (Lau et al., 2012). The physical mechanism behind these instabilities most likely leads to events of extreme mass loss. The timescales on which this envelope inflation occurs are too short to be captured correctly in MESA’s hydrostatic mode and can lead to numerical issues. The increase of the Bloeker (1995) wind scaling factor was not successful in avoiding numerical issues in each model, especially in those models where the aforementioned instabilities occur. Because of this, we opted to disregard models in which binary mass transfer occurs after the TP-AGB phase. A more elaborate approach to compute through the TP-AGB phase and these instabilities is provided in, for example, Rees et al. (in prep.).

2.2.2. Adopted binary physics

In our models, we evolved both binary components. This allowed us to consider the behaviour of both the donor and the accretor star for tracing potential contact scenarios (see Sect. 2.3). Only mass transfer from the initially more massive or ‘primary’ star onto the initially less massive or ‘secondary’ star was considered. Hence, in this work, references to primary (secondary) and donor (accretor) are equivalent. We mostly employ the names primary (subscript ‘1’) and secondary (subscript ‘2’) star. We assumed circular orbits for all binary systems.

2.2.2.1 Mass transfer and accretion

Whenever the primary star was on the MS, mass transfer was computed using the contact scheme (Marchant et al., 2016). In semi-detached binaries, this scheme uses MESA’s `roche_lobe` scheme, which ensures that the donor stays within its Roche lobe. When both stars (over-)fill their Roche lobe it switches to a different solver for the mass-transfer rate suitable for contact binaries. In this scheme, only the computation of the mass-transfer rate is handled. Energy transport between the components of the contact binary and the tidal distortion are not taken into account (for the effect of including those, see Fabry et al. 2022, 2023). For systems with post-MS primary masses smaller than $1.3 M_{\odot}$, the Kolb scheme (Kolb and Ritter, 1990) was used because this scheme is better suited for envelopes with larger pressure scale heights (Fragos et al., 2023). Both schemes were solved implicitly.

The mass-transfer efficiency β is defined as the effective, overall change in mass of the accretor over the mass transferred from the donor to the accretor, $\beta \equiv -\dot{M}_2 / \dot{M}_{\text{trans}}$. In this

definition, $\dot{M}_{\text{trans}} < 0$ and $\dot{M}_2 > 0$. \dot{M}_2 also includes the wind mass loss of the accretor. During conservative mass transfer in our models, $\beta \approx 1$, because typically $|\dot{M}_{\text{trans}}|$ is orders of magnitude larger than the absolute value of the wind mass-loss rate. When the accretor star spun up to its critical rotation rate $\Omega_{c,2}$, mass transfer was non-conservative and $\beta < 1$. When the accretor star's accretion timescale $\tau_{\text{acc}} \equiv M_2/\dot{M}_{\text{trans}}$ approached the star's dynamical timescale $\tau_{\text{dyn},2}$ (Eq. 1.3) we limited the accretion rate to that of 0.1 times the star's Kelvin-Helmholtz (or thermal) timescale τ_{KH} . This also resulted in non-conservative mass transfer, that is, $\beta < 1$. We did this because the accreting models tend not to converge numerically when $\tau_{\text{acc}} \sim \tau_{\text{dyn},2}$. Models for which the accretion rate was limited are marked in the results. The accretion of angular momentum during mass transfer was computed following Lubow and Shu (1975) and Ulrich and Burger (1976), which includes accretion through ballistic impact and a Keplerian disk.

2.2.2.2 Tides and angular momentum loss

Tidal synchronisation was computed uniformly over the components' structure using the convective synchronisation timescale from Hurley et al. (2002). Upon initialisation of the binary models, the rotation periods of both components were equal to the orbital period. In our models, orbital angular momentum evolved via mass loss from the system (through winds or isotropic re-emission) and spin-orbit coupling. In the former case, the lost mass was assumed to have the specific angular momentum of the star's orbit in which vicinity it was leaving the system.

2.2.3. Binary-star grid

In our grid, we varied the initial mass of the primary star $M_{1,i}$ (in units of M_{\odot}), the initial mass ratio $q_i = M_{2,i}/M_{1,i}$ with $M_{2,i}$ the initial mass of the secondary star, and the initial separation a_i (in units of R_{\odot}). Twenty primary masses were selected between 0.8 and $20.0 M_{\odot}$ with logarithmic mass spacing $\Delta \log_{10} M_{1,i} \approx 0.074$. At the high-mass end, we added three additional primary masses (13.1, 15.6 and $18.4 M_{\odot}$) for increased resolution, bringing the total number of primary masses to 23. Values between 0.1 and 0.9 were considered for the mass ratios, with linear spacing and steps of 0.1. We imposed a lower limit on the secondary mass of $0.5 M_{\odot}$ to avoid fully convective companions, which are difficult to converge numerically when they accrete. We added an additional mass ratio at $q_i = 0.97$ to model twin systems. Lastly, we chose the initial binary separations a_i such that the first phase of mass transfer occurred during all stages of the primary star's evolution. These stages at which mass transfer occurs are called Case A, B, and C, for when the donor star is on the MS, before core-helium ignition, and after core-helium ignition, respectively⁴. This distinction is related to the phases in which the (primary) star expands, as illustrated in Fig. 1.2. Case B phases were further divided into early (Case Be) and late (Case Bl) phases. The distinction is based on the presence of a deep convective zone in the envelope of the star⁵.

To ensure sufficient sampling of all these stages, we used the radius evolution of single-star models in combination with the volume-equivalent Roche lobe radius R_{RL} for a given

⁴As demonstrated in Ge et al. (2015), core-helium ignition can occur before the primary star reaches the base of the supergiant branch for $M_i \gtrsim 15 M_{\odot}$. Although mass transfer at this point would be classified as Case C, it behaves in a very similar way to Case B. This does not, however, occur in our models.

⁵For stars with convective envelopes during the main sequence, that is, initial masses $< 1.3 M_{\odot}$, the distinction between early and late Case-B mass transfer was not made.

mass ratio $q = M_2/M_1$ and separation a , computed through Eq. (1.5). For a given primary mass M_1 and mass ratio q , we selected a number of points along the radius evolution of the star, indicated by the dashed horizontal lines in Fig. 1.2. At each of these points, we assumed the star filled its Roche lobe, $R = R_{\text{RL}}$, and mass transfer ensued. From Eq. (1.5), we then got the separation a at which this happened. Assuming that the orbit stays approximately constant until mass transfer starts, we took this value for the separation a as our initial value, $a_i = a$. Although this method of sampling the initial separation space is adequate for closer binaries, it cannot accurately predict the division lines between later mass-transfer cases for a number of reasons (see, for example, the dividing line between Case B1 and Case C in Fig. 2.6). Firstly, the assumption that the orbital separation a stays approximately constant does not hold in systems with strong wind mass loss and tidal interaction prior to mass transfer. Secondly, post-MS donors use MESA’s Kolb scheme for mass transfer (Kolb and Ritter, 1990). This scheme can result in significant mass-transfer rates before the donor star formally overfills its Roche lobe, since it takes both the optically thick and thin Roche lobe overflow into account (Paxton et al., 2015).

2.2.4. Stopping conditions

In principle, we computed each binary model until one of the components, usually the initially more massive primary star, reached the end of core carbon burning. This is defined as the moment when the central mass fractions of He and C fall below 10^{-6} and 10^{-2} , respectively. Systems with MS primaries having predominantly radiative envelopes ($M_{1,i} > 1.3 M_{\odot}$) used MESA’s contact mass-transfer scheme (see Sect. 2.2.2.1) and could therefore be modelled through such phases. During a contact phase, the computation terminated when the condition for mass overflow through the second Lagrange point (L_2) or L_2 -overflow from Marchant et al. (2016) was met (see Sect. 2.3.3). For primaries with mostly convective envelopes (post-MS or $M_{1,i} \leq 1.3 M_{\odot}$), we used the Kolb mass-transfer scheme. The computation stopped whenever the secondary star overfilled its Roche lobe by more than $R_{\text{RL},2}$. When the mass-transfer rate \dot{M}_{trans} reached a value of $10 M_{\odot} \text{ yr}^{-1}$, the evolution was terminated. The timescale on which such fast mass transfer occurs nears typical dynamical timescales, which is not numerically feasible with our MESA setup. Lastly, reverse mass transfer in a semi-detached system from the secondary to the primary star was not considered in this study. The onset of reverse mass transfer was used as a stopping condition.

2.2.5. Birth probabilities

To describe the models in our grid as a population (Sect. 2.4.3–2.4.5), we computed their birth probability p_{birth} from the initial distribution function, which is the product of the distribution functions of the initial primary mass $M_{1,i}$, mass ratio q_i and period P_i . For the $M_{1,i}$ distribution, we used the Kroupa (2001) initial mass function (IMF),

$$\psi(M_{1,i}) = C_m M^{\alpha} \quad , \quad (2.2)$$

with $\alpha = -2.3$ as appropriate for primary star masses $\geq 0.5 M_{\odot}$ and C_m a normalisation constant. We assumed the other two initial distribution functions to be uniform in q_i and $\log_{10} P_i$, respectively,

$$\phi(q_i) = C_q \quad \text{and} \quad \chi(\log_{10} P_i) = C_p \quad , \quad (2.3)$$

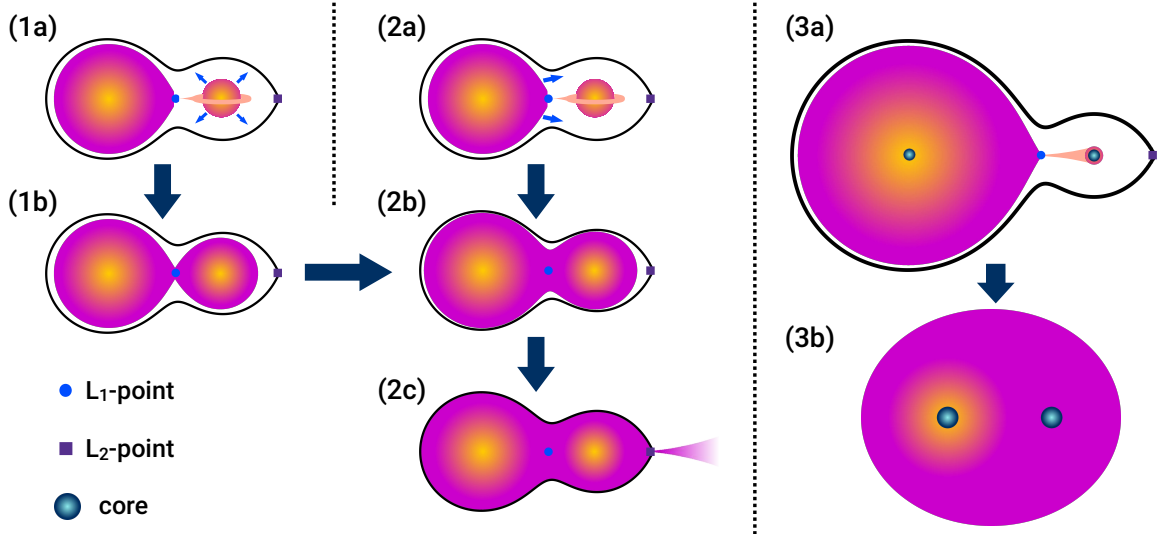


Figure 2.1: Schematic representation of the physical mechanisms leading to contact (not to scale). The filled blue circles and purple squares indicate the position of the L_1 - and L_2 - points, respectively. The filled grey-blue circles represent the stellar cores in Panel (3a) and (3b). Panel (1a) shows the expansion of the accretor leading to a contact binary (1b). This corresponds to the ‘Accretor expansion’ mechanism described in Sect. 2.3.1. Subsequent overflowing of the components’ Roche lobes leads to the formation of an overcontact binary (2b). The primary increasingly overfills its Roche lobe (2a) and can eventually fill the secondary’s Roche lobe (2b). This can eventually lead to L_2 -overflow (2c), which likely results in a stellar merger. The scenarios (1b–2b–2c) and (2a–2b–2c) correspond to the ‘ L_2 -overflow’ mechanism described in Sect. 2.3.3. In Panel (3a), runaway mass transfer from a (super-)giant (left) to an MS star (right) leads to the onset of a classical common-envelope phase (3b), where the cores of both stars revolve in the (super-)giant’s envelope. This corresponds to the ‘Runaway MT’ mechanism described in Sect. 2.3.5.

with C_q and C_p being normalisation constants. The birth probability p_{birth} of each model was then computed by integrating the product of the initial distribution functions over the parameter size in the model grid,

$$p_{\text{birth}} = \int_{\log_{10} P_l}^{\log_{10} P_u} \int_{q_l}^{q_u} \int_{M_l}^{M_u} \psi(M_{1,i}) \phi(q_i) \chi(\log_{10} P_i) dM_{1,i} dq_i d \log_{10} P_i \quad . \quad (2.4)$$

Here, $\log_{10} P_{u,1}$, $q_{u,1}$ and $M_{u,1}$ are the upper- and lower-boundaries of the parameter size of a model in the grid for $\log_{10} P_i$, q_i , and $M_{1,i}$, respectively. They were chosen as the midpoints between the initial parameter values of the model and its neighbouring models.

2.3. Physical mechanisms leading to contact

We use the following nomenclature of contact phases traced in our grid, based on the physical picture in Röpke and De Marco (2023) and illustrated in Fig. 2.1. Systems with MS and/or Hertzsprung-gap (HG) stars (i.e. Case A & Be) that both (over-)fill their Roche lobes or undergo (unstable) runaway mass transfer are referred to as contact binaries (Fig. 2.1.1b and 2.1.2b). Systems with a (super-)giant primary (i.e. Case B1 & C) and an MS secondary undergoing (unstable) runaway mass transfer enter a ‘classical’ common-envelope phase (Fig. 2.1.3b). What sets the onset of a classical CE phase apart from the formation of a

contact binary is that now the primary has a clear core-envelope boundary and the radius of the secondary is at least an order of magnitude smaller than that of the primary.

In this section, we discuss the different physical mechanisms that can lead to contact phases. As stated before, being in contact does not necessarily mean that the binary will merge. Hence, for each mechanism leading to contact, we discuss the likelihood of a merger or rather a longer-lived contact phase. Additionally, we explain how we trace each mechanism in the binary star models.

2.3.1. Expansion of accretor

Arguably the most intuitive way to form contact binaries is when the accreting secondary star expands during a mass-transfer phase and (over-)fills its Roche lobe. A schematic representation of this mechanism is shown in Fig. 2.1.1a–b. The timescale on which the secondary expands, generally defined as $\tau_{R/\dot{R}} \equiv R/\dot{R}$ with R the stellar radius and \dot{R} its time derivative, has implications for the evolution of the subsequent contact phase.

When the mass-transfer timescale $\tau_{\text{trans}} \equiv |M_1/\dot{M}_{\text{trans}}|$ is shorter than the secondary’s thermal or Kelvin-Helmholtz timescale⁶ defined in Eq. (1.2), the star is out of thermal equilibrium. In an effort to regain thermal equilibrium, the secondary expands on its thermal timescale (Ulrich and Burger, 1976; Kippenhahn and Meyer-Hofmeister, 1977; Webbink, 1976; Neo et al., 1977; Pols, 1994). A contact binary is formed if the increase in radius is sufficient for the secondary to fill its Roche lobe. Such a contact binary can rapidly merge on a thermal timescale, or evolve back to a semi-detached binary when the accretor regains thermal equilibrium and shrinks.

When the secondary is in thermal equilibrium during mass transfer, it expands on a nuclear timescale, defined in Eq. (1.1). Contact phases driven by the nuclear expansion of the accretor are longer lived since the accretor will not shrink inside its Roche lobe again until the end of the nuclear burning phase. As a result, such contact phases are expected to persist on a nuclear timescale, or until the stars merge.

The onset of contact phases through the expansion of the accretor is traced by checking whether at any point the accretor overfills its Roche lobe. These models are labelled as ‘Accretor expansion’ in the following sections. This is a stopping condition for models using the Kolb mass-transfer scheme. Models using the contact mass-transfer scheme can evolve through these contact phases. Hence, multiple contact phases might occur throughout the evolution of the system. If more than one contact phase occurs in a model using the contact scheme, only the onset of the first contact phase is considered for a better comparison with models using the Kolb scheme.

An example of a system forming a contact binary because of the thermal expansion of the accreting secondary star (shown up to the point of contact) is shown in Fig. 2.2. From the Hertzsprung-Russell diagram (HRD, Fig. 2.2a), it can be seen that, as a result of Case-A mass transfer, the primary and secondary become under- and over-luminous compared to their single-star counterparts, respectively. The single-star tracks are shown up to their

⁶Technically one should compare with the local thermal timescale in the surface layers of the accreting star, defined in Kippenhahn et al. (2013) (see also Temmink et al. 2023) as $\tau_{\text{KH}}^{\text{local}}(m) = \int_m^M c_P(m')T(m')dm'$, with $c_P(m)$ the heat capacity at constant pressure P and $T(m)$ the temperature at mass coordinate m . In practice, timescale comparisons should therefore be made at an order-of-magnitude level.

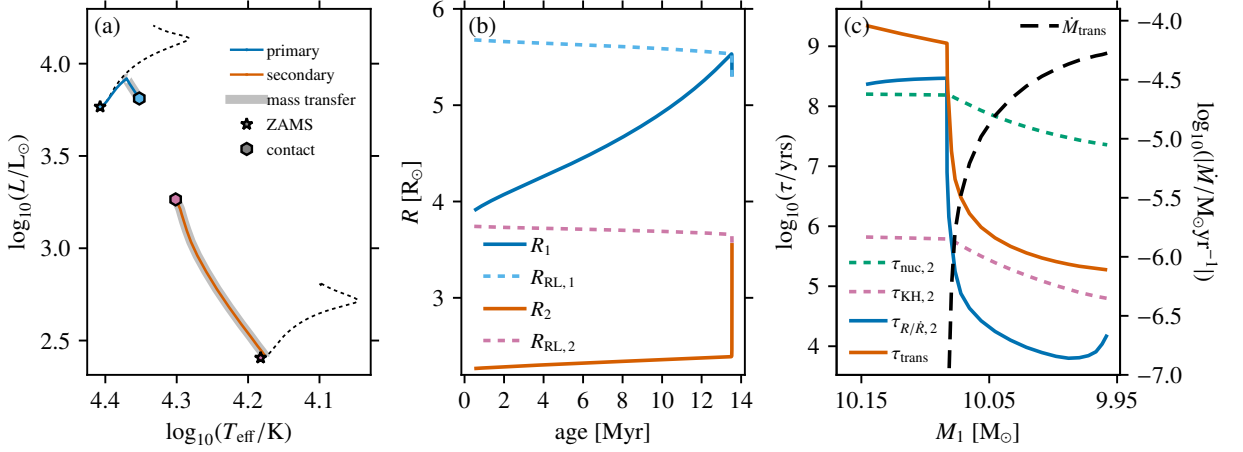


Figure 2.2: Example of a $M_{1,i} = 10.2 M_{\odot}$, $q_i = 0.4$, and $a_i = 12.4 R_{\odot}$ binary system forming a contact binary during the MS of the primary (Case A) because of the thermal expansion of the secondary (accretor) star. Panel (a) shows an HRD with the evolutionary tracks of the primary and secondary stars (solid lines). The dashed black lines show the evolutionary tracks of single stars with the same initial masses as the binary components and initial rotation rates of $\Omega/\Omega_c = 0.25$. Panel (b) shows the evolution of the radius R (solid lines) and Roche lobe radius R_{RL} (dashed lines) of both components. The timescales governing the evolution of the binary and the mass-transfer rate (black dashed line) are shown in Panel (c) as a function of the decreasing primary star mass. The secondary’s nuclear ($\tau_{\text{nuc},2}$) and thermal ($\tau_{\text{KH},2}$) timescales are shown with a dashed green and pink line, respectively. The expansion ($\tau_{R/\dot{R},2}$) and mass-transfer (τ_{trans}) timescales are shown with a solid blue and orange line, respectively.

terminal-age main sequence (TAMS). As a result of mass accretion, the secondary star expands rapidly and fills its Roche lobe (Fig. 2.2b). The expansion timescale $\tau_{R/\dot{R},2}$ becomes about an order of magnitude shorter than the secondary’s global thermal timescale $\tau_{\text{KH},2}$ due to the mass-transfer timescale τ_{trans} becoming comparable to $\tau_{\text{KH},2}$ (Fig. 2.2c). An example of a system forming a contact binary because of the nuclear expansion of the accretor is provided in Appendix A.1. The accretor expansion timescales of all systems forming contact binaries through accretor expansion are shown in Fig. A.8–A.9 in Appendix A.4.

2.3.2. Non-conservative mass transfer

As demonstrated in Packet (1981) and, for example, more recently in Ghodla et al. (2023), a star only has to accrete between ~ 2 to ~ 10 percent of its own mass to be spun up to the Roche critical rotation rate Ω_c . When a star is rotating at (near) this critical rotation rate, it may not be able to accrete any more material. It is then often assumed that the excess mass is lost through an enhanced stellar wind, or even instantaneously through a so-called ‘fast’ wind from the accretor, resulting in non-conservative mass transfer. In our models, instantaneous wind mass loss is invoked to expel the excess matter for accretors rotating near the critical rotation rate and for models in which the accretion timescale τ_{acc} is restricted to 10% of the Kelvin-Helmholtz timescale τ_{KH} . It is assumed that there is an energy source that can expel this excess mass. Let us consider the energy per unit mass ε required to drive away the mass to infinity, $\varepsilon = GM_2/2R_2$. This is under the simplifying assumption that the primary’s gravitational potential can be ignored and that the mass is lost from the surface of the accretor. Equating ε to $(L_1 + L_2)/\dot{M}_{\text{max}}$, we eventually find a maximum mass-loss rate

\dot{M}_{\max} the accretor can have under the condition that all this mass is driven away to infinity by the combined luminosity ($L_1 + L_2$) of the binary (Marchant, 2017),

$$\frac{\dot{M}_{\max}}{M_{\odot} \text{yr}^{-1}} = 10^{-7.19} f_{\text{eff}} \frac{R_2}{R_{\odot}} \frac{M_{\odot}}{M_2} \frac{(L_1 + L_2)}{L_{\odot}} . \quad (2.5)$$

The factor f_{eff} is a free parameter added to take into account the uncertainty on the exact radius at which the non-accreted mass is expelled, the fact that only the gravitational potential of the accretor is accounted for, the unknown fraction of the total luminosity that can be used to expel the non-accreted mass, and the unknown energy of the ejected mass at infinity.

Since the non-accreted mass in systems with $\dot{M}_2 > \dot{M}_{\max}$ cannot be expelled to infinity, it must remain in or around the binary system. Although it is unclear what exactly happens, the non-accreted mass can potentially lead to a contact phase, for example, if it fills the secondary's Roche lobe or introduces a drag on the binary components. Alternatively, the non-accreted matter can form an accretion disk. In this work, we merely flag such models and discuss the potential consequences for their evolution in Sect. 2.5.3.

In the models, we trace the failure to eject non-accreted matter in post-processing by using Eq. (2.5) and assuming $f_{\text{eff}} = 1.0$. Models for which the mass-loss rate of the accretor, defined as $\dot{M}_{\text{ej}} = (1 - \beta) \dot{M}_{\text{trans}}$, at one point exceeds \dot{M}_{\max} are labelled in the following sections as ‘Non-conservative MT + cannot eject’.

An example of a system in which the accretor cannot eject the non-accreted matter during non-conservative mass transfer is shown in Fig. 2.3. The system undergoes Case-Be and -C mass transfer. The primary is partially stripped in the former mass-transfer phase, and the remaining H+He envelope amounts to $\approx 20\%$ of the mass of the post-mass-transfer primary star. After core-He exhaustion, the star expands again, initiating a Case-C mass-transfer phase. During Case-Be mass transfer, the secondary star becomes over-luminous because it is out of thermal equilibrium. However, its luminosity decreases again when its rotation rate Ω reaches the critical rotation rate Ω_c (Fig. 2.3c). At this point ($M_1 \approx 9.5 M_{\odot}$), the mass-transfer efficiency β decreases to almost zero. During the non-conservative Case-Be mass transfer, the combined luminosity is insufficient to expel the non-accreted matter to infinity. This holds both for $f_{\text{eff}} = 0.1$ and $f_{\text{eff}} = 1.0$ (Fig. 2.3b).

2.3.3. Outflow from second Lagrange point

In the Roche potential, there are three equilibrium points located on the line connecting the centres of the binary components. From lowest to highest potential, these are L_1 (through which mass transfer occurs), L_2 and L_3 . The L_2 -point is always located on the side of the less massive star in the binary, and L_3 on the side of the more massive star. In Case-A and -Be binaries, mass loss from the L_2 -point (Fig 2.1.2c) takes away a significant amount of specific angular momentum from the system, which can lead to rapid orbital shrinkage and a subsequent merger. The rate of orbital shrinkage and hence the time until the merging event depends on the mass-loss rate and the outflow velocity through L_2 (Marchant et al., 2021). In Case B1 and -C binaries, L_2 indicates the onset of a classical CE.

We trace L_2 -overflow in our models when either one (semi-detached) or both (contact) components overflow(s) their Roche lobe. In the latter case, the radii of the components

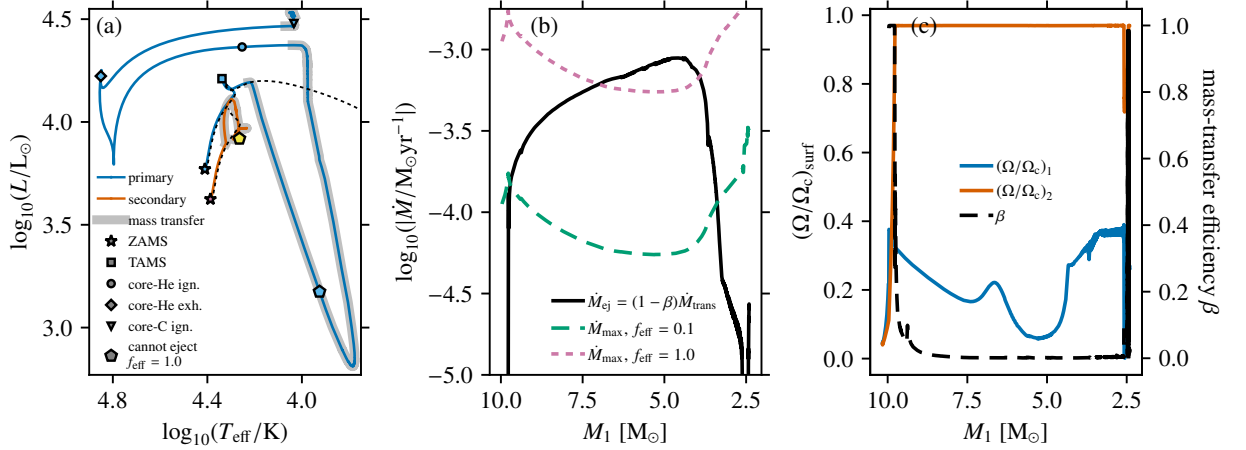


Figure 2.3: Example of a $M_{1,i} = 10.2 M_{\odot}$, $q_i = 0.9$, and $a_i = 39.2 R_{\odot}$ binary star model in which non-conservative mass transfer occurs and for which the non-accreted matter cannot be driven to infinity. Panel (a) is the same as Fig. 2.2a (‘ign.’ = ‘ignition’ and ‘exh.’ = ‘exhaustion’). In Panel (b), the mass-loss rate of the secondary (solid black line) is compared to the maximum mass-loss rate \dot{M}_{max} (dashed lines; pink for $f_{\text{eff}} = 1.0$, green for $f_{\text{eff}} = 0.1$) set by Eq. (2.5). The surface rotation rates (solid blue and orange lines) and mass-transfer efficiency (dashed black line) are shown in Panel (c) as a function of the primary mass.

are compared to L_2 volume-equivalent radii from Marchant et al. (2016). This is done during the computation of the model and the moment of L_2 -overflow is a stopping condition (Sect. 2.2.4). In semi-detached systems, we compare the radius of the primary star to the volume-equivalent radius R_{L_2} and the distance to the L_2 -point D_{L_2} from Misra et al. (2020) (similar fitting formulae for R_{L_2} are derived in Ge et al. 2020). This is done in post-processing, meaning that the outflow from L_2 is not modelled and does not affect the evolution of the model. We refer to, for example, Marchant et al. (2021) to see the effect of these outflows. In both cases, if L_2 -overflow occurs, the models are labelled ‘ L_2 -overflow’.

The evolution of a binary system experiencing L_2 -overflow is shown in Fig. 2.4. The primary and secondary become under- and over-luminous, respectively, during Case-Be mass transfer (Fig. 2.4a). As in the previous example, mass transfer is non-conservative and early on during the mass transfer the non-accreted matter cannot be driven to infinity (Fig. 2.4b). As the binary orbit shrinks during mass transfer, also the Roche lobe radius $R_{\text{RL},1}$ and the volume-equivalent radius $R_{L_2,1}$ decrease (Fig. 2.4c). After about $1.5 M_{\odot}$ is lost from the primary star, its radius decreases slower than $R_{\text{RL},1}$ and $R_{L_2,1}$. As a consequence, the star increasingly overfills its Roche lobe until it reaches the point of L_2 -overflow. The subsequent loss of mass and angular momentum from the L_2 -point will result in an accelerated orbital shrinkage, which is not accounted for in this model. The onset of L_2 -overflow is shown schematically in Fig. 2.1. In the evolutionary scenario depicted in Fig. 2.1.1a–1b–2b–2c, a contact binary is formed because of the expansion of the accretor. The components continuously overfill their Roche lobes (Fig. 2.1.2b) until the overcontact binary fills the L_2 -lobe (Fig. 2.1.2c). In the second scenario, from Fig. 2.1.2a–2c, the primary overfills its own Roche lobe (Fig. 2.1.2a) and later fills the Roche lobe of the secondary, forming an overcontact binary (Fig. 2.1.2b). Eventually, this overcontact binary fills the L_2 -lobe and L_2 -overflow occurs (Fig. 2.1.2c).

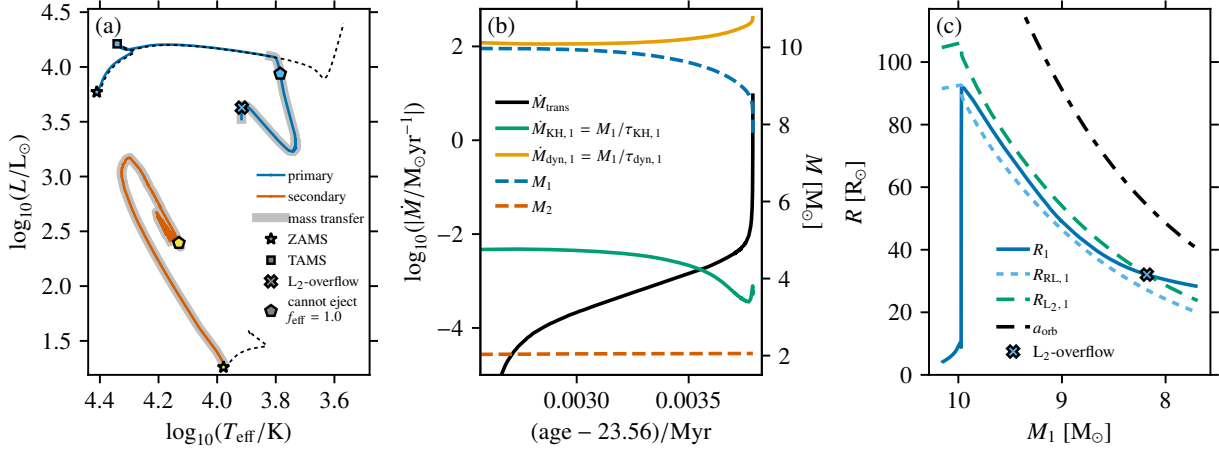


Figure 2.4: Example of a binary model with $M_{1,i} = 10.2 M_\odot$, $q_i = 0.2$, and $a_i = 175.7 R_\odot$ going through a phase of (delayed) runaway mass transfer. Panel (a) is the same as Fig. 2.2a (‘ign.’ = ‘ignition’). Panel (b) shows the mass-transfer rate \dot{M}_{trans} (solid black line), thermal mass-transfer rate $\dot{M}_{\text{KH},1}$ (solid green line) and dynamical mass-transfer rate $\dot{M}_{\text{dyn},1}$ (solid gold line) for the primary star on the left axis. The right axis shows the component mass evolution as a function of age (dashed blue and orange lines). In Panel (c), the radius R (solid blue line), Roche lobe radius R_{RL} (dashed light-blue line), L_2 -volume-equivalent radius R_{L_2} (dashed green line, Misra et al., 2020, Eq. 15) and orbital separation a_{orb} (dashed black line) evolution for the primary are shown as a function of the decreasing primary mass. The blue cross indicates the moment of L_2 -overflow.

2.3.4. Tidally driven contact

When a single star ascends the (super-)giant branch, its moment of inertia I increases, such that its surface rotation velocity decreases. In a binary and if the tidal synchronisation timescale τ_{sync} (Hurley et al., 2002, Eq. 27) is shorter than the expansion timescale $\tau_{R/\dot{R}}$, the star is tidally locked to the orbit and does not spin down. The transfer of angular momentum from the orbit to the spin of the star shrinks the orbit. Under certain circumstances, tidally driven orbital decay can lead to contact phases, which demonstrates the importance of considering the effect of tides in binaries.

In the most extreme case, the binary system becomes Darwin unstable (Darwin, 1879). This instability arises if

$$\frac{L_{\text{orb}}}{(I_1 + I_2)\Omega} < 3 \quad , \quad (2.6)$$

where L_{orb} is the orbital angular momentum, Ω is the orbital angular rotation velocity, and I_1 and I_2 are the moment of inertia of the primary and secondary star, respectively. This condition is derived under the assumption of a circular ($e = 0$, with e the eccentricity), coplanar (spins of components are aligned), and synchronised ($\omega_1 = \omega_2 = \Omega$) system. Here, ω_1 and ω_2 are the angular rotation rates of the primary and secondary, respectively. Moreover, solid-body rotation is assumed for the individual components, allowing the spin angular momenta $S_{1,2}$ to be written as $S_{1,2} = \omega_{1,2}I_{1,2}$. Especially for close or contact binaries, where τ_{sync} is typically of the order of a few years, the Darwin instability can lead to a dynamical inspiral of the components, resulting in a merger.

Models labelled ‘Tidally driven contact’ experience orbital decay caused by tides before the onset of contact, while orbital widening is expected from mass transfer ($q > 1$). We trace

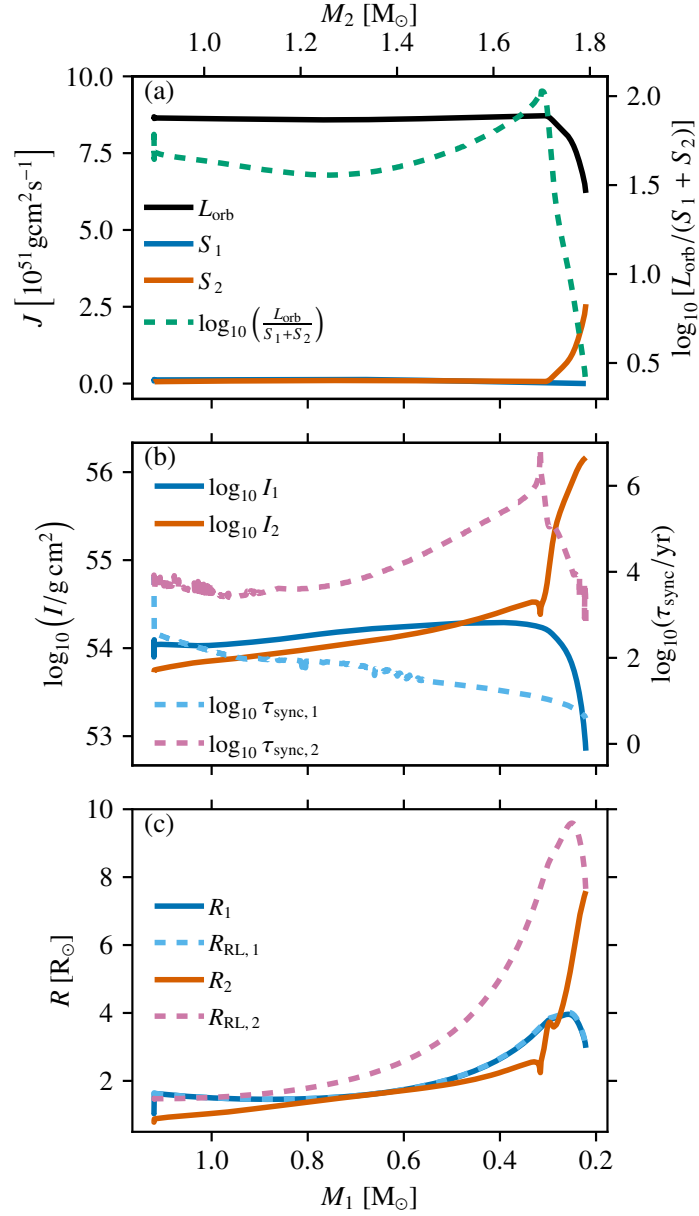


Figure 2.5: Example of a $M_{1,i} = 1.1 M_\odot$, $q_i = 0.8$ and $a_i = 4.1 R_\odot$ binary system in which tides lead to contact. In Panel (a) we show the exchange between the orbital angular momentum L_{orb} (solid black line) and the secondary’s spin angular momentum S_2 (solid orange line), which coincides with the decrease in $L_{\text{orb}} / (S_1 + S_2)$ (dashed green line). The primary’s spin angular momentum S_1 is shown with a solid blue line. Panel (b) shows the evolution of the moment of inertia (solid lines) and tidal synchronisation timescale (dashed lines) for both components. While the moment of inertia of the primary decreases around $M_1 = 0.3 M_\odot$, it sharply increases for the secondary. At the same time, the secondary star’s tidal synchronisation timescale decreases by approximately two orders of magnitude. Panel (c) shows the evolution of the primary’s and secondary’s radii (solid lines) and Roche lobe radii (dashed lines). While the former fills its Roche lobe, tides cause orbital shrinkage, which results in the secondary also filling its Roche lobe.

this condition in post-processing. This label is not used for systems which are at one point during their evolution Darwin unstable. Although these systems will experience orbital decay, this can happen on timescales longer than the evolutionary timescales of the system. However, most of the systems that are driven into contact by tides do eventually become Darwin unstable.

An example of a system in which tides lead to the onset of contact is shown in Fig. 2.5. In this low-mass binary, the primary overfills its Roche lobe near the end of the MS. During mass transfer, the primary star reaches the TAMS, but does not become a red giant because of the continuous stripping of its envelope. During the mass-transfer phase, the secondary star overtakes in evolution, leaves the MS and turns to the giant branch. At this point, the mass ratio of the system has already reversed, and mass transfer is almost conservative, widening the orbit. Two important changes occur when the secondary becomes a giant. First, there is the development of a deep convective envelope and an increase in radius, which lead to increased tidal coupling of the star: $\tau_{\text{sync},2}$ drops by several orders of magnitude (Fig. 2.5b). Because of this, the orbital and rotation period of the secondary synchronise. Secondly, the increase in radius and density redistribution (the envelope now has a deep convective zone) both increase the moment of inertia I_2 of the star (Fig. 2.5b). Following the conservation of angular momentum, the secondary spins down, yet it is immediately spun up again by tides. Hence, the spin angular momentum of the secondary S_2 increases and the orbital angular momentum L_{orb} decreases (Fig. 2.5a). Eventually, the system becomes Darwin unstable, as it fulfils the condition⁷ $L_{\text{orb}}/(S_1 + S_2) \lesssim 3$. Because of the decrease in L_{orb} , the orbit, which was widening from mass transfer, starts shrinking again. As a consequence of the shrinking Roche lobe, the primary star is stripped of its outer envelope increasingly rapidly, leading to a decrease in radius and an increase in mass-transfer rate (not shown). The shrinking of the Roche lobes eventually leads to the formation of a contact binary once the secondary also fills its Roche lobe (Fig. 2.5c). At the point when the contact binary is formed, the helium core mass M_{He} has increased beyond that of the primary star. This means that the secondary is closer to core helium ignition, that is, it has overtaken the primary in evolution.

2.3.5. Unstable mass transfer and CE phases

During mass transfer, the donor star's radius and Roche lobe can both either shrink or expand. Mass transfer is generally stable when the donor star shrinks faster or expands slower than its Roche lobe. However, when the donor star overfills its Roche lobe by increasing amounts as a reaction to mass loss, the binary enters an unstable runaway situation (e.g. Soberman et al., 1997). This happens, for example, when the Roche lobe shrinks while the donor expands (e.g. during mass transfer with $q < 1$ and/or because of orbital angular momentum loss). The responses of the donor's radius and Roche lobe radius are quantified in the mass-radius exponents $\zeta_{R_1} \equiv d \ln R_1 / d \ln M_1$ and $\zeta_{\text{RL}} \equiv d \ln R_{\text{RL},1} / d \ln M_1$, respectively (Webbink, 1984). If $\zeta_{R_1} < \zeta_{\text{RL}}$, mass transfer is unstable, and the mass-transfer rate keeps increasing, potentially reaching values larger than $1 M_{\odot} \text{yr}^{-1}$. During runaway (unstable) mass transfer, the primary star increasingly overfills its Roche lobe, and the secondary's expansion timescale becomes orders of magnitude lower than its thermal timescale. When the

⁷Since the stars in our models are in general not solid body rotators, we cannot assume that $S_{1,2} = \omega_{1,2} I_{1,2}$. Therefore, we use a modified version of the classical criterion for the Darwin instability: $L_{\text{orb}}/(S_1 + S_2) \lesssim 3$.

primary star is an MS or HG star (Case-A or -Be), a contact binary forms and merge on a timescale shorter than the primary’s thermal timescale because of the runaway expansion of both components. In Case-BI and -C binaries, runaway mass transfer leads to the engulfment of the secondary in the primary’s envelope, that is, a classical CE phase. A classical CE phase can lead to a merger or leave a close binary behind (see, e.g. Röpke and De Marco, 2023). The onset of a classical CE through runaway mass transfer is shown schematically in Fig. 2.1.3a–b.

We look for runaway mass transfer in post-processing and label such models ‘Runaway MT’ given the following three criteria. Firstly, the mass-transfer rate \dot{M}_{trans} needs to exceed the thermal-timescale mass-transfer rate, set by $\dot{M}_{\text{KH}} = M_1/\tau_{\text{KH},1}$. Secondly, the second time derivative of $\log_{10} \dot{M}_{\text{trans}}$ has to be positive. When this is the case, the rate of change in \dot{M}_{trans} is increasing, which is indicative of a runaway situation. Moreover, this condition also ensures that \dot{M}_{trans} does not decrease again, as is observed for stable Case-C mass transfer (see Sect. 2.4.2). Thirdly, the condition for unstable mass transfer described above needs to be fulfilled: $\zeta_{R_1} < \zeta_{\text{RL}}$. For semi-detached models using MESA’s `contact` mass-transfer scheme, $\zeta_{R_1} = \zeta_{\text{RL}}$ by definition. Hence, in this case, only the first two conditions are evaluated. We note that L_2 -overflow is not a necessary condition for the onset of runaway mass transfer. However, it does often occur in systems with runaway mass transfer.

An example of a binary system experiencing delayed runaway mass transfer is shown in Fig. 2.4 and was previously discussed to demonstrate L_2 -overflow in Sect. 2.3.3. The evolution of the mass-transfer rate \dot{M}_{trans} as a function of the binary system’s age is shown in Fig. 2.4b, where it is also compared to the thermal and dynamical mass-transfer rates. Shortly after \dot{M}_{trans} exceeds the former, the runaway nature of the evolution is observed, during which \dot{M}_{trans} starts nearing the dynamical mass-transfer rate. Simultaneously, we see in Fig. 2.4c that the slope of R_1 as a function of the decreasing M_1 becomes larger than that of $R_{\text{RL},1}$, which means that the primary increasingly overfills its Roche lobe. This continues up to the point where L_2 -overflow occurs, after which an accelerated orbital shrinkage is expected (see Sect. 2.3.3). In this example, the binary does not enter a runaway phase immediately at the onset of mass transfer. Therefore, it is an example of a delayed runaway mass-transfer phase (e.g. Hjellming and Webbink, 1987; Han and Podsiadlowski, 2006; Pavlovskii and Ivanova, 2015; Ge et al., 2015, 2020). Since in this particular example the primary star is not yet a supergiant at the onset of mass transfer, this system is not expected to enter a classical common-envelope phase, but rather become a contact binary that will most likely eventually merge.

2.4. Occurrence of contact phases

In this section, we present our contact tracing results for three initial primary masses (Sect. 2.4.1). Then, we focus on a particular region of the initial binary parameter space in which Case-BI and -C mass transfer are found to be stable (Sect. 2.4.2). Next, we look at the incidence of the different physical mechanisms leading to contact in a population of binary systems (Sect. 2.4.3), and put lower limits on the stellar merger and classical CE fractions of mass-transferring binaries (Sect. 2.4.4). Lastly, we compare the properties of Case-A contact systems found in our grid with those of observed systems (Sect. 2.4.5).

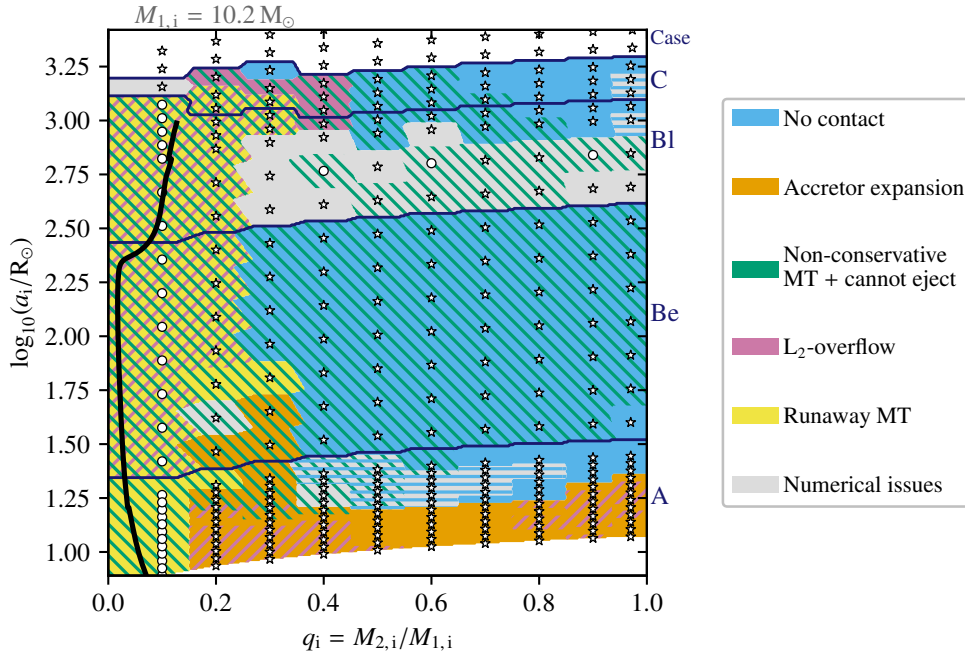


Figure 2.6: Occurrence of contact phases for models with initial primary masses $M_{1,i} = 10.2 M_{\odot}$ on the initial mass ratio–separation plane. Models marked with a dot are those for which accretion was limited to 0.1 times the secondary’s global thermal timescale τ_{KH} (see Sect. 2.2.2.1). The other ones are marked with a star symbol. The dark-blue quasi-horizontal lines indicate the initial mass transfer cases, which can be read from the right side. Systems on the left of the solid black line are Darwin unstable at the onset of mass transfer according to Eq. (2.6) and assuming $R_1 = R_{\text{RL},1}$.

2.4.1. Contact phases for different initial primary masses

2.4.1.1 Initial primary mass of $10.2 M_{\odot}$

In Fig. 2.6, we show our binary models in the initial mass ratio–separation (q_i - $\log_{10} a_i$) plane for a fixed initial primary mass $M_{1,i}$ of $10.2 M_{\odot}$. Systems with $M_{1,i} = 20.0$ and $1.6 M_{\odot}$ are shown in Fig. 2.7, and described in Sect. 2.4.1.2 and 2.4.1.3, respectively. The results for the other $M_{1,i}$ are shown in Appendix A.2. A table with the evolutionary outcomes of all computed MESA models as well as the model input and output files are available online⁸. An extract of this table can be found in Appendix A.7.

The coloured regions in Fig. 2.6 indicate the different physical mechanisms leading to contact (‘Accretor expansion’, ‘Non-conservative MT + cannot eject’, ‘ L_2 -overflow’, ‘Tidally driven contact’, and ‘Runaway MT’, see Sect. 2.3). They have been constructed using nearest neighbour interpolation. Models labelled ‘No contact’ undergo at least one phase of mass transfer but manage to avoid any form of contact until the end of our computations (see Sect. 2.2.4). In some models, reverse mass transfer occurs from the initially less massive secondary to the primary, but we do not consider this here for contact tracing. These models are also labelled ‘No contact’. The potential fates of reverse mass transfer systems are briefly described later in this section. Models labelled ‘Numerical issues’ were numerically unable to reach the desired stopping conditions of our computations (see Sect. 2.2.4). Lastly, models labelled ‘MT after TP’ are those for which Case-C mass transfer occurs after the TP-AGB phase. Their final fate is not further interpreted (see Sect. 2.2.1.2).

⁸<https://zenodo.org/doi/10.5281/zenodo.10148634>

In some regions of the initial binary parameter space, more than one of the above conditions are met, and we indicate this by the corresponding hatching (ancillary outcome). For the background colour (principal outcome), priority is given in the following order (highest to lowest priority): ‘Tidally driven contact’, ‘Runaway MT’, ‘Accretor expansion’, ‘L₂-overflow’, ‘No contact’, and ‘Numerical issues’. Regions in which ‘No contact’ is indicated by hatching contain models that make it to the end of core-He burning and are, therefore, strong candidates for avoiding contact but encountered numerical difficulties before they could reach the end of core-C burning (see Sect. 2.2.4). We use ‘Non-conservative MT + cannot eject’ exclusively as an ancillary outcome (hatching). Although this is a viable mechanism leading to contact (Sect. 2.3.2), it is uncertain to what evolutionary outcome it leads. For example, a system with ‘No contact’ as its principal outcome and ‘Non-conservative MT + cannot eject’ as its ancillary outcome can either avoid contact when, for example, an accretion or circumbinary disk is formed, or form a contact binary when the non-accreted matter fills the secondary’s Roche lobe.

For systems with $M_{1,i} = 10.2 M_{\odot}$, contact binaries form because of the expansion of the accreting secondary star for $q_i = 0.15$ – 1.00 in the initially closest Case-A binary systems (‘Accretor expansion’; Fig. 2.6). For $q_i = 0.15$ – 0.45 with $\log_{10}(a_i/R_{\odot}) \lesssim 1.23$ and $q_i = 0.75$ – 1.00 , these contact systems additionally experience L₂-overflow, which leads to orbital angular momentum loss and subsequent stellar mergers. For $q_i = 0.45$ – 0.75 , the contact binaries do not expand beyond the L₂-lobe. This behaviour is found consistently throughout the range of $M_{1,i} = 2.6$ – $20.0 M_{\odot}$ for q_i between 0.45 and 0.65 – 0.75 , where the upper boundary decreases with decreasing $M_{1,i}$. By comparing with the expansion timescales of the accretors (Figs. A.8–A.9) in systems avoiding L₂-overflow, we find that systems with $q_i \gtrsim 0.5$ likely produce longer-lived ($\tau_{\text{nuc},1}$) contact binaries, which may be observable. The contact binaries with $q_i \lesssim 0.5$ form through the thermal-timescale expansion of the accretor and merge or detach again on the accretor’s thermal timescale.

The initially wider Case-A ($\log_{10}(a_i/R_{\odot}) \gtrsim 1.23$) systems with $q_i = 0.15$ – 0.35 that avoid L₂-overflow reach mass-transfer rates \dot{M}_{trans} orders of magnitude larger than their thermal mass-transfer rate \dot{M}_{KH} . \dot{M}_{trans} eventually reaches the stopping condition value of $10 M_{\odot} \text{ yr}^{-1}$ (see Sect. 2.2.4). In the Case-Be models labelled ‘Accretor expansion’, the primary is an HG star and the secondary is expanding on a timescale orders of magnitude shorter than its thermal timescale. The resulting contact binary will likely experience L₂-overflow and merge.

The Case-A binary systems with $q_i \leq 0.15$ and $\log_{10}(a_i/R_{\odot}) \lesssim 1.37$ experience a phase of runaway mass transfer (‘Runaway MT’). In addition, the mass-accretion rate of the secondaries is limited to $10\dot{M}_{\text{KH},2}$, which brings the mass-transfer efficiency β almost down to zero right after the onset of mass transfer. The lack of further accretion quenches initially rapid expansion ($\tau_{R/\dot{R},2} < \tau_{\text{KH},2}$) of the secondary. Assuming that in reality this rapid expansion continues (the accretion rate in these models is limited for numerical reasons), the two MS stars are likely to form contact binaries.

In the region of $q_i = 0.35$ – 1.00 and $\log_{10}(a_i/R_{\odot}) \approx 1.2$ – 1.5 , we find Case-A systems that avoid contact (‘No contact’). In these systems, the primary stars are stripped in Case-A, Case-AB, and in some models even Case-ABC mass-transfer phases. Eventually, they reach or are expected to reach (horizontal hatching) the end of core carbon burning, or enter a phase of reverse mass transfer. The latter occurs for some of the binary systems with $q_i = 0.65$ – 1.00 close to the border between forming contact binaries and avoiding contact.

Here, the secondary (over-)fills its Roche lobe after the primary has detached, leading to a phase of accretion onto a stripped primary star. Other models that experience reverse mass-transfer phases are found at $q_i = 0.97$ and $\log_{10}(a_i/R_\odot) \approx 1.52\text{--}2.30$. Such phases are not considered further in our contact tracing.

For Case-Be systems, contact is likely avoided for $q_i \gtrsim 0.25\text{--}0.35$. The primary stars in these systems all follow the same evolutionary pathway as the example described in Fig. 2.3: the HG primaries are stripped and reach core-C exhaustion. The secondary stars are spun up by accretion and mass transfer becomes non-conservative. Tidal synchronisation timescales are longer than the spin-up timescales, hence tides are not able to prevent spin-up to the critical rotation rate as is the case in the closer-orbit Case-A systems. Virtually all systems fail to eject the non-accreted matter at one point during this phase of non-conservative mass transfer (‘Non-conservative MT + cannot eject’).

At $q_i \leq 0.25 - 0.35$, Case-Be binaries experience runaway mass transfer. All systems experience non-conservative mass transfer and fail to eject the non-accreted matter. Except for systems at $\log_{10}(a_i/R_\odot) \lesssim 1.78$ and $q_i = 0.15\text{--}0.35$, all of them also experience L_2 -overflow. The secondary stars are still on the MS. The primaries are HG stars without a clear core-envelope boundary (see Fig. A.5–A.7 in Appendix A.3 for the evolutionary state of all models at contact and/or termination). Hence, these systems are expected to evolve into contact binaries and not result in classical CEs.

We find runaway mass transfer in Case-BI systems with $q_i \leq 0.25$ and $\log_{10}(a_i/R_\odot) \lesssim 2.92$, and $q_i \leq 0.35$ and $\log_{10}(a_i/R_\odot) \gtrsim 2.92$ as well as a small set of Case-C systems with $q_i = 0.15\text{--}0.35$. The secondary stars in these systems are MS stars. The difference compared to the Case-Be systems experiencing runaway mass transfer is that all primary stars have now evolved into supergiants with a clear core-envelope boundary by the time mass transfer starts (this can be observed from, for example, the steeper drop in density and binding energy around the core-envelope boundary). As a consequence, all these systems are expected to enter a classical CE phase.

Following Rasio (1995), we have computed the mass ratios below which binary systems are Darwin unstable at the onset of mass transfer (black solid line in Fig. 2.6). Systems with supergiant donors with deep convective envelopes (Case BI and C) are Darwin unstable at the onset of mass transfer for $q_i \lesssim 0.1$. In Case-A and -Be binaries, this is the case for $q_i \lesssim 0.05$.

At $q_i = 0.15\text{--}0.45$, we find Case-C systems (and one Case-BI system) with runaway mass-transfer where the primary stars overflow their L_2 -lobes by a factor of more than one. The primaries have (almost) engulfed their companion and we witness the beginning of a classical CE phase.

For $q_i \geq 0.45$, Case-BI and -C binary systems evolve through a stable phase of mass transfer. The Case-BI systems are actually found to go through two stable mass-transfer phases, Case-BI and Case-BC. Thanks to the stability of these mass-transfer phases, contact is avoided. The stability of Case BI and -C mass transfer is described further in Sect. 2.4.2.

The region around the transition between early and late Case-B systems contains models for which MESA does not converge numerically because of the rapid spin-up of the accretor. These issues with the spin-up of the accretor occur in systems with initial primary masses down to $8.6 M_\odot$. For systems with initial primary masses of $\geq 13.1 M_\odot$, models with Case Be

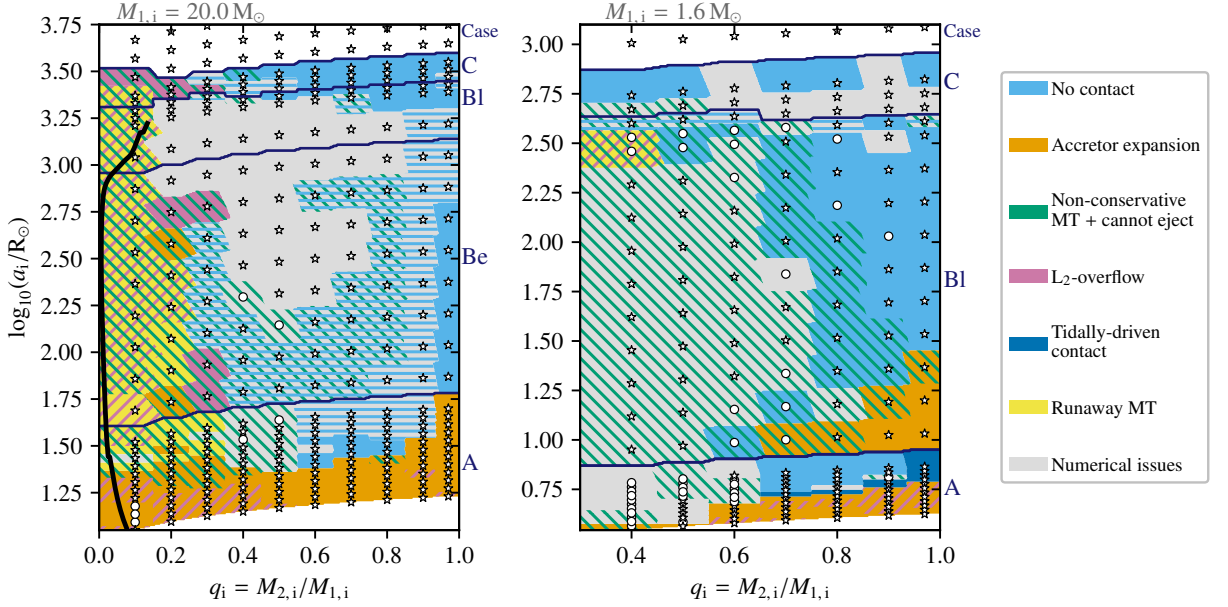


Figure 2.7: Same as Fig. 2.6, but for $M_{1,i} = 20.0 M_{\odot}$ (left) and $M_{1,i} = 1.6 M_{\odot}$ (right).

mass transfer are also affected. This can be seen in Figs. 2.7 and A.2.

2.4.1.2 Initial primary mass of $20.0 M_{\odot}$

For $M_{1,i} = 20.0 M_{\odot}$ (left panel in Fig. 2.7), the general picture is similar to that of models with $M_{1,i} = 10.2 M_{\odot}$ presented above. However, there are some notable differences.

Similarly to the models with $M_{1,i} = 10.2 M_{\odot}$, the initially closest Case-A systems form contact binaries through the expansion of the secondary star during mass transfer. For the twin systems ($q_i \approx 0.97$), this even happens for all the Case-A systems. Binary systems with $q_i \leq 0.15$ and $\log_{10}(a_i/R_{\odot}) \lesssim 1.37$ enter contact through accretor expansion, whereas binary systems in the equivalent region for $M_{1,i} = 10.2 M_{\odot}$ do so through a phase of runaway mass transfer. In general, it is found that the former holds for models with $M_{1,i} = 12.6\text{--}20.0 M_{\odot}$ and the latter for $M_{1,i} = 5.2\text{--}10.2 M_{\odot}$. For $M_{1,i} < 5.0 M_{\odot}$, models with $q_i = 0.1$ are not computed, so information about this region is not available.

Just as for the systems with $M_{1,i} = 10.2 M_{\odot}$, contact binaries with $q_i \leq 0.45$ formed through accretor expansion experience L_2 -overflow (Fig. 2.7, left). However, at $q_i \geq 0.75$, L_2 -overflow is found to be largely avoided during the first phase of contact, contrary to what is found for systems with $M_{1,i} = 10.2 M_{\odot}$. This, however, does not imply that these contact phases are long-lived ($\tau_{\text{contact}} \sim \tau_{\text{nuc},1}$) since the secondary has been found to shrink again after regaining thermal equilibrium ($\tau_{\text{contact}} \sim \tau_{\text{KH},2}$). In almost all of these systems, a second contact phase follows later in the evolution because of the nuclear timescale expansion of the secondary star. The primary stars are at this point either MS or post-MS stars. In the former case, the models have again been computed through the contact phase, which almost exclusively results in L_2 -overflow. In the latter case, the evolution is terminated when the accretor fills its Roche lobe (see Sect. 2.2.4).

Initially wider Case-A systems, with $\log_{10}(a_i/R_{\odot}) = 1.37\text{--}1.68$ and $q_i \leq 0.35$, go through a phase of runaway mass transfer and thus likely form contact binaries. Compared to the systems with $M_{1,i} = 10.2 M_{\odot}$, this region extends to higher values of q_i . At similar

initial separations and $q_i = 0.35\text{--}0.55$, MESA does not converge numerically. As in the equivalent region for $M_{1,i} = 10.2 M_\odot$ models, the solver fails to find a suitable solution for the accretor such that the rotation rate remains below the critical rotation rate.

Primary stars in Case-A systems with $q_i = 0.550\text{--}0.935$ and $\log_{10}(a_i/R_\odot) = 1.38\text{--}1.77$ are stripped in Case-A, Case-AB, and Case-ABC mass-transfer phases and avoid or are expected to avoid contact. Contrarily to similar systems with $M_{1,i} = 10.2 M_\odot$, none experience a phase of reverse mass transfer. There is, however, a set of models of twin systems with $q_i = 0.97$ and $\log_{10}(a_i/R_\odot) \approx 1.78\text{--}2.80$ where reverse mass transfer does occur, as in the binaries with $M_{1,i} = 10.2 M_\odot$.

In Case-Be binaries, the differences with respect to the equivalent $M_{1,i} = 10.2 M_\odot$ systems are more pronounced. Firstly, a few systems only experience L_2 -overflow and thus avoid runaway mass transfer. Closer inspection shows that in these systems, the radius of the primary star exceeds R_{L_2} by $\lesssim 20\%$ for $\lesssim 10^3$ yrs. It is uncertain whether these contact binaries (see Fig. 2.1.2c) are stable, given that the phase of L_2 -overflow is short and might not lead to sufficient angular momentum loss to cause significant orbital decay and hence a merger. Moreover, the primary star shrinks again rapidly afterwards, causing the binary to become semi-detached again. Secondly, Case-Be models have a harder time converging numerically. In these models, the primary stars are stripped in one or more mass-transfer phase(s), and continue core-He burning and core-C burning as stripped stars with a thin hydrogen layer ($\lesssim 1 M_\odot$). At these masses, MESA runs into numerical difficulties and the timesteps of the simulations drop well below one year. This is a known issue for this kind of stripped stars (Y. Götberg, 2022, priv. comm.) and has prevented us from computing the evolution to the end of core-C exhaustion for all models. A select number of models are computed with small timesteps until core-C exhaustion. In these models, the hydrogen surface layers expand during core-C burning and drive a stable and short-lived ($\sim 10^3$ yrs) Case-C mass-transfer phase. Mass transfer is stable because the donor stars shrink again when nearing core-C exhaustion and the core-mass fraction is > 0.5 , which typically signals stability (Temink et al., 2023). At lower initial primary masses, such as for models with $M_{1,i} = 18.4 M_\odot$ (see Fig. A.2 in Appendix A.2), the aforementioned numerical difficulties are less severe, allowing most stripped primaries to reach core-C exhaustion. Most of them avoid Case-C mass transfer, such that we do not expect contact phases.

From the left panel of Fig. 2.7, we see that for Case-Be, -Bl, and -C systems with $q_i \leq 0.25$ and $\log_{10}(a_i/R_\odot) \lesssim 2.5$, and $q_i \leq 0.15$ and $\log_{10}(a_i/R_\odot) = 2.50\text{--}3.42$, contact is reached again through runaway mass transfer. Among these, Case-Bl and Case-C systems are likely to enter classical CE phases. We also see two models at $q_i = 0.2$ with $\log_{10}(a_i/R_\odot) \approx 1.72$ and $\log_{10}(a_i/R_\odot) \approx 2.57$, respectively, that enter contact through accretor expansion. However, the accretor expansion is driven by numerical difficulties with finding accretors that spin below critical. Contact appears likely in these two models, albeit for another reason (unstable mass transfer or L_2 -overflow).

Just as for the $M_{1,i} = 10.2 M_\odot$ systems, there is a small region in the initial binary parameter space at $q_i \lesssim 0.35$ and $\log_{10}(a_i/R_\odot) \approx 3.4\text{--}3.5$ where runaway mass transfer does not occur, but a classical CE phase is expected from L_2 -overflow. For $q_i \gtrsim 0.35$, a similar region of stable Case-Bl and Case-C mass transfer as for the $M_{1,i} = 10.2 M_\odot$ systems is found (see Sect. 2.4.2).

In the same way as the $10.2 M_{\odot}$ initial primary mass models, the spin-up of the accretor leads to numerical convergence problems in both the Case B1 and -Be regions. At these higher masses, the problems persist down to initial separations of a few $100 R_{\odot}$.

2.4.1.3 Initial primary mass of $1.6 M_{\odot}$

At lower initial primary masses, more specifically $M_{1,i} = 1.6 M_{\odot}$, the situation is different than at higher masses (right panel in Fig. 2.7)⁹. Although the primary stars have radiative envelopes during the MS, none of our systems undergo Case-Be mass transfer, because of the resolution in a_i ¹⁰.

Case-A models at $q_i = 0.35$ – 0.65 encounter numerical issues when the accreting secondary star reaches critical rotation. Also in Case-B1 systems with mass ratios $q < 0.65$ – 0.75 , the models do not converge numerically. As can be seen from Figs. A.3–A.4, this is an issue that occurs for $M_{1,i} \leq 2.2 M_{\odot}$. Although this prevents us from including binary systems with $M_{1,i} \leq 2.2 M_{\odot}$ in further population analysis, specific regions of the initial binary parameter space can still be described and hold valuable information.

The expansion of the accretor star is leading to the formation of contact binaries in Case-A systems with $\log_{10}(a_i/R_{\odot}) \lesssim 0.57$ and $q_i = 0.35$ – 0.55 , and $\log_{10}(a_i/R_{\odot}) = 0.57$ – 0.79 and $q_i = 0.55$ – 1.00 (Fig. 2.7). Similar to contact systems with $M_{1,i} = 10.2 M_{\odot}$, systems with $q_i \gtrsim 0.80$ experience L_2 -overflow.

Case-A systems with $q_i = 0.65$ – 0.94 and $\log_{10}(a_i/R_{\odot}) = 0.73$ – 0.94 evolve through similar pathways as those in equivalent regions of the initial parameters space with $M_{1,i} = 10.2 M_{\odot}$ and $M_{1,i} = 20.0 M_{\odot}$. The primaries are stripped in Case-A and Case-B mass-transfer phases, after which reverse mass transfer occurs.

In between the Case-A systems at $q_i = 0.65$ – 1.00 that form contact binaries through accretor expansion and those that avoid contact, contact binaries form by tidal interaction. In our grid, such tidally driven contact in Case-A systems can be found for initial primary masses between 0.8 and $1.8 M_{\odot}$. For initial primary masses between 0.8 and $1.1 M_{\odot}$ tidally driven contact also occurs in the initially closest Case-B systems with $q_i = 0.97$ (Fig. A.4).

Case-B1 binary systems at $q_i = 0.65$ – 1.00 and $\log_{10}(a_i/R_{\odot}) = 0.91$ – 1.45 evolve into contact binaries because of the expansion of the accretor. The donor stars in these binaries have deep convective envelopes, resulting in mass-transfer rates $\gtrsim 10^{-5} M_{\odot}/\text{yr}$. Because of the relatively high mass transfer rates, the accretors are out of thermal equilibrium and expand with $\tau_{\text{dyn},2} < \tau_{R/\dot{R},2} < \tau_{\text{KH},2}$ and fill their Roche lobes. In comparison, the Case-A binaries at $\log_{10}(a_i/R_{\odot}) < 0.91$, which avoid contact, have mass transfer rates $\lesssim 10^{-7} M_{\odot}/\text{yr}$, resulting in a nuclear-timescale expansion of the accretor star. The three models at $q_i = 0.85$ – 1.00 not labelled ‘Non-conservative mass transfer + cannot eject’ have conservative mass transfer because they manage to reach contact before the secondary star rotates at its critical rotation rate.

⁹Note that the lower limit for initial secondary star masses is $0.5 M_{\odot}$. Hence, there are no models at $q_i < 0.4$.

¹⁰ $1.6 M_{\odot}$ stars only expand about 20% in radius ($\lesssim 1 R_{\odot}$) before the envelope becomes predominantly convective and Case-B1 mass transfer ensues when the star fills its Roche lobe. Given the average resolution of $\sim 5 R_{\odot}$ in the Case-B region of the grid for these initial primary masses, a narrow Case-Be region is not resolved.

At larger initial separations ($\log_{10}(a_i/R_\odot) = 1.07\text{--}2.64$), Case-BI systems with $q_i > 0.65\text{--}0.75$ avoid contact. The primary stars have their envelopes removed during the red giant (RG) phase and end up as (partially) stripped stars. Mass transfer is stable because of the relatively high initial mass ratios (the mass ratio becomes greater than one early on during mass transfer). The mass transfer stops when the entire hydrogen envelope is removed. A pure helium WD remains if the hydrogen-burning shell is stripped before the helium core grows to a mass above roughly $0.45 M_\odot$. If this is not the case, central helium ignition occurs and the primary ends up as a carbon-oxygen white dwarf. Systems with $\log_{10}(a_i/R_\odot) = 2.42, 2.27, 2.28, 2.12$ do not ignite helium in the centre, whereas the initially wider systems do. We find reverse mass transfer in all cases once the secondary star becomes an RG and fills its Roche lobe. Given that the primary stars are WDs, these systems might be observable as symbiotic binaries.

Case-BI systems with $q_i = 0.35\text{--}0.45$ and $\log_{10}(a_i/R_\odot) = 2.38\text{--}2.56$ go through a phase of runaway mass transfer and experience L_2 -overflow. Since the primary star is an RG with a deep convective envelope and the secondary star an MS star at the onset of mass transfer, we expect a classical CE phase. Initially slightly wider binary systems ($q_i = 0.35\text{--}0.65$ and $\log_{10}(a_i/R_\odot) \approx 2.60$) avoid runaway Case-BI mass transfer. After core-He exhaustion, Case-BC mass transfer starts and the model quickly fails to converge numerically. While there is no clear indication for future runaway mass transfer, we cannot rule it out. Binary systems with $q_i = 0.45\text{--}0.65$ and $\log_{10}(a_i/R_\odot) = 2.39\text{--}2.60$ only go through Case-BI mass transfer. The models stop when the primary stars evolve into a pure helium WD, and the secondaries climb the giant branch.

Finally, we find that in the initially widest Case-C systems, contact phases are avoided. Here, mass transfer is stable because the primary star is in its TP-AGB phase, during which it experiences enhanced mass loss in our models (Sect. 2.2.1.2). Moreover, the star's radius periodically decreases again, preventing a runaway situation. Models that failed to converge numerically experience Case-C mass transfer before or early on during the TP-AGB phase of the primary. Their outcomes are uncertain.

2.4.2. Stable Case-BI and -C mass transfer

For all initial primary masses considered in this work, Case-C mass transfer has been found to be stable over a wide range of initial mass ratios, even down to $q_i \approx 0.2$ in some cases (e.g. for $M_{1,i} = 15.5 M_\odot$, see Fig. A.2). This also applies to the initially widest Case-BI systems, but the exact extent of this region in the initial binary parameter space is unknown because of the aforementioned numerical difficulties.

The response of the donor star's radius to mass loss has been studied using models with polytropic equations of state in Hjellming and Webbink (1987) and detailed adiabatic mass loss computations such as in Ge et al. (2010a); Ge et al. (2015, 2020). It is found that donors with radiative or convective envelopes with core-mass fractions¹¹ greater than 0.5 shrink and hence have stable mass transfer (Temminck et al., 2023)¹². Donors with convective envelopes

¹¹The core-mass fraction is defined as the mass of the core over the total mass of the star.

¹²As discussed in Temminck et al. (2023), a major caveat of this simplified picture is the assumption that the response of the donor star is fully adiabatic, as assumed in, for example, Ge et al. (2010a); Ge et al. (2015, 2020). They show that even in giants with convective envelopes, the subsurface layers, right below the layers stripped by mass transfer, thermally readjust on timescales shorter than the dynamical timescale. Considering

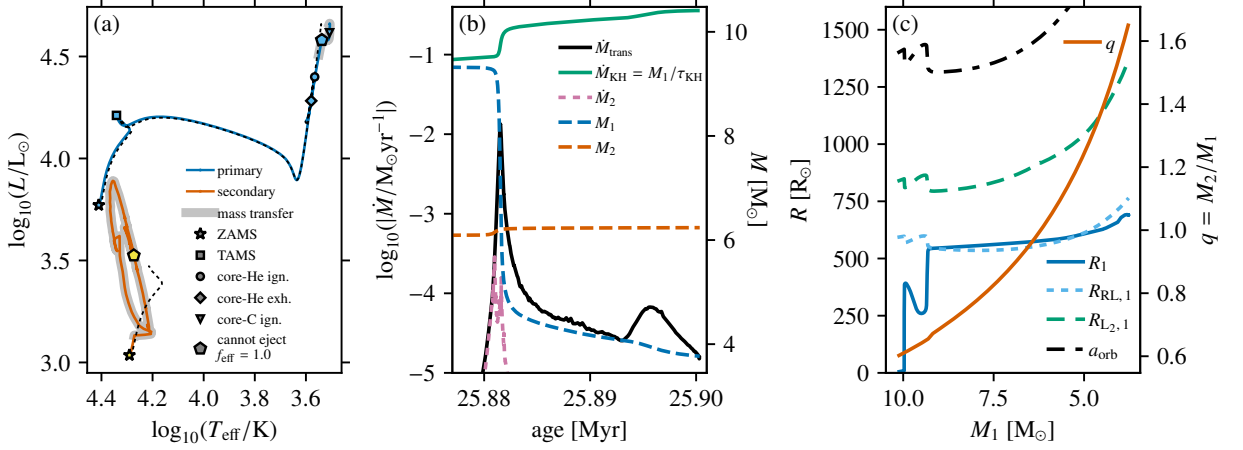


Figure 2.8: Example of a $M_{1,i} = 10.16 M_{\odot}$, $q_i = 0.6$, and $a_i = 1398.2 R_{\odot}$ binary model with stable Case-C mass transfer. Panel (a) is the same as Fig. 2.2a (‘ign.’ = ‘ignition’). Panel (b) is the same as Fig. 2.4b. Panel (c) is the same as Fig. 2.4c, with the addition of a solid orange line indicating the evolution of the mass ratio.

and core-mass fractions below 0.5 typically expand in response to mass loss and cause unstable mass transfer.

In our models, we identify two stabilising effects during Case-B1 and -C mass transfer. First, the primary star’s envelope is partially lost due to winds prior to mass transfer. This increases the core-mass fraction. At core helium ignition, values of the core-mass fraction in our stable Case-C models are 0.22, 0.15, 0.19, 0.26, and 0.31 for $M_{1,i} = 1.9, 4.4, 8.6, 14.3,$ and $20.0 M_{\odot}$, respectively. At core helium exhaustion, the values for the core-mass fraction are 0.26, 0.22, 0.28, 0.36, and 0.44, respectively. Only for the most massive primary stars with $M_{1,i} = 20.0 M_{\odot}$ at core helium exhaustion, the core-mass fraction approaches the stabilising value of 0.5. Hence, the increased core-mass fraction alone is insufficient to explain the mass transfer stability. However, stellar wind mass loss increases the mass ratio q towards unity before the onset of mass transfer. With q ’s approaching or exceeding one, orbits will (soon) widen, stabilising mass transfer.

Second, orbital widening can stabilise mass transfer. Because the mass transfer in these systems is non-conservative, it results in less orbital shrinkage \dot{a}/a than in the conservative case. Furthermore, this also causes orbital widening already at mass ratios $q < 1$, whereas this only occurs for $q \geq 1$ in conservative mass transfer (Tauris and van den Heuvel, 2006). How orbital widening stabilises mass transfer can be seen in the example of a $M_{1,i} = 10.2 M_{\odot}$, $q_i = 0.6$, and $a_i = 1398.2 R_{\odot}$ system undergoing stable Case-C mass transfer in Fig. 2.8. The orbital separation drops sharply before the onset of mass transfer because of an enhanced spin-orbit coupling when the primary becomes a supergiant. After the primary loses about $0.1 M_{\odot}$, the mass-transfer efficiency β becomes zero when the secondary star reaches critical rotation. The orbit starts to widen when the mass ratio reaches a value of 0.67 and the primary star’s Roche lobe radius stays nearly constant, preventing a situation of runaway mass transfer as described in Sect. 2.3.5. Further on, the primary star’s Roche lobe radius increases faster than the star’s radius, such that $R_1 < R_{\text{RL},1}$ at $q = 1.21$.

the local thermal timescale of these subsurface layers, they derive a maximum mass-loss rate for the donor for which it can thermally readjust and avoid the (unstable) adiabatic response.

At $M_1 = 7.2 M_\odot$ ($q = 0.87$, age = 25.8815 Myr) the mass-transfer rate reaches its peak, after which it decreases sharply. This model ends its evolution when the primary reaches core-C exhaustion, which happens during mass transfer as in most of our stable Case-C models.

2.4.3. Population properties

To understand what fraction of systems avoid or end up in contact and through which mechanism, we count the systems in each category (‘No contact’, ‘Accretor expansion’ etc.) and weigh them with their birth probability p_{birth} (see Sect. 2.2.5). We show the results for initial primary mass ranges of $[4.8; 12.6] M_\odot$ and $[12.6; 20.8] M_\odot$ in so-called sunburst charts in Fig. 2.9. Figure 2.10 shows the results for the whole mass range of $M_{1,i} \in [4.8; 20.8] M_\odot$ ¹³. We only consider binaries with $M_{1,i} \geq 4.8 M_\odot$ because models with lower masses have not been computed for the entire $q_i = 0.1\text{--}0.97$ range (Sect. 2.2.3). The sunburst charts in the top row show the incidences of the physical mechanisms leading to contact for mass-transferring binaries. The inner level of these charts shows the fraction of all mass-transferring binary systems in the specified mass range that end their evolution with the indicated outcome. In other words, they represent the principal outcomes, ‘Accretor expansion’, ‘Runaway MT’, ‘L₂-overflow’, and ‘No contact’ (see Sect. 2.4.1.1), which correspond to the outcomes indicated by the background colours in Figs. 2.6–2.7. Models expected to avoid contact but which encountered numerical issues before the primaries reached core-C exhaustion (‘No contact’ hatching in Figs. 2.6–2.7) are included in the principal ‘No contact’ outcomes. The outer level of the sunburst charts shows the incidence of ancillary outcomes, that is, the hatching in Figs. 2.6–2.7 (‘L₂-overflow’ and ‘Non-conservative MT + cannot eject’). We assign systems that experienced numerical issues a likely evolutionary outcome based on their initial mass ratio and first mass-transfer case. For more information, we refer to Appendix A.5. These outcomes are shown at the intermediate level of the charts in the ‘Numerical issues’ slice. On the bottom row of Fig. 2.9, we show the incidences of the principal outcomes per initial mass transfer case. The outer level of these charts shows the lower limits of the incidences for stellar mergers and classical CEs (see Sect. 2.4.4).

We find that the fractions for $M_{1,i} \in [4.8; 12.6] M_\odot$ and $M_{1,i} \in [12.6; 20.8] M_\odot$ are relatively similar (Fig. 2.9). The most noticeable differences are found for the systems going through a phase of runaway mass transfer (‘Runaway MT’) and systems failing to eject non-accreted matter (‘Non-conservative MT + cannot eject’). The lower fraction of systems that simultaneously avoid contact and fail to eject non-accreted matter for higher primary masses can be traced back to the mass-luminosity relation. In general, $L \sim M^\alpha$, where the exponent $\alpha > 1$ (Kippenhahn et al., 2013). So, even though the gravitational potential increases linearly with increasing mass, the luminosity increase is steeper since $\alpha > 1$. Hence, it is easier for higher mass systems to expel non-accreted matter.

The fraction of systems with runaway mass transfer in the lower mass range is 5% higher than in the higher mass range. At the same time, the fraction of systems with numerical issues is 7% higher in the higher mass range. However, the total fraction of systems with numerical issues that have runaway mass transfer as their most likely outcome is 4–6% in both mass ranges. The higher fraction of systems with runaway mass transfer in the lower mass range is thus not caused by increased numerical difficulties at higher masses but is

¹³To compute p_{birth} , the initial mass function is integrated from M_l to M_u (see Sect. 2.2.5). For the models with $M_{1,i} = 20.0 M_\odot$, $M_u = 20.8 M_\odot$. This explains why the initial primary mass range extends to $20.8 M_\odot$.

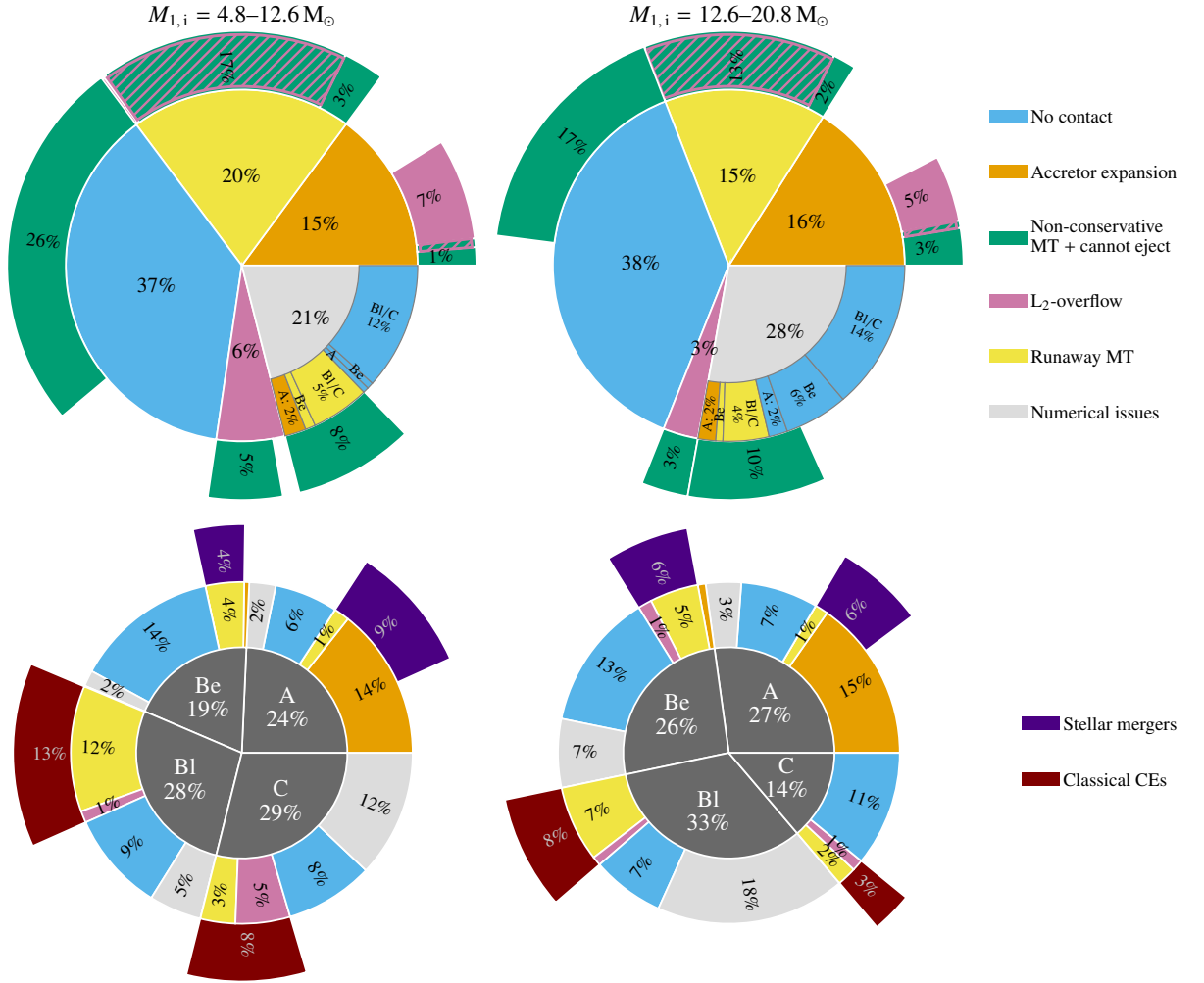


Figure 2.9: Sunburst charts displaying the fractions of evolutionary outcomes for mass-transferring binary systems in the grid over initial primary mass ranges of $[4.8; 12.6] M_{\odot}$ (left) and $[12.6; 20.8] M_{\odot}$ (right). Wedges with a percentage $< 1\%$ are not labelled. (*Top row*) The inner level shows the principal outcome of the evolution (‘Accretor expansion’, ‘Runaway MT’, ‘L₂-overflow’, and ‘No contact’), while the outer level shows the ancillary outcome (‘L₂-overflow’, ‘Non-conservative MT + cannot eject’). Ancillary ‘No contact’ outcomes are incorporated in the inner ‘No contact’ category. Models in the ‘Numerical issues’ category are assigned a likely evolutionary outcome based on their initial mass ratio q_i and mass-transfer case, displayed on the sunburst chart’s intermediate level. The labels ‘A’, ‘Be’, and ‘Bl/C’ refer to Case-A, Case-Be, and Case-Bl or -C mass transfer, respectively. (*Bottom row*) The inner level shows the percentage of Case-A, -Be, -Bl, and -C systems. We show the principal outcome per case on the middle level. The outer level shows the lower limits of the total fraction of stellar mergers and classical CEs per mass-transfer case.

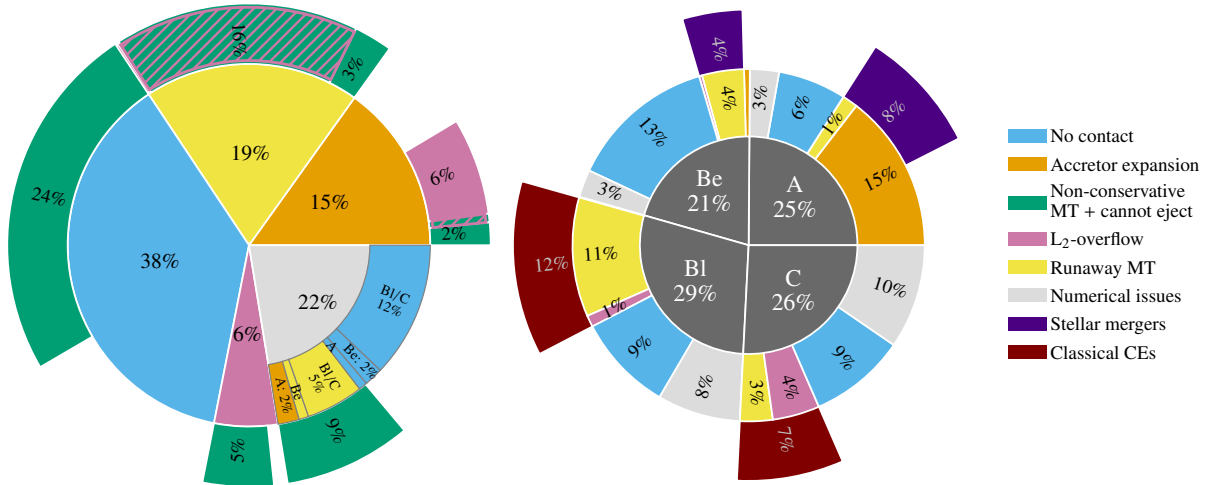


Figure 2.10: Sunburst charts displaying the fractions of evolutionary outcomes for mass-transferring binary systems in the grid over initial primary mass ranges of $[4.8; 20.8] M_{\odot}$. The left and right charts are equivalent to those in the top and bottom row of Fig. 2.9, respectively.

physical.

Excluding the systems with numerical issues, we find that $\geq 41\%$ of binaries with $M_{1,i} \in [4.8; 12.6] M_{\odot}$ and $\geq 34\%$ of binaries with $M_{1,i} \in [12.6; 20.8] M_{\odot}$ enter a contact phase (Fig. 2.9). Over the whole initial primary mass range of $M_{1,i} \in [4.8; 20.8] M_{\odot}$, the percentage of binaries entering a contact phase is $\geq 40\%$ (Fig. 2.10). These are lower limits because, in addition to excluding the systems with numerical issues, we do not take into account the binaries that avoid contact in our models but fail to eject non-accreted matter.

2.4.4. Stellar merger and classical CE incidence

We assume that all binaries experiencing runaway mass transfer and/or L_2 -overflow merge or enter a classical CE phase. Following the physical picture described in Sect. 2.3, we make the distinction based on the structure of the primary star. This means that Case-A and -Be binaries with runaway mass transfer and/or L_2 -overflow lead to stellar mergers, and Case-BI and -C binaries to classical CEs. Based on this, we compute lower limits on the incidences of stellar mergers and classical CEs, shown in the bottom row of Fig. 2.9 for initial primary mass ranges of $[4.8; 12.6] M_{\odot}$ and $[12.6; 20.8] M_{\odot}$, and for each initial primary mass in Table 2.1. This table also lists the critical mass ratios q_{crit} for which binaries with $q_i < q_{\text{crit}}$ merge or enter classical CE phases. The stellar merger and classical CE incidences are $\geq 13\%$ and $\geq 21\%$, respectively, for the primary mass range of $[4.8; 12.6] M_{\odot}$, and $\geq 12\%$ and $\geq 11\%$, respectively, for the primary mass range of $[12.6; 20.8] M_{\odot}$. Figure 2.10 shows similar charts for the total initial primary mass range of $[4.8; 20.8] M_{\odot}$, and we find that $\geq 12\%$ of mass-transferring binaries merge and $\geq 19\%$ evolve towards a classical CE phase. The stellar merger incidence for Case-A binaries of 8% (Fig. 2.10) is similar to the incidence of massive stars with strong, large-scale magnetic fields of $\sim 10\%$ (Donati and Landstreet, 2009; Fossati et al., 2015; Grunhut et al., 2017), which are likely formed by (pre-)MS stellar

mergers (Schneider et al., 2019).

The incidences reported in Figs. 2.9–2.10 and Table 2.1 are lower limits since the criteria given here do not take into account binary systems that merge as a result of a classical CE phase, binary systems that experience L_2 -overflow in later contact phases (so far if more than one contact phase occurred, we only considered the first one, see Sect. 2.3.1), and potential mergers among the models that had numerical issues. Furthermore, a certain fraction of models avoiding contact but failing to eject non-accreted matter (‘Non-conservative MT + cannot eject’) might in reality also merge (see discussion in Sect. 2.5.3). If we now assume that all contact binaries formed through the expansion of the accretor eventually merge (except those which survive contact and reach core-C exhaustion in either component), we find stellar merger incidences of $\geq 18\%$, $\geq 20\%$, and $\geq 19\%$ for initial primary masses of $[4.8; 12.6] M_\odot$, $[12.6; 20.8] M_\odot$, and $[4.8; 20.8] M_\odot$, respectively. For comparison, the merger incidence for O-type stars ($M_1 \gtrsim 15 M_\odot$) found by interpreting observations in the context of binary evolution and reported in Sana et al. (2012) is 20–30%.

We find that the incidences of stellar mergers of $\sim 12\%$ are similar for all initial primary masses (bottom row of Fig. 2.9 and Table 2.1). The classical CE incidence varies more significantly, from 12% at $M_{1,i} = 5.2 M_\odot$, to 33% at $M_{1,i} = 10.2 M_\odot$ and 9% at $M_{1,i} = 20.0 M_\odot$. The decrease in classical CE incidence from $10.2 M_\odot$ to $20.0 M_\odot$ is linked to the decrease in Case-C systems (bottom row of Fig. 2.9). Our values of $q_{\text{crit}} = 0.15\text{--}0.35$, correspond reasonably well with those for HG star donors from Temmink et al. (2023).

2.4.5. Comparison with observed contact binaries

In Fig. 2.11, our simulated population of Case-A contact binaries with initial primary masses of $4.8\text{--}20.8 M_\odot$ is compared to observed near-contact¹⁴ and contact systems in the Milky Way (MW), Large Magellanic Cloud (LMC) and Small Magellanic Cloud (SMC) from Ostrom (2001), Harries et al. (2003), Hilditch et al. (2005), Mahy et al. (2020), and Janssens et al. (2021), compiled in Menon et al. (2021). The sample consists of MS O+O, B+O and B+B massive contact systems, which is why we have chosen to compare only to Case-A binaries from our grid with initial primary masses $\geq 4.8 M_\odot$ (this is as low as we can go in terms of the initial primary mass while still having models at all q_i). The mass ratios of the observed systems are compared to the probability distribution function (PDF) of the models as a function of the mass ratio q at contact. For models that enter a contact phase through the expansion of the accretor, contact is defined as the moment when both the primary and the secondary overflow their respective Roche lobes. When runaway mass transfer is responsible for the onset of a contact phase, the moment at which $\dot{M}_{\text{trans}} > \dot{M}_{\text{KH},1}$ is taken as the moment of contact. To have a meaningful comparison with observed contact systems, the mass ratios at contact of the observed systems are defined here as the mass of the currently less massive component over the mass of the currently more massive one (whereas before q has always been defined as the mass of the initially less massive component over the mass of the initially more massive one). The probabilities used to construct the PDF are the birth probabilities p_{birth} computed via Eq. (2.4) in Sect. 2.2.5. We highlight the following contributions to the PDF: ‘accretor expansion’ systems are those that enter contact because of accretor expansion but do not experience L_2 -overflow, while the ‘accretor expansion + L_2 -overflow’ do. The third contribution comes from runaway mass transfer systems (‘runaway MT’). The ‘accretor expansion’ and ‘accretor expansion + L_2 -overflow’ systems are further

¹⁴Near-contact systems are systems in which for both components $R/R_{\text{RL}} \geq 0.9$ (Menon et al., 2021).

Table 2.1: Stellar merger and classical CE incidences, and critical mass ratios $q_{i, \text{crit}}$ for mass-transferring binaries with $M_{1,i} \in [4.8; 20.8] M_{\odot}$. For each initial primary mass, the incidence fractions are given per mass-transfer case.

$M_{1,i}$ [M_{\odot}]	Mergers [%]	Class. CEs [%]	$q_{i, \text{crit}}^a$
5.2	12.8	11.9	
A	10.2	-	0.35
Be	2.6	-	0.35
Bl	-	4.3	0.35–0.55
C	-	7.5	0.55
6.1	14.8	16.1	
A	12.0	-	0.35
Be	2.9	-	0.35
Bl	-	9.1	0.25–0.45
C	-	6.9	0.55
7.2	13.0	18.4	
A	8.2	-	0.35
Be	4.8	-	0.15–0.25
Bl	0	12.3	0.35–0.45
C	0	6.1	0.25
8.6	11.3	31.2	
A	7.3	-	0.35
Be	4.0	-	0.25–0.35
Bl	-	19.7	0.25–0.35
C	-	11.8	0.45
10.2	12.2	33.0	
A	8.0	-	0.25–0.35
Be	4.2	-	0.25–0.35
Bl	-	19.9	0.25–0.35
C	-	13.0	0.45
12.0	11.3	23.1	
A	7.0	-	0.35
Be	4.3	-	0.25–0.35
Bl	-	19.1	0.15–0.35
C	-	4.0	0.15–0.45
13.1	8.1	12.4	
A	5.7	-	0.35
Be	2.4	-	0.25–0.35
Bl	-	8.7	0.35–0.45
C	-	3.7	0.15–0.35
14.2	11.4	16.4	
A	5.6	-	0.35
Be	5.8	-	0.25–0.35
Bl	-	12.4	0.15–0.45
C	-	4.0	0.15–0.35
15.6	13.9	9.2	
A	6.9	-	0.35
Be	7.0	-	0.25–0.35
Bl	-	8.2	0.15–0.35
C	-	0.9	0.15
16.9	14.3	8.7	
A	6.8	-	0.35
Be	7.6	-	0.15–0.35
Bl	-	7.7	0.15–0.35
C	-	1.0	0.15
18.4	14.0	8.5	
A	6.5	-	0.35
Be	7.5	-	0.15–0.35
Bl	-	5.8	0.15–0.35
C	-	2.7	0.15–0.25
20.0	13.6	8.6	
A	6.8	-	0.35
Be	6.8	-	0.15–0.35
Bl	-	4.9	0.15
C	-	8.6	0.25–0.35

^(a) Case A and -Be systems with $q_i < q_{i, \text{crit}}$ form contact binaries through runaway mass transfer and/or L_2 -overflow, and merge. Case-Bl and -C systems form classical CEs through runaway mass transfer and/or L_2 -overflow.

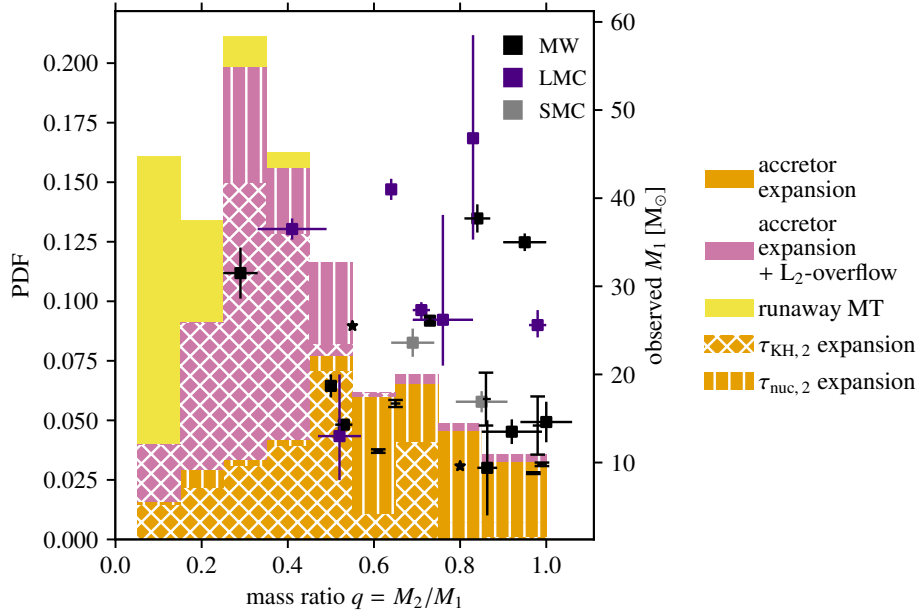


Figure 2.11: Probability density function (PDF) of contact systems formed in Case-A binaries with $M_{1,i} = 4.8\text{--}20.8 M_{\odot}$ as a function of the mass ratio q at the onset of contact. Data points (filled squares) show the observed mass ratio and primary mass (right axis) for all observed MW, LMC and SMC contact and near-contact systems from Ostrov (2001), Harries et al. (2003), Hilditch et al. (2005), Mahy et al. (2020), and Janssens et al. (2021), compiled in Menon et al. (2021), including the uncertainties on their values. Systems without reported uncertainties on q are indicated with a dash symbol, and those without reported uncertainties on q and M_1 are indicated with a star symbol.

divided into systems where the accretor expands on a nuclear and a thermal timescale prior to filling its Roche lobe. This division is made by comparing the mean of the expansion timescale $\tau_{R/\dot{R}}$ from the onset of mass transfer to the formation of a contact system with the mean of the thermal and nuclear timescales respectively (see Appendix A.4).

There is a striking difference between the PDF from the model systems and the observations. From the models, we expect two to three times more contact systems at $q < 0.5$ than at $q \geq 0.5$. Contrarily, observations show a dearth of contact binaries at $q < 0.5$. There are only a few models at $q \geq 0.5$ experiencing L_2 -overflow, while such systems are dominant at $q < 0.5$. For $q < 0.45$, there is an additional contribution of contact systems formed through runaway mass transfer. Among the contact binaries that do not experience L_2 -overflow or runaway mass transfer (‘accretor expansion’), it can be seen that at $q < 0.5$ contact is formed mostly on a thermal timescale, while for $q \geq 0.5$ contact is formed on the longer, nuclear timescale. Overall, 29% of the Case-A contact binaries in the mass range considered here form through the nuclear timescale expansion of the accretor. 59% of those (17% of the total) do not yet experience L_2 -overflow and are expected to be longer-lived.

We find a number of ways in which this (apparent) discrepancy can be resolved. Firstly, it should be noted that the sample of observed systems is small, especially if one disregards the near-contact systems, which have been considered in this comparison. The absence of observed systems at mass ratios $q < 0.5$ might be because they have simply not been observed yet. As argued in Abdul-Masih et al. (2022), a larger sample size, which requires a dedicated search for these massive contact binary systems, should shed light on whether

this is the case.

A second reason for the discrepancy could be that contact systems rapidly evolve to equal-mass systems, that is, to $q = 1$, and are therefore not observed as unequal-mass systems. However, following the same argument as in Abdul-Masih et al. (2022), the observed systems are uniformly distributed for $q \geq 0.5$. Should contact systems all equalise in mass, the bulk of them would be expected to be observed at $q \approx 1$. Furthermore, they find that based on the observed stability of the orbit, the systems in their sample will continue to evolve as unequal-mass contact binaries on a nuclear timescale.

Based on the different contributions to the PDF in Fig. 2.11, a third reason for the lack of contact systems at $q < 0.5$ can be found. The largest contribution to the PDF at these mass ratios comes from contact binaries that experience L_2 -overflow. As described in Sect. 2.3.3, this can lead to considerable orbital angular momentum loss and thereby likely stellar mergers. Case-A contact binaries formed through runaway mass transfer, which we find at $q < 0.45$, also lead to mergers (see Sect. 2.3.5). In other words, contact systems are almost exclusively observed at $q \geq 0.5$ because those at $q < 0.5$ merge shortly after they get into contact.

Considering that binaries with L_2 -overflow or runaway mass transfer merge quickly, we are left with a PDF that at $q < 0.5$ is dominated by contact systems formed by the thermal-timescale expansion of the accretor. As explained in Sect. 2.3.1, such contact binaries either detach or merge quickly. In the former case, these systems would be observed as semi-detached binaries. In the latter case, we argue that if the thermal expansion of the accretor continues during contact, it eventually leads to L_2 -overflow and a merger. Ge et al. (2023) find that the critical mass ratio q_{crit} below which binaries experience runaway mass transfer increases with decreasing metallicities. Therefore, at lower metallicities, we expect an even more significant fraction of binaries to experience runaway mass transfer and a subsequent quick merger. In conclusion, we find that contact systems are almost exclusively observed at $q \geq 0.5$ because those at $q < 0.5$ merge or detach shortly after they get into contact.

2.5. Discussion

In this section, we put into perspective the influence of mass-transfer efficiency on our contact tracing results (Sect. 2.5.1), the occurrence of stable mass transfer from (super-)giant donors (Sect. 2.5.2), and the potential fates of binaries with non-ejected matter (Sect. 2.5.3).

2.5.1. The role of mass-transfer efficiency

The mean mass-transfer efficiencies $\bar{\beta}$ of binaries in our grid (Fig. A.10 in Appendix A.6) are relatively low for Case-B and -C mass transfer. In these systems, the secondary usually reaches critical rotation after accreting $M_{\text{accreted}}/M_{2,i} < 3\%$ of its initial mass (with M_{accreted} the accreted mass), which is lower than the $\sim 5\text{--}10\%$ from Packet (1981) and consistent with the $\sim 2\%$ found by Ghodla et al. (2023). It should be noted that only a few percent of the secondary's outer envelope in terms of its mass is rotating near the critical rotation rate. With more efficient angular momentum transport, the relative mass accretion fraction would be higher than 3% because of a delay of critical surface rotation.

Because the secondary stars in our models accrete less matter than those in more conservative models, they also expand less. Compared to models with higher mass-transfer efficiencies, such as those from Pols (1994), Wellstein et al. (2001), de Mink et al. (2007),

Claeys et al. (2011), and Menon et al. (2021), we find fewer contact systems from accretor expansion. The difference is particularly noticeable for Case-B binaries, where virtually none of such systems are found in our models. Our results generally agree better with the model grids from Fragos et al. (2023). This is expected since similar assumptions with regard to mass-transfer efficiency are made in their models.

From observations of Be X-ray binaries in the SMC, Vinciguerra et al. (2020) infer a mass-transfer efficiency of $\sim 30\%$ for the progenitor systems (i.e. the systems before the primary has formed a compact object). Potential progenitors of Be X-ray binaries in our grid, those with post-CHeB (core helium burning) and MS components (see Figs. A.5–A.7 in Appendix A.3), have a wide range of mass-transfer efficiencies (see Fig. A.10). For Case-A binaries with $M_{1,i} = 6.1\text{--}8.6 M_{\odot}$ and Case C binaries with $M_{1,i} = 5.2\text{--}14.2 M_{\odot}$ the mass-transfer efficiency is consistent with the observationally constrained value of $\sim 30\%$.

Using observations of the classical Algol system δ Librae, Derviřođlu et al. (2018) found a mass-transfer efficiency of $\sim 100\%$. Based on the component masses derived for δ Librae, the initial primary mass would have been between $\approx 2.6 M_{\odot}$ ($q_i = 1.0$) and $\approx 4.1 M_{\odot}$ ($q_i = 0.25$, stable mass transfer). Our Case-A mass-transfer efficiency for $M_{1,i} \approx 2.6 M_{\odot}$ is $\sim 95\%$, which is consistent with the observationally constrained value. For $M_{1,i} \approx 4.1 M_{\odot}$, we find a Case-A mass-transfer efficiency of $\sim 25\%$, which is inconsistent with the value inferred for δ Librae.

Sen et al. (2022) computed a grid of Case-A systems with $M_{1,i} = 10\text{--}40 M_{\odot}$ at LMC metallicity ($Z = 0.0047$) and similar assumptions as ours with regards to rotation, tides and accretion of angular momentum. For thermal-timescale mass-transfer phases in systems avoiding contact on the MS, they find relatively low (time-averaged) mass-transfer efficiencies (peak around ~ 0.06). During the slower, nuclear-timescale mass transfer phases, the mass-transfer efficiency peaks around ~ 0.94 . This is consistent with our models, in which the rapid spin-up of the accretor during thermal-timescale mass transfer results in non-conservative mass transfer. For $M_{1,i} > 10 M_{\odot}$, the time-averaged mass-transfer efficiencies in our models range from ~ 0.4 to ~ 0.65 (Fig. A.10). The thermal timescale is several orders of magnitude shorter than the nuclear timescale (Eq. 1.2 and 1.1). From estimating the time-averaged mass-transfer efficiencies over the whole Case-A phase (thermal- and nuclear-timescale mass-transfer phases) in the models of Sen et al. (2022), we see that their values of the mass-transfer efficiency are closer to unity. The slightly different definitions of the mass-transfer efficiency and the different metallicities (and, therefore, wind mass-loss rates) between our grids likely explain this difference.

Our models' current assumption that stars cannot accrete anymore once they are at breakup velocities might be up for debate. Interactions with an accretion disk have been proposed to spin down the surface of the accretor and allow for additional accretion of material (Paczynski, 1991; Popham and Narayan, 1991). This contributes to the fact that the incidences of contact systems reported in Sect. 2.4.4 are lower limits because more accretion allows the accretor to expand more and potentially fill its Roche lobe. This could in turn increase the stellar merger incidences.

2.5.2. The stability of Case-B and -C mass transfer

In Sect. 2.4.2 we have described how non-conservative mass transfer and stellar wind mass loss from the donor prior to mass transfer can lead to stable mass transfer from (super-)giant donors (Case B1 and C) with initial mass ratios down to 0.1. Following the discussion in Sect. 2.5.1, these outcomes might also change with different assumptions regarding the mass-transfer efficiency. Just as for the formation of contact binaries, an increase in the mass-transfer efficiency leads to a higher incidence of classical CEs.

The presence of stable Case-B1 and -C mass transfer in our models agrees with what was found by Chen and Han (2008) for stars with $M_{1,i} \lesssim 8 M_{\odot}$, who also note that the effect of wind mass loss prior to the onset of mass transfer only has a minor effect on the stability.

We find that our critical mass ratios $q_{i,\text{crit}}$ for Case-B1 and -C mass transfer (Table 2.1) are higher than those from the adiabatic mass loss computations of Ge et al. (2010a) for $M_{1,i} > 10 M_{\odot}$, while being in relatively good agreement for stars with lower initial primary masses. These differences are likely caused by the fact that contrary to Ge et al. (2010a), we also take the response of the accretor and orbit into account. Another difference is that Ge et al. (2010a); Ge et al. (2015, 2020) derive the critical mass ratios under the assumption of fully conservative mass transfer. Our critical mass ratio ranges agree relatively well with similar simulations with fully non-conservative mass transfer (H. Ge, 2023, priv. comm.).

Picco et al. (2024) use the adiabatic mass-radius exponents ζ_{ad} (see Sect. 1.1.4.2) from Ge et al. (2020) to determine the stability of mass transfer in their detailed binary evolution models. Our critical mass ratios agree relatively well with the ones from their simulations of fully non-conservative mass transfer in binaries with $M_{1,i} = 8.0 M_{\odot}$.

The adiabatic mass-radius exponents ζ_{ad} are also used by Li et al. (2023) in their binary population synthesis computations. For binaries with $M_{1,i} = 8.0 M_{\odot}$ with non-conservative ($\beta = 0\text{--}0.5$) Case-B1 and -C mass transfer, they find values for $q_{i,\text{crit}} \approx 0.37\text{--}0.66$, which is in broad agreement with our values.

Similar stable Case-B1 and -C mass transfer has been found by Ercolino et al. (2023) for $M_{1,i} = 12.6 M_{\odot}$. The reported critical mass ratio $q_{\text{crit}} = 0.525\text{--}0.625$ is slightly higher than what is found in our models for stars with similar masses (Table 2.1). This difference can be attributed to the different stability criteria for mass transfer used in their work.

2.5.3. The fate of binaries with non-ejected matter

In the majority of our models with $\beta < 1$, the non-accreted mass cannot be ejected to infinity. This raises the question of where this excess material resides. Should the excess matter remain in the accretor's Roche lobe or the binary's L_2 -lobe, it can fill it up and lead to a situation similar to a contact binary. In this case, our grid would contain significantly more contact systems. For the orbital evolution, this scenario would essentially correspond to that of systems with higher mass-transfer efficiencies. Should the excess matter overflow the L_2 -lobe and hydrodynamic drag becomes significant, a classical CE could form. Alternatively, the matter could settle in a circumbinary disk or shell, which can significantly influence the further evolution of the binary (Wei et al., 2024).

Alternatively, a circumstellar disk may form, through which the secondary can potentially continue to accrete mass (Paczynski, 1991; Popham and Narayan, 1991). In this scenario, systems might show signs of circumstellar disks such as $H\alpha$ excess and emission features in Be/Oe stars. This could explain the fast-rotating $H\alpha$ emitters in the extended

MS turn-off observed in young clusters (Milone et al., 2018). Moreover, Bodensteiner et al. (2021) has found a significant close-binary fraction of $34_{-7}^{+8}\%$ for one of the clusters analysed in Milone et al. (2018), NGC 330.

2.5.4. The onset of contact through runaway mass transfer and L_2 -overflow

In Sect. 2.4.1, we find that runaway mass transfer and/or L_2 -overflow are responsible for the onset of contact for a significant fraction of the Case-A, -Be, -Bl, and -C binaries. In Case-A binaries, L_2 -overflow is of lesser importance for the onset of contact but leads to stellar mergers in contact binaries formed through the expansion of the accretor. Runaway mass transfer in Case-A systems leads to the formation of unstable contact binaries and subsequent stellar mergers. The same happens in Case-Be binaries, but now in unison with L_2 -overflow. The added effect of the orbital angular momentum loss associated with L_2 -overflow contributes to the instability of the contact binary formed through runaway mass transfer. In Case-Bl and -C binaries, the onset of runaway mass transfer and L_2 -overflow often occur quasi-simultaneously. In these systems, the L_2 -overflow serves as an additional indication that the secondary is being engulfed by the rapidly expanding envelope of the (super-)giant primary star during runaway mass transfer. Lastly, some Case-Bl and C systems do not experience runaway mass transfer but do have primary stars that extend far beyond the L_2 -lobe. In both cases, we expect the onset of a classical CE phase.

2.6. Summary and conclusions

Using a grid of ~ 6000 detailed binary evolution models including rotation, tidal interactions, the evolution of both components, and with component masses between 0.5 and $20.0 M_\odot$, we examine in which regions of the initial binary parameter space we expect contact phases, such as contact binaries and classical common-envelope (CE) phases, to occur. We identify five mechanisms that lead to contact: the expansion of the accretor, runaway mass transfer, L_2 -overflow, orbital decay because of tides, and non-conservative mass transfer.

We find that accretor expansion, L_2 -overflow, and runaway mass transfer lead to the formation of contact binaries in Case-A and -Be systems, and L_2 -overflow and runaway mass transfer to the onset of classical CEs in Case-Bl and -C systems. This distinction stems from the fact that primary stars in Case-Bl and Case-C systems have extended envelopes with a clear core-envelope boundary, which engulfs the more compact MS companion upon contact. Case-A binaries with initial primary masses below $2 M_\odot$ also form contact binaries because of the orbital decay caused by tides. Overall, the incidences of mass-transferring binaries forming contact binaries or entering a classical CE phase are $\geq 41\%$ and $\geq 34\%$ for $M_{1,i} \in [4.8; 12.6] M_\odot$ and $M_{1,i} \in [12.6; 20.8] M_\odot$, respectively. Over the entire mass range of $M_{1,i} \in [4.8; 20.8] M_\odot$, the incidence is $\geq 40\%$. These numbers are lower limits because they do not take into account the binaries that might enter a contact phase because of the interaction with non-accreted matter. Such systems are fairly common in our grid, and could alternatively result in systems with circumstellar disks and $H\alpha$ emission features. Potential observational counterparts could be found in the extended MS turn-off in young stellar clusters.

We find that mass transfer is non-conservative in a large part of the initial binary parameter space, which is caused by the spin-up of the accretors to critical rotation after accreting $< 3\%$ of their own mass. The mass transfer efficiencies are 15–65%, 5–25%, and 25–50% in Case-A, -B, and -C mass transfer, respectively, for primary-star masses above $3 M_{\odot}$. The incidence of systems entering a contact phase is sensitive to the mass-transfer efficiency. Given the relatively low mass-transfer efficiencies in our models, we might be underestimating this incidence. Another consequence of non-conservative mass transfer is that Case-BI and -C mass transfer is stable for mass ratios ≥ 0.15 –0.35.

By assuming that systems Case-A and -Be systems with $M_{1,i} \in [4.8; 20.8] M_{\odot}$ that experience L_2 -overflow and/or runaway mass transfer merge, and Case-BI and -C systems experiencing this enter a classical CE, we find stellar merger and classical CE incidences among mass-transferring binaries of $\geq 12\%$ and $\geq 19\%$, respectively. If we relax this assumption and assume that all contact binaries, except those for which either component reaches core-C exhaustion, eventually merge, the stellar merger incidence increases to $\geq 19\%$. Just as for the incidence of mass-transferring binaries reaching a contact phase, the stellar merger and classical CE incidences are lower limits, which are sensitive to the mass-transfer efficiency.

Lastly, we compare our population of massive ($M_{1,i} \gtrsim 5 M_{\odot}$) Case-A contact systems with observed (near-)contact systems. We find from our models that approximately two to three times as many contact binaries form with mass ratios $q < 0.5$ upon contact than with $q > 0.5$. Moreover, the majority of the systems with $q < 0.5$ form contact binaries because of runaway mass transfer or the thermal-timescale expansion of the accretor, with subsequent L_2 -overflow in more than half of the cases. Therefore, most of these systems quickly merge or detach. This is in agreement with the observations since almost no (near-)contact systems are observed with mass ratios below 0.5. Out of all systems forming contact binaries, 17% do so on the accretor’s nuclear timescale and avoid L_2 -overflow, and are expected to be stable and long-lived. The majority of these systems have $q > 0.5$ upon contact, which is again in excellent agreement with the observations.

Mergers and classical CEs are some of the most complex and fascinating outcomes of binary evolution. While we have identified the physical mechanisms that can lead to contact, the outcome of mergers and classical CEs still need to be explored in more detail and leave many open questions.

Acknowledgments We wish to thank the referee, Hongwei Ge, for his valuable comments and suggestions, which have helped us further improve this work. We thank S. Hekker, Ph. Podsiadlowski, D. Wei, V. Bronner, P. Marchant, and C. Wang for the meaningful discussions, suggestions, and comments. Additional software used in this work includes `PyMesaReader` (Wolf and Schwab, 2017), `MPI for Python` (Dalcín et al., 2005; Dalcín and Fang, 2021), `Astropy` (Astropy Collaboration et al., 2013, 2018, 2022), `NumPy` (Harris et al., 2020), `SciPy` (Virtanen et al., 2020), and `Matplotlib` (Hunter, 2007). The authors acknowledge support from the Klaus Tschira Foundation. This work has received funding from the European Research Council (ERC) under the European Union’s Horizon 2020 research and innovation programme (Grant agreement No. 945806). This work is supported by the Deutsche Forschungsgemeinschaft (DFG, German Research Foundation) under Germany’s Excellence Strategy EXC 2181/1-390900948 (the Heidelberg STRUCTURES Excellence Cluster).

Contact tracing of binary stars with fully conservative mass transfer

AUTHORS Jan Henneco and Fabian R. N. Schneider

CHAPTER INFO This brief chapter covers a small follow-up project based on the work described in Chapter 2. In this follow-up project, we computed a second binary evolution grid with fully conservative mass transfer. The main goal of this project was to see how the results from Chapter 2 would change if we assume that all the mass transferred from the donor star is accreted by the accretor star. This work is (currently) unpublished and will serve as the basis for follow-up work on the mass-transfer efficiency in the Stellar Evolution Theory group at the Heidelberg Institute for Theoretical Studies. I was the main author of this chapter. I computed, analysed, and interpreted the models. Fabian Schneider, my supervisor, was the main collaborator for this work, and we discussed the results together. This chapter is essentially an extension of Chapter 2. Therefore, explanations of the key concepts and definitions are not repeated here. It is advisable to read this chapter only after reading Chapter 2.

3.1. Introduction

The efficiency of mass transfer, that is, the fraction of mass received by the accretor star from the donor star that is actually accreted, has been a long-standing open question in binary evolution. Nevertheless, it is crucial to constrain this efficiency since it can heavily influence the outcome of binary evolution models (see, e.g. *de Mink et al. 2007* and *Claeys et al. 2011*). In the discussion section of Chapter 2 (Sect. 2.5.1), we already saw some examples of efforts to constrain the mass-transfer efficiency with a combination of observations of post-mass-transfer binaries and binary evolution models. It is clear from the results of Chapter 2 that with the assumption of rotation-limited accretion, that is, the quenching of accretion because of the spin-up of the accretor star to its critical rotation rate, the mass-transfer efficiency in models without strong tidal coupling becomes relatively low. In that sense, we can consider mass-transfer efficiency in the grid of binary evolution models in Chapter 2 to be the lower end of the mass-transfer efficiency range (assuming that no mass is accreted

at all is nonsensical). Therefore, in this work, we recompute the grid of binary evolution models from Henneco et al. (2024b) assuming fully conservative mass transfer and assess how this influences the outcomes of binary evolution.

3.2. Methods

We computed a grid of ~ 6000 binary evolution models using an almost identical setup to the one used in Chapter 2 (Henneco et al., 2024b), which is described in Sect. 2.2. The main difference with that setup is that we do not allow the binary components to rotate. We did this to ensure that mass transfer is fully conservative during the whole evolution since the spin-up of the accretor star is the main reason for non-conservative mass transfer (see Sect. 2.2.2.1). Additionally, we did not limit the accretion rate to that of 0.1 times the accretor’s thermal timescale (done in Henneco et al. 2024b to avoid convergence issues in some parts of the initial parameter space). Following Henneco et al. (2024b), we used MESA’s Kolb mass-transfer scheme for post-MS donors. However, contrary to the models in Henneco et al. (2024b), we use MESA’s `contact` scheme whenever both stars (over)fill their respective Roche lobes regardless of the mass-transfer case. In other words, the mass-transfer computations used in this model grid are identical to those used in the models presented in Chapter 2, except for the fact that we continue the evolution for post-MS contact systems when it would be terminated in the original models. Although MESA’s `contact` scheme is primarily meant for Case-A binary systems (Marchant et al., 2016), we are interested to see how early Case-B contact binaries evolve with this scheme and how likely they are to merge, especially since we expect more Case-Be contact binaries to form with fully conservative mass transfer. Donor stars in Case-Be binaries still have relatively dense, radiative envelopes, which justifies the usage of the `contact` scheme to an extent. For the wider Case-BI and Case-C systems in which both stars (over)fill their Roche lobes, the results from the `contact` scheme should be interpreted with caution.

To avoid confusion during the comparison between the original Henneco et al. (2024b) grid and the grid presented in this work, we refer to the former as the ‘NC grid’ or ‘NC models’ (NC = non-conservative since we allow systems to have non-conservative mass transfer) and the latter as the ‘C grid’ or ‘C models’ (C = conservative). The initial parameters ($M_{1,i}$, q_i , and a_i) of the C grid are identical to those of the NC grid, since this allows for one-to-one comparisons between models with the same initial parameters in the two grids.

3.3. Results and discussion

In Fig. 3.1, we see a similar diagram as in Fig. 2.6, which shows the occurrence of contact phases in the initial parameter space for models with $M_{1,i} = 10.2 M_{\odot}$. An obvious difference between these two diagrams is the absence of systems designated with ‘Non-conservative MT + cannot eject’, given that our models have fully conservative mass transfer. Following Fig. 2.6, we added a black line in Fig. 3.1 indicating the mass ratio below which systems become Darwin unstable if they were rotating. At the lowest initial mass ratios q_i , a substantial fraction of the Case-A, -Be, and -C mass-transfer models run into numerical issues. Similar issues are reported in the results in Chapter 2. The expansion timescales $\tau_{R/\dot{R}}$ of these accretors with convective envelopes tend to approach their dynamical timescales τ_{dyn} , which goes beyond our MESA setup’s capabilities to compute. The intricacies of accretor

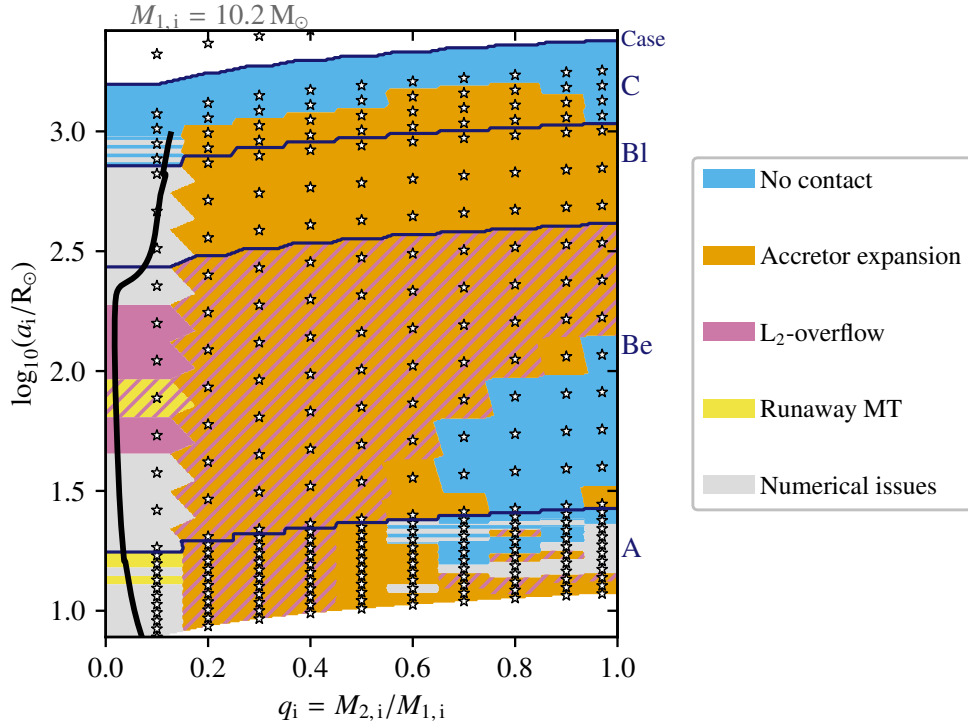


Figure 3.1: Occurrence of contact phases for models with initial primary masses $M_{1,i} = 10.2 M_{\odot}$ on the initial mass ratio–separation plane. Each MESA model is marked with a star symbol. The dark-blue quasi-horizontal lines indicate the initial mass transfer cases, which can be read from the right side. Systems on the left of the solid black line are Darwin unstable at the onset of mass transfer according to Eq. (2.6) and assuming $R_1 = R_{\text{RL},1}$.

expansion have been the topic of recent work by Lau et al. (2024), Zhao et al. (2024), and Schürmann and Langer (2024).

Both the C and NC initially closest Case-A binary models result in contact binaries. This follows from the fact that in the rotating close binary systems of the NC grid, tides efficiently spin down the accretor such that its rotation rate remains below the critical one. Mass transfer remains conservative, leading to the increasing expansion of the accretor and, hence, the formation of contact binaries. The tendency of Case-A systems with $q_i \leq 0.45$ to experience L_2 -overflow, and likely merge, is present in both grids. At larger initial separations, the Case-A outcome landscape looks considerably different. Whereas a large portion of the NC grid models at $\log(a_i/R_\odot) \sim 1.25$ avoid contact, those in the C grid form contact binaries. The continuous accretion and the resulting expansion of the accretor in these models can explain this. The accretors in their NC counterparts spin up because of weaker tidal torques, and mass transfer becomes non-conservative, avoiding a further expansion of the accretor. The line separating the Case-A from the Case-Be systems follows a trend at lower initial separations in the C grid. Since the models in the C grid do not rotate, they have smaller radii than rotating models. Consequently, their smaller radii can prevent them from filling their Roche lobe during the MS, whereas equivalent models from the NC grid do fill their Roche lobe because of their larger radius.

We see considerable differences between the C and NC grids for Case-Be systems. In the NC grid, only systems with $q_i \leq 0.25$ – 0.35 reach contact caused by runaway mass transfer or accretor expansion (Fig. 2.6). The other systems avoid contact, and their primaries evolve into stripped stars. When mass transfer is fully conservative, we see from Fig. 3.1 that a significant portion of Case-Be systems form contact binaries, experience L_2 -overflow, and likely merge. This is in stark contrast with the non-conservative models of the NC grid. Only Case-Be systems roughly below the line through $(q_i; \log a_i/R_\odot) \approx (0.65; 1.75)$ and $(q_i; \log a_i/R_\odot) \approx (0.97; 2.10)$ avoid contact. The primaries in these systems evolve into stripped stars. We ought to consider two trends to explain why these systems avoid contact: the trend with the initial mass ratio q_i and the trend with the initial separation a_i . Accretors in systems with lower mass ratios have smaller Roche lobes. Hence, when the accretor is expanding, in this case, on their thermal timescale because of the thermal-timescale mass transfer from the donor star, they fill their Roche lobe more easily than systems with larger mass ratios. Additionally, the initial response of the accretor’s Roche lobe is to shrink since the orbit of a binary with conservative mass transfer shrinks as long $q < 1$ (see Eq. 1.11). The lower the initial mass ratio, the longer the orbit and the accretor’s Roche lobe shrinks. To explain the trend with a_i , we need to consider the mass-transfer rates. Despite their larger Roche lobes (see Eq. 1.5), the accretors in the wider binaries expand more rapidly and to larger radii, eventually filling their Roche lobe. Based on this information, we expect the wider binaries to avoid contact and the closer binaries to form contact binaries. However, the determinative difference between these systems is the mass-accretion rate. We find that the mass-accretion rates (i.e. mass-transfer rates, since the mass transfer is fully conservative) in the wider binaries are consistently higher than those in the closer binaries, leading to the more rapid and extreme expansion of the accretor and the onset of contact. This is to be expected, given that the wider the orbit, the larger the radius of the donor star. Consequently, their thermal timescale, which is the timescale on which this Case-B mass transfer takes place, is shorter, leading to higher mass-transfer rates. This is consistent with what is found in Schneider et al. (2015).

Contrary to their non-conservative counterparts, Case-BI and -C systems with fully con-

servative mass transfer almost exclusively evolve to a contact configuration because of the expansion of the accretor. Only the widest mass-transferring binaries avoid contact. In these widest systems, the red supergiant donor stars never formally fill their Roche lobes, that is, there is only a phase of optically thin mass transfer (see Sect. 1.1.4) with relatively low mass transfer rates ($\dot{M}_{\text{trans}} \sim 10^{-13} M_{\odot} \text{yr}^{-1}$). The MS accretors are virtually unaffected by these extremely low accretion rates and continue to expand on their nuclear timescale. The Case-B1 and -C systems that do evolve into contact require some extra attention. Since the donor star is a supergiant, the ensuing contact phase does not qualify as a contact binary (see Sects. 1.1.5 and 2.3 or Röpke and De Marco 2023 for the definitions). However, they do not qualify as classical common envelopes either since the Roche-lobe-filling accretor star has taken on supergiant proportions itself. With fully conservative mass transfer, we thus see that the accretor star keeps expanding, whereas accretor stars that are allowed to spin up to their critical rotation rate stop expanding once the accretion is quenched. The contact phases resulting from the accretor expansion in Case-B1 and Case-C systems qualify as double-core common envelopes. This is a striking difference from the results from the NC grid, where no such double-core common envelopes are predicted to form.

So far, we have only covered the occurrence of contact phases for fully conservative systems with $M_{1,i} = 10.2 M_{\odot}$. We do not discuss the other primary masses because this will be part of future work, but show their equivalent figures to Fig. 3.1 in Appendix B.1.

We now zoom out to the population of binaries with initial primary masses in the range of [4.8; 20.8] M_{\odot} and look at the fractions of evolutionary outcomes for the C grid models in Fig. 3.2. Comparing this to their equivalent NC models, shown in Fig. 2.10 in Chapter 2, we see that the fraction of binary systems that reach a contact phase because of the expansion of the accretor is 3.66 times higher when mass transfer is fully conservative. The fraction of systems entering a contact phase because of runaway mass transfer is more than 3 times lower with fully conservative mass transfer because the accretors seem to fill their Roche lobes before mass transfer becomes unstable. Taking the systems reaching contact because of L_2 -overflow into account, we see that with fully conservative mass transfer, at least 67% or 2/3 of the binary systems in this initial primary mass range enter a contact phase. As a comparison, with non-conservative mass transfer, this lower boundary on the fraction of systems entering contact phases lies at 40%.

The fraction of binaries likely to merge is $\geq 23\%$ for models with fully conservative mass transfer, while this is twice as low ($\geq 12\%$) for the non-conservative models. This increase in the stellar merger fraction is primarily due to the increase in the fraction of Case-Be binaries forming contact binaries. In the non-conservative models, this happened only in a negligible fraction of Case-Be models. With conservative mass transfer, at least 26% of the binary models end up in double-core CEs. As discussed above, this type of contact configuration is absent from the NC grid. Only about 10% of binaries enter classical CEs with conservative mass transfer, almost half of the fraction of classical CEs in the NC grid.

In Fig. 3.3, we plot the probability distribution function of Case-A contact binaries in terms of their mass ratio q at the onset of contact and compare this with the mass ratios of observed massive contact binaries from Ostrov (2001), Harries et al. (2003), Hilditch et al. (2005), Mahy et al. (2020), and Janssens et al. (2021), compiled in Menon et al. (2021). This is the equivalent figure for Fig. 2.11 in Chapter 2, but now for the fully conservative models. We see that contrary to the non-conservative models, there are hardly any con-

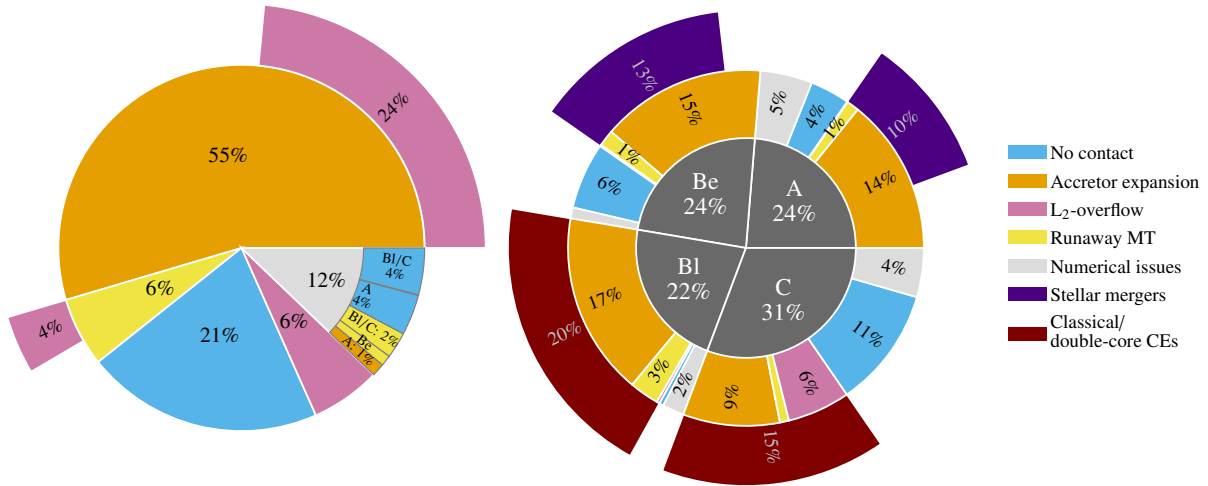


Figure 3.2: Sunburst charts displaying the fractions of evolutionary outcomes for mass-transferring binary systems in the fully conservative grid over initial primary mass ranges of $[4.8; 20.8] M_{\odot}$. Wedges with a percentage $< 1\%$ are not labelled. (*Left*) The inner level shows the principal outcome of the evolution (‘Accretor expansion’, ‘Runaway MT’, ‘L₂-overflow’, and ‘No contact’), while the outer level shows the ancillary outcome (‘L₂-overflow’). Ancillary ‘No contact’ outcomes are incorporated in the inner ‘No contact’ category. Models in the ‘Numerical issues’ category are assigned a likely evolutionary outcome based on their initial mass ratio q_i and mass-transfer case, displayed on the sunburst chart’s intermediate level. The labels ‘A’, ‘Be’, and ‘BI/C’ refer to Case-A, Case-Be, and Case-BI or -C mass transfer, respectively. (*Right*) The inner level shows the percentage of Case-A, -Be, -BI, and -C systems. We show the principal outcome per case on the middle level. The outer level shows the lower limits of the total fraction of stellar mergers and classical CEs per mass-transfer case.

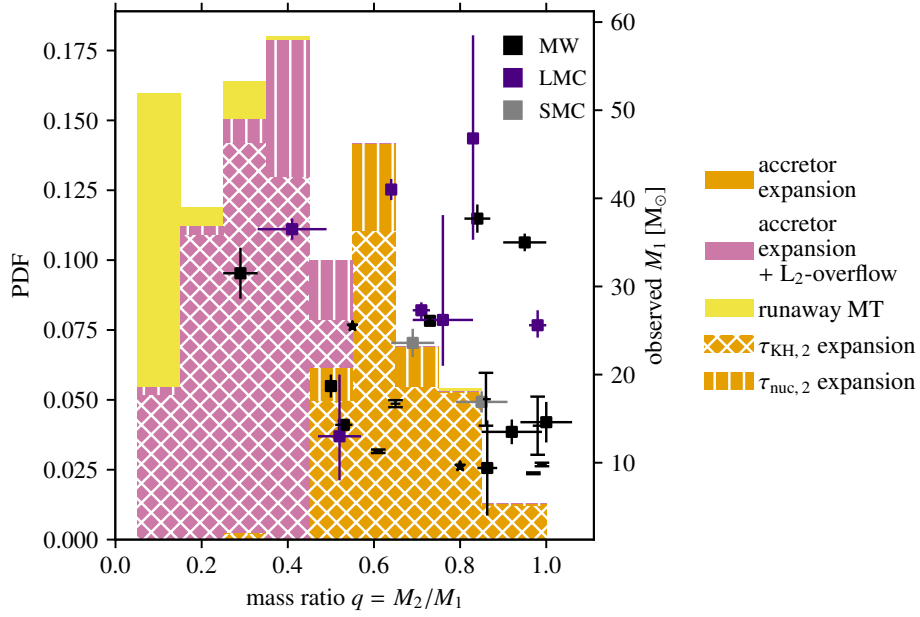


Figure 3.3: Probability density function (PDF) of contact systems formed in fully conservative Case-A binaries with $M_{1,i} = 4.8\text{--}20.8 M_{\odot}$ as a function of the mass ratio q at the onset of contact. Data points (filled squares) show the observed mass ratio and primary mass (right axis) for all observed MW, LMC and SMC contact and near-contact systems from Ostrov (2001), Harries et al. (2003), Hilditch et al. (2005), Mahy et al. (2020), and Janssens et al. (2021), compiled in Menon et al. (2021), including the uncertainties on their values. Systems without reported uncertainties on q are indicated with a dash symbol, and those without reported uncertainties on q and M_1 are indicated with a star symbol.

tact binaries entering contact because of the nuclear-timescale expansion of the accretor at mass ratios $q > 0.5$. Overall, the fraction of systems forming contact binaries because of the thermal-timescale expansion of the accretor dominates over those forming because of nuclear-timescale expansion for all mass ratios. Another striking difference is that virtually all conservative models likely merge because of L_2 -overflow. In summary, fully conservative mass transfer can explain the dearth of observed contact binaries with $q < 0.5$, given that virtually all of these are expected to merge, but does not predict a large fraction of long-lived (nuclear-timescale expansion of the accretor) contact binaries as the non-conservative models do.

3.4. Conclusions

We computed an equivalent grid to that of Henneco et al. (2024b), presented in Chapter 2, forcing the binary evolution models to have fully conservative mass transfer. In the original grid from Henneco et al. (2024b), the spin-up of the accretor star leads to non-conservative mass transfer in systems where tides cannot synchronise the accretor. We find that the efficiency of mass transfer strongly influences contact phase occurrence in the initial binary parameter space. Case-Be binaries, with HG donor stars, produce stripped-star binaries with non-conservative mass transfer yet evolve into unstable contact binaries when mass transfer is fully conservative. We see the appearance of double-core CEs, contact configurations between two objects of supergiant proportions, when we assume conservative mass transfer. In contrast, these objects are completely absent from the grid with non-conservative mass transfer. The lower boundary on the fraction of binary systems from the grid entering a contact phase because of the expansion of the accretor is almost four times as large for conservative mass transfer than it is for non-conservative mass transfer: 55% and 15%, respectively. The lower boundary on the fraction of stellar mergers almost doubles with conservative mass transfer: 23% compared to 12%. We find that the onset of unstable mass transfer occurs in a smaller fraction of the conservative systems because they reach contact by the expansion of the accretor before this can happen.

With this study, we do not attempt to determine which mass-transfer efficiency is most likely happening in nature. We merely demonstrate the considerable effects efficiency assumptions can have with respect to the occurrence of contact phases and stellar mergers. The academic exercise undertaken in this chapter is meant to look at the extreme case in which no mass is lost from the system (except through wind mass-loss), whereas the grid presented in Chapter 2 shows the other extreme. This exercise is unrealistic in the sense that stars do rotate and are expected to spin up to critical rotation rates in all but the closest binaries. However, as discussed in Chapter 2, the current implementation of rotation-limited accretion is most likely not accurate either. Therefore, future work ought to explore alternative mechanisms that, on the one hand, limit the mass-transfer efficiency while, on the other hand, allow for higher efficiencies than predicted by the current accretion-limited approach. The population studies presented in this chapter and Chapter 2 should be expanded upon and make them suitable for more in-depth comparisons with observed systems. From the observational side, there are exciting prospects with the first populations of intermediate- and high-mass (partially) stripped stars (Schootemeijer et al. 2018; Wang et al. 2021; El-Badry and Quataert 2021; Irrgang et al. 2022; El-Badry and Burdge 2022; El-Badry et al. 2022; Frost et al. 2022; Gilkis and Shenar 2023; Ramachandran et al. 2023; Drout et al. 2023; Götberg et al. 2023; Ludwig et al. in prep.). Since these are post-mass-transfer systems,

they might shed some light on realistic values of the mass-transfer efficiency.

Merger seismology: Distinguishing massive merger products from genuine single stars using asteroseismology

AUTHORS Jan Henneco, Fabian R. N. Schneider, Saskia Hekker, and Conny Aerts

CHAPTER INFO This chapter is a reproduction of the second paper I published as part of my doctoral studies, Henneco et al. (2024a), A&A, vol. 690, A65. In this work, we explored the asteroseismic differences between genuine single stars and post-main-sequence merger products to see if we could potentially use asteroseismology to distinguish the two types of stars. I was the main author of this paper and computed, analysed, and interpreted the results. The original idea for this project came from my supervisor Fabian Schneider. This work was done in close collaboration with Conny Aerts, with whom I frequently discussed and who provided detailed feedback throughout all stages of the project and publication process. All three co-authors (Fabian Schneider, Saskia Hekker, and Conny Aerts) provided helpful comments and suggestions regarding the main text and figures. The original Sect. 2 of Henneco et al. (2024a) titled ‘Asteroseismic diagnostics’ has been removed from the reproduction in this chapter. Its contents have been included in Sects. 1.2.1 and 1.2.2.

ABSTRACT Products of stellar mergers are predicted to be common in stellar populations and can potentially explain stars with peculiar properties. When the merger occurs after the initially more massive star has evolved into the Hertzsprung gap, the merger product may remain in the blue part of the Hertzsprung-Russell diagram for millions of years. Such objects could, therefore, explain the overabundance of observed blue stars, such as blue supergiants. However, it is currently not straightforward to distinguish merger products from genuine single stars or other stars with similar surface diagnostics. In this work, we made detailed asteroseismic comparisons between models of massive post-main-sequence merger products and genuine single stars to identify which asteroseismic diagnostics can be used to distinguish them. In doing so, we developed tools for the relatively young field of merger seismology. Genuine single stars in the Hertzsprung gap are fully radiative, while merger products have a convective He-burning core and convective H-burning shell while

occupying similar locations in the Hertzsprung-Russell diagram. These major structural differences are reflected in lower asymptotic period spacing values for merger products and the appearance of deep dips in their period spacing patterns. Our genuine single-star models with masses above roughly 11.4 solar masses develop short-lived intermediate convective zones during their Hertzsprung gap evolution. This also leads to deep dips in their period spacing patterns. Because of the lack of a convective core, merger products and genuine single stars can be distinguished based on their asymptotic period spacing value in this mass range. We performed the comparisons with and without the effects of slow rotation included in the pulsation equations and conclude that the two types of stars are seismically distinguishable in both cases. The observability of the distinguishing asteroseismic features of merger products can now be assessed and exploited in practice.

4.1. Introduction

Stellar mergers occur frequently in our Universe (Podsiadlowski et al., 1992; Sana et al., 2012; de Mink et al., 2014) and are driven by a plethora of mechanisms (Henneco et al., 2024b). Merger products, the stars left behind after the stellar merger events, are expected to have peculiar properties. These properties include large-scale surface magnetic fields (Ferrario et al., 2009; Wickramasinghe et al., 2014; Schneider et al., 2019), peculiar chemical compositions (e.g. α -rich young stars; Chiappini et al. 2015; Martig et al. 2015; Izzard et al. 2018; Hekker and Johnson 2019), peculiar rotation rates (Schneider et al., 2019; Wang et al., 2022), B[e] emission features (Podsiadlowski et al., 2006; Wu et al., 2020a), and masses above a cluster’s main sequence (MS) turn-off mass (blue stragglers; e.g. Rasio 1995; Sills et al. 1997, 2001; Mapelli et al. 2006; Glebbeek et al. 2008; Ferraro et al. 2012; Schneider et al. 2015).

Single-star evolution predicts that post-MS intermediate- and high-mass stars (stars with convective cores during core-hydrogen burning, i.e. initial masses $\geq 1.3 M_{\odot}$) evolve relatively quickly from the blue to the red side of the Hertzsprung-Russell diagram (HRD), crossing the Hertzsprung gap (HG) and becoming red supergiants. The theoretically predicted HG crossing times depend on the assumptions for (semi-)convective mixing (Kaiser et al., 2020; Sibony et al., 2023), but regardless of these assumptions, HG stars are expected to be rare. However, blue post-MS stars, most notably blue supergiants (BSGs), are abundant (Castro et al., 2014, 2018; de Burgos et al., 2023; Bernini-Peron et al., 2023). This is known as the blue supergiant problem. Several potential solutions to this problem exist. Extra mixing on the MS can enhance core masses, radii, and luminosities, while the stars reach cooler effective temperatures before the terminal-age main sequence (TAMS; Brott et al., 2011; Johnston et al., 2019; Kaiser et al., 2020; Johnston, 2021). Another way to populate the blue part of the HG is through the blue loop phase, during which red supergiants evolve towards hotter temperatures and appear as BSGs (Saio et al., 2013; Ostrowski and Daszyńska-Daszkiewicz, 2015). However, these single-star evolutionary channels do not produce the full population of observed BSGs (Bellinger et al., 2024). The products of post-MS stellar mergers, that is, mergers that occur after one of the components has left the MS, also appear as BSGs (Hellings, 1983, 1984; Podsiadlowski et al., 1990; Podsiadlowski, 1992; Morris and Podsiadlowski, 2007; Claeys et al., 2011; Vanbeveren et al., 2013; Justham et al., 2014; Menon and Heger, 2017; Menon et al., 2024). Furthermore, the variety in pre-merger systems, such as the mass ratio and the evolutionary stage at which the merger occurs, naturally explains

the variety of luminosities and effective temperatures of the observed BSGs.

Using 1D merger models, Menon et al. (2024) show that the surface diagnostics, such as luminosity, effective temperature, surface gravity, and N/O and N/C ratios, of post-MS merger products differ significantly from those of genuine single HG stars. Moreover, these surface diagnostics agree well with those determined from a sample of nearly 60 BSGs observed in the Large Magellanic Cloud. In their proof-of-principle study, Bellinger et al. (2024) show the potential of asteroseismology to distinguish MS stars with oversized cores because of extra mixing from core-helium burning stars with undersized cores among the population of BSGs. Core-helium burning stars with undersized cores can be the result of post-MS mergers or a blue loop phase. These stars have significantly different internal structures, which is reflected in the mean spacing between their oscillation modes. To distinguish between post-MS merger products and genuine single HG stars, Bellinger et al. (2024) propose searching for a temporal change in oscillation frequencies, which could be detectable for the faster-evolving genuine single HG stars. For lower-mass stars, Rui and Fuller (2021) find that one can distinguish post-MS merger products from genuine single red giant branch stars based on the mean spacing between the oscillation modes and mass estimates from other asteroseismic and surface diagnostics. One condition is that the red giant branch star needs to have a degenerate core before the merger. Other studies have explored the influence of mass accretion and mass loss on the seismic signals of red giant stars (Deheuvels et al., 2022; Li et al., 2022) and more massive B-type stars (Wagg et al., 2024) in binary systems.

Here, we focus on genuine and candidate merger product BSGs in the mass range between about $5 M_{\odot}$ and $20 M_{\odot}$. In this current era of high-cadence space photometry, multi-period non-radial oscillations have been detected in several BSGs in this mass regime, although the number of stars with firm detections remains limited compared to other classes of pulsators (see Kurtz, 2022, for a recent review). Multiple isolated oscillation modes have been detected in a set of about 40 BSGs with the ESA Hipparcos satellite (Lefever et al., 2007) and in specific BSGs with the Microvariability and Oscillations of Stars (MOST; Walker et al., 2003) mission by Saio et al. (2006), Moravveji et al. (2012a), and Moravveji et al. (2012b), the Convection, Rotation and planetary Transits (CoRoT; Auvergne et al., 2009) space telescope by Aerts et al. (2010b), the *Kepler*/K2 (Koch et al., 2010) missions by Aerts et al. (2017) and Aerts et al. (2018a), and the Transiting Exoplanet Survey Satellite (TESS; Ricker et al., 2016) by Sánchez Arias et al. (2023).

All of the above detections concern individual isolated frequencies in the amplitude spectra. However, BSG variability is more diverse than this. Bowman et al. (2019) and Ma et al. (2024) discovered a global low-frequency power excess in a sample of about 180 K2 or TESS BSGs, several of which are in the Large Magellanic Cloud. For many of these targets, Bowman et al. (2019) stress that the low-frequency power excess occurs in addition to many isolated significant frequencies with higher amplitudes. In his review of massive star variability, Bowman (2023) points out that the origin of the low-amplitude low-frequency variability is related to a spectrum of internal gravity waves triggered by core convection, but this is not yet firmly established (see also Cantiello et al., 2021, for interpretations in terms of sub-surface convection in regard to the power excess). Ma et al. (2024) used a BSG merger model from Bellinger et al. (2024) to explore two not mutually exclusive physical origins of the observed frequency spectra, namely sub-surface convective motions and internal gravity waves excited by the thin convective layer connected to the iron opacity bump in the envelope. They find waves to be the more plausible explanation for the overall observed

variability frequency spectra but warn that more 3D simulations are needed to come to firm conclusions.

In this work we made an in-depth model-by-model comparison between the asteroseismic predictions for post-MS merger products and genuine single HG stars based on 1D stellar structure models. We focused on stars with masses between 7.8 and $15.3 M_{\odot}$ at similar locations in the HRD and explored which asteroseismic diagnostics help us distinguish merger products from genuine single stars. With this mass range, we include stars below and inside the mass range considered in previous works (e.g. Bellinger et al. 2024) and also avoid the added complexity that stellar wind mass loss might have on the photometric signal (Krtićka and Feldmeier, 2018).

This chapter has the following structure. In Sect. 4.2, we describe our computational setup for the equilibrium stellar structure models and stellar oscillation calculations. Section 4.3 covers the results of our comparison between merger products and genuine single stars. Lastly, in Sect. 4.4 we discuss these results and draw our conclusions.

4.2. Methods

We computed the asteroseismic properties of merger products and genuine single stars by solving the stellar oscillation equations, which require an equilibrium stellar structure model as input. These equilibrium stellar structure profiles were taken from 1D stellar evolution models. Asteroseismology has shown that intermediate-mass stars born with a convective core have quasi-rigid rotation throughout their MS and undergo efficient yet poorly understood angular momentum loss once beyond the MS (Aerts et al., 2019; Aerts, 2021). From the results of the 3D merger simulations from Schneider et al. (2019) and the 1D follow-up study by Schneider et al. (2020), we expect merger products to be slow rotators. Moreover, as shown by Wang et al. (2022), merger products' slow rotation can explain the blue MS band in young stellar clusters. We thus expect slow rotation for both genuine HG stars and post-MS merger products. In first instance, it is therefore justified to ignore rotation in the equilibrium models used to solve the pulsation equations, as is common practice for post-MS stars. Ignoring rotation in the equilibrium models disregards the theory of rotationally induced mixing, but we mimicked its effects by means of simpler approximations for the internal mixing profiles (Pedersen et al., 2021). Following Henneco et al. (2021) we also ignored the centrifugal deformation of the equilibrium model, because it results in negligible frequency shifts. Henneco et al. (2021) furthermore show that for up to 70% of critical rotation, the inclusion of the centrifugal deformation at the level of the asymptotic pulsation mode predictions and the level of the equilibrium model combined lead to fractional frequency shifts well below 1%. Therefore, the effect of the centrifugal deformation may be neglected for initial asteroseismic modelling attempts for rotation rates up to 70% of the critical rotation rate. The procedure of including rotation only at the level of the stellar oscillation equations and ignoring the centrifugal deformation of the equilibrium model is common practice (Aerts, 2021) and is further elaborated in Aerts and Tkachenko (2023), to which we refer for details. Section 4.2.1 describes the computation of the equilibrium models for the genuine single HG stars and post-MS merger products. We show in Sect. 4.2.2 how we predicted the asteroseismic properties by solving the oscillation equations using the equilibrium models as input. The input files for the various codes used in this work are

available online¹.

4.2.1. Stellar model computations with MESA

4.2.1.1 Adopted stellar physics

We used the stellar structure and evolution code MESA (r12778; Paxton et al., 2011, 2013, 2015, 2018, 2019) to compute non-rotating single-star evolution models at solar metallicity ($Y = 0.2703$ and $Z = 0.0142$, Asplund et al. 2009). We used a combination of the OPAL (Iglesias and Rogers, 1993, 1996) and Ferguson et al. (2005) opacity tables suitable for the chemical mixture of Asplund et al. (2009). We did not enable MESA’s hydrodynamic solver, that is, all models are hydrostatic. We used the approx21 nuclear network. Each model was initialised at its zero-age main sequence (ZAMS) and evolved until core-helium exhaustion (i.e. when the central mass fraction of helium is below 10^{-6}).

The Ledoux criterion was employed to determine which regions of the stellar model were convective and the mixing length theory (MLT; Böhm-Vitense, 1958; Cox and Giuli, 1968) for the treatment of convective mixing, with a mixing length parameter of $\alpha_{\text{mlt}} = 2.0$ as the best estimate from asteroseismology of stars on the MS with a convective core (e.g. Fritzewski et al., 2024a). Semi-convective mixing was included with an efficiency of $\alpha_{\text{sc}} = 10.0$ (Schootemeijer et al., 2019). For thermohaline mixing, we used $\alpha_{\text{th}} = 1.0$ (Marchant et al., 2021). We added a constant envelope mixing of $\log(D_{\text{mix}}/\text{cm}^2\text{s}^{-1}) = 3$ to smooth out small step-like features in the chemical composition left behind by the receding convective cores and shrinking convective shells. This value used for D_{mix} is typical for what is deduced from asteroseismology of B stars (Pedersen et al., 2021).

Convective boundary mixing was handled through the overshooting scheme. For hydrogen-burning convective cores, we used the step overshooting scheme in MESA to extend the convective region by $0.20H_p$ (Martinet et al., 2021) beyond the boundary set by the Ledoux criterion. Here, H_p is the pressure scale height. We used exponential overshooting (Herwig, 2000) for helium-burning cores, with $f_{\text{ov}} = 0.015$. The magnitude of overshooting above helium-burning cores is not constrained adequately and yet can severely influence the final fate of stars (Temaj et al., 2024; Brinkman et al., 2024). We chose a moderately high value in a range consistent with observations of intermediate- (Constantino et al., 2016) and low-mass (Bossini et al., 2017) stars. This value of f_{ov} was chosen to avoid the occurrence of breathing pulses, which are instabilities of the convective helium-burning core that occur in models with lower values of overshooting. Whether these breathing pulses are numerical artefacts or physical instabilities is unclear, though recent evidence supports the former (Ostrowski et al., 2021). Above and below convective shells and below convective envelopes, we used exponential overshooting with $f_{\text{ov}} = 0.005$, which is consistent with values typically inferred for the Sun (Angelou et al., 2020).

We used the same setup as in Henneco et al. (2024b) to compute the wind mass-loss rate. For hot stars ($T_{\text{surf}} \geq 11$ kK, with T_{surf} the temperature of the outermost cell), we used the Vink et al. (2000) wind mass-loss prescription with a scaling factor of 1.0. The cool wind regime ($T_{\text{surf}} \leq 10$ kK) was divided based on whether the stars evolve into giants or supergiants. The cut is made at $\log(\mathcal{L}/\mathcal{L}_{\odot}) = 3.15$, with \mathcal{L} defined in Eq. (2.1). We evaluated \mathcal{L} when $T_{\text{surf}} < 11$ kK for the first time during the star’s evolution. The division

¹<https://zenodo.org/doi/10.5281/zenodo.12087024>

between giant and supergiant wind regimes at $\log(\mathcal{L}/\mathcal{L}_\odot) = 3.15$ corresponds roughly to a division at $10 M_\odot$. We used linear interpolation to compute the wind mass-loss rate between the hot and cool wind regimes.

4.2.1.2 Merger products via fast accretion

This work focuses on massive stars produced in early Case B (Case Be) mergers. These stellar mergers occur when the initially more massive or primary star is in the HG and does not yet have a (deep) convective envelope (Henneco et al., 2024b). To produce a merger product in MESA, we evolved a single star, using the assumptions described above, until it reached the HG. When the star reached a point in the HG at which its effective temperature T_{eff} is cooler than roughly its lowest MS value, we invoked the merger procedure. The merger procedure consisted of accreting a specified mass ΔM onto the single star with initial mass M_i on a timescale of $0.1\tau_{\text{KH}}$, with τ_{KH} the star’s current global thermal or Kelvin-Helmholtz timescale, defined as in Eq. (1.2). This procedure is similar to what is used in Justham et al. (2014), Rui and Fuller (2021), Deheuvels et al. (2022), and Schneider et al. (2024) to mimic the result of stellar mergers. Justham et al. (2014) assumed accretion happens on a timescale $\lesssim 10^4$ yr, Rui and Fuller (2021) used a fixed accretion rate of $10^{-5} M_\odot \text{ yr}^{-1}$, while Schneider et al. (2024) assumed accretion to happen on the star’s thermal timescale, that is, at an accretion rate $\dot{M}_{\text{acc}} = M_\star/\tau_{\text{KH}}$. Although the technical setup is essentially the same, Deheuvels et al. (2022) studied the effect of accretion in a binary system rather than for stellar mergers, which occur on shorter timescales. Schneider et al. (2024) used their setup to study both merger and accretion products.

During the fast accretion phase, an extended convection region develops in the star’s envelope. After this phase, we mixed the outer envelope, that is, the region from the top of the convective hydrogen-burning shell to the surface with $\log(D_{\text{mix}}/\text{cm}^2\text{s}^{-1}) = 12$ for a time $0.01\tau_{\text{KH}}$. We did this to smooth out the abrupt changes in the chemical composition profile left behind by the extended convection zone. Afterwards, we evolved the merger models until the end of core helium exhaustion.

4.2.1.3 Limitations of the fast accretion method

Stellar mergers are complex phenomena that include a wealth of physical processes. 3D merger simulations, such as those in Lombardi et al. (2002), Ivanova et al. (2002), Glebbeek et al. (2013), and Schneider et al. (2019) currently are our best windows into the merging process and the products that result from it, but they are computationally expensive. As a result, these 3D simulations are limited to only a handful of initial binary parameters. The fast accretion method provides a quick and flexible zeroth-order approximation for merger product structures. We now list some of its main limitations.

First, before stars merge, they evolve through a contact phase, preceded by a mass-transfer phase (this is true if we consider a merger driven by binary evolution channels and not through dynamical interactions). During both phases, the structure can be altered significantly (Henneco et al., 2024b). With the fast accretion method, we assumed that the star onto which the companion is accreted is unaltered by any previous mass-transfer and contact phases.

Second, fast accretion does not account for the chemical composition of the merger product because the chemical composition of the accreted material is taken to be the same as the surface chemical composition of the accretor. With this assumption, we primarily

underestimate the amount of helium in the envelope of the merger product. Moreover, it does not account for the mixing of stellar material from the two components during the merger phase. As a result, neither the internal chemical structure nor the surface chemical abundances can be reproduced correctly by the fast accretion method. We stress that we used the fast accretion method to create effective merger product structures of the kind in which the less evolved secondary star is mixed in with the more evolved primary star’s envelope. Generally, mass is expected to be lost from both components during the merger phase (see e.g. Schneider et al. 2019). Therefore, ΔM is the mass effectively added to the primary’s envelope. The added mass fraction $f_{\text{add}} = \Delta M/M_i$ should not be confused with the mass ratio of the merger product’s progenitor binary system. From smoothed particle hydrodynamic simulations of mergers (e.g. Lombardi et al., 2002; Gaburov et al., 2008a; Glebbeek et al., 2013), we know that if the H-rich core of the secondary star has lower entropy than that of the primary star, it can sink to the centre of the merger product. In such cases, the merger product rejuvenates and becomes an MS star (Glebbeek et al., 2013). One needs different merging schemes to create these kinds of merger products, such as entropy sorting (Gaburov et al., 2008b). While such merger products warrant their own investigations (Henneco et al. in prep.), our work focuses solely on long-lived B-type or BSG merger products.

Third, the fast accretion method does not reproduce the strong surface magnetic fields expected from both 3D magnetohydrodynamic simulations (Schneider et al., 2019) and the recent observation of a massive magnetic star that shows strong signs of having been formed in a merger (Frost et al., 2024). Although internal magnetic fields are less well constrained than surface magnetic fields (Donati and Landstreet, 2009), it cannot be excluded that they also result from binary mergers. As shown by, for example, Prat et al. (2019), Van Beeck et al. (2020), Dhoub et al. (2022), and Rui et al. (2024), internal magnetic fields can significantly influence the frequencies of g modes.

4.2.2. Stellar oscillation calculations with GYRE

For the computation of the stellar oscillations, we used the stellar pulsation code GYRE (v7.0; Townsend and Teitler, 2013; Townsend et al., 2018) with the equilibrium models produced with MESA as input. We used the MAGNUS_GL6 solver and the boundary conditions from Unno et al. (1989) to compute adiabatic² oscillations for $(\ell, m) = (1, 0)$ and $(\ell, m) = (2, 0)$ modes (no rotation). For the computation of oscillation modes with rotation in the inertial frame, we used the TAR in GYRE (see Sect. 1.2.2). Even though we only considered slow to moderate rotation in this work, the use of the TAR is required (as opposed to treating the Coriolis acceleration as a perturbation), which we demonstrate in Appendix C.1. Core and envelope rotation rates inferred from asteroseismology show that low- and intermediate-mass stars have nearly uniform radial rotation profiles during their MS and HG or sub-giant evolution (Aerts et al., 2019). We currently have internal rotation profiles inferred from asteroseismology for only a handful of high-mass stars, which show core-to-envelope rotation rate ratios between 1 and 5 without proper error estimation (Bursiens et al., 2023; Aerts and Tkachenko, 2023). Considering this, we assumed a uniform (solid-body) rotation profile for the GYRE computations. We computed $(\ell, m) = (1, 0)$, $(1, \pm 1)$, $(2, 0)$, $(2, \pm 1)$, and $(2, \pm 2)$ modes with rotation.

²It is appropriate to use the adiabatic approximation for the computation of oscillation modes in B-type stars (Aerts et al., 2018b).

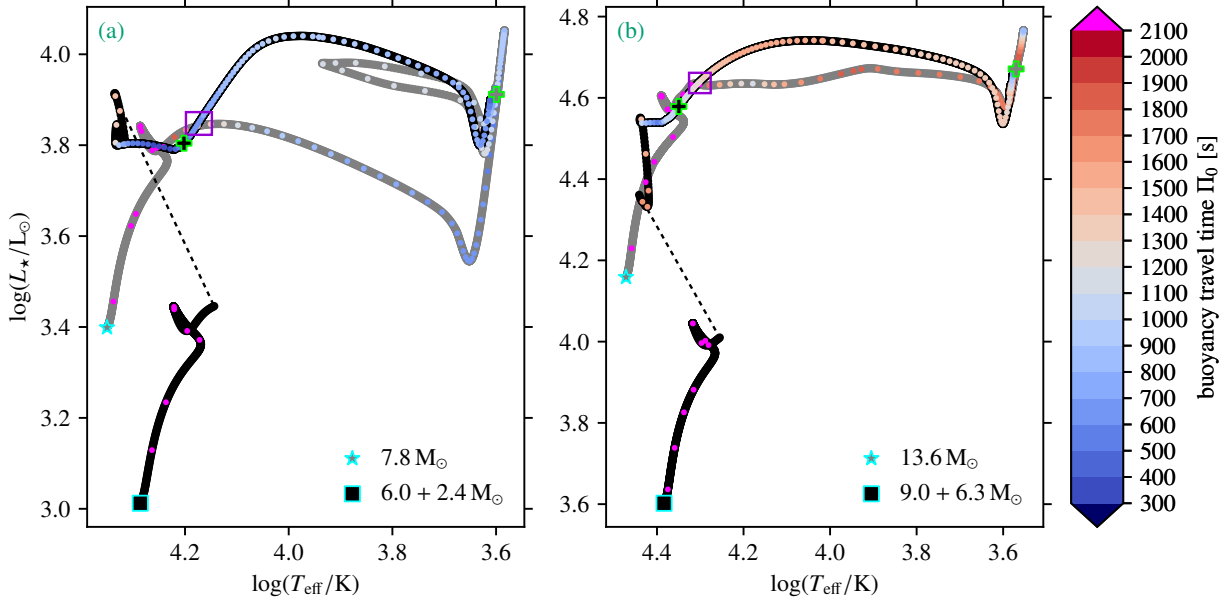


Figure 4.1: HRD with evolutionary tracks for a merger product of $M_{\star} = 6.0 + 2.4 M_{\odot}$ and a genuine single star with an initial mass of $M_{\star} = 7.8 M_{\odot}$ (Panel a), and a merger product of $M_{\star} = 9.0 + 6.3 M_{\odot}$ and a genuine single star with an initial mass of $M_{\star} = 13.6 M_{\odot}$ (Panel b). The merger and genuine single-star tracks are shown in black and grey, respectively. To avoid cluttering, the track of the merger model is not shown during the fast accretion phase. A dashed black line replaces it. Each evolutionary track is connected to its label through a symbol on the HRD at the ZAMS. The green plus symbols indicate the position in the HRD after 10^6 years have passed since the merging or TAMS for the merger product and single star, respectively. The colours on the tracks are related to the buoyancy travel time, Π_0 . The violet box indicates the position at which we compare the asteroseismic properties of the merger product and genuine single star in Sects. 4.3.1.1 and 4.3.1.2.

4.3. Results

4.3.1. Detailed comparison between Case-Be merger products and genuine single HG stars

We compared the predicted asteroseismic properties of merger products formed through the fast accretion method described in Sect. 4.2.1.2 and genuine single stars in the HG. We focused on two merger products resulting from early Case B mergers: an $M_{\star} = 8.4 M_{\odot}$ product of a star with $M_i = 6.0 M_{\odot}$ and $\Delta M = 2.4 M_{\odot}$ (added mass fraction $f_{\text{add}} = 0.4$) and an $M_{\star} = 15.3 M_{\odot}$ product of star with $M_i = 9.0 M_{\odot}$ and $\Delta M = 6.3 M_{\odot}$ ($f_{\text{add}} = 0.7$). We compared both merger products with appropriate genuine single-star counterparts. To find these genuine single star counterparts, we compared the merger products' HRD tracks with a range of genuine single star tracks of different masses and selected those that cross in the blue region of the HRD ($\log T_{\text{eff}}/\text{K} \gtrsim 4.0$). Hence, we compared the $6.0 + 2.4 M_{\odot}$ and $9.0 + 6.3 M_{\odot}$ merger products with $7.8 M_{\odot}$ and $13.6 M_{\odot}$ genuine single stars, respectively.

The evolutionary tracks of the merger products and genuine single stars are shown in Fig. 4.1. Each track has been colour-coded with the value of the buoyancy travel time Π_0 , defined in Eq. (1.25). Each HRD track is also marked with a plus symbol, which indicates the position of the star 1 Myr (10^6 yr) after the TAMS for genuine single stars, and 1 Myr after the merger event for merger products. Given that the plus symbol is located in the

blue region of the HRD for the merger products, it is clear that they spend at least 1 Myr there and are, hence, likely to be observed as B-type stars or BSGs. Genuine single stars have already moved towards the red region of the HRD within 1 Myr and are, therefore, less likely to be observed as B-type stars or BSGs. The merger products' luminosities increase during their evolution on the HG (around $\log T_{\text{eff}}/\text{K} = 4.2$ for the $6.0 + 2.4 M_{\odot}$ product and $\log T_{\text{eff}}/\text{K} = 4.4$ for the $9.0 + 6.3 M_{\odot}$ product), which is caused by the onset of core He burning. We defined the onset of core He burning as when the central He mass fraction falls below 99% of its value at the TAMS. For the $13.6 M_{\odot}$ genuine single star, core He ignition also occurs already on the HG around $\log T_{\text{eff}}/\text{K} = 4.1$. Our genuine single stars with masses $\gtrsim 11.4 M_{\odot}$ ignite helium in their cores on the HG.

4.3.1.1 Comparison between a $6.0 + 2.4 M_{\odot}$ merger product and a $7.8 M_{\odot}$ genuine single star

We find a clear difference between the respective Π_0 values of the merger product and genuine single star during the time their evolutionary tracks cross in the HRD, indicated by the violet box in Fig. 4.1a. The merger product has $\Pi_0 = 678$ s and for the genuine single star we find $\Pi_0 = 1485$ s. This difference comes from the fact that the g-mode cavities, which determine the value of Π_0 (Eq. 1.25), have significantly different shapes. From the propagation³ and Kippenhahn diagrams in Fig. 4.2, we see that the merger product has two g-mode cavities, one near the convective He-burning core (inner cavity) and one further out (outer cavity). Because of the mass accretion onto the primary star during the merger, it has a higher envelope mass and, consequently, a higher temperature at the base of the envelope. The higher temperature leads to a larger H-shell burning luminosity. This then drives a convective zone in and above the H-burning region. This convective region is responsible for separating the g-mode cavity into two parts. The genuine single star is fully radiative and hence has a single g-mode cavity (Figs. 4.2c and 4.2d). From Fig. 4.2a, we also see that the pure g modes are mostly confined to the inner cavity and only have a few radial nodes in the outer cavity. To correctly apply Eq. (1.25), which is derived within the asymptotic theory ($n \gg 1$), we only integrated over the inner cavity. Integrating over both cavities results in Π_0 values that are lower by up to 10 s, which is of the order of the period precision for time series from space missions such as *Kepler* and the TESS continuous viewing zone (Van Reeth et al., 2015a; Pedersen et al., 2021; Garcia et al., 2022b,a). Even though the merger product has a smaller mode cavity than the genuine single star, the BV frequency reaches higher values at low radial coordinates (see Figs. C.2 and C.3), which results in a higher value of the integral in the denominator of Eq. (1.25), and hence a smaller value of Π_0 compared to the genuine single star.

The difference in terms of asteroseismic properties between the merger product and genuine single star can be further appreciated from the comparison between their PSPs for $(\ell, m) = (1, 0)$ and $(2, 0)$ modes without rotation and with radial orders n_{pg} between -1 and roughly -200 (Fig. 4.3). We see that for high radial orders (long mode periods P_n), the mean values of the PSPs differ significantly, as expected from our earlier estimation based on Π_0 . Next to the difference in mean PSP values, we see that modes with the same number of radial nodes have different mode periods in the two models. The modes of the merger product have shorter mode periods for the same number of nodes compared to the modes of

³Alternative versions of the propagation diagrams as a function of the relative radial coordinate r/R_{\star} can be found in Appendix C.2.

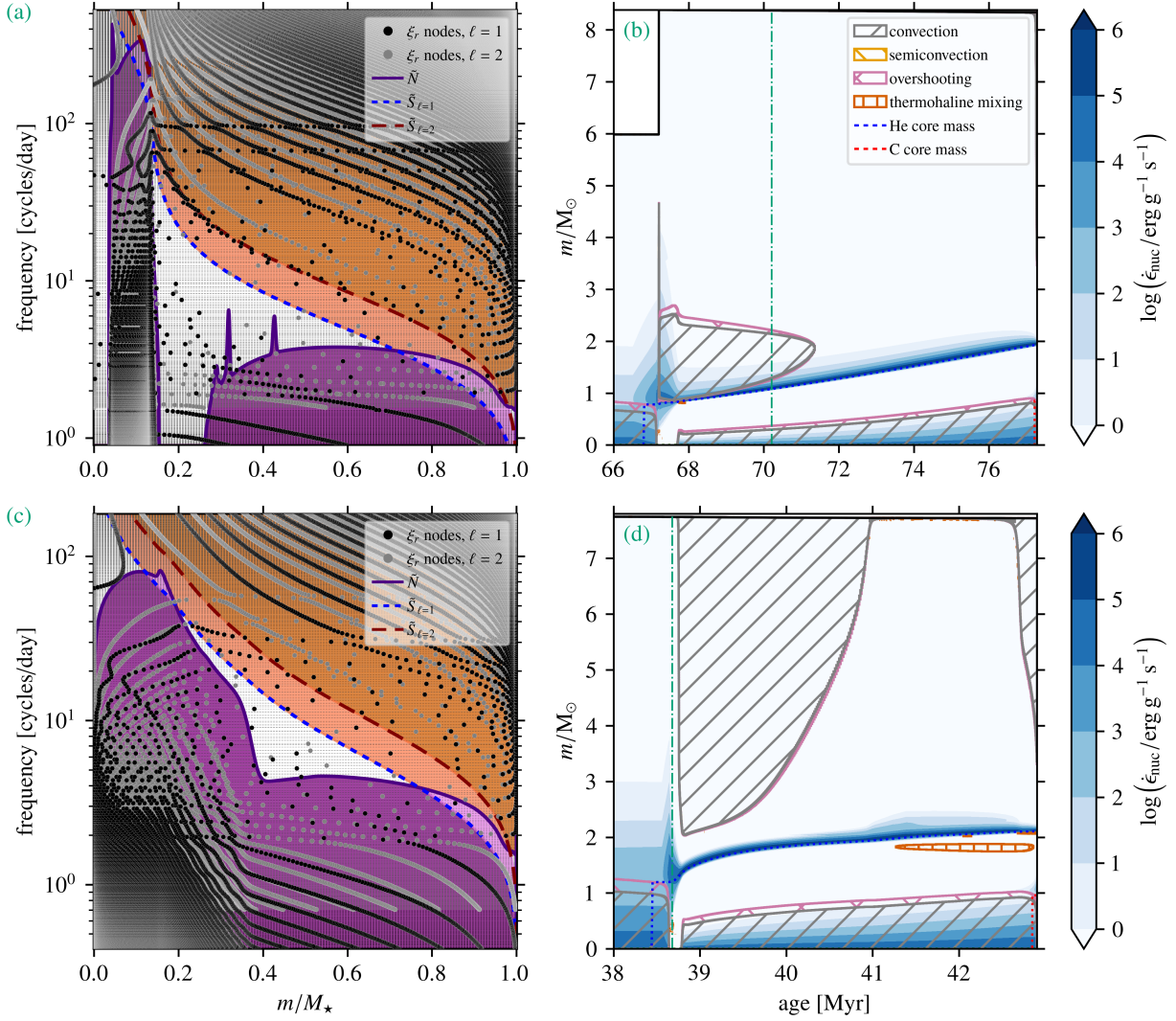


Figure 4.2: Propagation and Kippenhahn diagrams for the $M_\star = 6.0 + 2.4 M_\odot$ merger product and $M_\star = 7.8 M_\odot$ genuine single star. Panels (a) and (c) show propagation diagrams for $\ell = 1, 2$ and $m = 0$ modes without rotation for the merger product with $M_\star = 6.0 + 2.4 M_\odot$ and genuine single star with $M_\star = 7.8 M_\odot$, respectively. The black (grey) dots represent the radial nodes of the oscillation modes, or more specifically, the locations where the radial wave displacement $\xi_r(r) = 0$ for the $\ell = 1$ ($\ell = 2$) modes. The purple regions show the g-mode cavity or cavities, while the orange region shows the p-mode cavity. Panels (b) and (d) show Kippenhahn diagrams for the merger product with $M_\star = 6.0 + 2.4 M_\odot$ and a genuine single star with $M_\star = 7.8 M_\odot$, respectively. The dash-dotted green lines indicate the models for which the respective propagation diagrams in Panels (a) and (c) are shown, which is when their HRD tracks overlap, indicated by the violet box in Fig. 4.1a. Both Kippenhahn diagrams show the evolution of the models up to core-helium exhaustion.

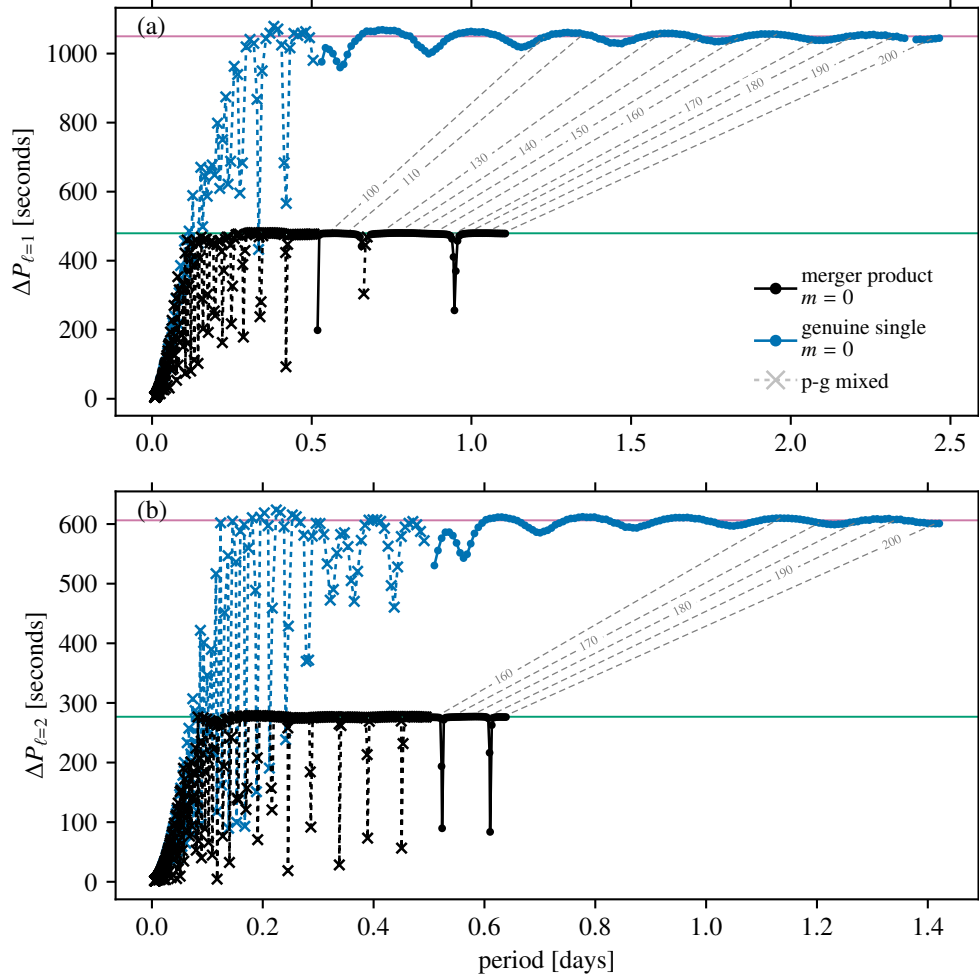


Figure 4.3: PSPs for the $6.0 + 2.4 M_\odot$ merger product (black) and the $7.8 M_\odot$ genuine HG star (blue) without rotation at the time of comparison (violet box in Fig. 4.1). The dashed grey lines connect pure g modes with the same radial order n_g . The dashed black and grey lines with cross symbols indicate p-g mixed modes. These p-g mixed modes have at least one node in the radial direction, that is, $n_p > 0$. Panel (a) and (b) show the PSPs for $(\ell, m) = (1, 0)$ and $(2, 0)$ modes, respectively. The green and purple horizontal lines indicate the Π_ℓ values for the merger product and genuine single star, respectively.

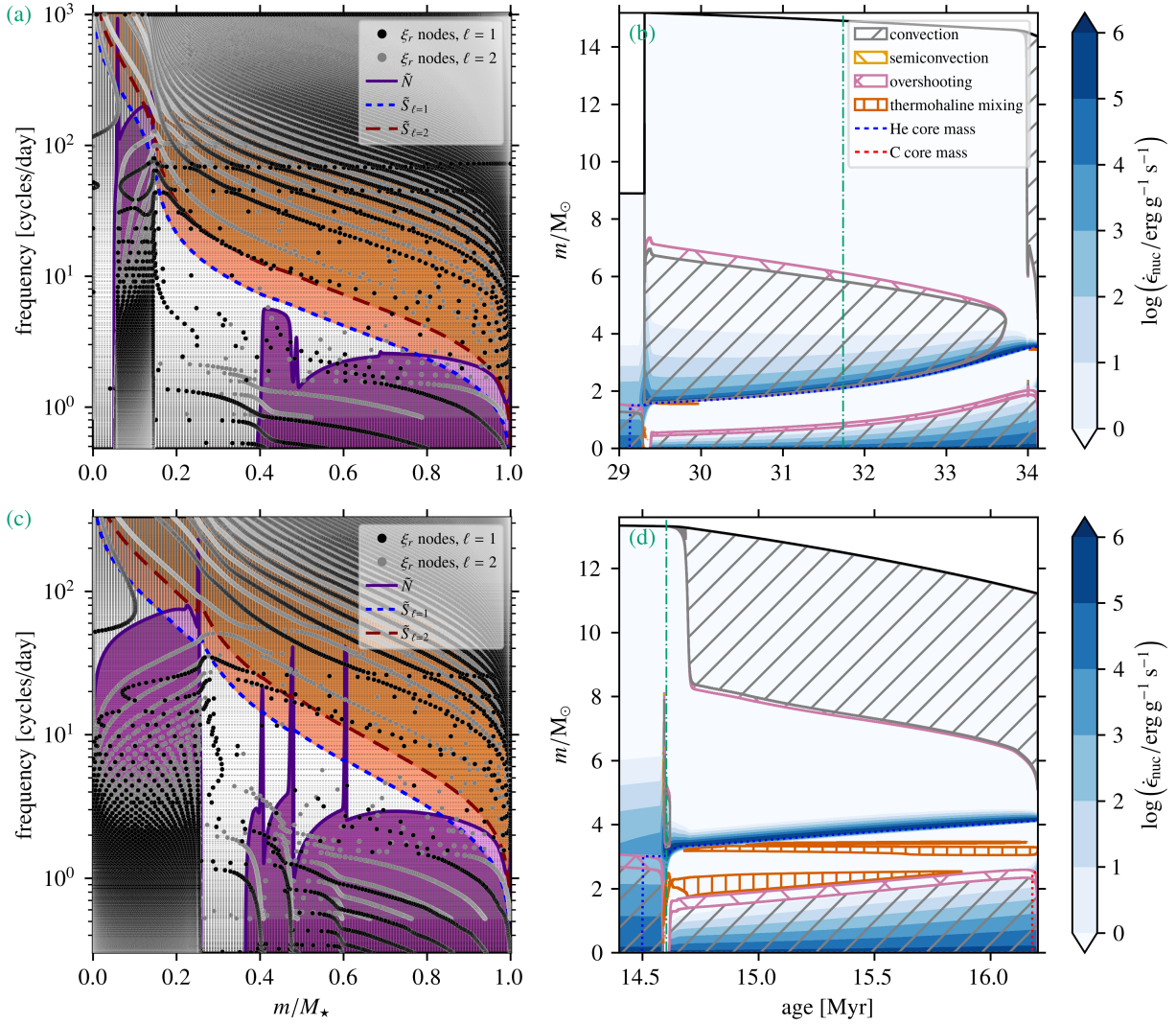


Figure 4.4: Same as Fig. 4.2 but for the merger product with $M_\star = 9.0 + 6.3 M_\odot$ and a genuine single star with $M_\star = 13.6 M_\odot$.

the genuine single star. This period shift increases with increasing mode period (increasing radial order n_g), both for $(\ell, m) = (1, 0)$ and $(2, 0)$ modes. Lastly, we see another clear difference between the respective PSPs of the merger product and genuine single star in the form of relatively deep and narrow dips. These dips arise whenever a star has two g-mode cavities. We elaborate further on the nature of these deep dips in Sect. 4.3.2.

4.3.1.2 Comparison between a $9.0 + 6.3 M_\odot$ merger and a $13.6 M_\odot$ genuine single star

Figure 4.1b shows the HRD tracks for a $9.0 + 6.3 M_\odot$ merger product and a $13.6 M_\odot$ genuine single star. During their time in the blue side of the HRD, both stars are observable as BSGs ($\log L_\star/L_\odot \gtrsim 4.0^4$, Urbaneja et al. 2017; Bernini-Peron et al. 2023). The Π_0 values for the merger product and genuine single star when their HRD track cross (indicated by the violet box in Fig 4.1b) are $\Pi_0 = 1276$ s and $\Pi_0 = 2104$ s, respectively. As expected from Mombarg et al. (2019) and Pedersen et al. (2021), these values are higher than for their lower-mass

⁴The lower luminosity limit for the BSGs is not well defined. For this work we used a limit based on observed BSGs.

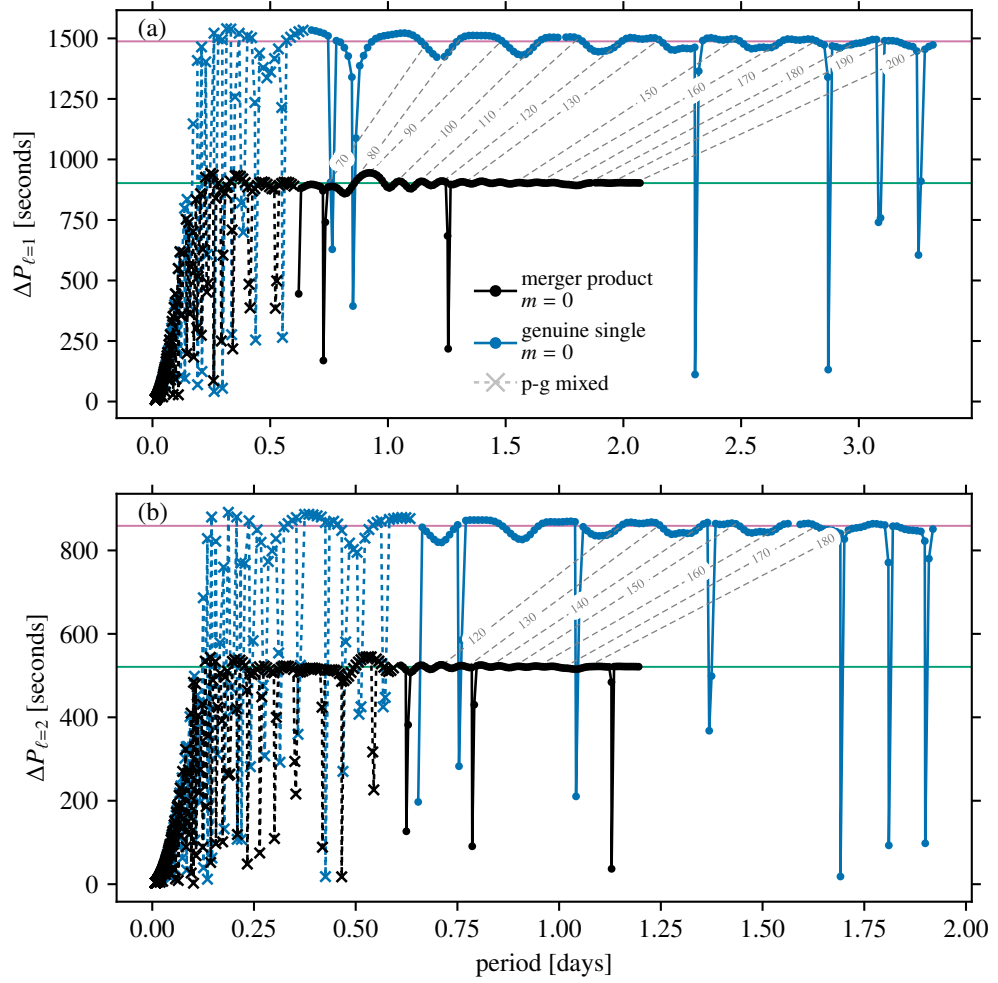


Figure 4.5: Same as Fig. 4.3 but for a 9.0 + 6.3 M_{\odot} merger product (black) and a 13.6 M_{\odot} genuine HG star (blue).

analogues described in Sect. 4.3.1.1. The absolute difference between the Π_0 values is 828 s for this comparison. For the lower-mass counterparts described in Sect. 4.3.1.1, the absolute difference between the Π_0 values is 807 s. These values are of the same order of magnitude, while the absolute difference is somewhat larger for the more massive merger product and genuine single star. At slightly lower effective temperatures, the values of Π_0 become more comparable than at the effective temperatures the $9.0 + 6.3 M_\odot$ merger product and $13.6 M_\odot$ genuine single star models are compared, but they remain distinguishable based on their asymptotic period spacing. The propagation and Kippenhahn diagrams for these models (Fig. 4.4) show that their structures are more comparable than their lower-mass counterparts. Notably, the $13.6 M_\odot$ genuine single star has a convective shell above the H-burning shell, the so-called intermediate convective zones (ICZs). The extent and lifetime of these ICZs are sensitive to the assumptions for convective mixing in the stellar models (e.g. Kaiser et al., 2020; Sibony et al., 2023, see also our Appendix C.3). Because of the ICZ, the $13.6 M_\odot$ genuine single star has two g-mode cavities, just like the merger product. The main difference between the two models remains, as for the lower-mass counterparts, the absence of a convective core in the structure of the genuine single star, which has the largest influence on the value of Π_0 .

Figure 4.5 shows the PSPs for the $9.0 + 6.3 M_\odot$ merger product and the $13.6 M_\odot$ genuine single star. The PSPs for the merger product look similar to those of its lower-mass counterpart (see Fig. 4.3). We find some key differences when comparing the PSPs of the genuine single star with those of its lower-mass counterparts. First, we see the presence of deep dips with similar morphologies as those in the merger product’s PSPs. As mentioned in the previous section, these are related to the existence of an inner and outer g-mode cavity. Second, we see relatively strong quasi-periodic wave-like variability in the ΔP_n values. Such variability is also present for pure g modes in the $7.8 M_\odot$ genuine single star (Fig. 4.3), but to a lesser extent. As discussed in Sect. 1.2.2, such wave-like variability in PSPs is caused by mode trapping (Pedersen et al., 2018; Michielsen et al., 2019, 2021), which itself can be caused by sharp features or structural glitches in the $\tilde{N}(r)$ -profile. We see from Fig. 4.4c that both the inner and outer g-mode cavities of the $13.6 M_\odot$ genuine single star have prominent spike features. These features are remnants of an extended, relatively short-lived ($\Delta T \sim 10^3$ yr), non-uniform (blocky) convection zone that appears after the TAMS and before the development of the ICZ (see Appendix C.3). The non-uniform structure of this convection zone appears at higher and lower spatial and temporal resolutions, and might be the result of an insufficient treatment of convection. We do note that similarly structured convection zones at the onset of the ICZ appear also in the models of Kaiser et al. (2020) for different treatments of convection. We do not discuss the nature of this short-lived, non-uniform convection zone further, but we note that the peaks it introduces in the $\tilde{N}(r)$ profile influence the oscillation modes. In the outer cavity, where the g-modes only have a handful of nodes, the location of the nodes is influenced by mode trapping caused by the peaks. The strong peaks at the outer edge of the inner g-mode cavity are responsible for the strongest mode trapping and, hence, the quasi-periodic wave-like variability in the PSPs mentioned above. In Appendix C.4, we demonstrate how we disentangled the deep dips and quasi-periodic variability in the $13.6 M_\odot$ genuine single star’s PSP.

4.3.2. Deep dips in pure g-mode PSPs

From the results in Sect. 4.3.1, it has become clear that stellar models with two g-mode cavities, that is, models with either a convective hydrogen-burning shell or ICZ, show deep,

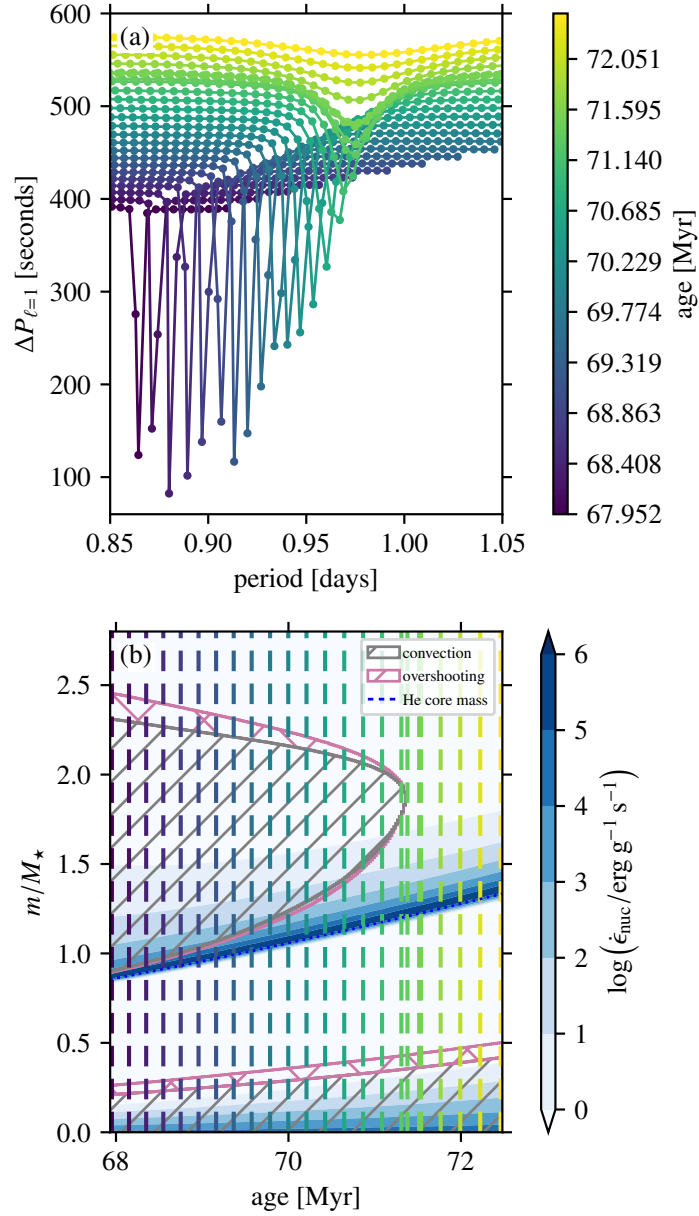


Figure 4.6: Temporal evolution of the deep PSP dip for the merger product with $M_\star = 6.0 + 2.4 M_\odot$. Panel (a) shows the PSP dip for $(\ell, m) = (1, 0)$ modes around 0.92 days. Panel (b) shows a zoomed-in view of the Kippenhahn diagram from Fig. 4.2c. The colours of the vertical dashed lines correspond to those in Panel (a).

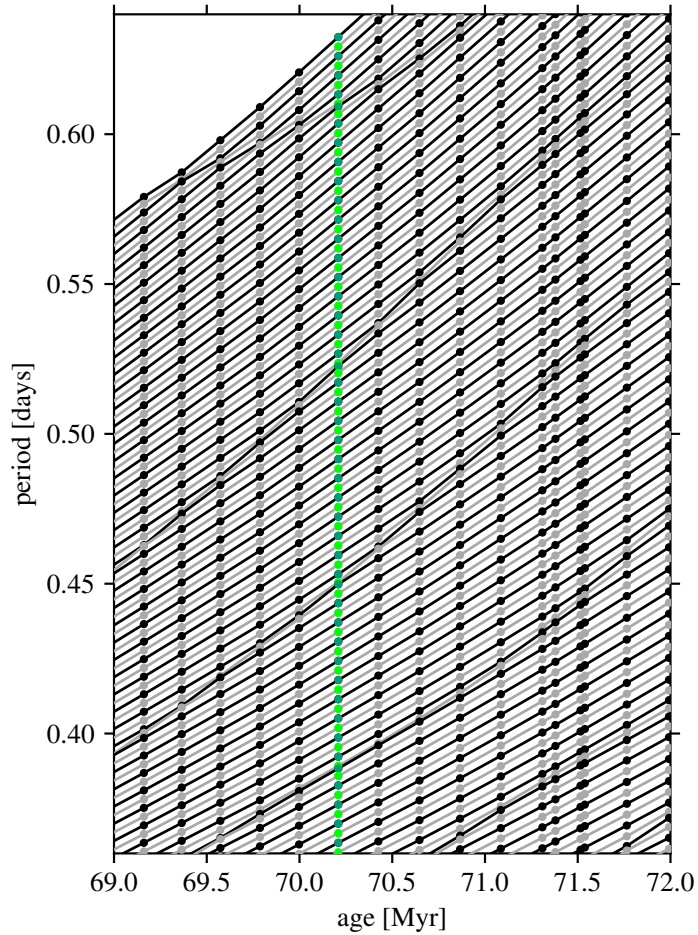


Figure 4.7: Zoomed-in view of a mode-bumping diagram for $(\ell, m) = (2, 0)$ modes of the merger product with $M_{\star} = 6.0 + 2.4 M_{\odot}$. The black (grey) lines show the evolution of the mode period of g modes with even (odd) radial order n_{pg} . The green (lime) symbols indicate periods of the even (odd) modes shown in Fig. 4.8.

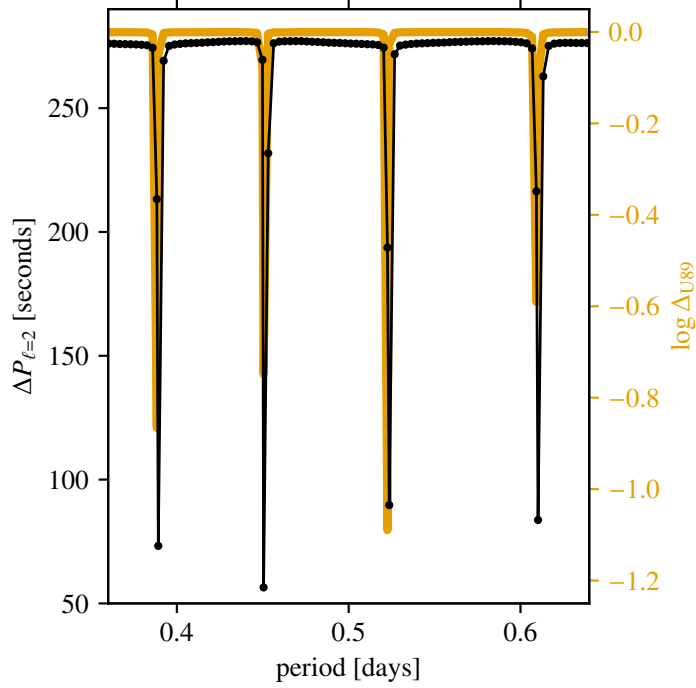


Figure 4.8: PSP for $(\ell, m) = (2, 0)$ modes with $n_{\text{pg}} \in [-202; -111]$ for the merger product with $M_{\star} = 6.0 + 2.4 M_{\odot}$ (black line, left axis) and Δ_{U89} (orange line, right axis).

narrow dips in their PSPs. In this section, we explore the nature of these deep dips.

First, we looked at how these deep dips evolve. From Fig. 4.6a, we see that the dip location for a specific $(\ell, m) = (1, 0)$ dip moves to longer periods over time. This follows from the deep dip’s physical origin. We also see that the width of the dip increases with time and eventually becomes relatively shallow. The transition from a deep, sharp dip to a shallow morphology coincides with the disappearance of the convective zone (Fig. 4.6b). In other words, the width of the dip is inversely proportional to the width of the evanescent zone between the two g-mode cavities.

Next, we examined the evolution of the g-mode periods with time in Fig. 4.7. The mode periods (this time shown for $\ell = 2$ modes) increase in time with a quasi-constant slope. For some modes, we observe so-called mode bumping (see e.g. Vanlaer et al. 2023); the period increases faster or more slowly than the periods of adjacent modes of consecutive radial order, causing the mode periods to be close in value. In such avoided crossings, the mode exchanges energy (couples) with its consecutive mode, which then experiences a faster or slower period increase until it bumps the next mode. This mode bumping sequence continues until the evanescent (convection) zone disappears at around 71.0–71.5 Myr.

Lastly, we show a part of the PSP for $(\ell, m) = (2, 0)$ modes of the $6.0 + 2.4 M_{\odot}$ merger product in Fig. 4.8. For each mode in the PSP, we computed the value of Δ_{U89} , which is the ratio of the kinetic energy of a mode in the inner cavity over its kinetic energy in both cavities (Unno et al., 1989):

$$\Delta_{\text{U89}} = \frac{\int_{r_1}^{r_2} 4\pi r^2 \rho [\xi_r(r)^2 + \ell(\ell + 1)\xi_h(r)^2] dr}{\int_0^{R_{\star}} 4\pi r^2 \rho [\xi_r(r)^2 + \ell(\ell + 1)\xi_h(r)^2] dr}. \quad (4.1)$$

In this expression, r_1 and r_2 are the radii of the inner and outer turning points of the inner g-mode cavity, respectively, and $\xi_r(r)$ and $\xi_h(r)$ are the radial and horizontal wave displace-

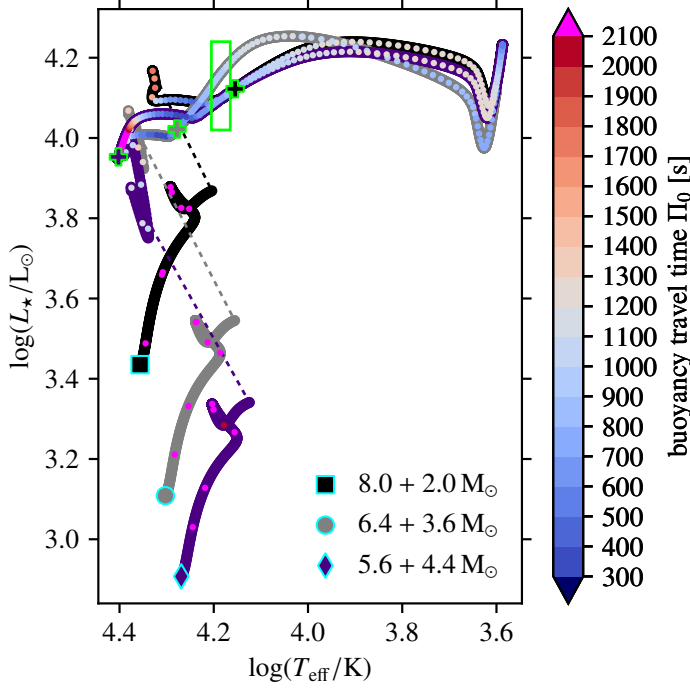


Figure 4.9: Same as Fig. 4.1 but for $8.0 + 2.0 M_{\odot}$ ($f_{\text{add}} = 0.25$, black square), $6.4 + 3.6 M_{\odot}$ ($f_{\text{add}} = 0.56$, grey circle), and $5.6 + 4.4 M_{\odot}$ ($f_{\text{add}} = 0.79$, indigo diamond) merger products. The lime rectangle indicates the region in which the three merger products occupy the same region of the HRD and have similar structures.

ment, respectively. For modes that are mostly confined to the inner g-mode cavity, $\Delta_{U89} \approx 1$, while for modes with a considerable amount of kinetic energy in the outer cavity, $\Delta_{U89} < 1$. We see from Fig. 4.8 that modes within the deep dips consistently have $\Delta_{U89} < 1$, meaning that a significant fraction of their kinetic energy sits in the outer g-mode cavity.

Putting the pieces together, we arrive at the nature of the deep dips in the PSPs of models with two g-mode cavities. We find that several inner-cavity g modes tunnel through the evanescent zone, where they interact with outer-cavity g-modes. During this interaction, the coupled modes' periods converge, they exchange energy, and their periods diverge again. The fact that the mode periods converge to the same value causes the deep, narrow dips in the PSPs. The virtual line connecting a sequence of avoided crossings in Fig. 4.7 shows the period evolution of a specific outer-cavity mode. The inversely proportional relation between the dips' width and the evanescent zone's size also follows from this explanation (Fig. 4.6). Namely, when the evanescent zone is smaller, more inner-cavity modes can tunnel through and couple with outer-cavity modes. This can be appreciated even further when comparing the width of the deep dips for $(\ell, m) = (1, 0)$ and $(\ell, m) = (2, 0)$ modes (Figs. 4.3 and 4.5). Dipole modes ($\ell = 1$) have a weaker damping rate than quadrupole ($\ell = 2$) modes (Aerts et al., 2010a, Chapter 3.4). Hence, more inner-cavity dipole modes can tunnel through the evanescent zone and interact with the outer-cavity g-modes, leading to wider dips.

4.3.3. Effect of the added mass fraction, f_{add}

As the results in the previous sections have shown, it is, in principle, possible to distinguish merger products from genuine single stars based on their g-mode PSPs. In this section,

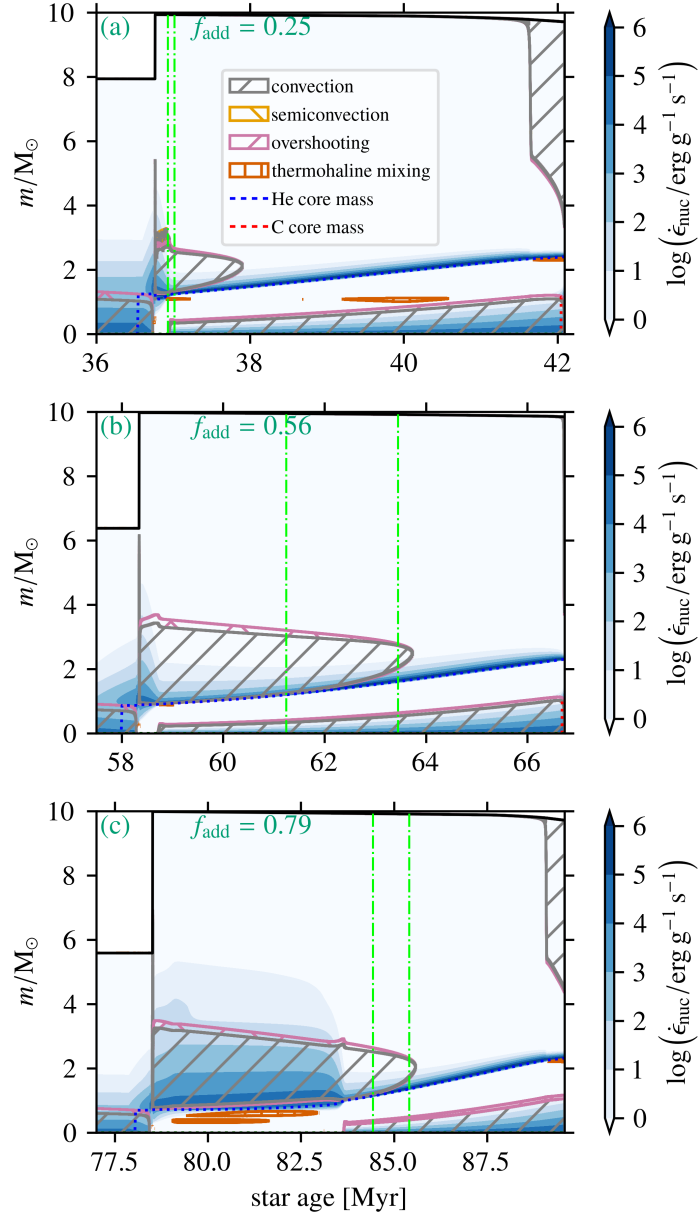


Figure 4.10: Kippenhahn diagrams for $8.0 + 2.0 M_{\odot}$ ($f_{\text{add}} = 0.25$, a), $6.4 + 3.6 M_{\odot}$ ($f_{\text{add}} = 0.56$, b), and $5.6 + 4.4 M_{\odot}$ ($f_{\text{add}} = 0.79$, c) merger products. The left (right) lime vertical line indicates the left (right) bound of the lime rectangle in Fig. 4.9.

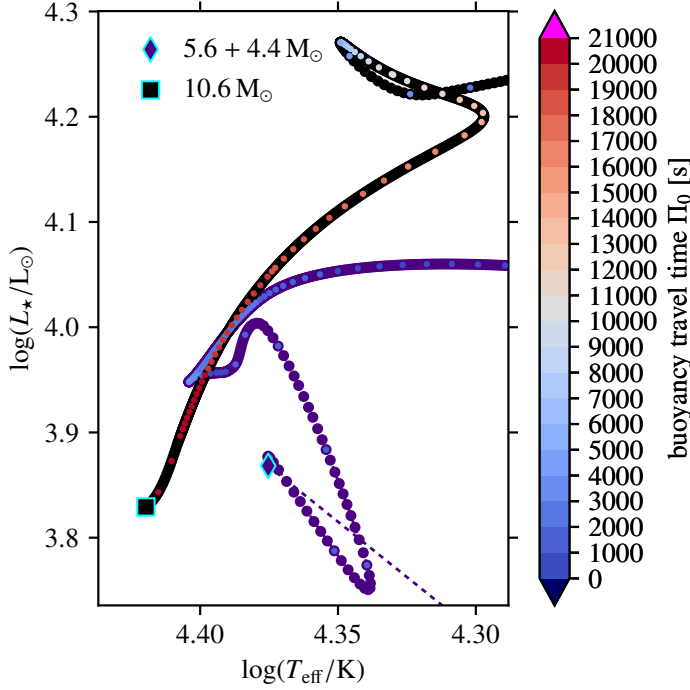


Figure 4.11: Zoomed-in view of the part of the HRD track of the $5.6 + 4.4 M_{\odot}$ merger product from Fig. 4.9 that coincides with the MS of a $10.6 M_{\odot}$ genuine single star. We draw attention to the different colour bar scaling than in Fig. 4.9.

we briefly explore how the added mass fraction f_{add} influences our results. We stress again that f_{add} is a measure of the mass effectively added to the primary star during the merger procedure and should not be confused with the mass ratio of the progenitor binary system (see Sect. 4.2.1.3). We compare the HRD tracks of three $10 M_{\odot}$ merger products with varying added mass fractions f_{add} in Fig. 4.9. The following merger products are considered: $8.0 + 2.0 M_{\odot}$ ($f_{\text{add}} = 0.25$), $6.4 + 3.6 M_{\odot}$ ($f_{\text{add}} = 0.56$), and $5.6 + 4.4 M_{\odot}$ ($f_{\text{add}} = 0.79$). Although core He ignition, indicated by the luminosity rise on the HG, occurs at different effective temperatures for the three merger products, they eventually become core-He burning BSGs, which occupy a similar region in the HRD. We indicate this part of the HRD with a lime rectangle. All merger products have a similar structure during this time: a convective core and a convective H-burning shell. This can be seen in Fig. 4.10, in which the vertical lime lines indicate the age range when the star is located within the lime rectangle on the HRD in Fig. 4.9. The main difference is that models with higher added mass fractions have smaller He-core masses. Despite this, the convective core masses during core He burning are similar because the merger products are all $10 M_{\odot}$ stars that have relaxed to their new structure. This is true for the mass- and f_{add} -ranges considered at the time of the comparison made here, but in general, the final CO core mass depends strongly on f_{add} (Schneider et al., 2024). The similar structures of the merger products are reflected in their Π_0 values (Fig. 4.9). Closer inspection shows that the values of Π_0 in the overlapping region are $\Pi_0 = 734\text{--}819$ s, $906\text{--}1034$ s, and $717\text{--}822$ s for the $8.0 + 2.0 M_{\odot}$, $6.4 + 3.6 M_{\odot}$, and $5.6 + 4.4 M_{\odot}$ merger products, respectively. The Π_0 values for the $6.4 + 3.6 M_{\odot}$ merger product are considerably higher than for the other merger products, which is related to the fact that by the time it occupies the same region of the HRD as the other merger products, its inner g-mode cavity has shifted outwards because of the growing convective core and

shrinking convective H-burning shell. The main cause for the differences in Π_0 is the point in evolution when the models are compared. If we compare the merger products to the left of the lime rectangle in Fig. 4.9, the differences in their Π_0 values are more evident. This is because the merger products ignite helium at different effective temperatures. However, these differences might be method-dependent (see Sect. 4.2.1.3), and we opted not to interpret this further than warranted by the nature of our current models. We discuss future steps to improve these comparisons in Sect. 4.4. Lastly, we note from Figs. 4.9 and 4.10c that the $5.4 + 4.6 M_\odot$ merger product spends a considerable amount of time (between the ages of 79.0 and 83.5 Myr) in the MS region of the HRD. During this time, the merger product has not yet ignited He in its core and has a $\sim 2 M_\odot$ convective H-burning shell. Since such a star would be observed in the same region of the HRD as MS stars, we compare it to a $10.6 M_\odot$ genuine single MS star in Fig. 4.11. During the time the merger product's and MS star's HRD tracks cross, their Π_0 values are 2000–3000 s and 19000–20000 s, respectively. This almost order-of-magnitude difference in Π_0 values follows from the different structures of the stars (see also Eq. 1.25): $10.6 M_\odot$ MS stars have a convective core and hence a g-mode cavity in the radiative envelope only. The merger product has an inner and outer g-mode cavity, with the bulk of the g modes trapped in and hence sensitive to the inner cavity (see Sect. 4.3.1) Therefore, even if a Case Be merger product is found in the MS region of the HRD, it will be clearly distinguishable from genuine single MS stars based on their respective mean PSP values. This also means that if such merger products contaminate a sample of genuine MS stars, they may influence the inference of the convective core sizes.

4.3.4. Comparison for oscillation equations including rotation

In Fig. 4.12 we compare the PSPs of the $6.0 + 2.4 M_\odot$ merger product and $7.8 M_\odot$ genuine single star with $\Omega = 0.2\Omega_c$. Here, $\Omega_c = \sqrt{GM_\star/R_{\text{eq}}^3} \simeq \sqrt{8GM_\star/27R_\star^3}$ is the Roche critical angular rotation frequency (Maeder, 2009). As motivated at the beginning of Sect. 1.2.2, we opted for a relatively slow rotation rate in this work. The angular rotation frequencies for both the merger product and genuine single star correspond to a surface rotation velocity of $v_{\text{surf}} = 38 \text{ km s}^{-1}$. These values for the surface rotation velocity are realistic given the efficient slow-down of stars beyond the TAMS as shown by asteroseismology of single stars (Aerts, 2021).

Given the significant difference in the mean PSP values between merger products and genuine single stars, and the relatively low rotation rates, the PSPs remain easily distinguishable with rotation included in the pulsation equations. The appearance of the deep dips in the merger product's PSPs also persists. Their positions shift because of the rotational modulated frequency shifts due to the inclusion of the Coriolis acceleration in the pulsation equations (see Aerts and Tkachenko 2023 for details).

4.3.5. Observability

We have not yet considered the observability of the modes predicted in this work. This depends on many aspects, the most important one being the intrinsic amplitude a mode gets when excited by the physical mechanism responsible for it. Even for genuine single intermediate- and high-mass stars, we have neither a complete theory to predict the excitation of the observed gravity modes nor the intrinsic amplitudes. Indeed, current excitation predictions cannot explain all the non-radial oscillations detected in modern space photom-

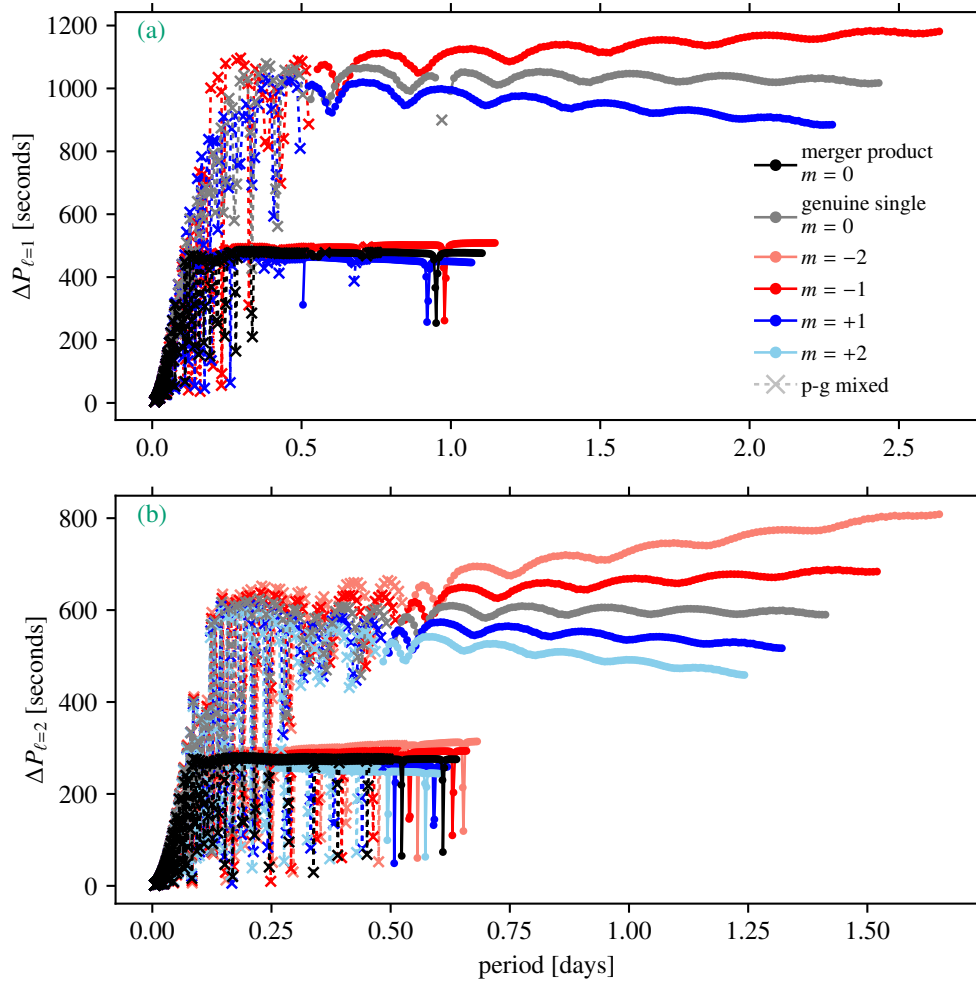


Figure 4.12: PSPs for a $6.0 + 2.4 M_{\odot}$ merger product and a $7.8 M_{\odot}$ genuine HG star with $\Omega = 0.2\Omega_c$ in the inertial frame. Panel (a) shows the PSPs for $(\ell, m) = (1, -1)$, $(1, 0)$, and $(1, +1)$ modes, and Panel (b) those for $(\ell, m) = (2, -2)$, $(2, -1)$, $(2, 0)$, $(2, +1)$, and $(2, +2)$ modes.

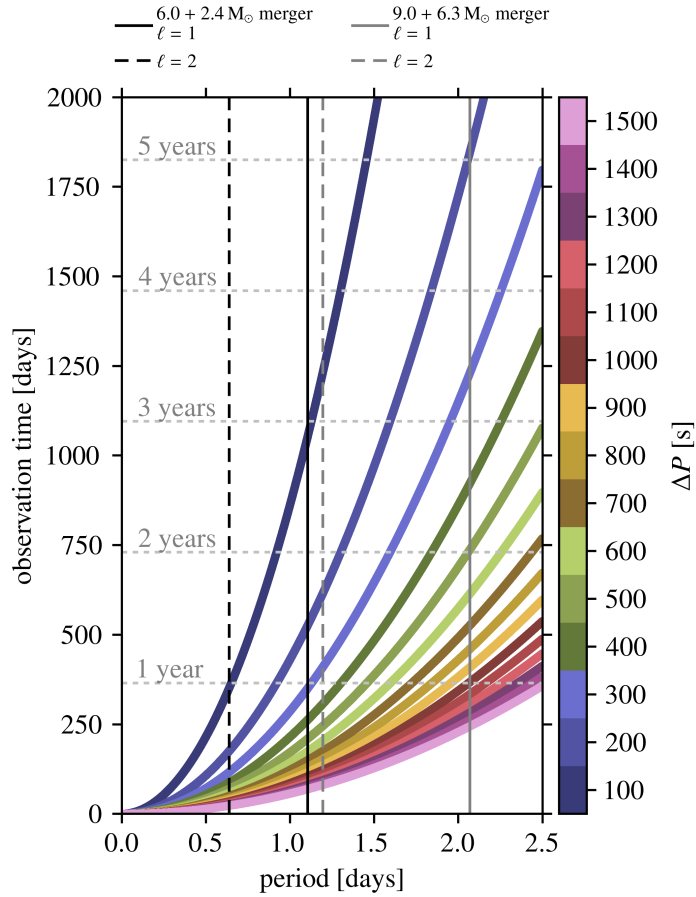


Figure 4.13: Observation times required for different period spacings, ΔP , in a period range relevant for the PSPs of merger products in our work. The horizontal dashed silver lines indicate the number of years on the y-axis. The vertical solid and dashed lines show the maximum period (i.e. the period for the mode at $n_{\text{pg}} = -200$) for the $(\ell, m) = (1, 0)$ and $(\ell, m) = (2, 0)$ modes, respectively, for the non-rotating $6.0 + 2.4 M_{\odot}$ (black) and $9.0 + 6.3 M_{\odot}$ (grey) merger products (see Figs. 4.3 and 4.5).

etry of such pulsators (e.g. Hey and Aerts, 2024; Balona, 2024, for summaries on the shortcomings of the theory revealed by the observations). Despite these limitations, especially the lack of knowledge about the modes' intrinsic amplitudes, we performed basic tests of the observability of the oscillation modes predicted in this work.

4.3.5.1 Frequency resolution from the observation's time base

To estimate the observational baseline required to resolve the period spacings predicted in this work, we started from the fact that the frequency resolution, $\delta\nu$, is inversely proportional to the observational baseline, T_{obs} :

$$\delta\nu = \frac{1}{T_{\text{obs}}}. \quad (4.2)$$

Using that the period P is inversely proportional to the frequency ν and that $\delta\nu = \nu_2 - \nu_1$, we can rewrite Eq. (4.2) as

$$\frac{1}{P_2} - \frac{1}{P_1} = \frac{1}{T_{\text{obs}}}, \quad (4.3)$$

which then gives

$$T_{\text{obs}} = \frac{P_1 P_2}{P_1 - P_2} = \frac{P_1^2 - \Delta P P_1}{\Delta P}, \quad (4.4)$$

where we have used that the period spacing $\Delta P = P_1 - P_2$. We see from Eq. (4.4) that we require a different observational baseline depending on the period P_1 and the g-mode period spacing ΔP we want to observe. We show the results for a range of period spacings and periods relevant for the PSPs of merger products (which have lower PSP values than the genuine single stars) in this work, in Fig. 4.13. We see that for the $\ell = 1$ modes of the $6.0 + 2.4 M_{\odot}$ merger product (mean $\Delta P_n \approx \Pi_{\ell} = 479$ s), period spacings down to 200 s can be resolved with observational baselines of two years, and everything down to 100 s when three years of data are available (for modes with $n_{\text{pg}} \geq -200$). The period spacings for $\ell = 2$ modes (mean $\Delta P_n \approx \Pi_{\ell} = 277$ s) should be resolved down to 100 s with an observational baseline of one year. The mean ΔP_n value for $\ell = 1$ modes of the higher-mass $9.0 + 6.3 M_{\odot}$ merger product is larger than for its lower-mass counterpart (mean $\Delta P_n \approx \Pi_{\ell} = 902$ s) and period spacings of $\Delta P \geq 500$ s between $\ell = 1$ modes with $n_{\text{pg}} \geq -200$ can in principle be resolved with a baseline of two years. For $\ell = 2$ g modes (mean $\Delta P_n \approx \Pi_{\ell} = 521$ s), period spacings down to 100 s can be resolved with an observational baseline of less than four years. Given that inner- and outer-cavity g modes' periods converge when they couple (see Sect. 4.3.2), the period spacings in the deep PSP dips can be relatively small. Therefore, resolving all of these dips with reasonable observational baselines might be impossible. However, as discussed in Sect. 4.3.2, the deep dips do not consist of a single set of modes. Hence, even when the deep dip's minimum cannot be resolved, the overall deep dip's signature might still be discernible in observational PSPs. We note that we did not consider any form of noise in these estimates of the observational baselines.

4.3.5.2 Mode instability for the opacity mechanism

Stellar oscillation computations in this work have been performed in the adiabatic approximation (see Sect. 4.2.2). This approximation does not allow us to predict whether modes are excited or damped, that is, which modes are unstable. Even without the adiabatic approximation, GYRE only considers the so-called heat-engine mechanism (also known as the opacity or κ -mechanism) to predict the instability (i.e. the balance between excitation and damping) of modes (Aerts et al., 2010a). While offering a basic understanding for MS pulsators with large amplitudes, this mechanism is known to under-predict the number of observed oscillation modes that occur at μmag level. Many reasons are known to form the basis of the limitations (e.g. ignoring radiative levitation in MS B-type pulsators Rehm et al., 2024, to mention just one). Other excitation mechanisms include stochastic forcing, convective driving, and non-linear resonant mode excitation as observed in single and close binary pulsators (e.g. Guo et al., 2020, 2022; Van Beeck et al., 2024). Gaia Collaboration et al. (2023a), Balona (2024), and Hey and Aerts (2024) all illustrate that g-mode pulsators form a continuous group of pulsating B-, A-, and F-type stars. Indeed, a significant fraction of these observed pulsators fall outside predicted instability strips based on current mode excitation mechanisms. The situation is even less understood for stars in the HG. In other words, the theory of mode excitation needs to be refined appreciably to explain the observed oscillations in stars in the modern high-cadence, high-precision space photometry for intermediate- and high-mass stars, including mergers.

By solving the oscillation equations for our models with GYRE in its non-adiabatic mode⁵ and for the current input physics of stellar evolution theory of single and merger stars, we find that none of the oscillation modes in our models are unstable (that is, the imaginary parts of the mode frequency are negative). This is the case in both our merger product and genuine single-star models.

4.3.5.3 Wave displacements at the stellar surface

Irrespective of whether the modes treated in this work are predicted to be unstable, the modes' amplitudes throughout the stellar interior and up to the stellar surface can be assessed. We provide plots of the wave displacement profiles $\xi_r(r)$ and $\xi_h(r)$, and the differential mode inertia profile dE/dr for a specific set of oscillation modes for the merger products and genuine single stars described in Sects. 4.3.1.1 and 4.3.1.2. These plots can be found in Appendix C.5. The differential mode inertia is the radial derivative of the denominator of Eq. (4.1) (see also Eq. 3.139 in Aerts et al. 2010a). To have a chance to observe these pulsation modes, their wave displacements should not disappear near the surface. Although we find that the wave displacements and differential mode inertias are diminished for the pure inner-cavity g modes in stars with two g-mode cavities, there is still a non-negligible mode signal near the surface. The p-g mixed modes, which have shorter mode periods (higher frequencies), couple efficiently, resulting in even larger displacements and differential mode inertias. We stress that this does not immediately mean they are observable, as this depends on the intrinsic amplitude the mode gets from the excitation mechanism.

4.3.5.4 Mode suppression by internal magnetic fields

Fuller et al. (2015) show that a strong magnetic field can suppress mixed modes in red giants. A similar phenomenon may be active in pulsating B stars (Lecoanet et al., 2022). It is thus worthwhile to ask what its effect could be for mode observability in HG BSGs and merger products.

As mentioned in Sect. 4.2.1.3, we did not consider the presence of strong internal magnetic fields resulting from the merger process. We can estimate what the internal magnetic field strength would be if we assume a dipole magnetic field, that is, $B(r) = B_{\text{surf}}(R_{\star}/r)^3$, with B_{surf} the surface magnetic field of our merger product (Schneider et al., 2020). B_{surf} can be estimated from the surface magnetic field of the MS merger product from Schneider et al. (2019) and assuming flux freezing, that is, $B_{\text{MS}}R_{\text{MS}}^2 = B_{\text{surf}}R_{\star}^2$, with $B_{\text{MS}} = 9 \times 10^3$ G and $R_{\text{MS}} = 5 R_{\odot}$ the surface magnetic field and MS radius of the 3D magnetohydrodynamic merger product from Schneider et al. (2019).

We can now compare this field strength with the critical magnetic field strength $B_{\text{crit}} = \sqrt{\pi\rho/2\omega^2r}/N$, defined in Fuller et al. (2015) as the magnetic field strength above which the magnetic tension overcomes the buoyancy force. Here, ω is the angular mode frequency. We find that, using ω values from the range of mode frequencies predicted in this work, $B(r) < B_{\text{crit}}$ in the outer g-mode cavity of the $6.0 + 2.4 M_{\odot}$ merger product at the time it is compared with the $7.8 M_{\odot}$ genuine single star, while in the inner g-mode cavity $B(r) > B_{\text{crit}}$ (for modes with a period of 1 day, $B_{\text{crit}} \sim 10^4\text{--}10^7$ G in the inner g-mode cavity and $B_{\text{crit}} \sim 5 \times 10^4\text{--}10^7$ G in the outer g-mode cavity). Under these assumptions, we would expect the inner cavity g-modes to be suppressed by the magnetic field. However, this does

⁵The setup for these computational is identical to the one described in Sect. 4.2.2, except for that we used the MAGNUS_GL2 solver. This solver is more appropriate for non-adiabatic computations.

not consider, among other uncertainties, that the magnetic field strength can be severely attenuated (Quentin and Tout, 2018) or even expelled (Braithwaite and Spruit, 2017) when propagating through convective regions. Furthermore, Landstreet et al. (2007), Landstreet et al. (2008), and Fossati et al. (2016) show that the magnetic field strength in massive MS stars disappears faster than predicted from flux freezing alone.

4.4. Discussion and conclusions

Considering an ensemble of early Case B merger product models and genuine single HG stars, Bellinger et al. (2024) conclude that these two classes of objects cannot be distinguished from one another based on their mean PSP values. However, these authors compared the $\Pi_{\ell=1}$ values of all their models in the sets of merger products and genuine single stars (masses of 10–20 M_{\odot}) at all points during their BSG evolution simultaneously. Because of relatively large variations in Π_{ℓ} with evolutionary time and mass, which we also find in our models, there is a significant overlap between the ranges of Π_{ℓ} of the two types of stars, which led to their conclusion that they are indistinguishable based on Π_{ℓ} . However, from our case-by-case comparison between models of these two classes at similar positions in the HRD, we conclude that the mean PSP value is consistently and significantly lower for merger products than for genuine single stars. We stress that for accurate predictions of the mean PSP value from the stellar structure, that is, Π_{ℓ} , the integral in the denominator of Eq. (1.25) has to be evaluated over the proper g-mode cavity if more cavities are present in the model. In such cases, when the evanescent zone separating the cavities is substantial in size, the bulk of the g modes will be trapped in the inner cavity. Integrating over multiple cavities, as done in Bellinger et al. (2024), leads to a deviation in the predictions of $\lesssim 10$ s. This deviation is an order of magnitude smaller than the differences between the mean PSP values of post-MS merger products and genuine single HG stars found in our work but is comparable to the period precision of time series data from space missions.

We find that when a star has two g-mode cavities, which is the case for early Case B merger products at all the masses considered in this work and genuine single HG stars with $M_{\star} \gtrsim 11.4 M_{\odot}$, some inner-cavity g modes couple to outer-cavity g modes. This coupling leads to the formation of deep dips in the PSPs and can be used as a diagnostic to distinguish merger products from genuine single stars in the mass range roughly below 11.4 M_{\odot} . At higher masses, both the merger products and genuine single stars have two mode cavities, resulting in deep dips in their PSPs. In general, the appearance of deep PSP dips might not be unique to merger products since blue loop stars also have two mode cavities (Ostrowski and Daszyńska-Daszkiewicz, 2015). Further detailed comparisons between genuine single HG stars, merger products, and blue loop stars should shed light on whether other differences can be used to identify blue loop stars in a population of BSGs.

From our initial results in Sect. 4.3.3, we conclude that the added mass fraction, f_{add} , has a relatively minor impact on the asteroseismic properties of our merger products. Depending on f_{add} , we see that the merger products ignite He in their cores at different effective temperatures, leading to different stellar structures when the merger product occupies the same region of the HRD. With this exercise, we explored how the pre-merger conditions might influence the asteroseismic properties of the merger product, even though f_{add} cannot be directly related to the mass ratio. Future exploration based on a grid of more complete merger models will allow us to determine whether the binary parameters at the time of merging are detectable in the asteroseismic properties of the merger product.

We find that the PSPs of early Case B merger products and genuine single HG stars are distinguishable when we ignore rotation, as well as when we include rotation at a level of $\Omega = 0.2\Omega_c$. Taking rotation into account in the stellar oscillation computations for merger products is an important step forward for realistically predicting their asteroseismic properties. The modes most frequently observed are prograde sectoral dipole and quadrupole modes ($\ell = m = 1$ and $\ell = m = 2$, respectively; Li et al. 2020; Pedersen et al. 2021). Furthermore, the fact that merger products are slow rotators is not firmly established, so asteroseismic predictions of fast-rotating merger products are warranted. Despite the many uncertainties on internal angular momentum transport, rotating equilibrium models with more realistic rotation profiles, such as those recently computed from 2-to-1D models by Mombarg et al. (2024b), should be considered for such an exercise.

Finally, we conducted a set of preliminary tests to determine the observational potential of the modes predicted in our work. We find that it should, in principle, be possible to resolve period spacings down to 200 s, which is far below the mean PSP values predicted in this work, with five years of time series data. Depending on the depth of the deep PSP dips, which in turn depends on how close the periods of modes in the inner and outer g-mode cavity lie, it might not be possible to resolve their minima at longer periods with less than five years of time series data. We stress again that a full assessment of the observability is plagued by uncertainties related to mode instability, the observable mode amplitudes at the stellar surface, and interior magnetic fields. Even though these uncertainties are pointed out here, we cannot meaningfully address mode observability as long as the mode excitation mechanisms remain non-compliant with the observations, as they are today, and are unable to provide us with reliable predictions for the intrinsic mode amplitudes.

Acknowledgments We thank the anonymous referee for their valuable comments and suggestions, which have triggered further research and helped us to improve the presentation of our results. We thank J. Saling for the valuable insights from his Bachelor thesis titled “Formation of Blue Supergiants in Stellar Mergers” (University of Heidelberg, 2023). We thank T. Van Reeth, M. Michielsen, E. Bellinger, D. Bowman, E. Laplace, A. Noll, B. Bordadáguia, Q. Coppée, F. Ahlborn, C. Johnston, and R. Townsend (in no particular order) for the meaningful discussions and valuable comments and suggestions. Additional software used in this work includes PyGYRE (Townsend and Rosenberg, 2020), PyMesaReader (Wolf and Schwab, 2017), MPI for Python (Dalcín et al., 2005; Dalcin and Fang, 2021), Astropy (Astropy Collaboration et al., 2013, 2018, 2022), NumPy (Harris et al., 2020), and SciPy (Virtanen et al., 2020). We used Matplotlib (Hunter, 2007), matplotlib-label-lines (Cadiou, 2022), and mkip (Marchant, 2020) for plotting. The authors acknowledge support from the Klaus Tschira Foundation. This work has received funding from the European Research Council (ERC) under the European Union’s Horizon 2020 research and innovation programme (Starting Grant agreement N° 945806: TEL-STARS, Consolidator Grant agreement N° 101000296: DipolarSound, and Synergy Grant agreement N° 101071505: 4D-STAR). While funded by the European Union, views and opinions expressed are however those of the author(s) only and do not necessarily reflect those of the European Union or the European Research Council. Neither the European Union nor the granting authority can be held responsible for them. This work is supported by the Deutsche Forschungsgemeinschaft (DFG, German Research Foundation) under Germany’s Excellence Strategy EXC 2181/1-390900948 (the Heidelberg STRUCTURES Excellence Cluster).

Asteroseismic predictions for a massive main-sequence merger product

AUTHORS Jan Henneco, Fabian R. N. Schneider, Max Heller, Saskia Hekker, and Conny Aerts

CHAPTER INFO This chapter is a reproduction of the last paper I wrote during my doctoral studies. At the time of writing, this paper is close to submission. In this chapter, we explore if and how the product of a merger between two main-sequence stars differs asteroseismically from a genuine single star with similar surface diagnostics. I was the main author of this paper and computed, analysed, and interpreted the results. Max Heller, a master's student in the Stellar Evolution Theory group at HITS, developed one of the codes used in this work and wrote Sect. 5.2.2.3 about it. Fabian Schneider, Saskia Hekker, and Conny Aerts advised me during this project and contributed to the text in the form of comments, suggestions and corrections.

ABSTRACT The products of stellar mergers between two massive main-sequence stars appear as seemingly normal main-sequence stars after a phase of thermal relaxation, if not for certain peculiarities. These peculiarities, such as strong magnetic fields, chemically enriched surfaces, rejuvenated cores, and masses above the main-sequence turnoff mass, have been proposed to indicate merger or mass accretion origins. Since these peculiarities are not limited to the merger product's surface, we use asteroseismology to predict how the differences in the internal structure of a merger product and a genuine single star manifest via properties of non-radial stellar pulsations. We use the result of a 3D (magneto)hydrodynamic simulation of a stellar merger between a 9 and an 8 M_{\odot} main-sequence star, which was mapped to 1D and evolved through the main sequence. We compare the predicted pressure and gravity modes for the merger product model with those predicted for a corresponding genuine single-star model. The pressure-mode frequencies are consistently lower for the merger product than for the genuine single star, and the differences between them are more than a thousand times larger than the current best observational uncertainties for measured mode frequencies of this kind. Even though the absolute differences in gravity mode period spacings vary in value and sign throughout the main-sequence life of both stars, they, too,

are larger than the current best observational uncertainties for such slow modes. This, combined with additional variability in the merger product’s period spacing patterns, shows the potential of identifying merger products in future-forward modelling. We also attempt to replicate the merger product’s structure using three widely applied 1D merger prescriptions and repeat the asteroseismic analysis. Although none of the 1D prescriptions reproduces the entire merger product’s structure, we conclude that the prescription with shock heating shows the best potential, provided that it can be calibrated on binary-evolution-driven 3D merger simulations. Our work focuses on a particular kind of massive main-sequence merger and should be expanded to encompass the various possible merger product structures predicted to exist in the Universe.

5.1. Introduction

When two massive¹ main-sequence (MS) stars merge, they form a new MS star with potentially peculiar properties. For example, it has been proposed and shown that such mergers produce strong, large-scale surface magnetic fields in the resulting merger products (Ferrario et al., 2009; Wickramasinghe et al., 2014; Schneider et al., 2019). Should it indeed be true that such merger products are slow rotators, as found in Schneider et al. (2019) and Schneider et al. (2020), they are a natural explanation for the blue MS band in young stellar clusters (Wang et al., 2022), and can also appear as blue stragglers in star clusters (Rasio, 1995; Sills et al., 1997, 2001; Mapelli et al., 2006; Glebbeek et al., 2008; Ferraro et al., 2012; Schneider et al., 2015). Further along their evolution, MS merger products can appear as red stragglers in a population of red supergiants, which can lead to cluster age underestimations of ~60% (Britavskiy et al., 2019).

Despite these peculiarities, it is currently not straightforward to distinguish massive MS merger products from genuine single MS stars based on surface diagnostics alone. If one or more unambiguous distinguishing features of merger products were to be found, they could be used to confirm, for example, their slow-rotation hypothesis. To find such distinguishing features, we ought to go beyond the stars’ surface diagnostics and assess any differences in their internal structure, which are expected from merger simulations (Lombardi et al., 1996; Sandquist et al., 1997; Sills et al., 2001; Freitag and Benz, 2005; Dale and Davies, 2006; Glebbeek et al., 2013; Schneider et al., 2019; Ballone et al., 2023). Asteroseismology has proven to be the ideal tool to do so (see, e.g. Hekker and Christensen-Dalsgaard 2017; Aerts 2021; Kurtz 2022; Bowman 2023 for recent reviews). Bellinger et al. (2024) and Henneco et al. (2024a) used asteroseismology to identify distinguishing features of different physical object classes appearing as blue supergiants, including post-MS merger products. Wagg et al. (2024) used asteroseismic predictions of rejuvenated MS accretors to assess whether they can be distinguished from MS stars with the same mass that have not accreted matter. They conclude that the effects of accretion on the accretor’s internal structure produce a measurable difference in its asteroseismic signal compared to that of regular MS stars.

An obvious prerequisite for using asteroseismology is that the stars show pulsations. This is indeed the case for massive MS stars. Thanks to space-based asteroseismic observations with, for example, Convection, Rotation and planetary Transits (CoRoT, Auvergne et al., 2009), *Kepler*/K2 (Koch et al., 2010), and the Transiting Exoplanet Survey Satel-

¹With massive stars we refer to intermediate- and high-mass stars, which have initial masses M_i of $1.3 M_\odot \lesssim M_i \lesssim 8 M_\odot$ and $M_i \gtrsim 8 M_\odot$, respectively.

lite (TESS, Ricker et al., 2016) a wealth of MS pulsators have been found and characterised (Aerts, 2021). Fewer detections are currently available for stars with masses above roughly $8 M_{\odot}$, which is the mass regime this work focuses on. Yet, the future looks bright thanks to the ongoing TESS and upcoming PLANetary Transits and Oscillations of stars (PLATO, Rauer et al., 2024) missions. Mode excitation calculations (e.g. Bouabid et al., 2013; Moravveji, 2016; Szewczuk and Daszyńska-Daszkiewicz, 2017) also predict massive MS stars to exhibit a variety of pulsations. Moreover, it is becoming increasingly clear that our current excitation theories tend to under-predict the number of excited linear modes (e.g. Rehm et al., 2024), as well as the actual observed modes in stars (e.g. Balona, 2024; Hey and Aerts, 2024). Additional mode excitation theories for MS stars, such as non-linear resonant mode coupling (Guo et al., 2022; Van Beeck et al., 2024), are currently not included in mode instability predictions while such modes were found to be common among B-type pulsators (Van Beeck et al., 2021). Finally, tidal excitation (Guo, 2021, for a review) cannot be ignored given the high fraction of massive stars in close binaries (Sana et al., 2012).

This work consists of two parts. In the first part, we determine whether it is possible to distinguish a massive MS merger product from a genuine single MS star following a quasi-identical evolution in the Hertzsprung-Russel diagram (HRD). To do so, we make use of the 3D magnetohydrodynamic (MHD) merger product model from Schneider et al. (2019), which we map to 1D following Schneider et al. (2020) to follow its post-merger evolution. In the second part, we repeat the first part’s analysis, using 1D merger prescriptions instead of a 3D merger product model. 3D simulations of stellar mergers are computationally expensive, and hence, a limited number of 3D merger models are available. Multiple 1D merger prescriptions have been developed in an attempt to alleviate this problem. Contrary to 3D simulations, these 1D merger prescriptions do not model the merger phase itself but instead predict the structure of the merger product based on those of the binary components before the merger. Therefore, in the second part of this work, we investigate whether using three of these 1D merger prescriptions (entropy sorting, Python Make Me A Massive Star, and fast accretion) results in similarly structured merger product models as the one resulting from the 3D simulation. We then assess to what extent any asteroseismic differences between the MS merger product and its corresponding genuine single star found in the first part of this work are recovered with the 1D merger models.

The structure of this work is as follows. Section 5.2 covers the methods used to create merger products, evolve them and their genuine single-star counterparts, and predict their pulsations. We show our results and discuss them in Sect. 5.3, and the conclusions can be found in Sect. 5.4.

5.2. Methods

5.2.1. Stellar evolution computations with MESA

We used the 1D stellar structure and evolution code MESA (r12778, Paxton et al., 2011, 2013, 2015, 2018, 2019) to compute the input models for the various merger prescriptions and evolve the resulting merger products. We computed the genuine single-star models using the same MESA setup and, hence, input physics. The choices for the input physics and setup were based on those from Schneider et al. (2020), except that we did not include rotation at the level of the equilibrium models, we did not model any accretion from the disk formed during the merger event, and we ignored the magnetic field produced in the merger

process (Schneider et al., 2019). The number of works on the effect of magnetic fields on non-radial pulsations grows steadily (see, e.g. Prat et al. 2019, Van Beeck et al. 2020, Dhouib et al. 2022, Rui et al. 2024, Bessila and Mathis 2024, Bhattacharya et al. 2024, and Hatt et al. 2024), however, we aim to assess the effects of the structure and composition of MS merger products separately from the effects of magnetic fields. Ignoring rotation in the equilibrium models and only taking it into account at the level of the oscillation equations (see Sect. 5.2.3) is justified by the small effect of the centrifugal deformation of the star on predicted frequencies (Henneco et al., 2021; Dhouib et al., 2021) and is common practice for slow to moderate rotators (Aerts, 2021; Aerts and Tkachenko, 2023). We compensated for the resulting lack of rotationally induced mixing by mimicking its effect with a constant envelope mixing of $\log(D_{\text{mix}}/\text{cm}^2\text{s}^{-1}) = 3$. This envelope mixing was also used to smooth out small chemical glitches introduced during the merger and left behind by the receding convective core during the MS evolution. This is a typical value for envelope mixing inferred from asteroseismic modelling of single B-type stars (Pedersen et al., 2021; Burssens et al., 2023).

We used mixing length theory (MLT, Böhm-Vitense, 1958; Cox and Giuli, 1968) to treat convection in our models with a mixing length parameter of $\alpha_{\text{mlt}} = 1.8$. We assessed the stability against convection using the Ledoux criterion. Additional mixing was included in the form of thermohaline mixing with an efficiency of $\alpha_{\text{th}} = 2.0$ and semi-convective mixing with an efficiency of $\alpha_{\text{sc}} = 1.0$ (semi-convective mixing only appears in our models during thermal relaxation phases, not during the MS evolution). We used the exponential overshoot scheme to account for convective boundary mixing above convective cores with $f_{\text{ov}} = 0.019$. This value for f_{ov} was based on observational constrains from $\approx 10 M_{\odot}$ MS stars by Castro et al. (2014) (see also Schneider et al., 2020). We used the Vink et al. (2001) wind mass-loss prescription with a scaling factor of one (we only consider the MS evolution, i.e. the hot star regime for wind mass loss). All models were computed at solar metallicity ($Y = 0.2703$ and $Z = 0.0142$, Asplund et al. 2009), with a combination of the OPAL (Iglesias and Rogers, 1993, 1996) and Ferguson et al. (2005) opacity tables suitable for the chemical mixture from Asplund et al. (2009). The models were terminated when the central hydrogen mass fraction X_{c} dropped below 10^{-6} .

5.2.2. Merger models and prescriptions

This section describes how we obtained a 1D model for an MS merger product from the 3D MHD simulation from Schneider et al. (2019) and three 1D merger prescriptions used to approximate this model. The 3D MHD simulation, as well as the three 1D methods, used $9 M_{\odot}$ and $8 M_{\odot}$ single-star 1D MESA models evolved up to 9 Myr. At this point, their central hydrogen mass fractions were $X_{\text{c}} = 0.60$ and $X_{\text{c}} = 0.62$, respectively, and the mass ratio $q = M_2/M_1 = 0.89$. A limitation that all of the methods described below share, including the 3D MHD merger product model, is that mass transfer before and during the contact phase, which precedes the stellar merger, is not included in this initial study of MS merger asteroseismology. From detailed binary evolution calculations, such as those from Pols (1994), Wellstein et al. (2001), de Mink et al. (2007), Claeys et al. (2011), Marchant et al. (2016), Mennekens and Vanbeveren (2017), Laplace et al. (2021), Menon et al. (2021), and Henneco et al. (2024b), we know that mass transfer can significantly alter the structure of the binary components. The impact of ignoring the mass transfer phase prior to merging will be assessed in a future study (Heller et al. in prep.).

5.2.2.1 3D MHD model

Following Schneider et al. (2019) and Schneider et al. (2020), we started from the chemical composition and entropy profiles of the $16.9 M_{\odot}$ merger product resulting from the 3D MHD simulation of Schneider et al. (2019). These were used to relax a 1D stellar model in MESA with the same total mass, chemical composition profile, and entropy structure (i.e. thermal structure) as the 3D merger product (see Appendix B of Paxton et al. 2018 for a technical description of this relaxation routine). The resulting 1D model was then used as the starting point of a MESA evolution run with the physical and numerical choices described in Sect. 5.2.1. As described in Schneider et al. (2020), the $8 M_{\odot}$ secondary star’s core sinks to the centre of the merger product, and the $9 M_{\odot}$ primary star’s more evolved and more He-rich core ends up in the layer around it. Consequently, the merger product’s inner envelope is enriched in He and other products of hydrogen burning. During the initial phases of the evolution of the merger product, the merger product thermally relaxes, leading to a rapid expansion and subsequent contraction phase. During this contraction phase, the merger product has a transient ($\Delta t \approx 9000$ yr) convective core reaching a mass of $\approx 11 M_{\odot}$ (for comparison, when the star arrives again on the MS after thermally relaxing, its convective core mass $\approx 7 M_{\odot}$). We refer to this merger product model as the ‘3D MHD merger product’ or the ‘3D MHD model’ to distinguish it from the 1D merger product models. The corresponding acronym in figures, sub-, and super-scripts is ‘MHD’.

5.2.2.2 Entropy sorting

Entropy sorting is based on the relation between the entropy and buoyancy of stellar material. In an ideal case, a star in hydrostatic equilibrium has a monotonically increasing entropy profile, except for convective regions, where the entropy profile is approximately flat (Lombardi et al., 1996). The layers with lower entropy have lower buoyancy and are thus found closer to the star’s centre. In a simplified picture, when two stars merge, the layers with the lowest entropy will sink to the centre of the merger product. Using this principle, we combined the structures of the $9 M_{\odot}$ and $8 M_{\odot}$ progenitor stars based on their entropy profiles. Starting from the centre, we selected the layer from either star with the lowest entropy, creating a new structure with a monotonically increasing entropy profile. Analogous to the 3D MHD model, we used the chemical composition profile² to relax a MESA model with a total mass of $16.9 M_{\odot}$ ³. The relaxed model was subsequently evolved in MESA. It went through a similar thermal relaxation phase with the appearance of a transient convective core, further described in Sect. 5.3.2.1. We did not employ any artificial smoothing of the merger product’s structure; small chemical and structural glitches were smoothed out during the relaxation phase and subsequent MS evolution because of the envelope mixing described in Sect. 5.2.1. We refer to the merger product constructed through entropy

²Although it might seem like a logical thing to use the entropy-sorted entropy profile as well for the relaxation routine, doing so leads to abnormally high central temperatures and densities in the relaxed model. This is caused by the fact that the entropy sorting model is not in hydrostatic equilibrium prior to relaxing, i.e. the central entropy has not adjusted to the merger product’s mass. For the 3D MHD merger product and PyMMAMS model this is not a problem since they are in hydrostatic equilibrium.

³Contrary to the 3D MHD model, the chemical composition profiles resulting from entropy sorting is that of a $17.0 M_{\odot}$ stellar model. In other words, we did not yet account for the $0.1 M_{\odot}$ lost during the merger in the 3D MHD simulation. Since we do not want to make assumptions for the composition of the lost material during the merger, we relaxed the original $17.0 M_{\odot}$ MESA model to a $16.9 M_{\odot}$ model, as opposed to stripping the $0.1 M_{\odot}$ from the merger product’s surface after relaxation.

sorting as the ‘entropy-sorted model’ or ‘entropy-sorted merger product’, with the acronym ‘ES’.

A limitation of the entropy sorting method is that it does not consider any form of entropy generation. During the merging phase, shocks can increase the entropy in both companions and, in general, additional mixing occurs. We see the consequences of this in our case study of the merger between the $9 M_{\odot}$ and $8 M_{\odot}$ stars. Assuming the stars are born together, the more massive $9 M_{\odot}$ primary star has a more evolved, He-rich core with a lower mean entropy than the core of the $8 M_{\odot}$ secondary star. By applying entropy sorting, we thus find that the core of the primary sinks to the centre of the merger product (this is further described in Sec. 5.3.2.1), whereas we found from the 3D MHD model that the secondary’s core has sunk to the centre.

5.2.2.3 PyMMAMS: entropic variable sorting with shock heating

The Make Me A Massive Star (MMAMS) routine is a 1D merger prescription originally presented in Gaburov et al. (2008b) and includes an approximation for the shock heating (entropy generation) that occurs during stellar head-on collisions (as opposed to slower inspiral mergers driven by binary evolution). MMAMS performs stellar mergers by first shock heating the progenitors and then sorting them using the entropic variable A (Gaburov et al., 2008b)

$$A = \frac{\beta_{\text{gas}} P}{\rho^{5/3}} \exp \left[\frac{8}{3} \frac{(1 - \beta_{\text{gas}})}{\beta_{\text{gas}}} \right], \quad (5.1)$$

which is closely linked to the specific entropy. Here, β_{gas} is the ratio of gas pressure P_{gas} over total pressure P . The entropic variable is used together with a pressure estimate from hydrostatic equilibrium to compute the density of the progenitor shells in the merger product. MMAMS builds the merger remnant starting at the center, with the more dense shells being placed closer to the core. The merger product is then dynamically relaxed by solving the equations of hydrostatic equilibrium. Shock heating changes the entropic variable profile of the stars, leading to changes in the post-merger composition profiles compared to entropy sorting. The shock heating prescription was obtained from smoothed particle hydrodynamic (SPH) simulations of stellar head-on collisions for progenitors of different initial masses, mass ratios and evolutionary stages (Gaburov et al., 2008b). The prescription includes a correction factor to account for energy conservation before and after the merger.

Currently, MMAMS is available as part of the AMUSE framework (Portegies Zwart et al., 2009; Pelupessy et al., 2013; Portegies Zwart et al., 2013; Portegies Zwart and McMillan, 2018; Portegies Zwart et al., 2019). For better portability and modifiability, we translated MMAMS to Python (Heller et al., in prep.). It is this Python version, Python Make Me A Massive Star (PyMMAMS), that we used in this work. We implemented several modifications in PyMMAMS compared to the original MMAMS code. For example, we introduced a new re-meshing scheme, which alleviates the double-valuedness in regions of the merged star, where progenitor mass elements of very different compositions ended up next to each other. Our re-meshing scheme aims to improve upon the mixing scheme included in the original code, which mixed stellar matter over steep composition gradients. These gradients are located at the interface of single- and double-valued regions, that is, parts of the merger product where shells of material coming from only one of the progenitors touch shells of material consisting of a mixture of both progenitors. In the original mixing scheme from MMAMS, these gradients were softened, which in some cases led to hydrogen from the enve-

lope being mixed into the helium core of a post-MS merger product, distorting the merger product’s further evolution.

Certain numerical solvers used to compute the shock heating in (Py)MMAMS have been found to fail for mass ratios $q = M_2/M_1$ below 0.1 and above 0.8. Since the mass ratio of our progenitor binary system is $q = 0.89$, we compute the shock heating for a $q = 0.8$ and use that to alleviate this shortcoming of (Py)MMAMS.

Even though PyMMAMS includes the effect of shock heating, the shock-heating prescription has been calibrated for head-on collisions. These tend to be more energetic than the slower inspiral of binary components of a stellar merger driven by binary evolution. Therefore, we consider PyMMAMS and entropy sorting to be the two extremes regarding shock heating, with the actual amount of shock heating likely somewhere in between.

We refer to the merger product model obtained with PyMMAMS as the ‘PyMMAMS model’ or ‘PyMMAMS merger product’. The corresponding acronym is ‘PM’.

5.2.2.4 Fast accretion

The last 1D merger method used in this work is fast accretion. This method consists of accreting a certain amount of mass onto a star, in this case, the $9 M_\odot$ primary star, in a timescale shorter than or equal to the primary star’s global thermal timescale. We closely followed the setup of Henneco et al. (2024a) and accreted $7.9 M_\odot$ of material with the same chemical composition as the surface of the primary star during 10% of the primary star’s global thermal timescale τ_{KH} . We initiated this fast accretion phase when the primary star reached an age of 9 Myr. The main limitations of this method are described in Henneco et al. (2024a). We describe its restrictions specifically for reproducing massive MS merger products in Sects. 5.3.2.3 and 5.4. The merger product constructed with the fast accretion method is referred to as the ‘fast accretion model’ or ‘fast accretion merger product’. For this model, we use the acronym ‘FA’.

5.2.3. Oscillation mode predictions with GYRE

We used the stellar oscillation code GYRE (v7.0; Townsend and Teitler, 2013; Townsend et al., 2018) to predict the oscillation modes for the equilibrium models obtained from the 1D MESA models described above. We used the MAGNUS_GL6 solver with the boundary conditions from Unno et al. (1989). For g modes in the absence of rotation, we computed $(\ell, m) = (1, 0)$ and $(\ell, m) = (2, 0)$ modes. For predictions with rotation, we used the traditional approximation of rotation (TAR, Eckart, 1960; Berthomieu et al., 1978; Lee and Saio, 1987; Townsend, 2003; Mathis, 2009) as implemented in GYRE to compute $(\ell, m) = (1, 0)$, $(\ell, m) = (1, \pm 1)$, $(\ell, m) = (2, 0)$, $(\ell, m) = (2, \pm 1)$, and $(\ell, m) = (2, \pm 2)$ modes in the inertial (observer’s) frame. All these computations of g modes were conducted with the adiabatic approximation, which is appropriate to compute the frequencies of g modes in B-type stars (Aerts et al., 2018b).

We computed p modes under non-adiabatic conditions because they are more sensitive to the star’s outer layers, where the thermal timescale becomes relatively short and non-adiabatic effects may become important. We used the MAGNUS_GL2⁴ solver together with GYRE’s CONTOUR initial search method for these non-adiabatic p-mode computations. In

⁴As stated by the GYRE documentation, this solver is more appropriate for non-adiabatic computations, given that it does not lead to convergence issues.

the absence of rotation, we computed p modes of $(\ell, m) = (1, 0)$ and $(\ell, m) = (2, 0)$. The effects of rotation were included through the first-order Ledoux perturbative approach (see Aerts and Tkachenko 2023 for more details on this approach) for $(\ell, m) = (1, \pm 1)$, $(\ell, m) = (2, \pm 1)$, and $(\ell, m) = (2, \pm 2)$ p modes. We did not add atmosphere models to the equilibrium model output used by GYRE because the MS stars treated in this work are not expected to have extended atmospheres.

5.3. Results

Figure 5.1 shows the MS evolutionary tracks of the $16.9 M_{\odot}$ merger product constructed from the 3D MHD simulation described in Sect. 5.2.2.1, and a genuine single $17.4 M_{\odot}$ star in an HRD. We chose a mass of $17.4 M_{\odot}$ for the genuine single-star model because we found that its evolutionary track in the HRD overlaps almost completely with that of the $16.9 M_{\odot}$ merger product. Since the massive MS merger product’s HRD track overlaps with a higher-mass genuine single-star track ($\Delta M_{\star} = 0.5 M_{\odot}$), we find that the merger product has a higher L_{\star}/M_{\star} -ratio compared to the genuine single star (L_{\star} and M_{\star} are the luminosity and total mass of the star, respectively). This higher L_{\star}/M_{\star} -ratio follows from the fact that the He-rich core material of the more evolved star ends up in the lower envelope of the merger product, leading to a higher mean molecular weight μ there. This can be seen from the chemical composition profiles in Fig. 5.2. Following the mass-luminosity relation for MS stars, $L_{\star} \propto M_{\star}^3 \mu^4$ (Kippenhahn et al., 2013), we see that the He enrichment compensates for the merger product’s lower mass. In addition to the similar values in luminosity and effective temperature, we see from Fig. 5.3 that throughout their MS evolution, the merger product and genuine single star also have similar radii R_{\star} and convective core radii R_{cc} when they occupy the same position in the HRD.

From the horizontal bar markers on the HRD tracks in Fig. 5.1, we see that for the same effective temperature T_{eff} and luminosity L_{\star} , the two stars are at different MS ages, that is, they have different central hydrogen mass fractions X_{c} . In earlier times, the genuine single star still has more hydrogen in its convective core than the merger product when they are at the same position in the HRD. With increasing time, this difference in X_{c} becomes smaller, reaching a minimum around the time when both stars have $X_{\text{c}} \approx 0.20$. At later times, the merger product has a higher value for X_{c} than the genuine single star for the same T_{eff} and L_{\star} .

Although it is instructive to compare the asteroseismic predictions for our models at certain values of X_{c} (as done, for example, in Wagg et al. 2024), we opted to compare models when they have similar luminosities and effective temperatures. We make this choice because we want to identify distinguishing features in the asteroseismic predictions for a merger product and genuine single star with similar surface diagnostics, which we get from observations. Therefore, in practice, we compare the models at specific X_{c} values for the merger product. At each of these points in the HRD, we compare the predictions for the merger product with those for the genuine single-star model closest in terms of L_{\star} and T_{eff} . In other words, we compare the models at the positions in the HRD marked by the grey horizontal markers in Fig. 5.1. The corresponding genuine single-star models have only slightly different values of X_{c} (at most 2.3%), which can be seen by comparing the top and bottom x -axes in Figs. 5.3 and 5.4.

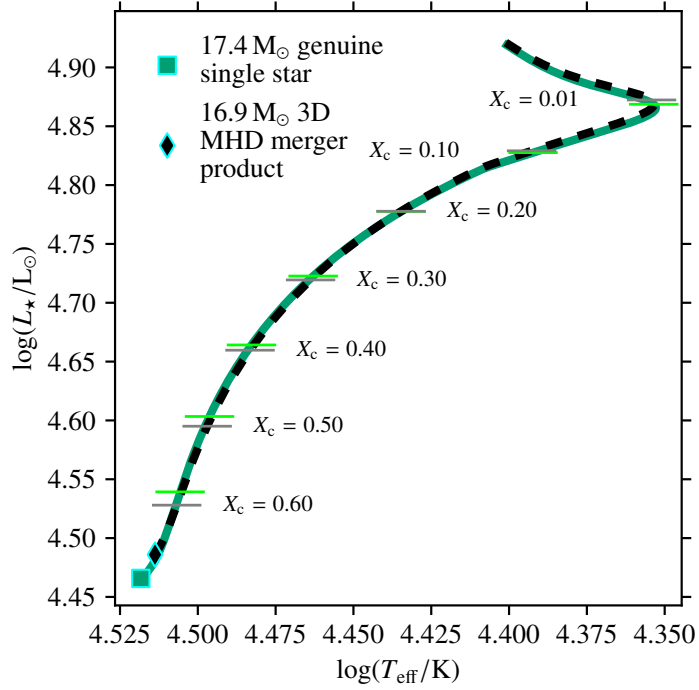


Figure 5.1: HRD with MS evolutionary tracks for the $16.9 M_{\odot}$ 3D MHD merger product (black dashed line) and the $17.4 M_{\odot}$ genuine single star (green solid line). The grey and lime-coloured horizontal markers indicate different evolutionary stages, using the central hydrogen mass fraction X_c as a proxy for the evolutionary age, for the merger product and genuine single star, respectively.

5.3.1. Asteroseismic comparison

The $16.9 M_{\odot}$ merger product and $17.4 M_{\odot}$ genuine single star find themselves in the region of the HRD associated with β Cephei (β Cep) pulsators (Aerts et al., 2010a; Aerts, 2021). Stars in this class have recently been shown to pulsate in numerous low-order p and g modes (e.g. Burssens et al., 2023), as well as in some high-order g modes (e.g. Daszyńska-Daszkiewicz et al., 2017) when observed in modern space photometry. In this section, we compare the predictions for the g and p modes in this merger product and genuine single star, with and without rotation.

5.3.1.1 Gravity modes

We start by looking at the difference between the buoyancy travel times Π_0 (Eq. 1.25) for the two objects at different points along their evolution, shown in Fig. 5.4. The buoyancy travel times span a range of roughly 20×10^3 s to 30×10^3 s (5.56–8.33 h). The absolute differences between the buoyancy travel times of the merger product and genuine single star (Fig. 5.4b) have a median value of 173 s and lie in the interval $[-349; 426]$ s. If we convert this to the asymptotic period spacing via Eq. (1.24), we find that the median values of the difference in Π_{ℓ} are 122 s and 71 s for $\ell = 1$ and $\ell = 2$, respectively. These values are considerably higher than the currently best uncertainties for observed period spacing values of B-type stars $\sigma_{\Delta P} = 50$ s (Degroote et al., 2010; Moravveji et al., 2015; Pedersen et al., 2021). At earlier evolutionary stages (higher values of X_c), the genuine single star has a longer buoyancy travel time than the merger product. Around $X_{c, \text{merger}} \approx X_{c, \text{single}} \approx 0.15$, the merger product overtakes the genuine single star in Π_0 . In summary, we see that the Π_0

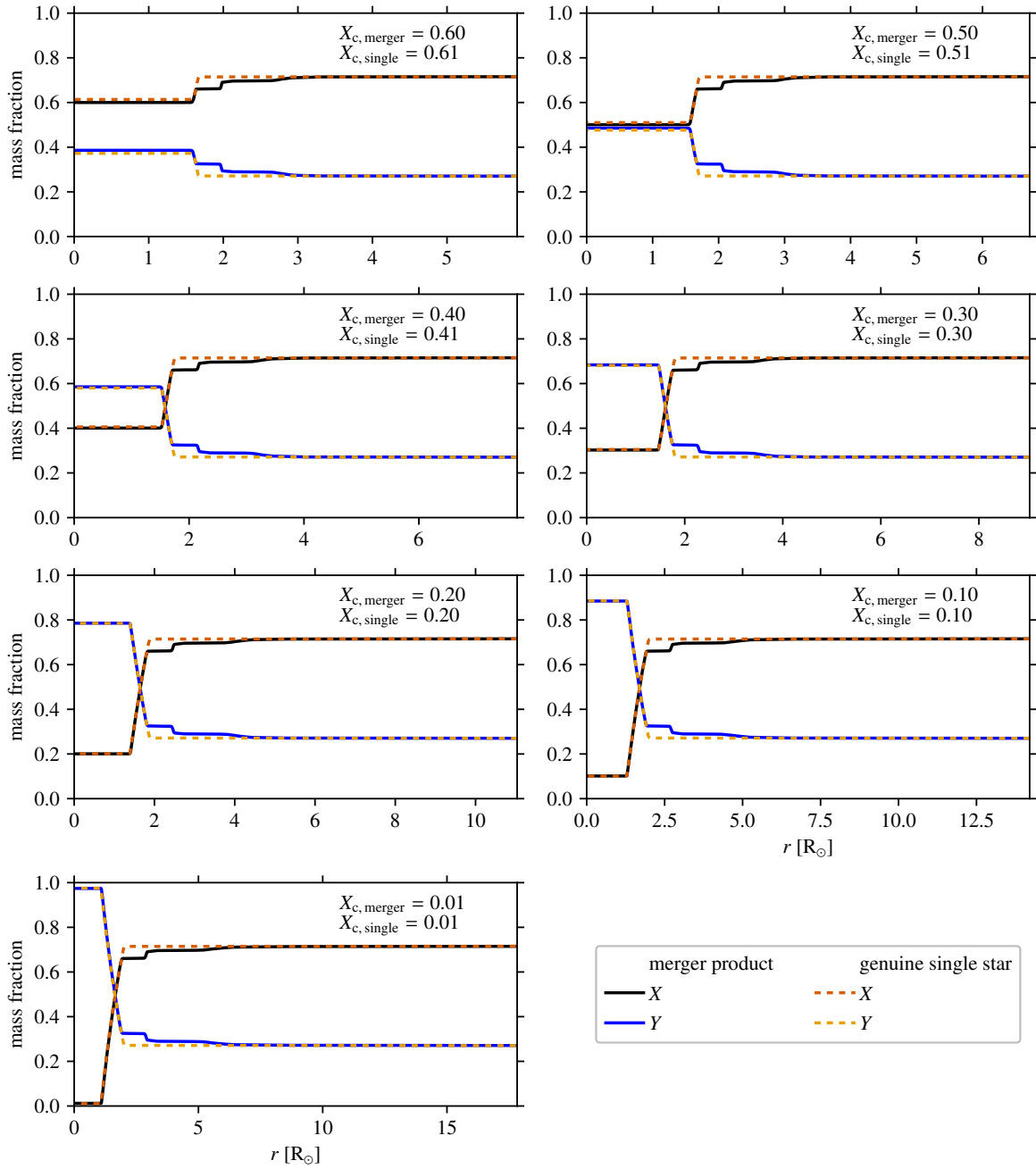


Figure 5.2: Evolution of the radial hydrogen mass fraction X and helium mass fraction Y profiles of the $16.9 M_{\odot}$ 3D MHD merger product (solid lines) and the $17.4 M_{\odot}$ genuine single star (dashed lines). Each panel is labelled with the corresponding central hydrogen mass fractions of the merger product and the genuine single star and compares the merger product and genuine single star when they have similar L_{\star} and T_{eff} (see beginning of Sect. 5.3).

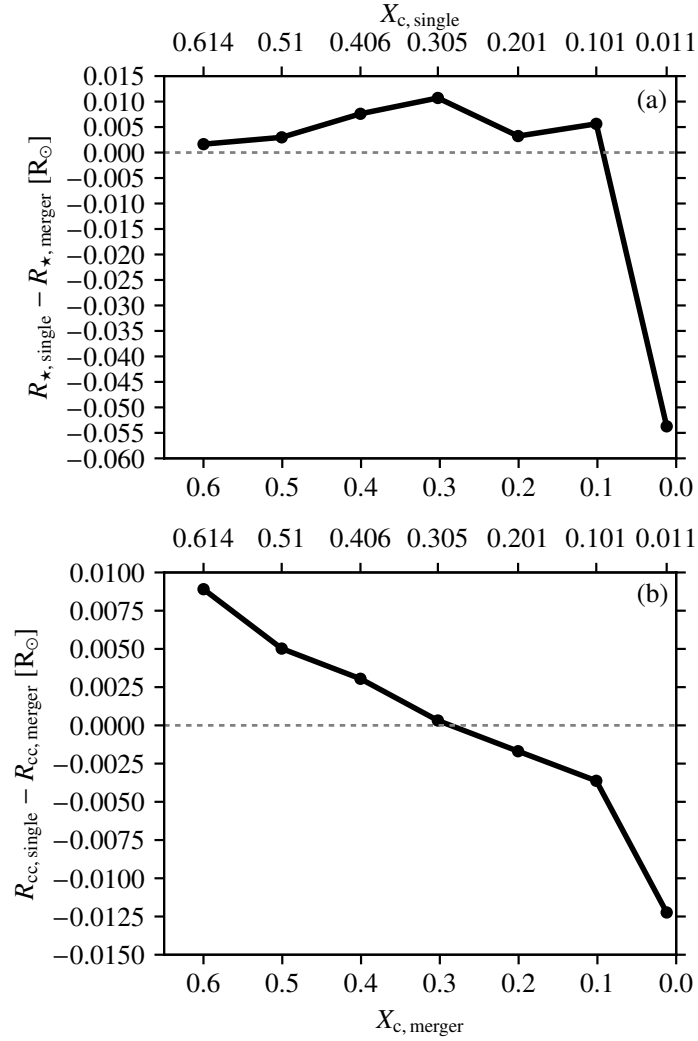


Figure 5.3: Absolute difference in stellar radius R_{\star} (panel a) and convective core radius R_{cc} (panel b) of the $16.9 M_{\odot}$ 3D MHD merger product and the $17.4 M_{\odot}$ genuine single star as a function of their respective central hydrogen mass fractions X_c . The central hydrogen mass fraction for the merger product (genuine single star), $X_{c,merger}$ ($X_{c,single}$), is shown on the bottom (top) x -axis.

values differ for the merger product and genuine single star during large parts of their MS lifetimes, and this difference follows a trend with X_c .

To explain these differences in Π_0 for these two types of stars, we compare their g-mode cavities shown in the propagation diagrams in Fig. 5.5. We identify multiple differences. First, there is the location of the inner boundary of the mode cavity r_i , which is equal to the convective core radius R_{cc} . Since we integrate \tilde{N}/r to compute Π_0 , the latter’s value is the most sensitive to that of \tilde{N} at this inner boundary. From Fig. 5.3b, we see that the absolute difference between $R_{cc,merger}$ and $R_{cc,single}$ is at most $0.0125 R_\odot$ and it follows a similar trend as $\Delta(\Pi_0)$ in Fig. 5.4b. This follows from the fact that a larger convective core leads to a smaller g-mode cavity. Second, the leftmost BV frequency peaks (‘glitch 1’ in the top left panel of Fig. 5.5), caused by the chemical gradient left behind by the receding convective core, are wider for the genuine single star at all points along the MS. If this were the only difference between the two g-mode cavities, we would expect lower Π_0 values of the genuine single star than for the merger product. Third, to the right of this BV frequency peak (glitch 1), we see that the genuine single star’s \tilde{N} is lower across multiple solar radii, and the merger product has an additional peak (‘glitch 2’) in its \tilde{N} -profile. This peak results from the transient convective core of the merger product during its thermal relaxation phase described in Sect. 5.2.2.1. The effect of $\tilde{N}_{merger} > \tilde{N}_{single}$ in this region is to lower Π_0 for the merger product compared to the one for the genuine single star. Considering all three effects together, we see that the differences in the merger product’s and genuine single star’s respective Π_0 follow the same trend as the convective core radius, but that the point at which the merger product’s Π_0 becomes larger than the one of the single star occurs later in the evolution than for the convective core radius because of differences in \tilde{N} in the near-core and envelope regions of both models.

We now turn our attention to the PSPs for $\ell = 1$ modes (those for $\ell = 2$ modes are shown in Fig. D.1 in Appendix D.1) in the absence of rotation. Figure 5.6 shows PSPs constructed using GYRE predictions (see Sect. 5.2.3) for the $16.9 M_\odot$ 3D MHD merger product and the $17.4 M_\odot$ single star at different points along their MS evolution. As expected from the asymptotic period spacing $\Pi_\ell = \Pi_0 / \sqrt{\ell(\ell + 1)}$, the mean values of the PSPs for the two models are relatively similar. At $X_{c,single} = 0.61$, we see a quasi-periodic departure of the PSP from its asymptotic behaviour ($\Delta P_n = \text{constant}$). This quasi-periodic variation is caused by the steep chemical gradient left behind by the receding convective core. These chemical gradients are deduced from the H and He profiles plotted in Fig. 5.2 and cause sharp variations in the BV frequency \tilde{N} (Eq. 1.20) shown in the propagation diagrams in Fig. 5.5. These ‘glitches’ in the BV frequency can ‘trap’ g modes as observed in stars. Mode trapping alters the mode periods as long as the local wavelength of the mode is larger than or similar to the radial extent of the glitch. From both theory (Miglio et al., 2008; Cunha et al., 2015, 2019, 2024) and observations (Moravveji et al., 2015, 2016; Michielsen et al., 2021, 2023), we know that the occurrence rate of dips in the PSP is related to the location and width of the sharp variation in \tilde{N} within the g-mode cavity. Generally, the more the convective core recedes, the higher and broader the \tilde{N} profile (see Aerts 2021) and the higher the probability of mode trapping. This is apparent from the PSPs for our models shown in Fig. 5.6. Because of the similar location of the sharp \tilde{N} -variations (glitch 1) with respect to the outer g-mode cavity in the merger product and a genuine single star, the periodicity in the PSP variations is relatively similar. However, there appears to be an additional component to

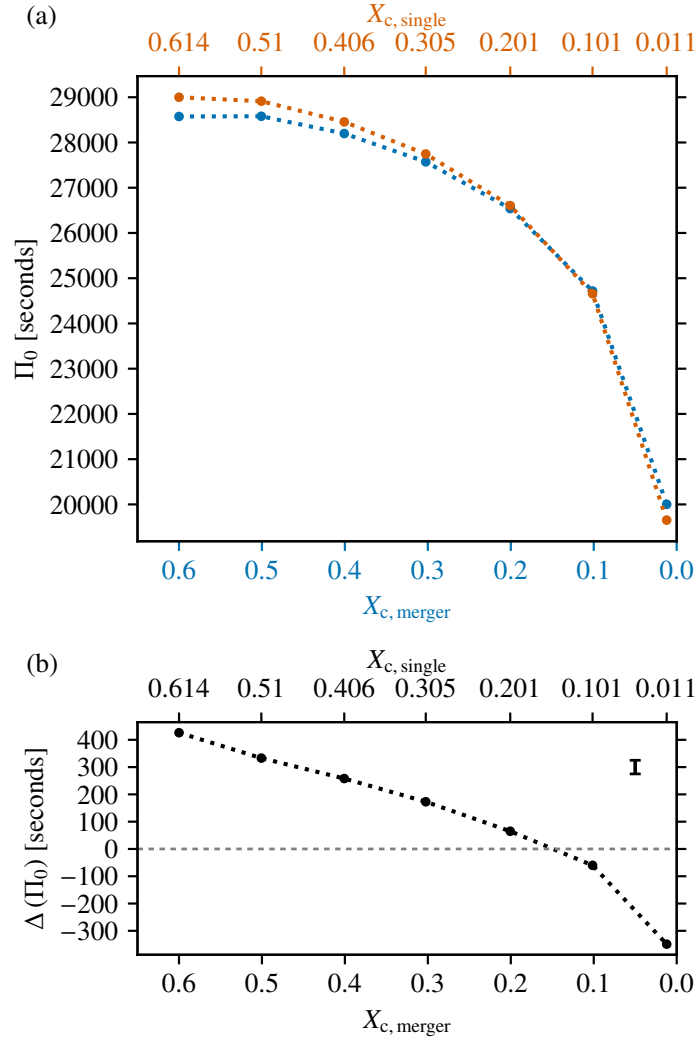


Figure 5.4: Comparison between the buoyancy travel time Π_0 of the $16.9 M_{\odot}$ 3D MHD merger product (blue line) and the $17.4 M_{\odot}$ genuine single star (red line) as a function of their respective central hydrogen mass fractions X_c (Panel a). The Panel (b) shows the absolute differences in Π_0 , $\Delta(\Pi_0) = \Pi_{0, \text{single}} - \Pi_{0, \text{merger}}$. The error bar in panel (b) shows $\sigma_{\Delta P} = 50$ s.

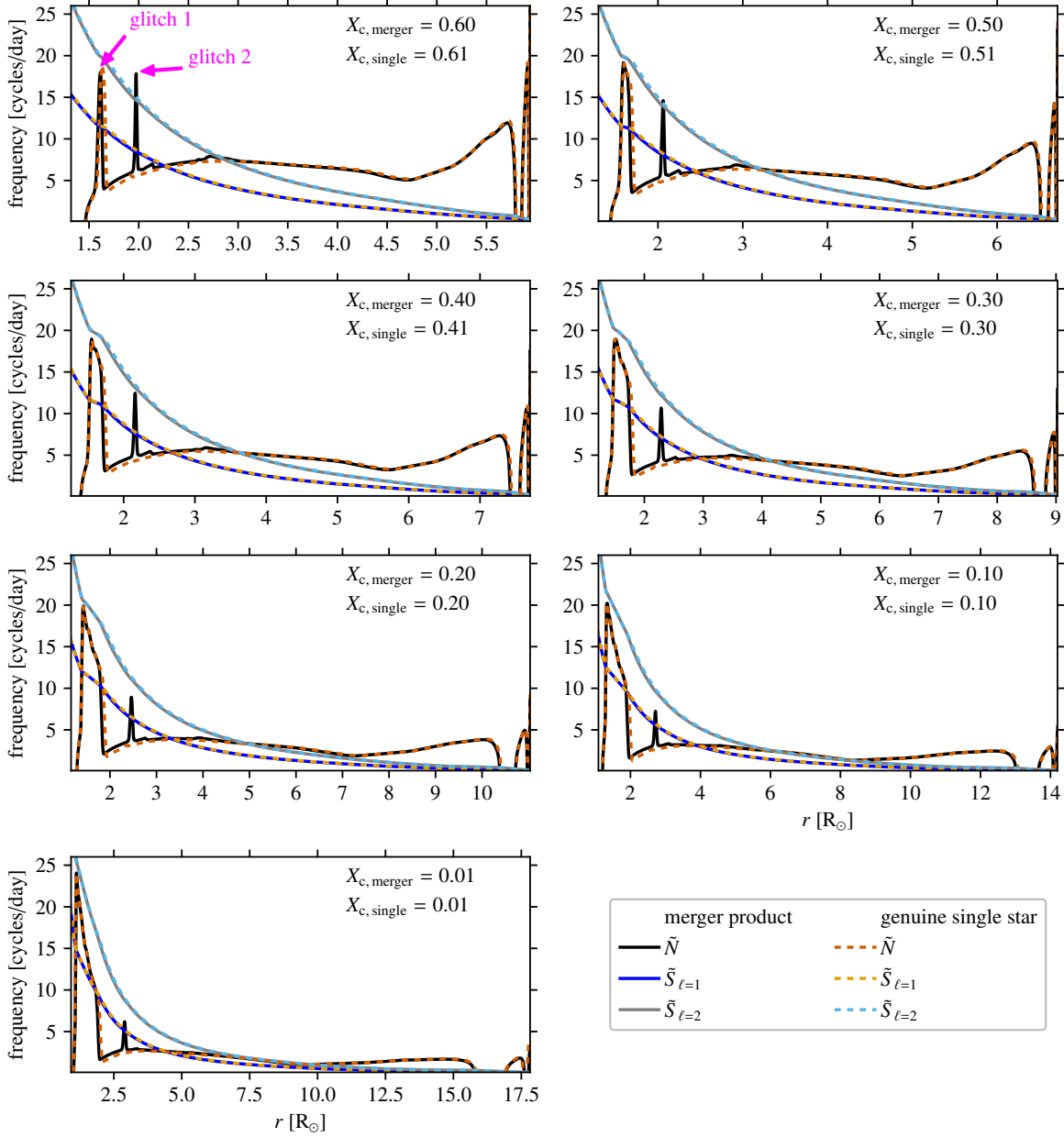


Figure 5.5: Propagation diagrams for the $16.9 M_{\odot}$ 3D MHD merger product and the $17.4 M_{\odot}$ genuine single star as a function of the radius at different evolutionary stages. Each panel compares the merger product and genuine single star when they have similar L_{\star} and T_{eff} (see beginning of Sect. 5.3). The BV frequency \tilde{N} and Lamb frequencies \tilde{S}_{ℓ} of the merger product are plotted with solid lines, those of the genuine single star with dashed lines. The convective-core region is not shown for clarity.

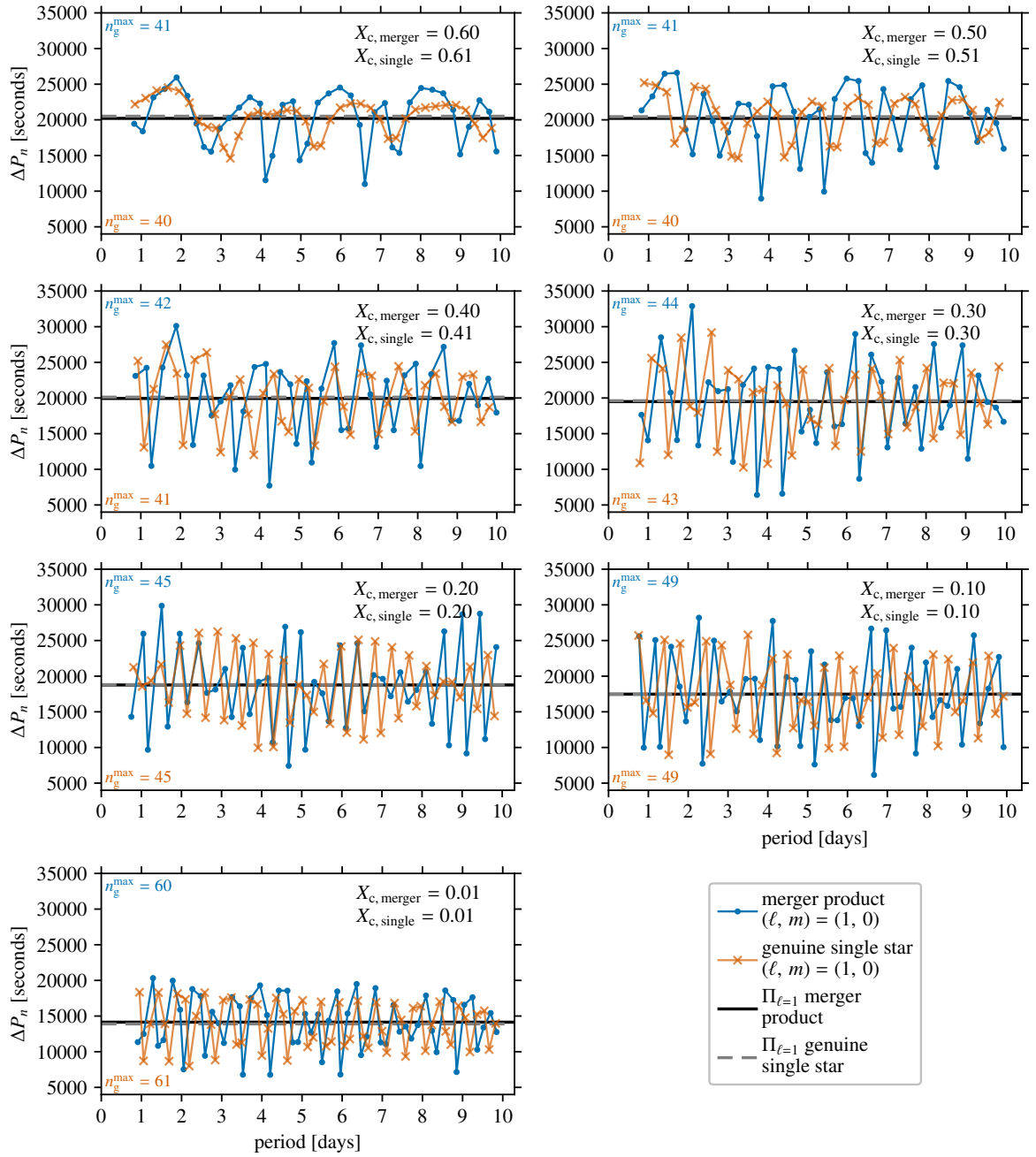


Figure 5.6: Period spacing patterns for $\ell = 1$ g modes without rotation for the $16.9 M_{\odot}$ 3D MHD merger product (blue solid lines, dot markers) and the $17.4 M_{\odot}$ genuine single star (orange solid lines, cross markers) at different evolutionary stages. Each panel compares the merger product and genuine single star when they have similar L_{\star} and T_{eff} (see beginning of Sect. 5.3). The horizontal solid black and dashed grey lines indicate the values of the asymptotic period spacing values $\Pi_{\ell=1}$ for the merger product and genuine single star, respectively. The n_g^{\max} values show the maximum radial order plotted for the merger product (blue) and genuine single star (red).

this variation, most clearly seen at $X_{c, \text{merger}} = 0.60$ in the PSPs of the merger product. The second peak in the BV frequency profiles of the merger product (glitch 2, to the right of glitch 1) causes additional variation in the PSPs. This peak is a remnant of the transient convective core described in Sect. 5.2.2.1. Such narrow glitches can trap g modes with local wavelengths comparable to or larger than the width of the glitch (Cunha et al., 2024, and references therein). For modes with a period around 10 days (these are the shortest-wavelength modes considered here), the local wavelengths are $\lambda_{\text{local}} \approx 0.03 R_{\odot}$ and $\lambda_{\text{local}} \approx 0.15 R_{\odot}$ at $X_{c, \text{merger}} = 0.60$ and $X_{c, \text{merger}} = 0.01$, respectively. The full-width-half-maxima (FWHM), which we use as a proxy for the radial extent of the Gaussian-like shape of the glitches, are $\text{FWHM}_{\text{glitch}} \approx 0.02 R_{\odot}$ and $\text{FWHM}_{\text{glitch}} \approx 0.08 R_{\odot}$ for $X_{c, \text{merger}} = 0.60$ and $X_{c, \text{merger}} = 0.01$, respectively. This shows that we expect the extra glitches in the BV frequency profiles of the merger product to affect the g modes since $\lambda_{\text{local}} \gtrsim \text{FWHM}_{\text{glitch}}$.

The amplitude of the PSP variation, that is, the departure of ΔP_n from the asymptotic value Π_{ℓ} , depends on the sharpness, height, and width of the variation in \tilde{N} (Miglio et al., 2008; Cunha et al., 2015, 2019, 2024). The \tilde{N} profiles of 26 Slowly Pulsating B-type (SPB) pulsators observed by *Kepler* and modelled in Pedersen et al. (2021) show a large variety in their sharpness, height, and width. Here we see that the PSP variations amplitudes are similar for the two models, albeit slightly higher for the merger product. The glitches in the BV frequency profiles of the genuine single star are sharper than those for the merger product, while the extra glitch in the BV frequency profile of the merger product introduces additional quasi-periodic variability with a different occurrence rate. Despite the similar magnitude of the amplitudes, their differences are typically larger than the observational uncertainties measured for ΔP_n of B-type stars, $\sigma_{\Delta P}$.

We now repeat the comparison above in the presence of rotation. As argued in Sects. 5.2.1 and 5.2.3, we include the effects of rotation (more specifically, the Coriolis force) at the level of the pulsation equations. Figure 5.7 shows the PSPs for prograde ($m > 0$) and retrograde ($m < 0$) sectoral ($\ell = |m|$) g modes predicted for the merger product and genuine single star at $X_{c, \text{merger}} = 0.50$ and $X_{c, \text{single}} = 0.51$, respectively. We consider rotation rates of $\Omega/\Omega_c = 0.10\text{--}0.60$, with $\Omega_c = \sqrt{GM_{\star}/R_{\text{eq}}^3} \approx \sqrt{8GM_{\star}/27R_{\star}^3}$ the Roche critical angular rotation frequency (Maeder, 2009), G the gravitational constant, and R_{eq} the stellar radius at the equator of a rotationally deformed star. As expected from Bouabid et al. (2013), the period spacings ΔP_n between the prograde modes become smaller with longer oscillation periods and with higher rotation rates, resulting in a negative slope of the PSP, while the retrograde PSPs have positive slopes, in agreement with observations of SPB pulsators (Pápics et al., 2014, 2015, 2017; Szewczuk and Daszyńska-Daszkiewicz, 2018; Szewczuk et al., 2021; Pedersen et al., 2021). Overall, we see that the PSPs of the merger product and genuine single star have similar morphologies, that is, they follow the same trends. For prograde modes, the largest differences between the PSPs of the two models are found at shorter periods, whereas the PSPs become virtually indistinguishable at longer periods. The main differences in PSP variability are caused by the slightly different positions of the glitches. Whereas the average value ΔP_n for the merger product is lower than that for the genuine single star at $X_{c, \text{merger}} = 0.50$, the opposite is true for prograde modes with longer periods when we take into account the effects of rotation. This is true for all rotation rates considered here. This can be seen in Fig. 5.8, where we show the estimated differences

the larger-period end⁵ of the prograde-mode PSPs by fitting a quadratic function. We use a fit through the PSPs because it is not possible to do a one-to-one comparison between the modes of these models. Comparing these estimated differences with $\sigma_{\Delta P}$, we see that even when the PSPs are seemingly indistinguishable, the differences ΔP_n could technically be observed for most prograde dipole ($\ell = 1$) modes and some prograde quadrupole ($\ell = 2$) in stars with $\Omega/\Omega_c \leq 0.20$.

The PSPs for retrograde modes become ‘stretched’ towards longer periods, accentuating the differences in PSP variability between the merger product and genuine single star even more. Lastly, we note the presence of relatively deep dips in the period spacing patterns of both the merger product and genuine single star for different mode morphologies and rotation rates. We do not find such deep dips in the non-rotating case for $\ell = 1$ modes in the period range shown in Fig. 5.6, but they are present at longer periods (higher radial order n_g) and in the $\ell = 2$ modes (see Fig. D.1). Closer inspection shows that these deep dips are caused by the coupling between g modes in the main inner g-mode cavity and those in the subsurface g-mode cavity. This is reminiscent of the g-g-mode coupling described in Unno et al. (1989) and Henneco et al. (2024a).

5.3.1.2 Low-order pressure modes

Figure 5.9 shows the frequencies of the low-radial order $\ell = 1$ and $\ell = 2$ p modes with radial orders $n_p \leq 4$ and without rotation. Pressure modes with higher radial orders are not observed in β Cep stars (Fritzewski et al., 2024b). We compare the predicted modes for the $16.9 M_\odot$ 3D MHD merger product and the $17.4 M_\odot$ genuine single star at different stages during their MS evolution⁶. Because of their similar p-mode cavities, the p modes in the merger product and genuine single star span a similar frequency range. It is also clear from Fig. 5.9 and Fig. 5.10 that the p-mode frequencies of the genuine single star are higher by at most 0.3 cycles per day ($3.5 \mu\text{Hz}$). Furthermore, this frequency difference increases with radial order n_p and decreases with MS age (Fig. 5.10). Even the smallest frequency difference, which we predict for the fundamental ($n_p = 0$) $\ell = 1$ mode at $X_c = 0.30$, has a relative value of $\sim 10\%$. This is 1000 times larger than the observed relative p-mode frequency uncertainty of $\sim 0.01\%$ reported in Aerts et al. (2019) and the absolute p-mode frequency uncertainty of $\sigma_v^p \simeq 0.01 \mu\text{Hz}$ found for the prototypical β Cep star HD 129929 by Aerts et al. (2003, 2004). Overall, the merger product’s p modes are more closely spaced than the genuine single star’s.

The difference in p-mode frequencies can be explained by the merger product’s lower mean density in its envelope, as seen from Fig. D.2 in Appendix D.2. The decrease of the difference in p-mode frequencies between the two models with MS age can be attributed to the fact that the merger product’s and genuine single star’s mean envelope density become similar. Since p modes with higher radial order have more nodes in the region of the star when the merger product and genuine single star differ significantly, they are more sensitive to these differences than those with fewer radial nodes.

Analogue to the g modes, we consider the effect of rotation on the p modes and its

⁵We only consider modes with periods P_n satisfying $(P_n - P_n^{\min}) / (P_n^{\max} - P_n^{\min}) > 0.75$, with P_n^{\min} and P_n^{\max} the minimum and maximum period shown in Fig. 5.7.

⁶We find no pure p modes, i.e. modes with $n_g = 0$ for the models at $X_{c,\text{merger}} = 0.01$ and $X_{c,\text{merger}} = 0.10$ because the structures of the g- and p-mode cavities start to overlap more in frequency, leading to mode mixing (Unno et al., 1989), hence, we leave these evolutionary stages out.

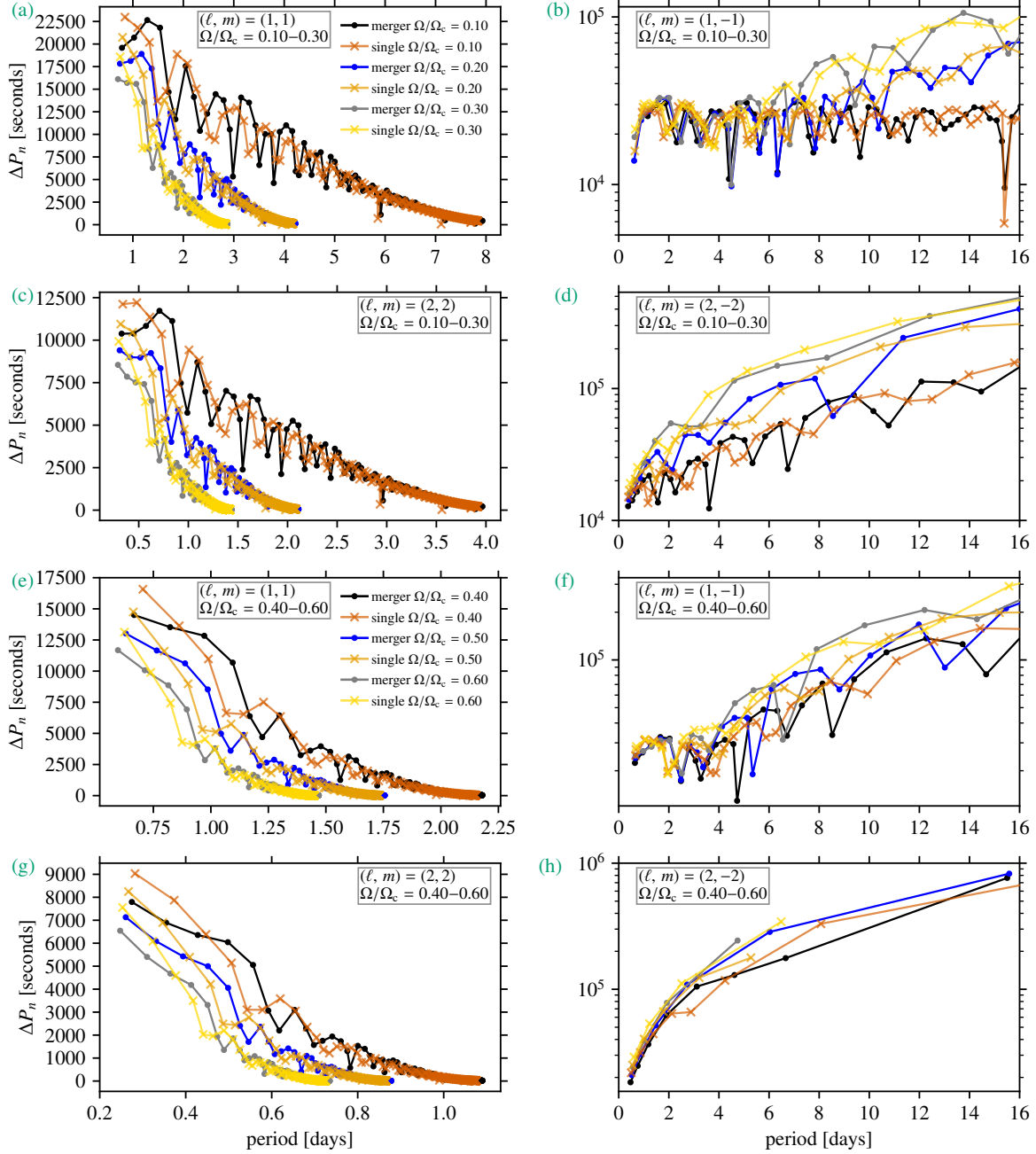


Figure 5.7: Period spacing patterns for $(\ell, m) = (1, \pm 1)$ and $(\ell, m) = (2, \pm 2)$ g modes with rotation rates of $\Omega/\Omega_c = 0.10-0.30$ (Panels a–d) and $\Omega/\Omega_c = 0.40-0.60$ (Panels e–h) for the $16.9 M_\odot$ 3D MHD merger product and the $17.4 M_\odot$ genuine single star at $X_{c,\text{merger}} = 0.50$ and $X_{c,\text{single}} = 0.51$, respectively. The black, blue, and grey lines with dot markers correspond to the merger product’s PSPs, while the red, orange, and gold lines with cross markers correspond to the PSPs of the genuine single star. The PSPs are shown in the inertial (observer’s) frame.

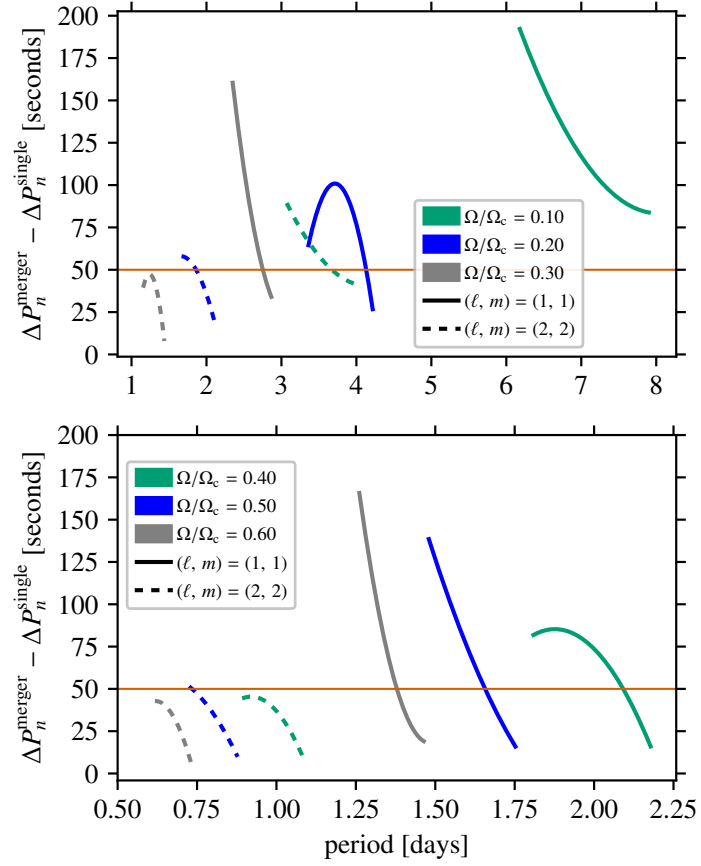


Figure 5.8: Differences between the quadratic function fits of the PSPs for prograde modes shown in Fig. 5.7 for $\Omega/\Omega_c = 0.10$ – 0.30 (top) and $\Omega/\Omega_c = 0.40$ – 0.60 (bottom). The solid and dashed lines show the differences for the $(\ell, m) = (1, 1)$ and $(\ell, m) = (2, 2)$ modes, respectively. The horizontal red line shows the average value of $\sigma_{\Delta P}$ from observations of SPB pulsators.

influence on the frequency difference found in the absence of rotation. We treat the rotation perturbatively, which is a good approximation for p modes (Aerts et al., 2019) and show the results of the inclusion of rotation for the models at $X_{c, \text{merger}} = 0.50$ in Figs. D.3 and D.4 in Appendix D.3. Figure D.3 shows the mode frequencies and radial orders of $(\ell, m) = (1, \pm 1)$, $(2, \pm 1)$, and $(2, \pm 2)$ p modes predicted for the $16.9 M_{\odot}$ 3D MHD merger product and $17.4 M_{\odot}$ with $\Omega/\Omega_c = 0.50$. As expected, prograde ($m > 0$) p modes are shifted to higher frequencies, while retrograde ($m < 0$) p modes are shifted to lower frequencies in the inertial frame. The zonal modes ($m = 0$) are unaffected by rotation in the first-order Ledoux perturbative approach. Hence, we do not show them here again. Qualitatively, the frequency differences between the merger product and genuine single star look similar to those in the non-rotating case (Fig. 5.9). Quantitatively, we see from Fig. D.4 that the differences between the p-mode frequencies of the same radial order are of the same order of magnitude as in the non-rotating case. Varying the rotation rate Ω/Ω_c does not affect the frequency differences between the merger product and genuine single star in a significant way. The effect of rotation is strongest for sectoral modes ($\ell = |m|$), where the differences increase with the rotation rate for prograde modes and decrease for retrograde modes.

5.3.2. Comparison with and between 1D merger methods

We now investigate if and how the predictions made in Sect. 5.3.1 differ when we use 1D merger prescriptions. As mentioned in Sect. 5.1, we consider three commonly used 1D merger prescriptions: entropy sorting, entropic variable sorting with shock heating (PyMMAMS), and fast accretion (see Sect. 5.2.2). The HRD in Fig. 5.11 shows evolutionary tracks of the merger products acquired with all four methods (the 3D MHD simulation and the three 1D methods). We see that the tracks do not coincide in the HRD, which results in each merger product approximately overlapping with a genuine single star of a different mass. As detailed at the beginning of Sect. 5.3, The track for the entropy-sorted model comes closest to that of the 3D MHD model; its corresponding genuine single star has a mass of $17.15 M_{\odot}$. Using the entropy sorting method, we under-predict Π_0 by at most 450 s in comparison to the 3D MHD model. The error one would make by using entropy sorting instead of the 3D MHD model would thus be around $9 \times \sigma_{\Delta P}$. In other words, the error we make by using entropy sorting is of the same order as the difference in Π_0 between the 3D MHD merger product model and its corresponding genuine single star (see Sect. 5.3.1.1). With entropy sorting, we under-predict this Π_0 difference between the merger product and its corresponding genuine single star compared to the 3D MHD merger product (Fig. 5.12b). This difference has a median value of 213 s and lies in the interval $[-36; 402]$ s.

The HRD tracks of the PyMMAMS and fast accretion merger products lie below that of the 3D merger product, corresponding to genuine single-star models with masses of $17.0 M_{\odot}$ and $16.9 M_{\odot}$, respectively (Fig. 5.11). With both methods, we under-predict Π_0 compared to the 3D MHD merger product by at least 657 s and 257 s, and at most 850 s and 590 s for the PyMMAMS and fast-accretion merger product, respectively. Both offsets are significantly larger than $\sigma_{\Delta P}$. With the PyMMAMS method, we over-predict the difference in Π_0 compared to its corresponding genuine single star. The median value of this difference is 420 s and it lies in the interval $[246; 583]$ s. With the fast accretion method, we under-predict the difference in Π_0 between the merger product and the genuine single star. This absolute difference has a median value of -87 s and lies in the interval $[-726; 61]$ s. The Π_0 difference between all merger products and their genuine single-star counterparts increases abruptly in absolute value at $X_{c, \text{merger}} = 0.01$. We attribute this to the fact that there is a noticeable difference

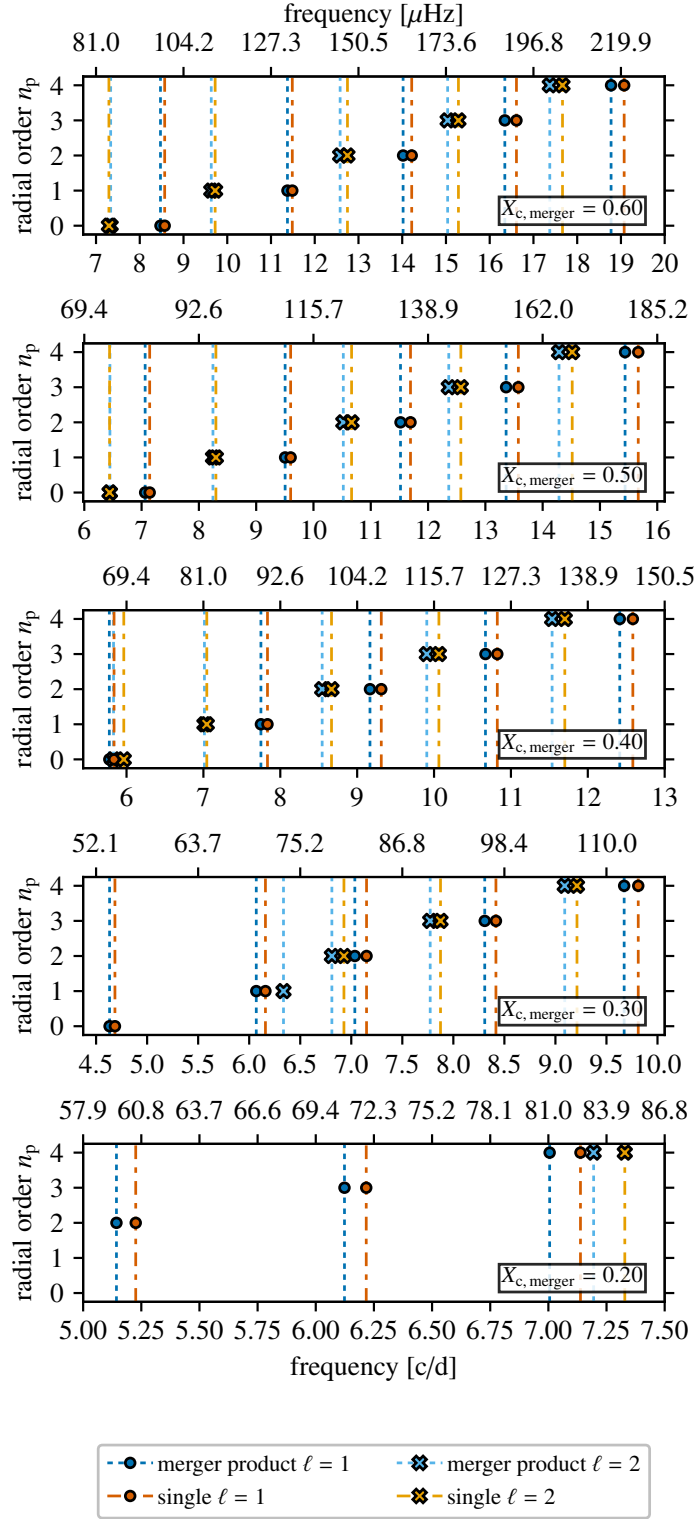


Figure 5.9: Frequencies and radial orders n_p of $\ell = 1$ and $\ell = 2$ p modes with $n_p \leq 4$ for the 16.9 M_{\odot} 3D MHD merger product (blue and light-blue markers) and the 17.4 M_{\odot} genuine single star (red and orange markers) at different evolutionary stages, in the absence of rotation. The models at $X_c = 0.01$ and $X_c = 0.10$ are absent because of the lack of pure p modes at these evolutionary stages. The dot and cross markers show the value of the radial order n_p for the $\ell = 1$ and $\ell = 2$ modes, respectively. The dotted and dash-dotted lines are drawn to accentuate the frequency differences and improve the legibility of the frequency values.

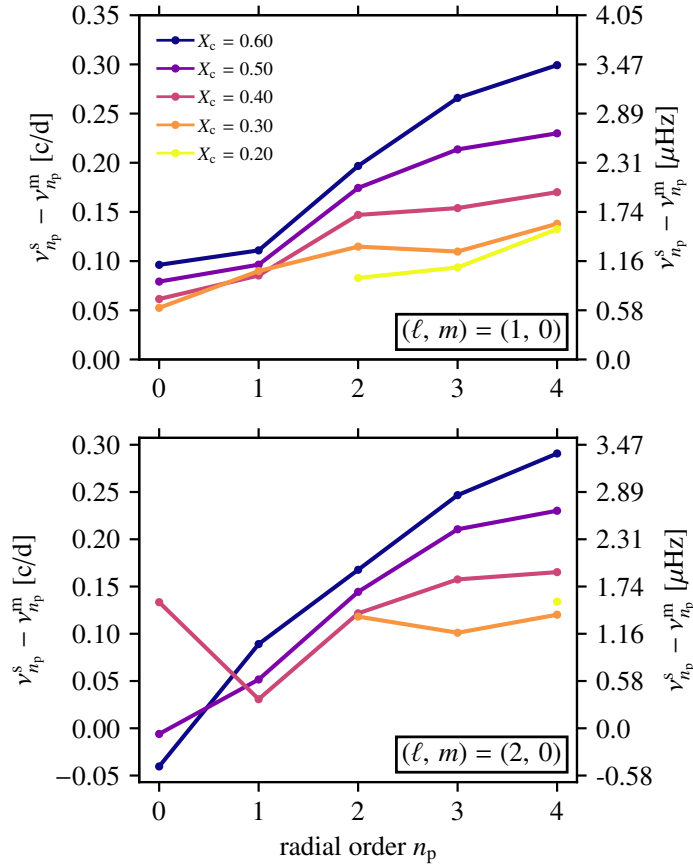


Figure 5.10: Absolute differences between the $17.4 M_{\odot}$ genuine single star’s p-mode frequencies $\nu_{n_p}^s$ and the $16.9 M_{\odot}$ 3D MHD merger product’s p-mode frequencies $\nu_{n_p}^m$ per radial order n_p , in the absence of rotation. The $(\ell, m) = (1, 0)$ and $(\ell, m) = (2, 0)$ modes are shown in the upper and lower panel, respectively. The lines are colour-coded according to the merger product’s central hydrogen fraction X_c .

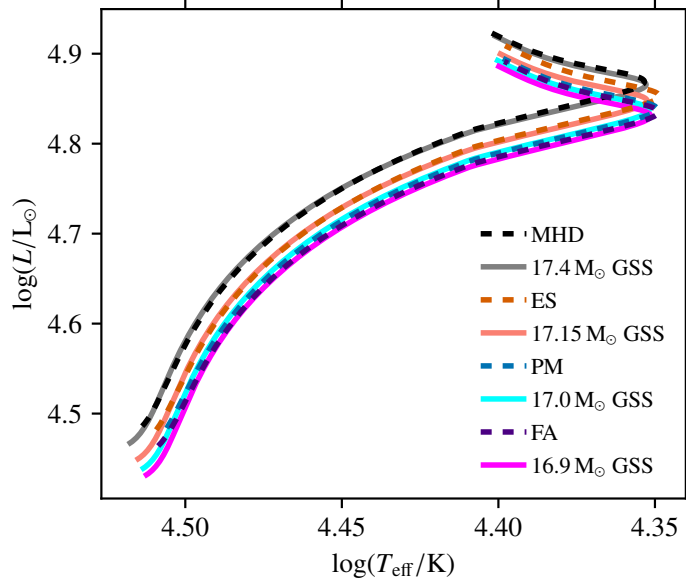


Figure 5.11: HRD with the evolutionary tracks of the $16.9 M_{\odot}$ merger product computed with the 3D MHD simulation (MHD, black dashed line), entropy sorting (ES, red dashed line), PyMMAMS (PM, blue dashed line), and fast accretion (FA, indigo dashed line). The corresponding $17.4 M_{\odot}$, $17.15 M_{\odot}$, $17.0 M_{\odot}$, and $16.9 M_{\odot}$ genuine single stars evolutionary tracks are drawn with grey, orange, cyan, and magenta solid lines, respectively.

between the HRD tracks around the Henyey hook (the point where $\log T_{\text{eff}}$ starts increasing; see Fig. 5.11). The overall differences in the Π_0 values and differences in Π_0 between the merger products obtained through 1D methods and their corresponding genuine single stars can be explained by the differences in the merger products’ BV profiles compared to the 3D MHD merger product. We highlight these differences in the following sections.

5.3.2.1 Entropy-sorted merger product

From Fig. D.5 (Appendix D.4), we see that the near-core region of the entropy-sorted merger product model is enriched in He, yet to a lesser radial extent than what we found in the model for the 3D MHD merger product. Contrary to the 3D MHD merger product, the entropy-sorting method does not lead to the He-rich core of the primary star ending up in a shell around the secondary’s core. The He enrichment stems from transient convective zones appearing around the core-envelope boundary during the thermal relaxation phase, mixing He-rich core material into the near-core region. Whereas the 3D MHD model has an extended transient convective core during thermal relaxation, the entropy-sorted model has smaller convective zones appearing at different radial coordinates and times. This leads to a staircase pattern in the chemical composition profiles and multiple Gaussian-like glitches in the BV frequency profile, as can be seen in Fig. D.8.

Looking at the predicted PSPs for the entropy-sorted merger model and its $17.15 M_{\odot}$ genuine single-star counterpart in Fig. 5.13, we see a similar trend in the asymptotic period spacings Π_{ℓ} as in the case of the 3D MHD merger product. The values of Π_{ℓ} for the merger product and genuine single star differ by more than $\sigma_{\Delta P}$, yet these differences are, in general, somewhat higher (except at $X_{c, \text{merger}} = 0.60$) than what we predict for the 3D MHD merger product. The variability in the PSPs of the entropy-sorted model is seemingly more chaotic than that for the 3D MHD merger product because the modes are affected

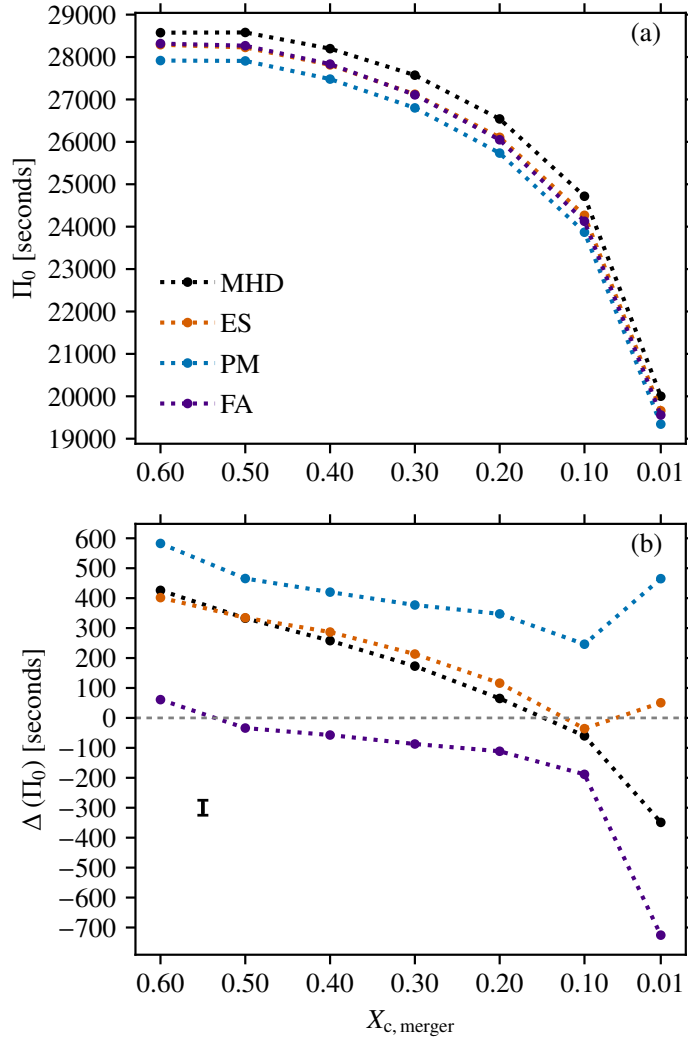


Figure 5.12: Comparison between the buoyancy travel time Π_0 for the $16.9 M_{\odot}$ 3D MHD (MHD, black line), entropy-sorted (ES, red line), PyMAMMS (PM, blue line), and fast accretion (FA, indigo line) merger products (Panel a), and the absolute differences $\Delta(\Pi_0) = \Pi_{0, \text{single}} - \Pi_{0, \text{merger}}$ with their respective genuine single star models (Panel b). The error bar in Panel (b) shows the $\sigma_{\Delta P}$.

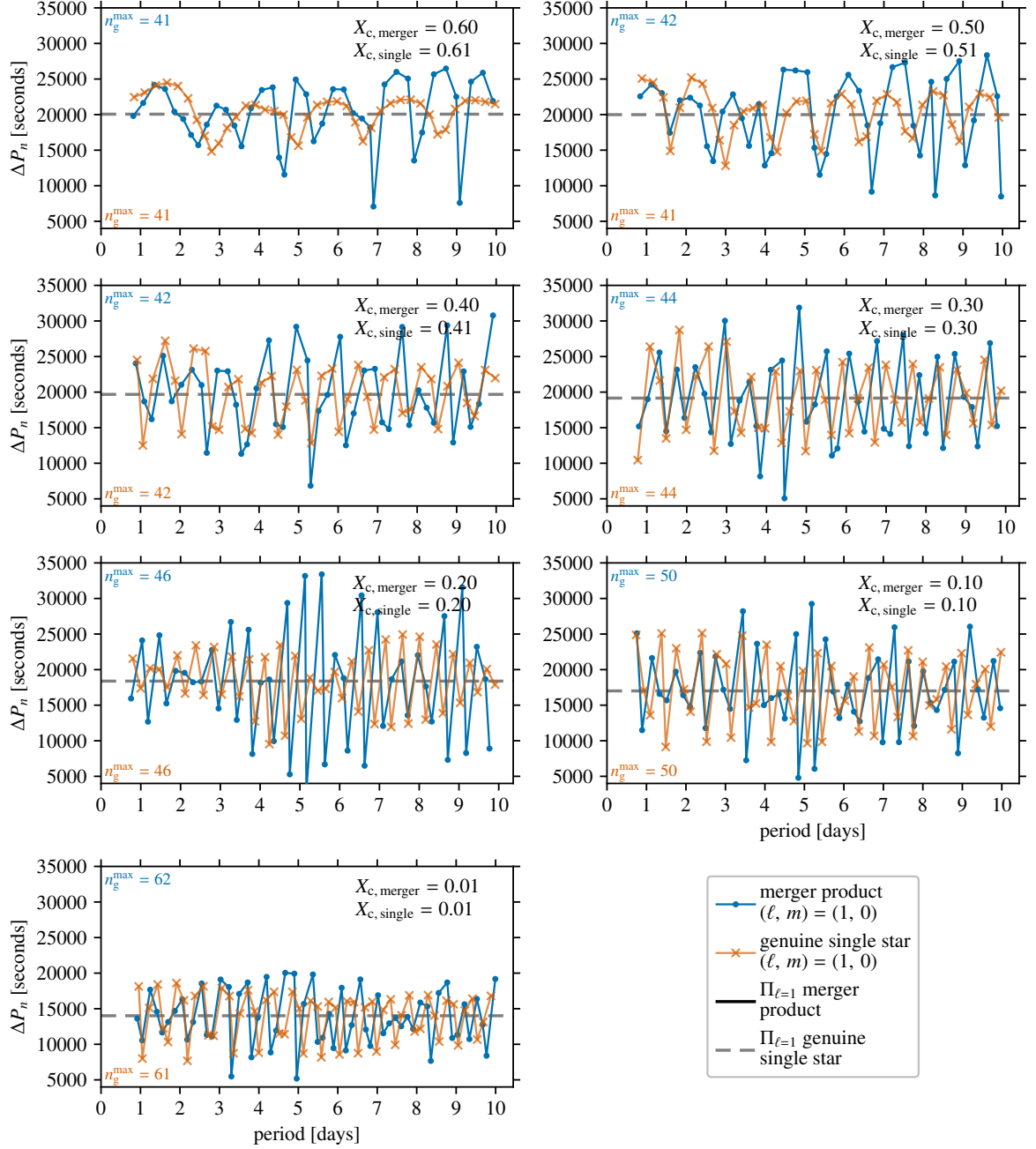


Figure 5.13: Same as Fig. 5.6, now for the 16.9 M_\odot entropy sorted merger product (blue solid lines, dot markers) and the 17.15 M_\odot genuine single star (orange solid lines, cross markers).

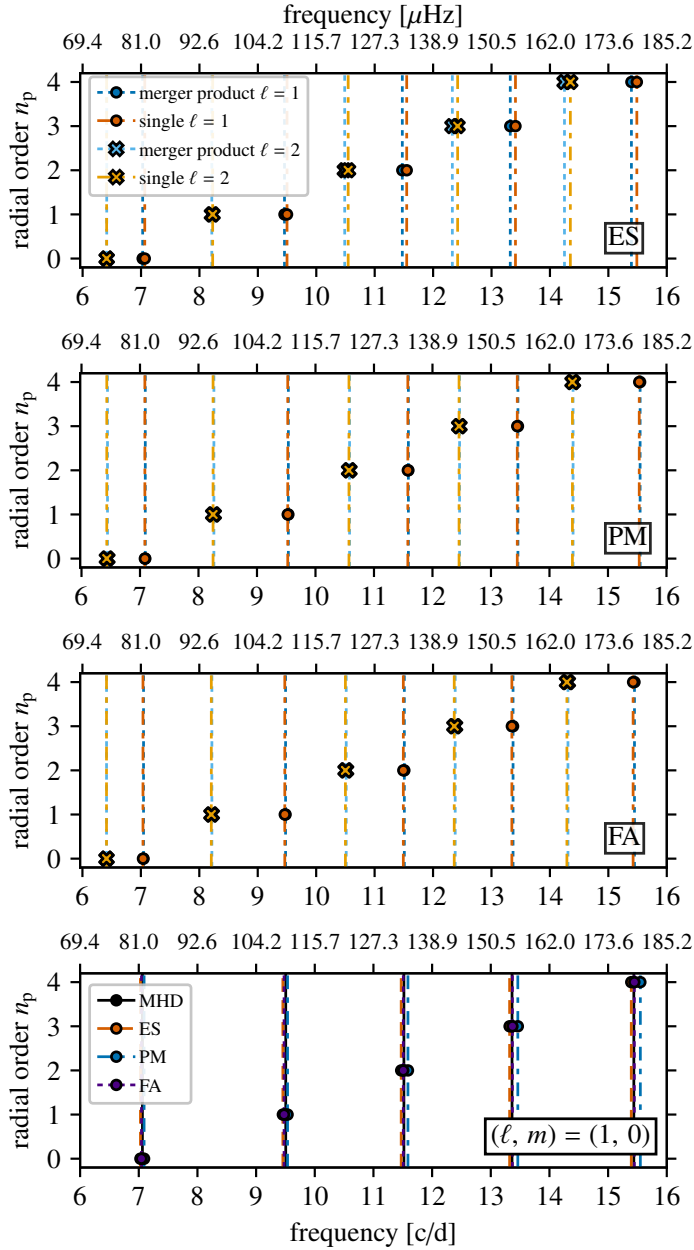


Figure 5.14: Mode frequencies and radial orders n_p for $(\ell, m) = (1, 0)$ and $(\ell, m) = (2, 0)$ p modes in the absence of rotation at $X_{c, \text{merger}} = 0.50$ for the entropy-sorted (ES), PyMMAMS (PM), and fast accretion (FA) merger product models and their corresponding genuine single-star models. In the top three panels, the colour, line, and marker conventions are the same as in Fig. 5.9. The bottom panel shows the $(\ell, m) = (1, 0)$ p mode frequencies for the 3D MHD, entropy-sorted, PyMMAMS, and fast accretion models together.

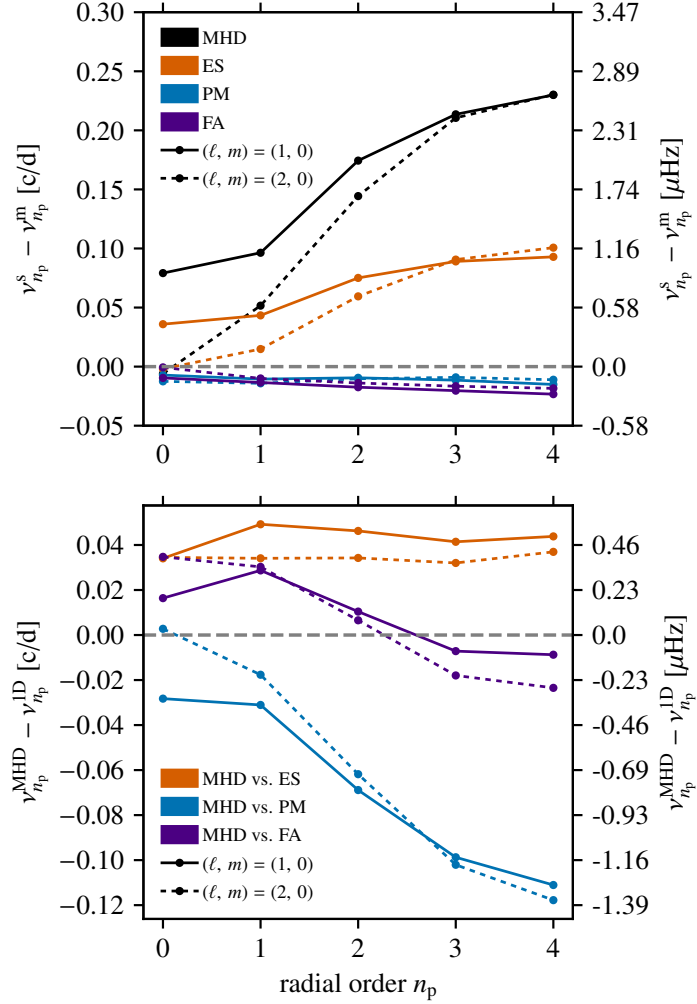


Figure 5.15: Absolute differences between the $17.4 M_{\odot}$, $17.15 M_{\odot}$, $17.0 M_{\odot}$, and $16.9 M_{\odot}$ genuine single star’s p mode frequency $\nu_{n_p}^s$ and the $16.9 M_{\odot}$ 3D MHD (MHD), entropy-sorted (ES), PyMMAMS (PM), and fast-accretion (FA) merger product’s frequency $\nu_{n_p}^m$ per radial order n_p , in the absence of rotation (top panel). The bottom panel shows the difference in p-mode frequencies per radial order for p modes computed with the 3D MHD merger model as input in GYRE and those computed with the respective 1D models used as input.

by multiple Gaussian-like glitches. The amplitude of the variability is also higher for the entropy-sorted model.

From Figs. 5.14 and 5.15, we see that the predicted p modes for the entropy-sorted merger product model behave qualitatively similarly to those predicted for the 3D MHD model. However, we under-predict the differences in $\ell = 1$ and $\ell = 2$ p-mode frequencies between the merger product and genuine single star by up to 0.14 cycles/day ($1.62 \mu\text{Hz}$) compared to the 3D MHD model, which is more than two orders of magnitude larger than $\sigma_v^p \approx 0.01 \mu\text{Hz}$ (Aerts et al., 2003, 2004). Furthermore, the frequency error we make by using entropy sorting instead of the 3D MHD model, shown in the bottom panel of Fig. 5.10, is on the order of 0.03–0.05 cycles/day (0.35 – $0.58 \mu\text{Hz}$) and is also significantly larger than σ_v^p . We attribute these frequency shifts to the different chemical and density structures (Figs. D.5 and D.8) the two merger product models have in their p-mode cavities (see Sect. 5.3.1.2).

5.3.2.2 PyMMAMS merger product

Thanks to the addition of shock heating in the PyMMAMS prescription, it performs better in reproducing the overall merger product structure expected from the 3D MHD simulation. Contrary to the entropy sorted model, the PyMMAMS prescription results in the secondary’s core sinking to the centre of the merger product and the primary’s core forming a shell around it (see Fig. D.6). However, as can be seen by comparing the chemical composition profiles for the 3D MHD and PyMMAMS merger products (Figs. 5.2 and D.6), the He-enrichment of the merger product’s envelope is limited to the near-core region (up to $r \approx 1.8 R_\odot$ at $X_c = 0.60$) in the PyMMAMS model, whereas the enrichment extends further out to $r \approx 3.0 R_\odot$ in the 3D MHD model. A second difference between the 3D MHD, entropy-sorted, and PyMMAMS models is the lack of an extended transient convective core during the merger product’s thermal relaxation phase before settling back on the MS in the latter model. The Gaussian-like glitch, present in the 3D MHD and entropy-sorted model (albeit at different locations), is missing in the PyMMAMS model. As a result, the BV frequency profiles for this merger product and its corresponding $17.0 M_\odot$ genuine single star-model look almost identical (Fig. D.9). Only the radial extent of the BV frequency peak of the merger product is larger than in the genuine single-star model because of the He-enrichment in the near-core region. The lack of a Gaussian-like glitch in the BV frequency profile of the PyMMAMS model causes there to be no additional variability in the merger model’s PSPs (Fig. 5.16). The two PSPs have roughly the same quasi-periodic behaviour, albeit with a relatively small phase shift likely caused by the more extended BV frequency peak of the PyMMAMS merger product. However, the phase shift and difference in ΔP_n are still larger than the currently best uncertainty of g-mode periods $\sigma_p^g \approx 2.56 \times 10^{-4}$ days (Moravveji et al., 2015) and $\sigma_{\Delta P}$, respectively.

Because of the virtually identical chemical composition profiles and p-mode cavities (Figs. D.6 and D.9), we find that the p-mode frequency absolute differences between the PyMMAMS merger model and its corresponding genuine single star are negative and ≤ 0.02 cycles/day ($\leq 0.23 \mu\text{Hz}$), as can be seen from the top panel of Fig. 5.10. This is an order of magnitude larger than σ_v^p . The p-mode frequency error compared to the 3D MHD model (bottom panel of Fig. 5.10) is on the order of 0.1 cycles/day ($1.16 \mu\text{Hz}$), several orders of magnitude larger than σ_v^p .

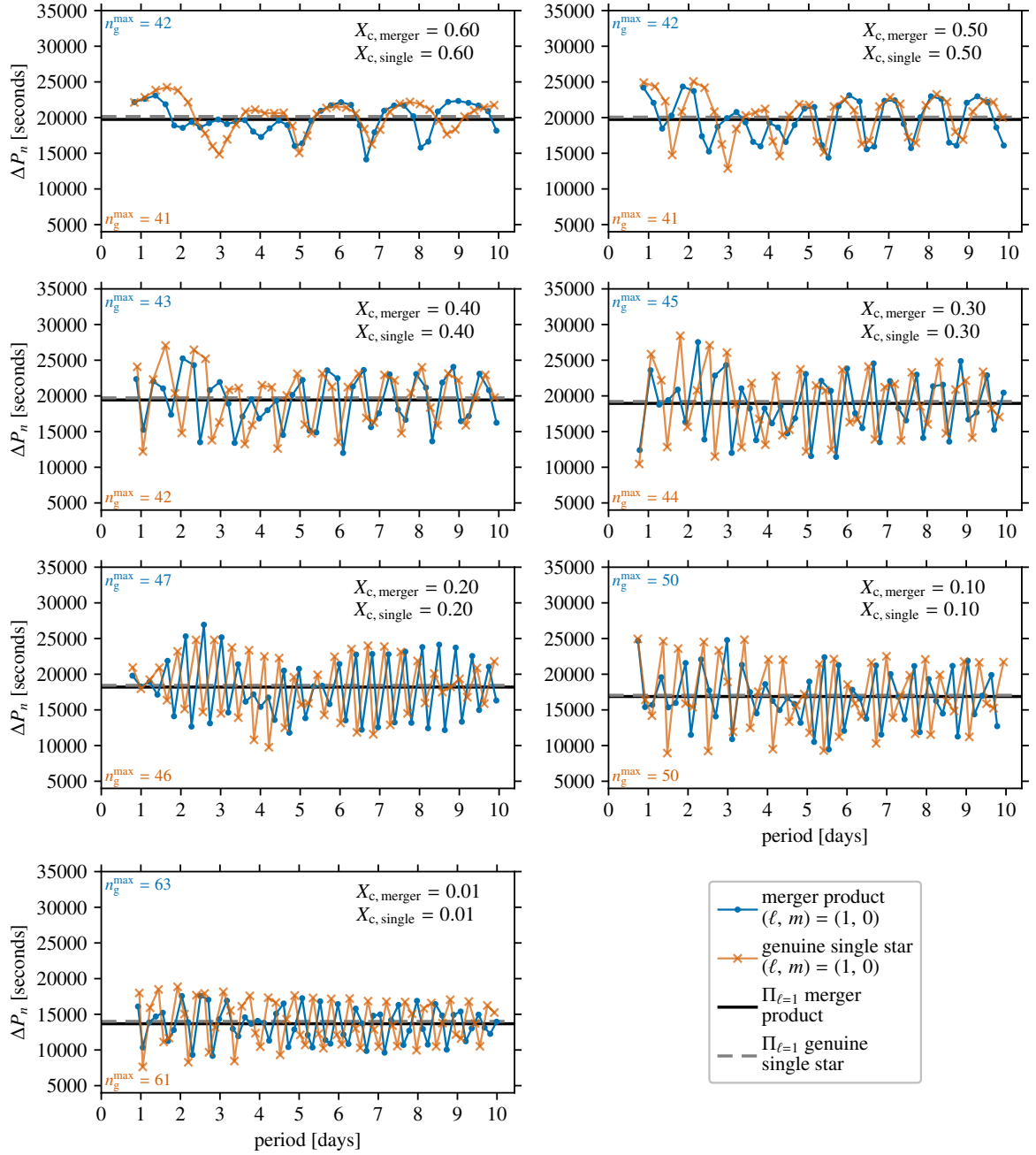


Figure 5.16: Same as Fig. 5.6, now for the $16.9 M_{\odot}$ PyMMAMS merger product (blue solid lines, dot markers) and the $17.0 M_{\odot}$ genuine single star (orange solid lines, cross markers).

5.3.2.3 Fast accretion merger product

Although the fast accretion method has proven to be sufficient in reproducing low-mass (Rui and Fuller, 2021) and massive (Henneco et al., 2024a) post-MS merger products, it does not perform well for MS merger products. For massive post-MS merger products, the sub-thermal-timescale accretion onto a blue Hertzsprung gap star emulating the merger leads to the formation of long-lived blue supergiant stars with distinct structures. In the MS case, we see that the fast accretion phase leads to a transient convective core, yet this core has a smaller extent than what we found in the 3D MHD and entropy-sorted model. This transient convective core and the subsequent receding rejuvenated convective core leave an imprint in the chemical composition profile (Fig. D.7), which results in double-peaked BV frequency profile in the near-core region (Fig. D.10), similar to the one found in Wagg et al. (2024). From Henneco et al. (2024a), we expect that the extent of this transient convective core depends on the mass added to the primary star and the accretion timescale. We see from Fig. 5.17 that the second BV frequency peak influences the PSP variability mostly in the number of modes found in the PSP dips and the amplitude, which are both higher for the merger product.

On the level of the p modes, we see similar behaviour as for the PyMMAMS model. Since we assumed that the composition of the accreted material is that of the surface of the accreting star, the envelope of the merger product is not enriched in helium. Because of the small radial extent of the transient convective core during the merger procedure, the p-mode cavity is virtually identical to the $16.9 M_{\odot}$ genuine single star’s p-mode cavity. The frequency differences between the merger product and genuine single star are at most 0.025 cycles/day ($0.289 \mu\text{Hz}$). The frequency error compared to the 3D MHD merger product’s p-modes is in the interval $[-0.025; 0.036]$ cycles/day ($[-0.289; 0.417] \mu\text{Hz}$), but is larger in absolute value than σ_v^p for all radial orders (bottom panel of Fig. 5.10).

5.3.2.4 Potential improvements to 1D merger prescriptions

Since none of the 1D merger prescription models is able to reproduce the interior structure and asteroseismic predictions of the 3D MHD model, we briefly discuss some ways in which these methods could potentially be improved. Both the mean asymptotic period spacing values and PSP variability morphology of the 3D MHD merger product model are not reproduced well with the fast accretion method. A potential improvement to this method would be to abandon the assumption that the chemical composition of the accreted material is the same as that of the accretor’s surface and instead accrete the full chemical composition of the secondary star. However, this has the drawback that one needs to make assumptions about the mixing of this material in the accretor’s envelope.

The PyMMAMS model performed worse than the entropy-sorted model, but has the highest potential for improvement, especially since it predicts the correct overall chemical structure of the merger product (secondary core in the centre, primary core around it). As mentioned in Sect. 5.2.2.3, the main difference between entropy-sorting and PyMMAMS is the inclusion of shock heating in the latter. Evidently, the shock heating, calibrated on more energetic head-on collisions, does not lead to a satisfactory reproduction of the 3D MHD model. However, provided that more 3D binary merger simulations become available, they could be used to calibrate the shock heating prescription in PyMMAMS to better reproduce the structures resulting from these slower, less energetic binary inspiral mergers (Heller et al., in prep.).

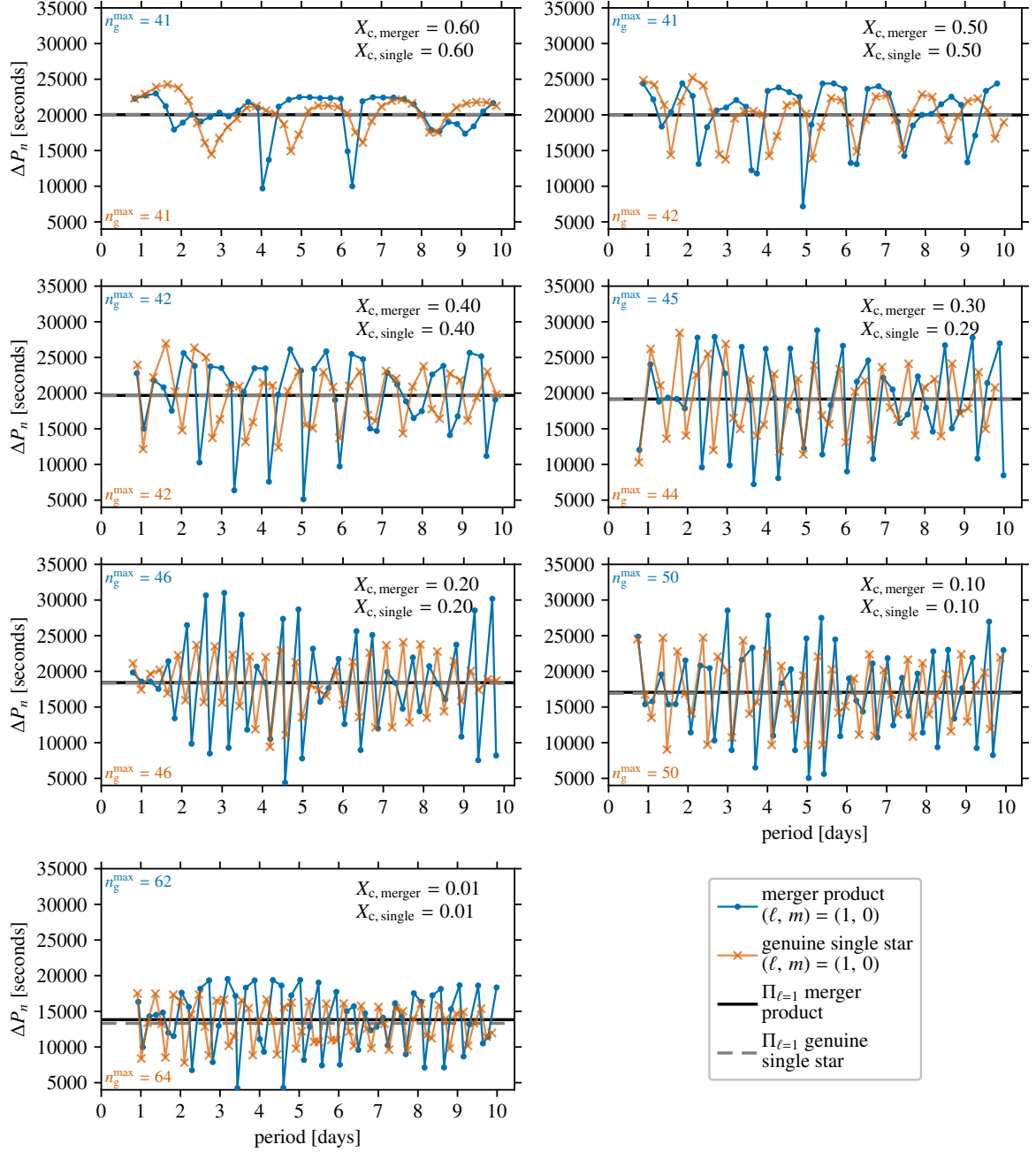


Figure 5.17: Same as Fig. 5.6, now for the $16.9 M_{\odot}$ fast accretion merger product (blue solid lines, dot markers) and the $16.9 M_{\odot}$ genuine single star (orange solid lines, cross markers).

5.4. Discussion and conclusions

We find from the results presented in Sect. 5.3 that even though the resulting product of a stellar merger between a $9 M_{\odot}$ and a $8 M_{\odot}$ MS star leads a seemingly ‘normal’ MS life, its structure and composition are rather anomalous compared to genuine single stars. The $16.9 M_{\odot}$ merger product obtained from the 3D MHD simulation of Schneider et al. (2019) has an abnormally high convective core radius and stellar radius for its respective mass. More specifically, throughout its MS evolution, the merger product’s convective core and stellar radii are similar to those of a more massive $17.4 M_{\odot}$ genuine single star with similar effective temperature and luminosity. Given that the merger product overlaps in the HRD with a more massive star, its L_{\star}/M_{\star} -ratio is higher than that of genuine single stars. We have shown in Sect. 5.3 that this can be explained by the He-enrichment of the envelope of the merger product.

These structural and chemical anomalies lead, as shown in Sect. 5.3.1.1, to different asymptotic period spacings Π_{ℓ} and hence mean PSP values for the merger product and genuine single star. The differences in the asymptotic period spacing are on the order of several 100 s, which is larger than the current best uncertainties on g-mode period spacing patterns of $\sigma_{\Delta P} \simeq 50$ s. However, as we have shown, this difference in the asymptotic period spacing changes as the star evolves (Fig. 5.4). Also, for prograde sectoral modes computed under the TAR, the differences in mean PSP value are smaller, and these mean values are higher for the merger product than for the genuine single star, whereas the opposite is true in the non-rotating case (at $X_c = 0.50$). In other words, if observed period spacing patterns are available, their mean value likely does not unambiguously allow us to distinguish this type of merger product from genuine single stars.

The quasi-periodic variation found in the PSPs has the additional potential of singling out merger products from photometric light curves. The merger product’s PSP variability contains approximately the same component as the genuine single star’s, namely that caused by the strong BV frequency peak in their near-core regions. However, the extra glitch in the merger product’s BV frequency profile introduces a second component to this variability. Although it is harder to see at later MS stages, this second component in the merger product’s variability distorts the somewhat regular behaviour of the variability that we would expect without the effect of the Gaussian-like glitch. This becomes clear when comparing the PSPs of the merger product and the genuine single star. A promising diagnostic for the presence of a merger product would be to look for such irregularities in observed PSPs. For that, mode identification (assigning n , ℓ , and m values to individual modes) is required, which currently lies within the realm from combined *Gaia* and TESS space photometry (Hey and Aerts, 2024; Fritzewski et al., 2024b). Eventually, tools such as those developed by Cunha et al. (2024, and references therein) could be used to link merger products’ particular PSP variability to their internal structure. However, the exact location of the Gaussian-like glitch in our models depends on the extent of the transient convective core after the merger and, hence, on our assumptions for the mixing length and overshooting parameters.

As described in Sect. 5.3.1.2, frequencies of p modes are lower and more closely spaced in the merger product compared to the genuine single star, which we attribute to the merger product’s lower mean density and sound speed in its p-mode cavity. These mean values converge with MS age, making the differences in p-mode frequencies smaller. Nevertheless, the differences are still larger than the current best relative uncertainties on observed p-mode frequencies of 0.01% (Aerts et al., 2019, Table 1). Additionally, the differences increase

with increasing radial order because of the higher sensitivity of these modes to the chemical composition in the p-mode cavity. We also found that the frequency differences between the merger product and genuine single star are virtually insensitive to the rotation rate as a consequence of the first-order Ledoux perturbative approach used to include rotation on the level of the pulsation equations only. Especially at higher rotation rates, the effects of the centrifugal deformation of the star on p modes should not be ignored (see Aerts and Tkachenko 2023 for an overview). Overall, our analysis shows that the differences in p-mode frequencies are on the order of 0.10 cycles/day ($1.16 \mu\text{Hz}$) and depend strongly on the chemical composition of the p-mode cavity, which is the part of the star where the merger product deviates the most from its corresponding genuine single star.

While the differences between the mean ΔP_n and/or p-mode frequencies ν_p of a merger and genuine single star of similar mass are comfortably above the current best observational uncertainties, applications will benefit from additional constraints aside from asteroseismic ones. Surface diagnostics such as abundances and L_\star/M_\star estimates, for example, could help to firmly identify MS merger products. Moreover, fitting observed properties with genuine single-star and merger models and their pulsation predictions may lead to systematic offsets in their derived masses, ages, pulsation frequencies, etc. between the two best solutions. For such forward modelling applications to become possible, extensive grids of merger product models are required in addition to single-star model grids.

In this work, we have compared models when they occupy similar positions in the HRD. However, this approach ignores the often considerable observational uncertainties on the effective temperature and luminosity of stars. Hence, what is missing from our analysis, and ought to be assessed in future work, is the sensitivity of our results to changes in the location of the models in the HRD. More specifically, it should be assessed how much our results would change if we compare the merger product at a specific point during its evolution to genuine single-star models with effective temperatures and luminosities within the ranges of their typical uncertainties. If the differences in the predicted asteroseismic characteristics are systematic, it would allow us to use them confidentially in future efforts to distinguish massive MS merger products from genuine single stars.

In our assessment of the performance of the three 1D merger methods, we find that none of the 1D methods can replicate the 3D MHD model structure. Entropy sorting performs best for this particular merger product even though this is likely coincidental. This method fails to reproduce the behaviour found in the 3D merger product model where the He-rich core of the primary star forms a layer around the secondary star's core, leading to He-enrichment in the lower envelope. The PyMMAMS prescription does lead to an overall correct chemical structure for the merger product, yet, the radial extent of the He-enrichment of the envelope is less than in the 3D MHD model. By design, the fast accretion method is unable to reproduce the overall structure of the 3D MHD model, which is unlikely to improve by accreting material with a more realistic composition (see Sect. 5.3.2.4). Because of the sensitivity of both g and p modes to the interior chemical structure, the asteroseismic predictions differ depending on which 1D merger prescription we used. More importantly, none of the asteroseismic predictions based on 1D merger prescription equilibrium models managed to reproduce those for the 3D MHD model within the observational uncertainties. In other words, all 1D methods introduce errors in the predicted ΔP_n and ν_p that are larger than the current best observational uncertainties. Moreover, even with the best-performing method, entropy sorting, the error we make in Π_0 is of the same order as the predicted Π_0 differences between the 3D MHD merger model and its corresponding genuine single star.

Therefore, it would be quite problematic if one were to use these 1D merger methods to create merger models for asteroseismic fitting and forward modelling purposes. Overall, as explained in Sect. 5.3.2.4, the PyMMAMS model has the most potential to produce merger product models consistent with those obtained from 3D simulations on the condition that it is calibrated for binary mergers.

It is imperative to keep in mind when interpreting the results presented in this work that we focus on one particular type of MS merger product, formed through the merger of two relatively young MS stars with a mass ratio close to one. From, for example, the set of merger products described in Glebbeek et al. (2013), we know that depending on the age and binary configuration of a stellar merger’s progenitor system, qualitatively different merger products can be achieved that might have different asteroseismic characteristics compared to equivalent genuine single stars. To answer the question of whether we can use asteroseismology to distinguish MS merger products from genuine single stars and to eventually create grids of MS merger models for forward modelling, the analysis presented in this work ought to be repeated on a range of different MS merger products. Doing this requires a cohesive set of 3D merger simulations, similar to those of Glebbeek et al. (2013), but for mergers driven by binary evolution. As demonstrated in this work, we should be wary of resorting to 1D merger prescriptions unless they are calibrated on the results of 3D simulations. Additionally, more realistic predictions for the asteroseismic fingerprints of stellar merger products also require us to take large-scale magnetic fields into account in our evolution models and asteroseismic predictions, given that they are predicted (Schneider et al., 2019; Ryu et al., 2024) and inferred from observations (Schneider et al., 2020; Frost et al., 2024) to be present in these stars.

Acknowledgments We thank T. Neumann for the valuable insights from her Bachelor thesis titled ‘Probing merger methods in a $9 M_{\odot}$ and $8 M_{\odot}$ binary star system’ (University of Heidelberg, 2022). We thank L. Buchele, T. Van Reeth, and Q. Coppée (in no particular order) for the meaningful discussions and valuable comments and suggestions. Additional software used in this work includes PyGYRE (Townsend and Rosenberg, 2020), PyMesaReader (Wolf and Schwab, 2017), MPI for Python (Dalcín et al., 2005; Dalcín and Fang, 2021), Astropy (Astropy Collaboration et al., 2013, 2018, 2022), NumPy (Harris et al., 2020), and SciPy (Virtanen et al., 2020). We used Matplotlib (Hunter, 2007) for plotting. The authors acknowledge support from the Klaus Tschira Foundation. This work has received funding from the European Research Council (ERC) under the European Union’s Horizon 2020 research and innovation programme (Starting Grant agreement N° 945806: TEL-STARS, Consolidator Grant agreement N° 101000296: DipolarSound, and Synergy Grant agreement N° 101071505: 4D-STAR). While funded by the European Union, views and opinions expressed are however those of the author(s) only and do not necessarily reflect those of the European Union or the European Research Council. Neither the European Union nor the granting authority can be held responsible for them. This work is supported by the Deutsche Forschungsgemeinschaft (DFG, German Research Foundation) under Germany’s Excellence Strategy EXC 2181/1-390900948 (the Heidelberg STRUCTURES Excellence Cluster).

Conclusions and outlook

In this last chapter, we will look back and summarise the conclusions that can be drawn from the work presented in this thesis. From these conclusions, we formulate an outlook for what the future of binary evolution modelling, contact tracing, and merger seismology might hold.

6.1. Binary evolution and contact tracing

We can conclude several things from the contact tracing exercise presented in Chapters 2 and 3. We looked at the different physical mechanisms responsible for mass-transferring binary systems evolving into a contact configuration and what this implied for their potential to result in a stellar merger. It was found that in this respect, it is important to consider not only the mechanism driving the system into contact, but also the overall structure of the binary components. We identified the expansion of the accretor and runaway mass transfer as the drivers behind contact-binary formation during Case-A and Case-Be mass transfer. Runaway mass transfer and the expansion of the donor star beyond the L_2 -point were found to be indicative of the onset of classical common envelope phases when one of the binary components is a (super)giant, that is, when it has a deep convective envelope (Case-B1 and -C mass transfer). We found that by taking the evolution of the full binary system into account, Case-B1 and Case-C systems with initial mass ratios above roughly 0.3 (this depends on the initial primary mass) have stable mass transfer, despite the conventional assumption that their mass transfer turns unstable in this part of the initial binary parameter space. Nevertheless, attempting to trace the onset of runaway mass transfer in Chapter 2 and 3 has again highlighted the uncertainties associated with determining the onset of unstable mass transfer. One way to alleviate these uncertainties would be to consider not only the adiabatic, but also the hydrodynamic response of the donor star to mass loss, in combination with the evolution of the accretor star and binary orbit.

Another important uncertainty in binary evolution is the mass-transfer efficiency. From our work in Chapter 2, we concluded that when mass transfer is limited by the spin-up of the accretor, its efficiency is relatively low except in the binary systems where tides efficiently synchronise the accretor. Moreover, if the mass-transfer efficiency is indeed this low, we expect the majority of systems to be unable to eject all of the non-accreted matter, which

could severely impact their further evolution and observational signatures. The so far ill-constrained efficiency of angular momentum accretion, angular momentum transport in the interior of the accretor and in the accretion disk, and potential interactions between this disk and the surface of the accretor (Paczynski, 1991; Popham and Narayan, 1991) all contribute to the uncertainty of the mass-transfer efficiency. Dedicated efforts in these separate topics are required if we want to have more stringent constraints on the mass-transfer efficiency from the theoretical side. For example, future work could explore new mass-transfer efficiency prescriptions that include a model for the interaction between the accretor’s surface and the accretion disk. The results from Chapter 3 accentuated the need to constrain this efficiency, since, from them, we conclude that the occurrence of contact phases changes drastically when all mass transfer is assumed to be fully conservative. With this assumption, the fraction of mass-transferring binary systems that form contact binaries and subsequently merge approximately doubles. Moreover, with fully conservative mass transfer, Case-B1 and a considerable fraction of Case-C systems evolve towards a double-core CE phase, which did not occur in the non-conservative models. From the observational side, attempts to constrain the mass-transfer efficiency have mostly been based on individual post-mass-transfer binary systems (see, e.g. Vinciguerra et al., 2020; Derviřođlu et al., 2018). In the future, our two grids can be used to synthesise populations of binary systems and compare them to large, concise sets of observations of massive stars, such as those from the BLOeM survey (Shenar et al., 2024). Such efforts could provide us with more substantiated constraints on the mass-transfer efficiency.

Despite our best efforts, the low-mass binary models computed in Chapter 2 and 3 were plagued with numerical issues during mass transfer. This turns out to be a recurring issue in low-mass binary grid computations. In the future, it would, therefore, be valuable to invest in alleviating these numerical issues and computing complete grids of low-mass binaries, especially since our results from Chapter 2 have shown that these systems follow unique evolutionary paths (e.g. the tidal instability described in Sect. 2.3.4).

Lastly, we conclude that the grids used in Chapters 2 and 3 have by no means been fully exploited. They can serve as the basis of future work on, e.g., stripped stars, merger products, and serve as input for 3D merger and classical/double-core CE simulations.

6.2. Merger seismology

From the results in Chapter 4, we concluded that the predicted asteroseismic characteristics of Case-Be merger products in the Hertzsprung gap differ enough from those of genuine single stars so that they could be used to identify merger products with asteroseismology. However, that is based on the assumption that these modes are excited and not damped out by, for example, internal magnetic fields. Moreover, currently available observations of high-mass blue supergiant stars do not seem to show isolated oscillation modes in their Fourier spectra (Bowman et al., 2019; Ma et al., 2024). To test these predictions for the asteroseismic fingerprints of merger products, we ought to expand this analysis to intermediate-mass post-MS stars in the Hertzsprung gap. For such stars, more high-quality data from the *Kepler* mission are available. Testing asteroseismic predictions for merger products in this mass regime, especially against data previously discarded because of strange features, could allow us to validate our predictions and improve them, for example, by adding currently missing physics. In general, future work should explore different parts of the initial binary parameter space for merger products, constrained in Chapter 2 and 3, to get a more complete

image of how post-MS merger products can differ asteroseismically from not only genuine single stars, but other B-type stars such as blue loop stars. Moreover, the work presented in this thesis and in the works of Bellinger et al. (2024) and Wagg et al. (2024) has opened the door to asteroseismic predictions for other types of binary products, such as (fast-rotating) accretors and stripped-star donors.

The comparison between an MS merger product and a genuine single MS star, explored in Chapter 5, showed that the differences in their predicted asteroseismic characteristics are less pronounced than for post-MS merger products. These differences in the g-mode period spacings and p-mode frequencies, in combination with the detection of additional components in the variability of the merger product's PSPs and constraints from surface diagnostics, can, nevertheless, potentially help us identify merger products. Given that these differences are larger than the current smallest uncertainties for period spacings and frequencies, unknowingly fitting observed merger products to grids of single-star models can lead to offsets in their inferred properties. That said, the work presented in Chapter 5 should be viewed as a proof-of-concept study and should be expanded to other merger products with different binary progenitors. Because of the second conclusion of this work, namely that current 1D merger prescriptions fail to reproduce the internal structures and hence asteroseismic characteristics of the 3D MHD merger product, the extension of this work to other kinds of merger products should initially be based on the results of 3D simulations. Only when 1D merger prescriptions have been calibrated for binary mergers (as opposed to dynamic collisions) should they be used to construct grids of merger models fit for asteroseismic purposes such as forward modelling.

Furthermore, several physical ingredients are missing from our current merger product models. For example, we have, so far, only considered solid-body rotation in our predictions and only on the level of the stellar pulsation equations. Using the advances in the theory of angular momentum transport (see Aerts et al., 2019, for a review), we should assess if and how the peculiar internal structures of merger products affect their internal rotation profiles and how this affects their pulsations. Simulations predict (Schneider et al., 2019; Ryu et al., 2024) and observations give strong indications (Frost et al., 2024) that merger products are highly magnetic stars. Such magnetic fields can influence the internal structure, angular momentum transport, and pulsations of stars considerably (e.g. Aerts et al., 2019; Mathis et al., 2021; Rui et al., 2024). Hence, their various effects should be included in the next generation of stellar merger product models.

Overall, in this thesis, we have explored the evolutionary pathways and physical mechanisms leading to stellar mergers and other types of contact phases. With this detailed knowledge of the progenitors of stellar mergers, we have then focussed on their products and how these might be distinguished from genuine single stars. By doing so, we ventured onto the relatively young and exciting interface between binary physics and asteroseismology. We have demonstrated some of the benefits the synergy of binary physics and asteroseismology brings, and conclude that the future of this synergy looks immensely bright.



Appendices for Chapter 2: ‘Contact tracing of binary stars: Pathways to stellar mergers’

A.1. Nuclear timescale expansion of the accretor

Here, we present an example of a model forming a contact binary from the nuclear timescale expansion of the secondary (accretor) star. The evolution of the Case-A system with $M_{1,i} = 10.2 M_{\odot}$, $q_i = 0.9$, and $a_i = 12.5 R_{\odot}$ is shown in Fig. A.1. After regaining thermal equilibrium, the primary star detaches and later fills its Roche lobe again because of nuclear expansion. The detachment phase is short compared to the evolutionary timescale and only visible by a slight wiggle in the HRD (Fig. A.1a). During the first, thermal-timescale mass-transfer phase, the secondary star expands on its thermal timescale (Fig. A.1b). However, during the second, nuclear-timescale mass-transfer phase, the secondary remains in thermal equilibrium and its radius evolves on a nuclear timescale (Fig. A.1c) and increases with mass accretion. Because R_2 grows faster in time than $R_{\text{RL},2}$, the secondary eventually fills its Roche lobe simultaneously with the primary, and a contact binary is formed.

A.2. Contact tracing results for other $M_{1,i}$

Figures A.2–A.4 contain the contact tracing results for the initial primary masses $M_{1,i} = 0.8, 0.9, 1.1, 1.3, 1.9, 2.2, 2.6, 3.1, 3.7, 4.3, 5.2, 6.1, 7.2, 8.6, 12.0, 13.1, 14.2, 15.6, 16.9,$ and $18.4 M_{\odot}$.

A.3. Evolutionary states at contact or termination of models

In Figs. A.5–A.7, we show the evolutionary state of the binary components for all systems in our grid at contact or at termination for systems that avoid contact.

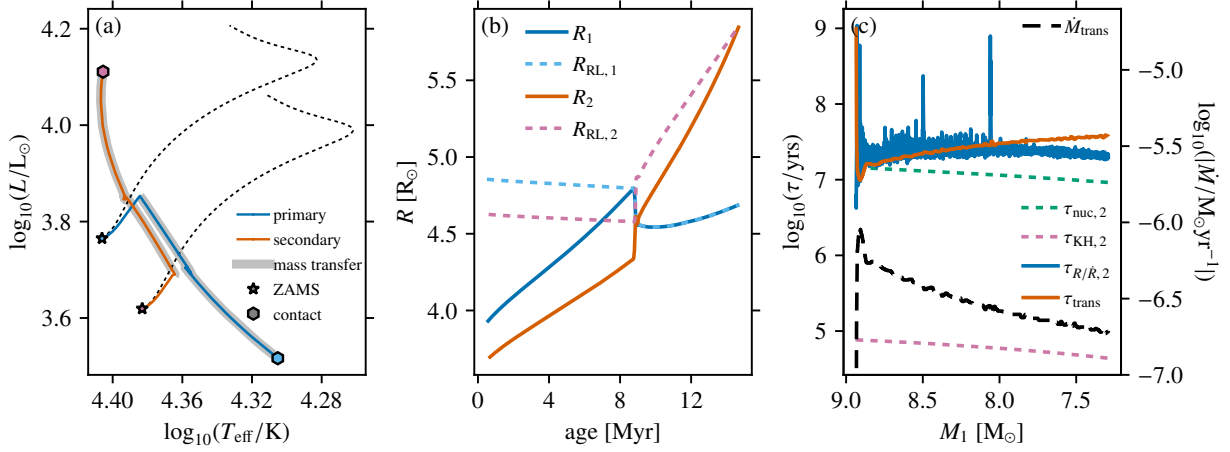


Figure A.1: Same as Fig. 2.2 but for a $M_{1,i} = 10.2 M_{\odot}$, $q_i = 0.9$, and $a_i = 12.5 R_{\odot}$ binary.

A.4. Expansion timescales for Case-A contact systems

In Figs. A.8–A.9, the Case-A region of the initial binary parameter space is shown for all initial primary masses of the grid. The contact systems formed through the expansion of the accretor and those which experience L_2 -overflow are indicated with the same colour scheme as in Fig. 2.6. Each model is marked with a red or blue square based on whether the mean of the accretor’s expansion timescale is of the order of its mean thermal or nuclear timescale, respectively.

A.5. Assignment criteria for evolutionary outcomes of models with numerical issues

Table A.1 lists the criteria used to determine the evolutionary outcome of models that experience numerical issues. The outcome assignment criteria for these models are based on the outcomes of neighbouring models and information from equivalent systems at different initial primary masses.

Table A.1: Evolutionary outcome assignment criteria for models with numerical issues.

q_i -range	Case A	Case Be	Case Bl/C
$q_i < 0.3$	Accr. exp. ^a	Runaway MT	Runaway MT
$q_i \geq 0.3$	No contact	No contact	No contact

^(a) ‘Accr. exp.’ = ‘Accretor expansion’.

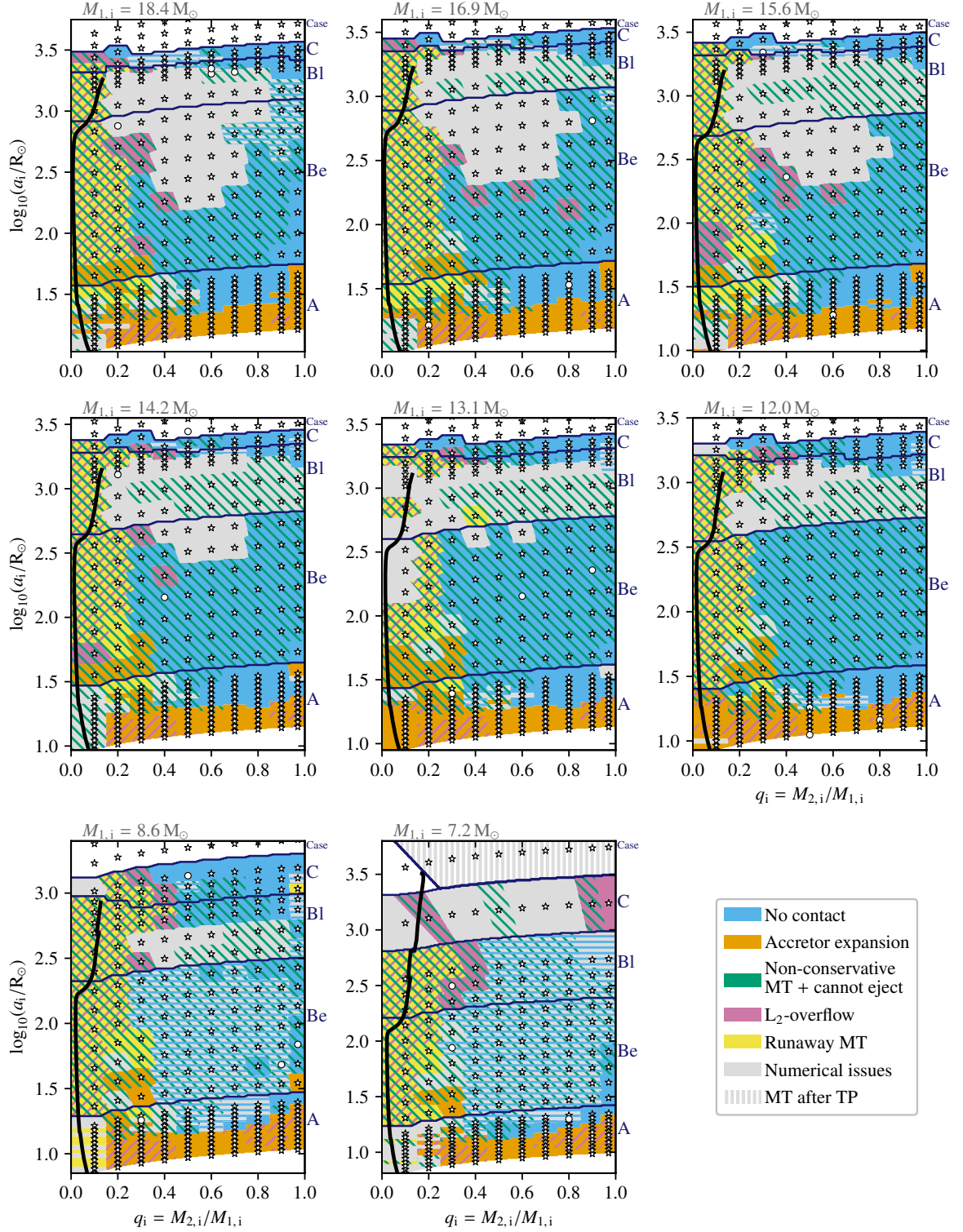


Figure A.2: Contact tracing results for $M_{1,i} = 7.2\text{--}18.4 M_{\odot}$. Models with $M_{1,i} = 7.2 M_{\odot}$ and initial separations larger than the Case-C systems experience numerical issues after the TP-AGB phase (see Sect. 2.2.1.2). Only the model with $q_i = 0.1$ avoids these issues and does not initiate mass transfer.

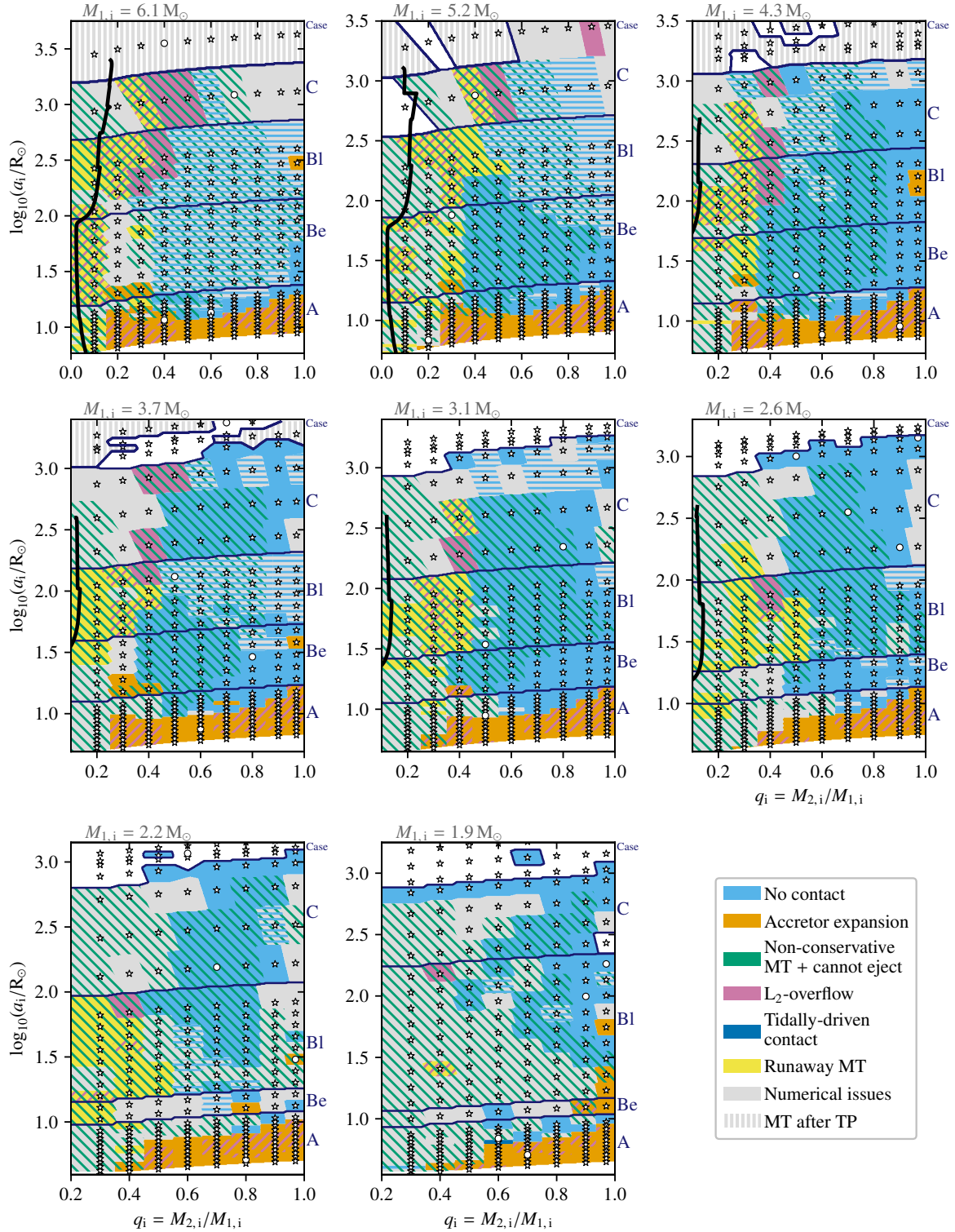


Figure A.3: Contact tracing results for $M_{1,i} = 1.9\text{--}6.1 M_{\odot}$. Models with $M_{1,i} = 3.7\text{--}6.1 M_{\odot}$ experience numerical issues after the TP-AGB phase (see Sect. 2.2.1.2). This explains the unexpected onset of mass transfer at initial separations larger than those of systems avoiding mass transfer. For $M_{1,i} = 1.9\text{--}2.2 M_{\odot}$ we find certain models where mass transfer starts when the primary is on the WD cooling track and experiences sudden radial expansion.

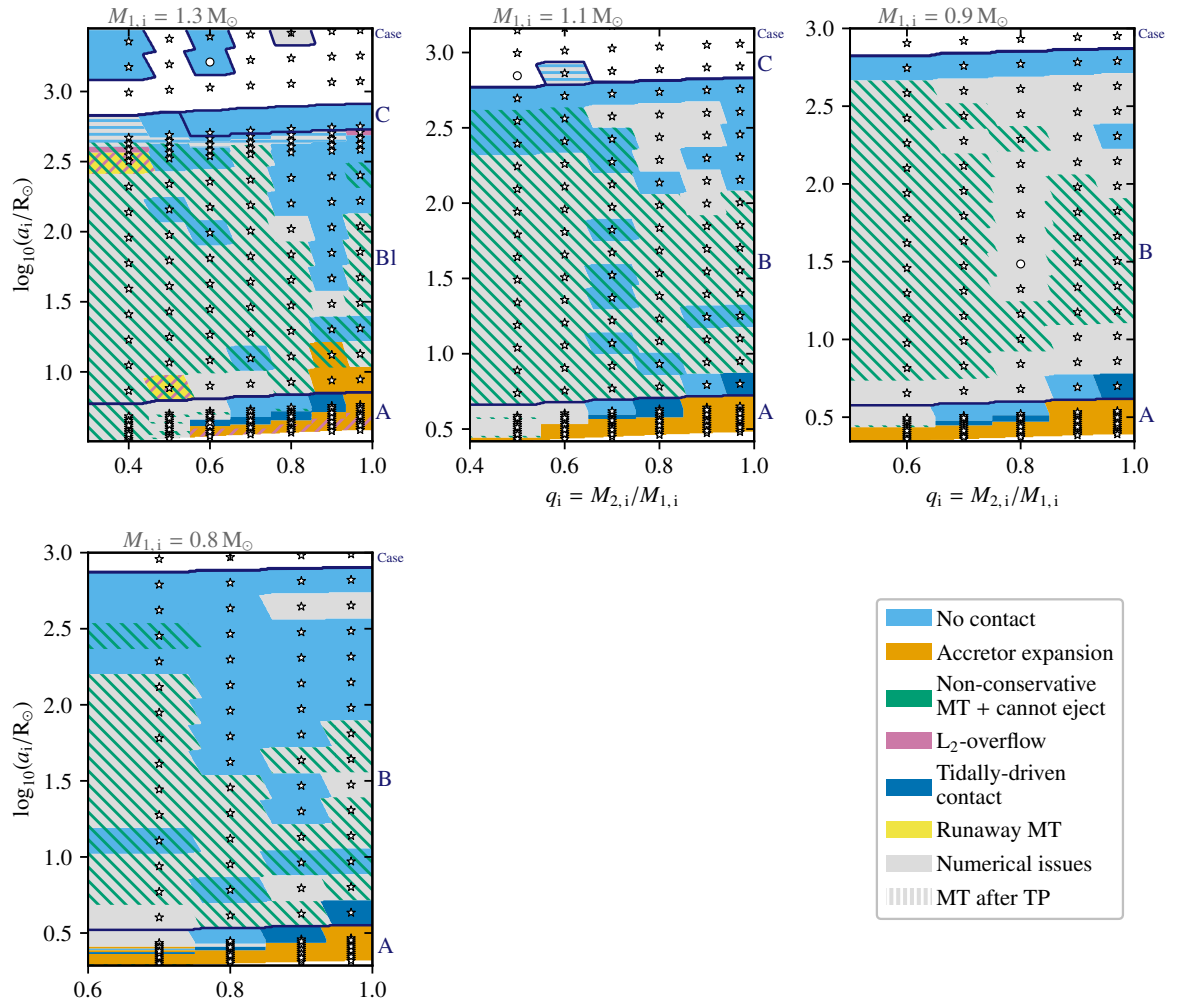


Figure A.4: Contact tracing results for $M_{1,i} = 0.8$ – $1.3 M_{\odot}$. For $M_{1,i} = 1.1$ – $1.3 M_{\odot}$ we find certain models where mass transfer starts when the primary is on the WD cooling track and experiences sudden radial expansion.

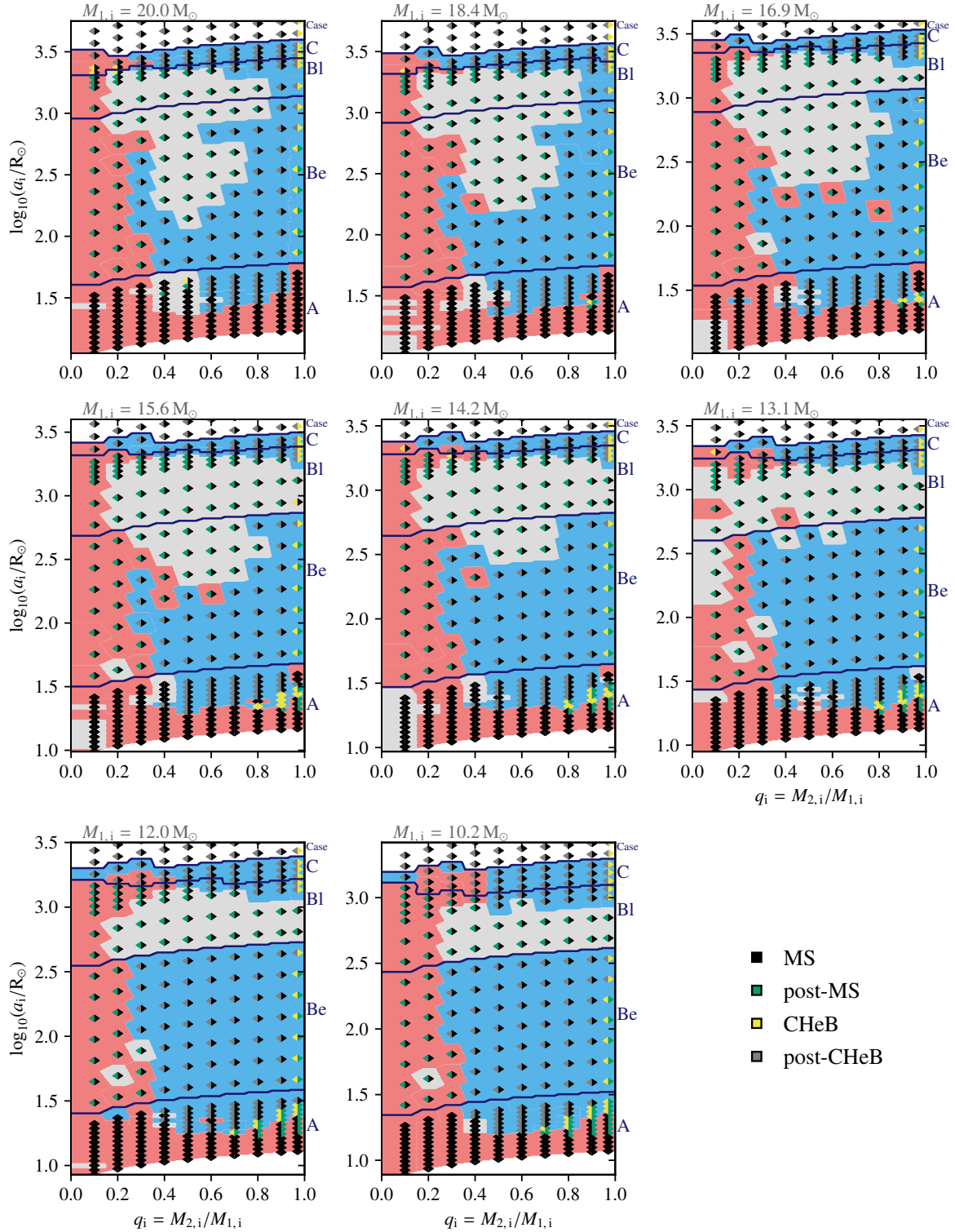


Figure A.5: Evolutionary state of the primary (left triangle) and secondary (right triangle) at contact or termination for $M_{1,i} = 8.6\text{--}20.0 M_{\odot}$. The pink, blue and grey background colours indicate systems that get into contact, avoid contact and fail to converge numerically, respectively. Post-MS stars are those that have exhausted hydrogen but have not yet ignited helium in their core. ‘CHeB’ stands for core helium burning.

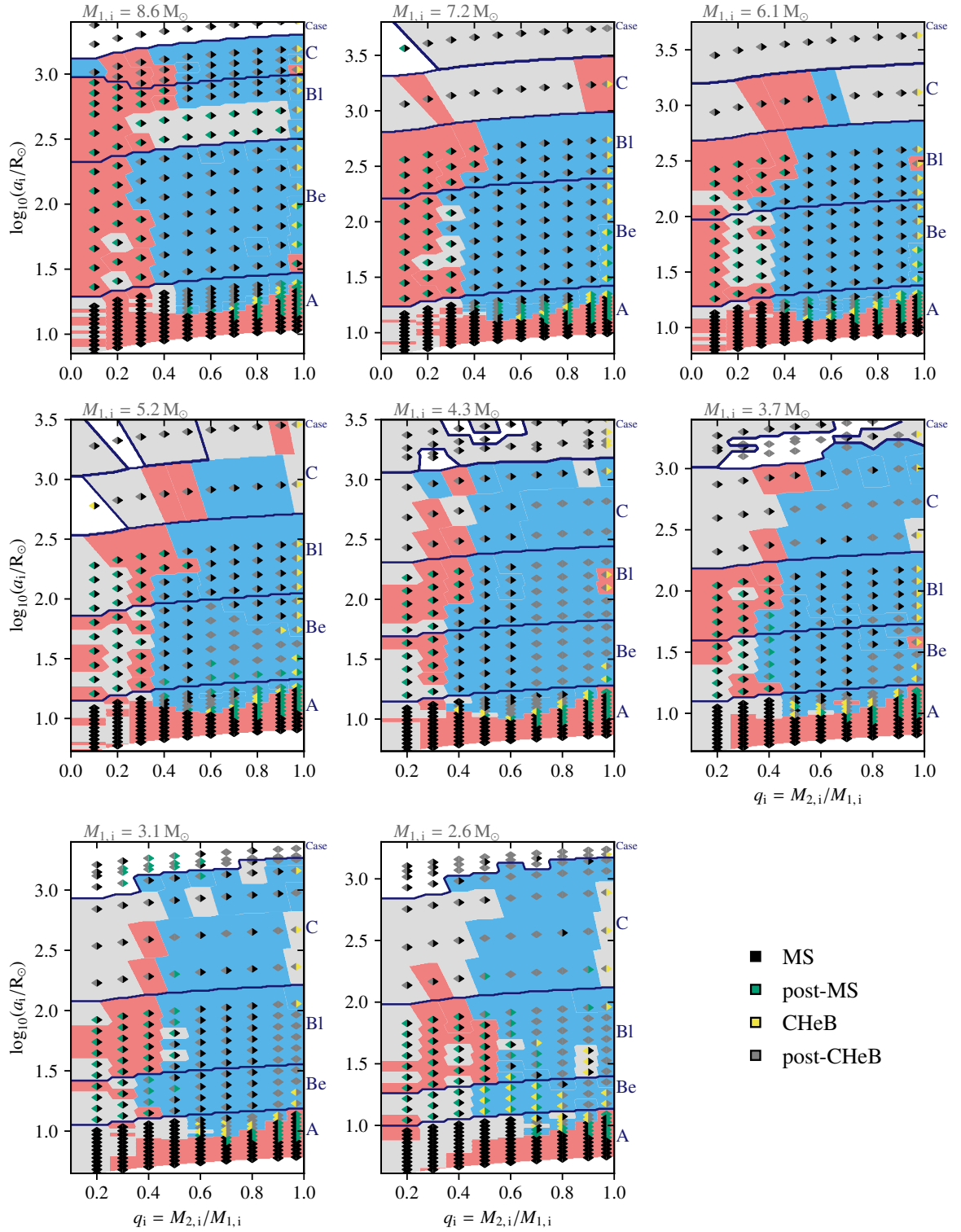


Figure A.6: Same as for Fig. A.5 but for $M_{1,i} = 1.9\text{--}7.2 M_{\odot}$.

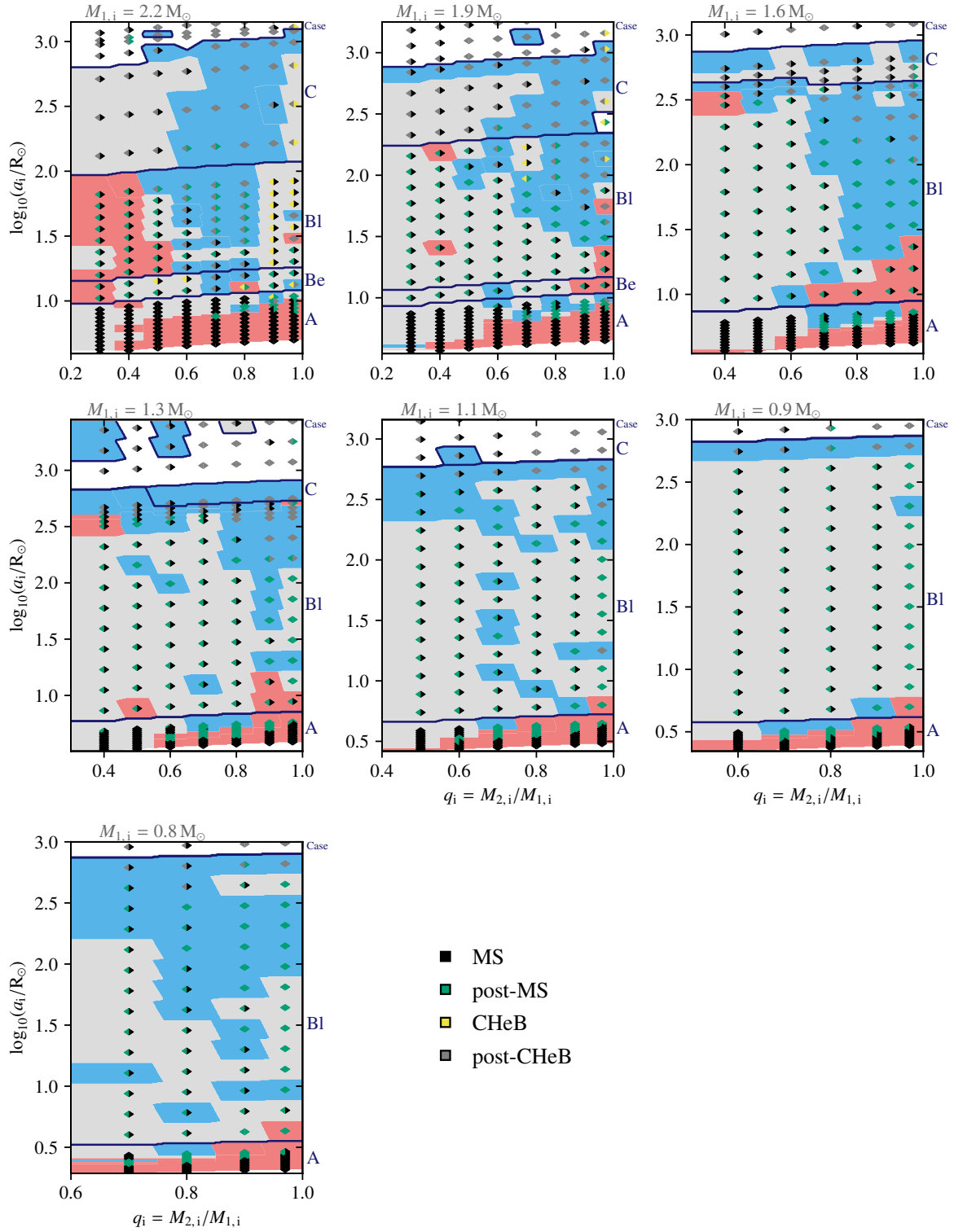


Figure A.7: Same as for Fig. A.5 but for $M_{1,i} = 0.8\text{--}1.6 M_\odot$.

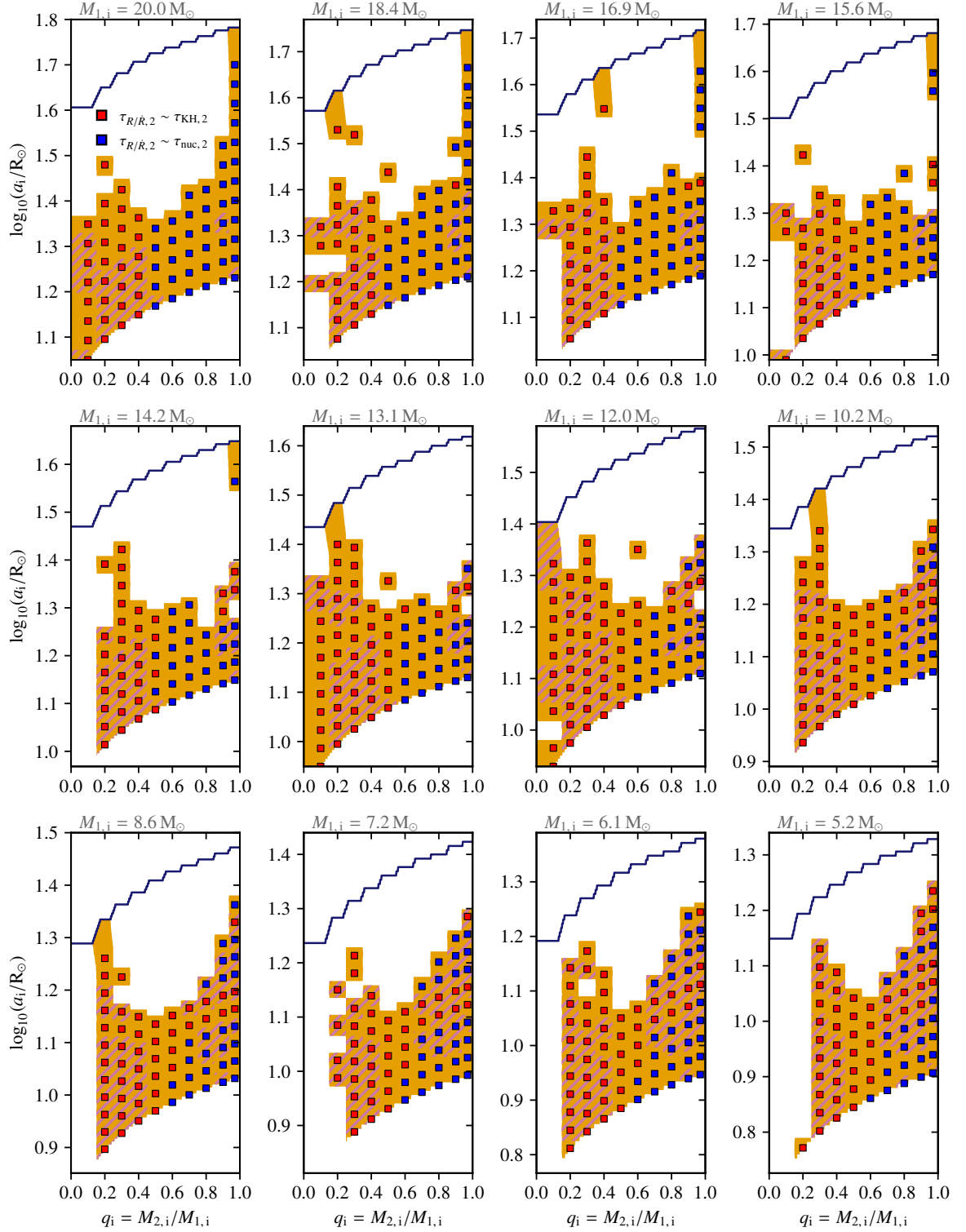


Figure A.8: Expansion timescales for Case-A contact systems formed through the expansion of the accretor star with $M_{1,i} = 5.2\text{--}20.0 M_{\odot}$. In models marked with filled red (blue) squares, the accretor expands on its thermal (nuclear) timescale prior to the onset of contact. The colour scheme is the same as in Fig. 2.6. The dark blue solid line indicates the division between Case-A and -Be systems.

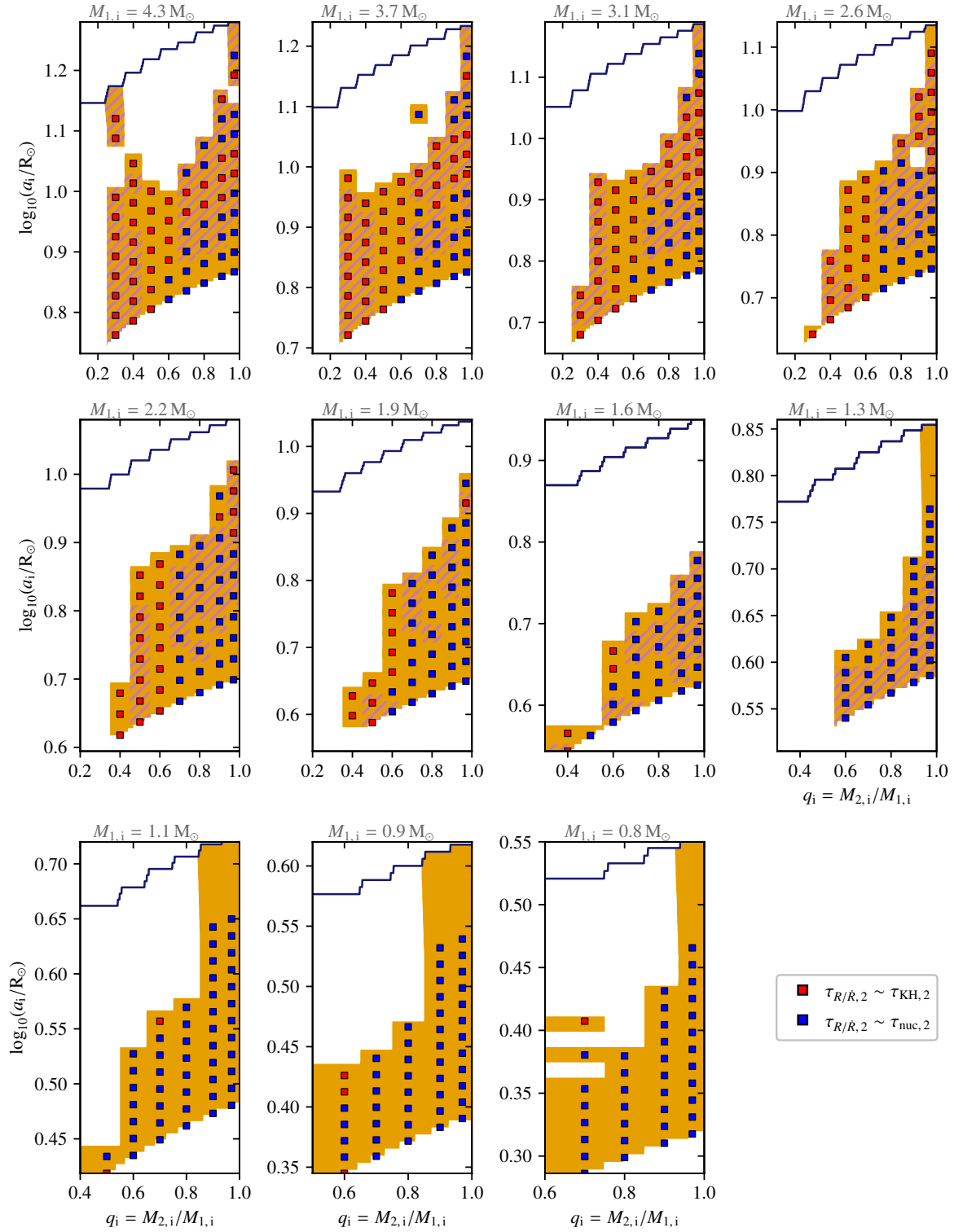


Figure A.9: Same as Fig. A.8 but for $M_{1,i} = 0.8\text{--}4.3 M_\odot$.

A.6. Mass-transfer efficiency

We show the mean mass-transfer efficiency $\bar{\beta}$ for Case-A, -B, and -C mass transfer as a function of the initial primary mass $M_{1,i}$ in Fig. A.10. We use the birth probabilities p_{birth} (Sect. 2.2.5) of each model as weights for the computation of these mean values. The value of the mass-transfer efficiency for each individual model is averaged over time. We only consider mass transfer in systems that avoid contact.

First, we see that for all mass-transfer cases, the mean mass-transfer efficiency $\bar{\beta}$ is relatively high for $\log_{10}(M_{1,i}) < 0.25$ – 0.45 . For $\log_{10}(M_{1,i}) > 0.25$ – 0.45 , $\bar{\beta}$ has moderate to low values. The high values of $\bar{\beta}$ for binaries with lower initial primary masses should be regarded as an approximation since for all mass-transfer cases the models avoiding contact are sparse due to numerical issues (Fig. A.3–A.4). The models that avoided numerical issues have high mass-transfer efficiencies.

Case-A mass transfer has low to moderate mean mass-transfer efficiencies for $\log_{10}(M_{1,i}) > 0.45$. The initially closest Case-A binaries go through conservative mass transfer before they form contact binaries and are, therefore, not taken into account for the computation of $\bar{\beta}$. Case-A binaries that avoid contact are on initially wider orbits. The accretors in these systems have longer tidal synchronisation times, so tides are unable to prevent them from rotating critically. As discussed in Sect. 2.5.1, Case-A mass transfer consists of a short thermal-timescale phase, which is mostly non-conservative, and a more conservative, longer nuclear-timescale phase. This results in values of $\bar{\beta}$ between ~ 0.15 and ~ 0.65 .

Case-B mass transfer in binaries with $\log_{10}(M_{1,i}) > 0.25$ have relatively low values of $\bar{\beta}$, with values between ~ 0.05 and ~ 0.25 . In virtually all systems with Case-B mass transfer, the accretors reach critical rotation after accreting a few percent of their own mass, which quenches accretion (Sect. 2.4.1 and 2.5.1).

Case-C mass transfer is generally highly non-conservative (Sect. 2.4.2). However, the contribution of Case-C systems with relatively short mass-transfer phases before core-C exhaustion in which the accretor is not spun up to critical rotation increases the value of $\bar{\beta}$ for $\log_{10}(M_{1,i}) > 0.25$.

The contribution of both conservative and non-conservative mass transfer in Case-A and -C mass transfer cases, for the former in terms of mass-transfer phases (thermal and nuclear) and for the latter in terms of systems (highly non-conservative models and conservative models), results in somewhat similar mean mass-transfer efficiencies.

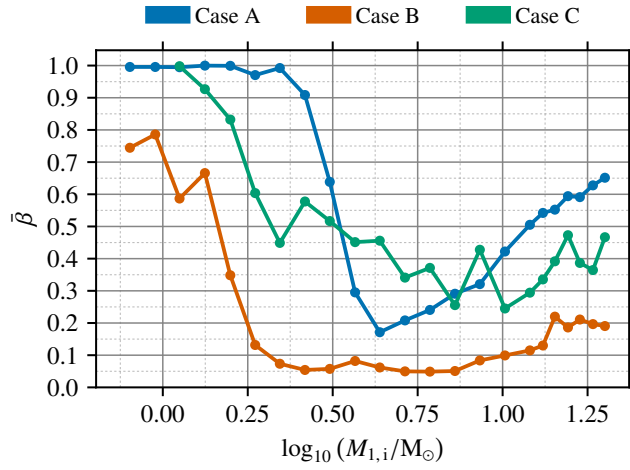


Figure A.10: Mean mass-transfer efficiency $\bar{\beta}$ per mass-transfer case for each initial primary mass $M_{1,i}$.

A.7. Table with contact tracing results

Table A.2 contains an extract of the table containing the contact tracing results for all our models.

Table A.2: Extract of the table with the contact tracing results of all 5957 binary MESA models. The full table is available online at <https://zenodo.org/doi/10.5281/zenodo.10148634>.

$M_{1,i}$ [M_{\odot}]	$M_{2,i}$ [M_{\odot}]	$\log_{10}(a_i/R_{\odot})$	$\log_{10}(P_i/d)$	$M_{1,f}$ [M_{\odot}]	$M_{2,f}$ [M_{\odot}]	$\log_{10}(a_f/R_{\odot})$	$\log_{10}(P_f/d)$	$\log_{10}(a_{gr}/\text{yrs})$	AE ^e	RMT ^f	NCCE ^e	L2O ^f	TDC ^g	NC ^h	MTPP ^f	NI ^j	Case [A,B,C]	ES ₁ ^k	ES ₂ ^l
0.80	0.56	0.407	-0.392	0.65	0.71	0.324	-0.517	10.343	1	0	0	0	0	0	0	0	[1,0,0]	MS	MS
0.95	0.57	2.745	3.090	0.53	0.57	2.865	3.342	10.481	0	0	0	0	0	1	0	0	[0,1,0]	post-CHeB	MS
1.12	0.90	0.616	-0.165	0.22	1.79	1.130	0.607	9.953	0	0	0	0	1	0	0	0	[1,1,0]	post-MS	post-MS
1.33	0.53	2.629	2.872	0.78	0.59	2.641	2.958	9.631	0	0	1	0	0	1	0	1	[0,1,1]	post-CHeB	MS
1.58	1.11	0.681	-0.130	1.13	1.55	0.668	-0.148	9.387	1	0	0	1	0	0	0	0	[1,0,0]	MS	MS
1.87	1.68	2.254	2.169	0.50	1.55	2.660	2.898	9.308	0	0	0	0	0	1	0	0	[0,1,1]	post-CHeB	post-CHeB
2.21	0.66	1.554	1.166	2.21	0.67	1.438	0.992	8.926	0	1	1	0	0	0	0	0	[0,1,0]	post-MS	MS
2.62	1.83	0.934	0.140	0.30	2.61	1.821	1.563	8.986	0	0	0	0	0	1	0	0	[1,1,0]	post-MS	post-MS
3.10	1.24	0.832	-0.007	3.07	1.27	0.809	-0.041	8.339	1	0	0	1	0	0	0	0	[1,0,0]	MS	MS
3.68	3.57	0.988	0.116	2.12	5.12	1.141	0.346	8.300	0	0	0	0	0	0	0	0	[1,0,0]	MS	post-MS
4.35	2.17	2.035	1.710	0.79	2.22	2.432	2.472	8.834	0	0	1	0	0	1	0	0	[0,1,1]	post-CHeB	MS
5.16	0.52	1.207	0.497	5.11	0.52	1.111	0.355	7.976	0	1	1	1	0	0	0	0	[0,1,0]	post-MS	MS
6.11	3.67	4.357	5.105	1.60	3.67	4.625	5.641	7.860	0	0	0	0	0	0	1	0	[0,0,1]	post-CHeB	MS
7.24	5.79	1.202	0.309	1.70	9.10	1.881	1.369	7.770	1	0	0	0	0	0	0	0	[0,1,0]	post-MS	post-MS
8.57	5.14	2.385	2.072	1.24	5.27	2.871	2.963	7.557	0	1	1	0	0	1	0	0	[0,1,0]	post-CHeB	MS
10.16	6.10	1.399	0.557	1.30	6.34	2.298	2.070	7.448	0	0	1	0	0	1	0	0	[1,1,1]	post-CHeB	MS
12.03	10.83	1.246	0.253	5.72	16.68	1.489	0.622	7.282	1	0	0	1	0	0	0	0	[1,0,0]	MS	post-MS
13.14	6.57	2.637	2.371	3.80	6.72	2.784	2.729	7.227	0	0	1	0	0	1	0	0	[0,1,1]	post-CHeB	MS
14.25	11.40	1.243	0.224	12.72	12.88	1.222	0.192	6.910	1	0	0	0	0	0	0	0	[1,0,0]	MS	MS
15.57	15.10	1.403	0.425	7.01	22.92	1.691	0.862	7.129	1	0	0	0	0	0	0	0	[1,0,0]	MS	post-MS
16.88	1.69	3.262	3.323	16.19	1.69	3.066	3.036	7.037	0	1	1	1	0	0	0	0	[0,1,0]	post-MS	MS
18.44	14.75	2.152	1.532	5.89	14.84	2.601	2.307	7.027	0	0	1	0	0	1	0	0	[0,1,0]	post-CHeB	MS
20.00	19.40	3.510	3.532	14.61	16.50	3.562	3.660	6.986	0	0	0	0	0	1	0	0	[0,0,1]	post-CHeB	CHeB

^(a) ‘i’ = ‘initial’ ^(b) ‘f’ = ‘final’ – at contact or termination ^(c) Accretor expansion ^(d) Runaway mass transfer ^(e) Non conservative mass transfer + cannot eject ^(f) L₂-overflow ^(g) Tidally driven contact ^(h) No contact ⁽ⁱ⁾ Mass transfer after thermal pulses ^(j) Numerical issues ^(k) Primary’s evolutionary state at contact or termination. MS: before core-H exhaustion. Post-MS: after core-H exhaustion and before core-He ignition. CHeB: after core-He ignition and before core-He exhaustion. Post-CHeB: after core-He exhaustion. ^(l) Secondary’s evolutionary state at contact or termination.

Appendices for Chapter 3: ‘Contact tracing of binary stars with fully conservative mass transfer’

B.1. Contact tracing results for other $M_{1,i}$

Figures B.1–B.3 contain the contact tracing results for the initial primary masses $M_{1,i} = 0.8, 0.9, 1.1, 1.3, 1.6, 1.9, 2.2, 2.6, 3.1, 3.7, 4.3, 5.2, 6.1, 7.2, 8.6, 12.0, 13.1, 14.2, 15.6, 16.9, 18.4,$ and $20.0 M_{\odot}$ with fully conservative mass transfer.

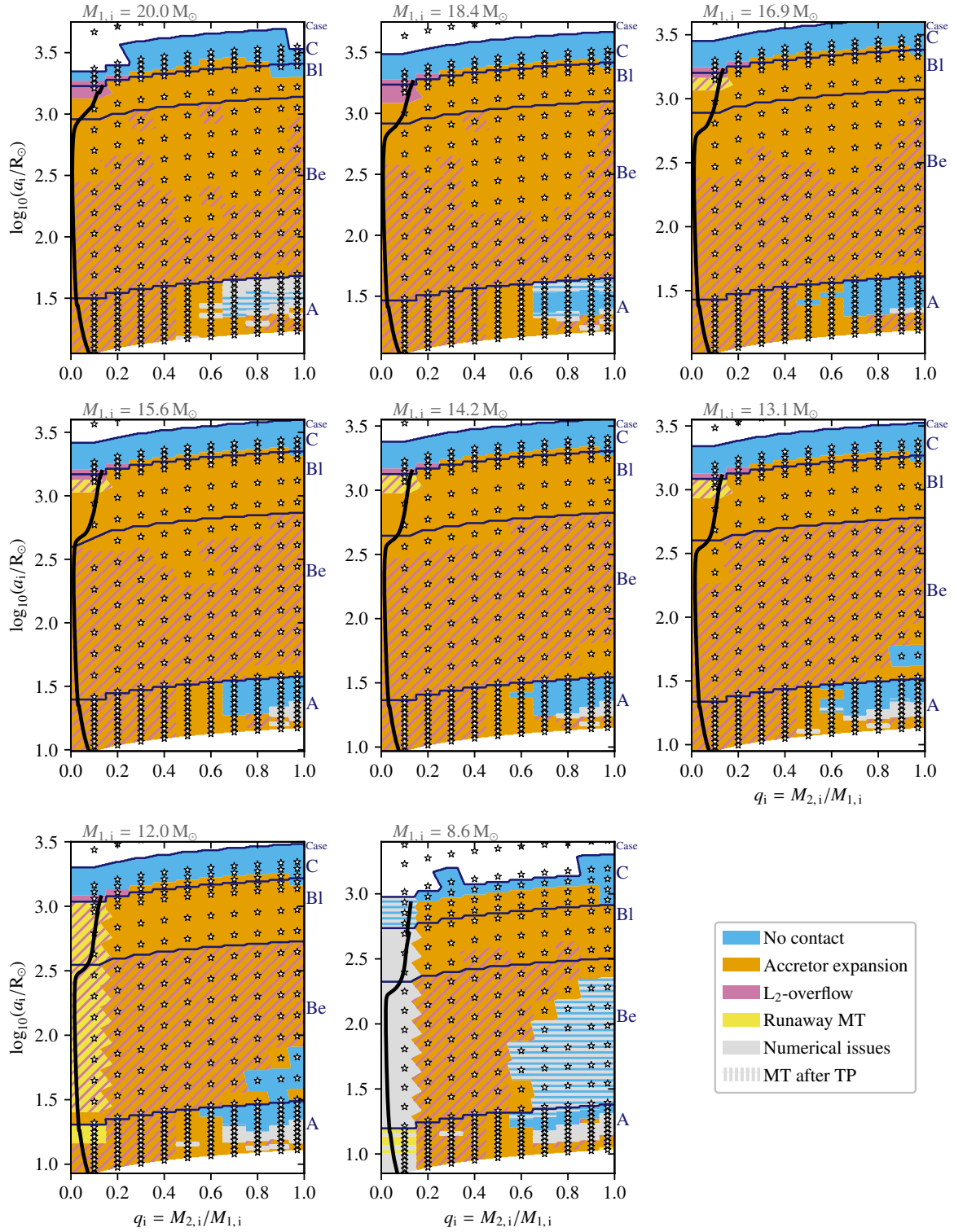


Figure B.1: Contact tracing results for $M_{1,i} = 8.6\text{--}20.0 M_{\odot}$ with fully conservative mass transfer (individual panels are equivalent to the plot in Fig. 3.1).

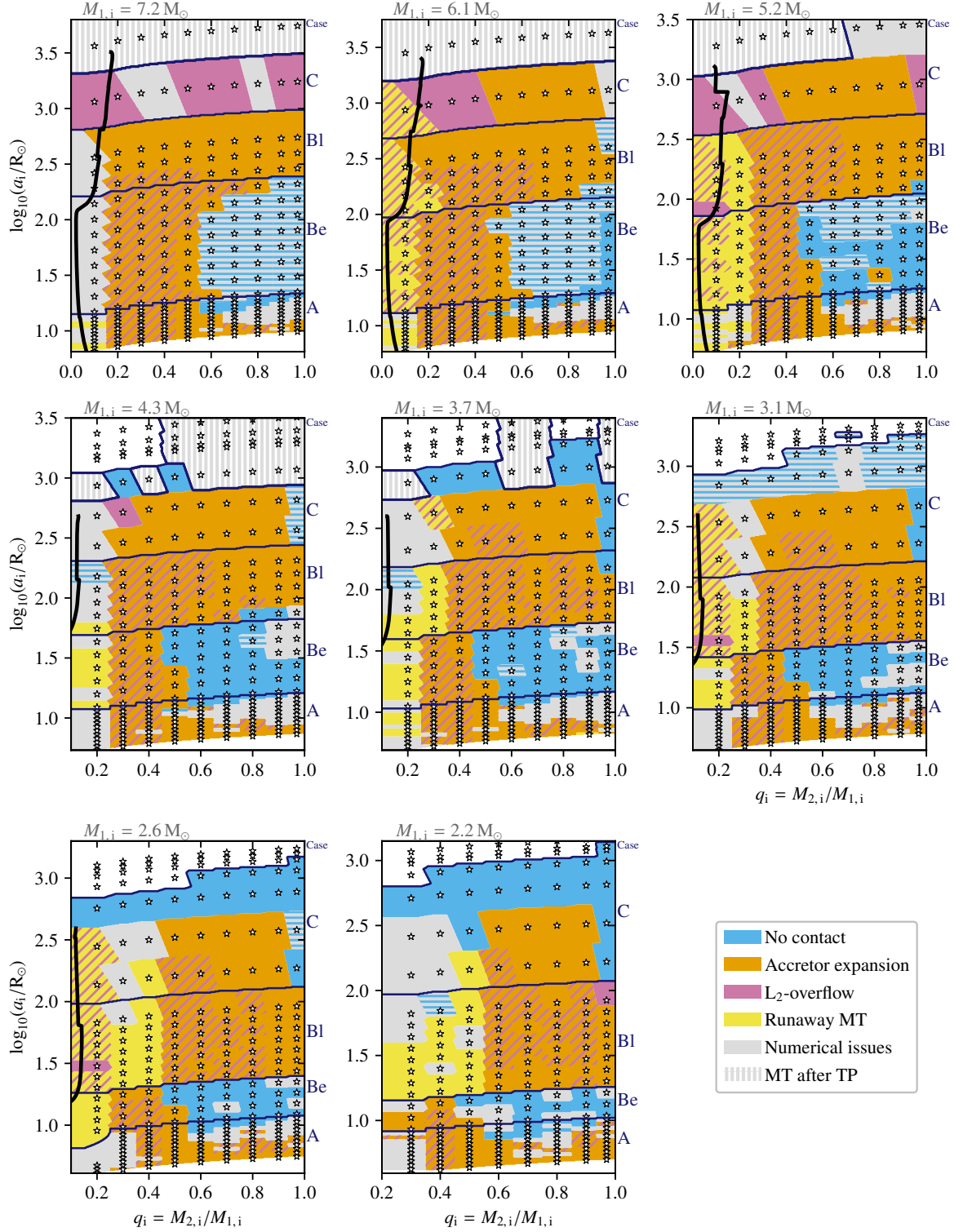


Figure B.2: Contact tracing results for $M_{1,i} = 2.2\text{--}7.2 M_{\odot}$ with fully conservative mass transfer (individual panels are equivalent to the plot in Fig. 3.1).

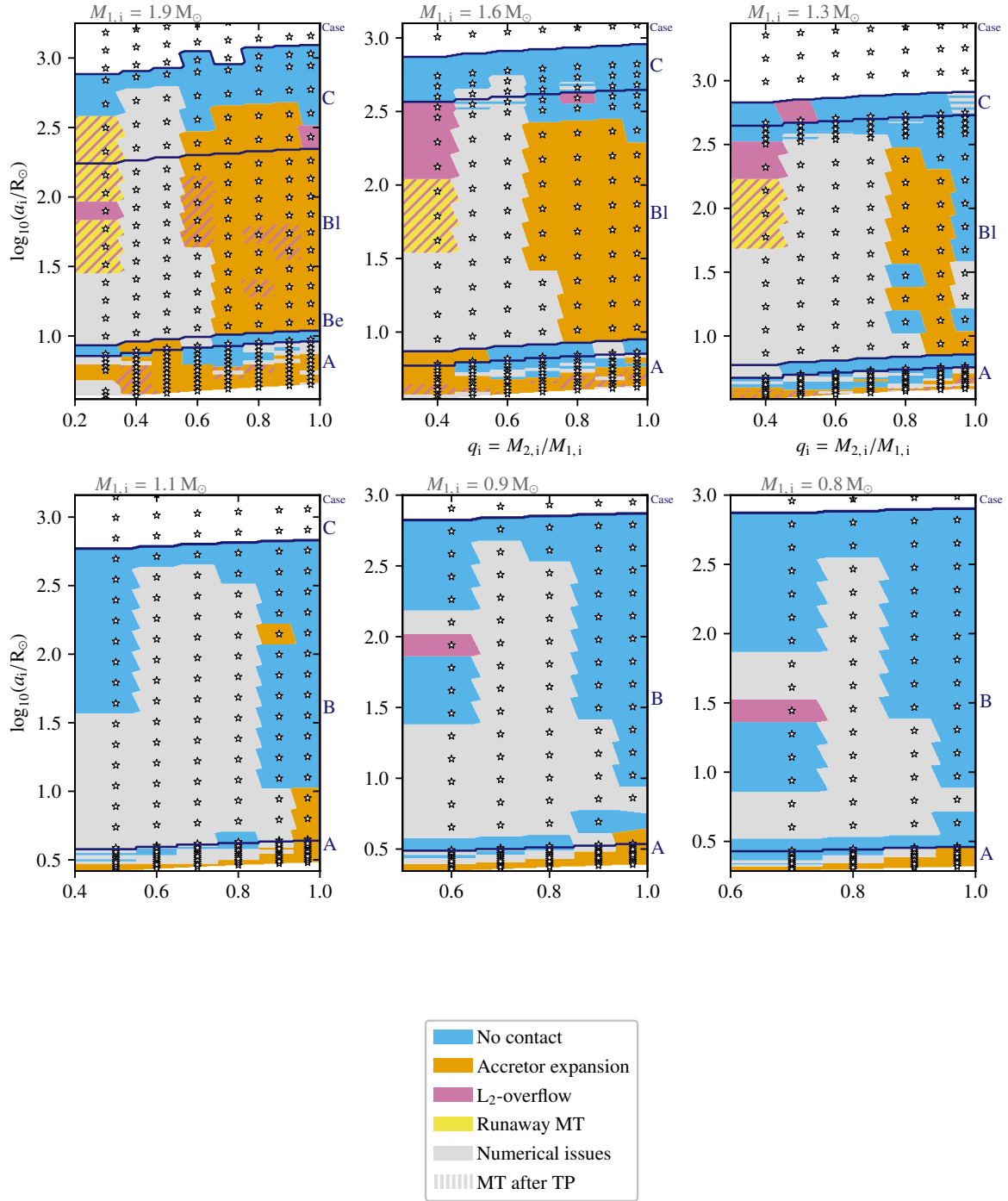


Figure B.3: Contact tracing results for $M_{1,i} = 0.8\text{--}1.9 M_{\odot}$ with fully conservative mass transfer (individual panels are equivalent to the plot in Fig. 3.1).



Appendices for Chapter 4: ‘Merger seismology: Distinguishing massive merger products from genuine single stars using asteroseismology’

C.1. Inclusion of slow rotation: TAR versus perturbative inclusion of the Coriolis acceleration

We computed the spin parameters s (see Sect. 1.2.2) for the $(\ell, m) = (1, 0)$ modes from the non-rotating calculations for the $6.0 + 2.4 M_{\odot}$ merger product to determine whether we expect the modes to be super-inertial ($s < 1$) or sub-inertial ($s > 1$). We find values for s between 0.02 ($n_{\text{pg}} = -20$) and 0.13 ($n_{\text{pg}} = -200$) when we assume $\Omega = 0.2\Omega_{\text{c}}$, which means that the modes are super-inertial. However, the condition that $s \ll 1$, which is required for treating the Coriolis acceleration as a perturbation, is not strongly satisfied, especially for the higher-order modes. From the PSPs shown in Fig. C.1, it is apparent that including the Coriolis acceleration as a perturbation leads to significant deviations from the solutions obtained using the TAR. These deviations are larger than the typical measurement errors for such modes, which are smaller than the plotted symbols in Fig. C.1 (Van Reeth et al., 2015a). This shows that even though the oscillation modes considered in this work are super-inertial when $\Omega = 0.2\Omega_{\text{c}}$, one should use the TAR instead of the first-order Ledoux perturbative approach (see Aerts and Tkachenko 2023 for details). This is especially true when the goal is to fit observed modes against theoretically predicted modes of such models (not in this work).

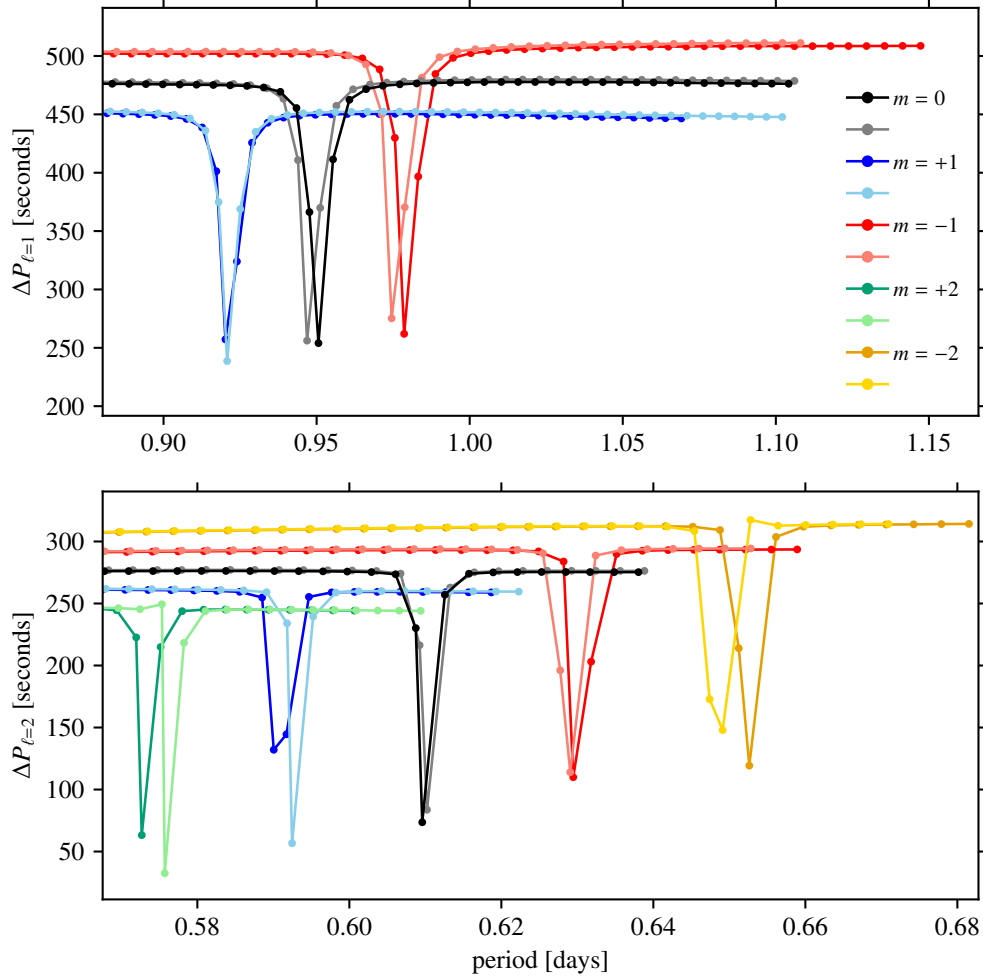


Figure C.1: PSPs for a 6.0 + 2.4 M_{\odot} merger product with $\Omega = 0.2\Omega_c$ in the inertial frame using the TAR and treating the Coriolis force as a perturbation. Light colours (grey, light blue, salmon, light green, and gold) indicate the results when the Coriolis force is treated as a perturbation. Dark colours (black, blue, red, bluish-green, and orange) show those for when the TAR is used. Panel (a) shows the PSPs for $(\ell, m) = (1, -1)$, $(1, 0)$, and $(1, +1)$ modes, and Panel (b) those for $(\ell, m) = (2, -2)$, $(2, -1)$, $(2, 0)$, $(2, +1)$, and $(2, +2)$ modes.

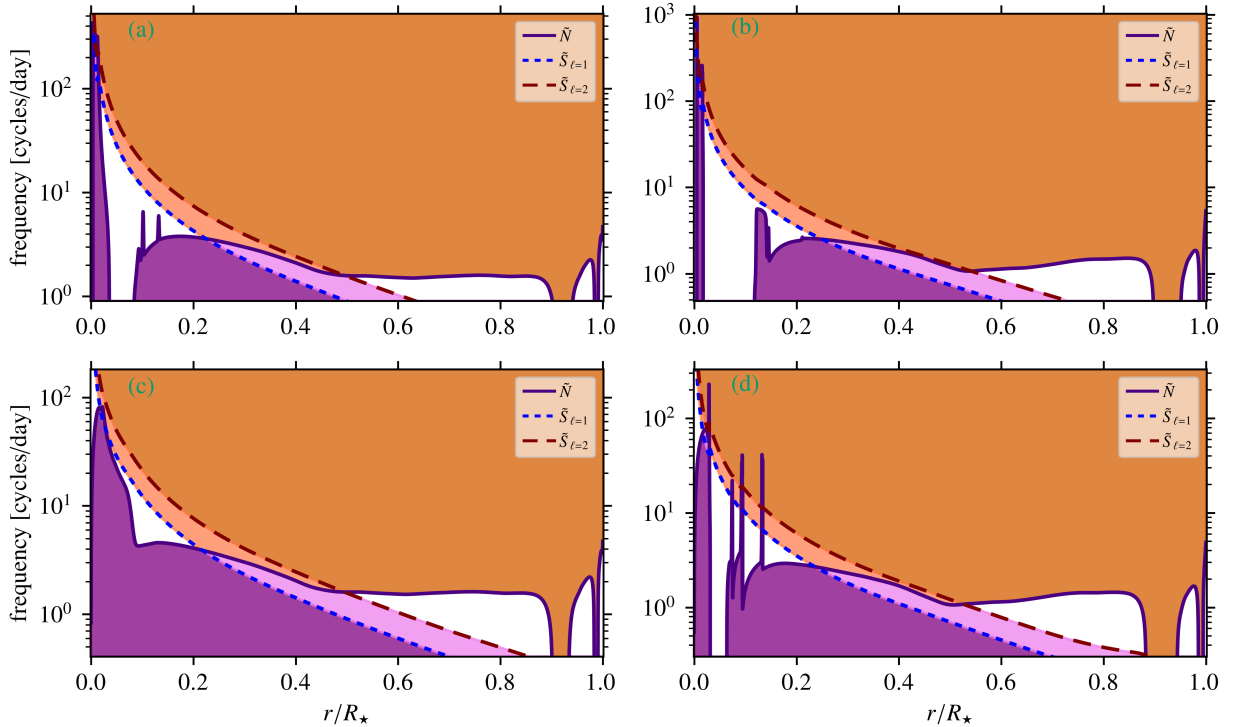


Figure C.2: Propagation diagrams of the $6.0 + 2.4 M_{\odot}$ merger product (a) and $7.8 M_{\odot}$ (c) genuine single star, and the $9.0 + 6.3 M_{\odot}$ merger product (b) and $13.6 M_{\odot}$ genuine single star (d) from Fig. 4.2 and Fig. 4.4, respectively, now as a function of the relative radial coordinate, r/R_{\star} . The ξ_r nodes are left out for clarity.

C.2. Propagation diagrams as a function of radial coordinate

In Fig. C.2 we show the propagation diagrams from Figs. 4.2 and 4.4 as a function of the relative radial coordinate r/R_{\star} instead of relative mass coordinate m/M_{\star} . The ξ_r nodes are left out for clarity. Figure C.3 shows zoomed-in views of the inner 20% in relative radial coordinate of propagation diagrams in Fig. C.2.

C.3. Effect of semi-convection efficiency on ICZs

In Fig. C.4a we show a zoomed-in view of the Kippenhahn diagram of the $13.6 M_{\odot}$ genuine single star during its HG evolution. The structure of the ICZ, which was first described in Sect. 4.3.1.2, is clearer here. A more extended, non-uniform convection zone appears when the star arrives on the HG, which is responsible for the spiky features in the outer g-mode cavity of the $13.6 M_{\odot}$ genuine single star (see Sect. 4.3.1.2). Afterwards, a uniform ICZ appears, which persists until core-He ignition. As mentioned in Sect. 4.3.1.2 and demonstrated by Kaiser et al. (2020) and Sibony et al. (2023), the extent and lifetime of these ICZs depend on the assumptions made for (semi-)convective mixing. To demonstrate this effect in our setup, we computed the same model with a semi-convection efficiency of $\alpha_{sc} = 0.1$, shown in Fig. C.4b. With lower values of α_{sc} , an ICZ also appears. We note that the ICZ has a different morphology and lifetime. As shown in the main text of this work, ICZs are

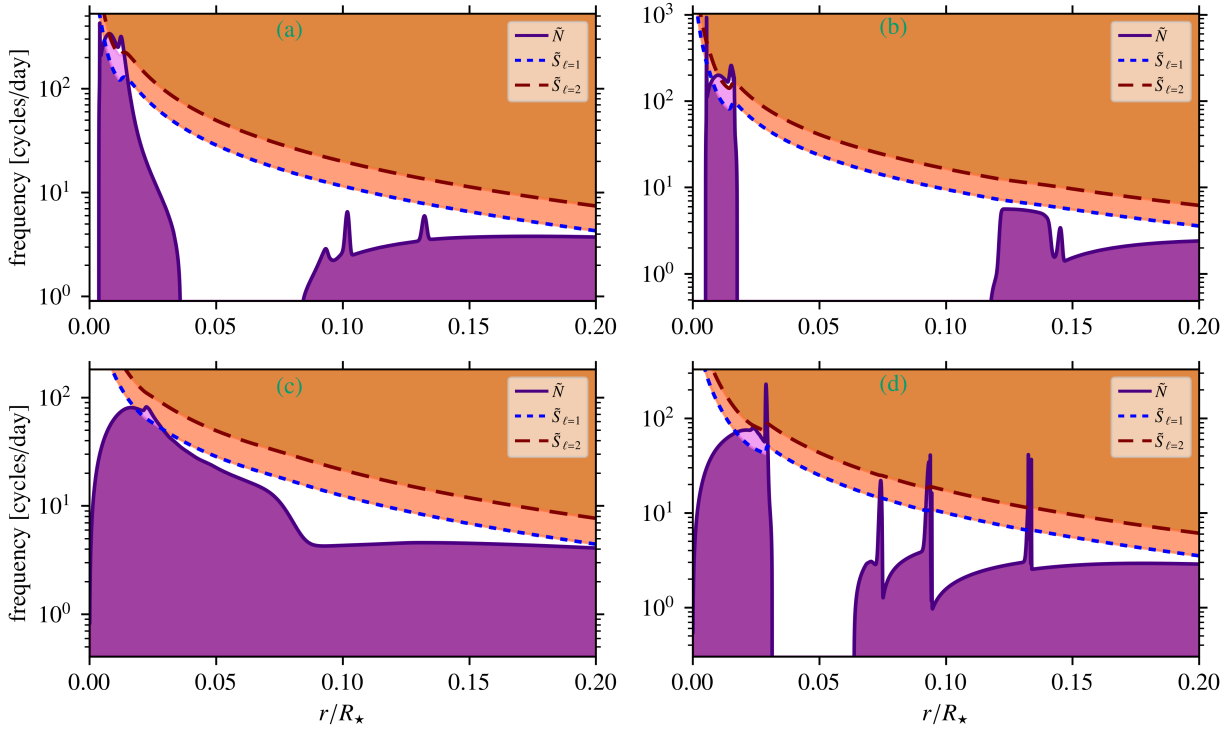


Figure C.3: Same as Fig. C.2 but now zoomed in on the region with $r/R_\star \leq 0.2$.

responsible for the appearance of deep dips in the PSPs of genuine single stars. The detection of these deep dips in the PSPs of genuine single stars with ICZ, if detectable at all, thus depends on the assumptions for (semi-)convection and on the time in the evolution that a genuine single HG star is observed. However, as demonstrated in Sects. 4.3.1.1 and 4.3.1.2, even without an ICZ, merger products and genuine single stars are distinguishable based on their asymptotic period spacing values.

C.4. Disentangling of dip structures in genuine single stars with an ICZ

Figure C.5 shows a part of the $13.6 M_\odot$ genuine single star’s PSP for $(\ell, m) = (1, 0)$ modes without rotation, which is shown in full in Fig. 4.5. As in Fig. 4.8, we add the value of Δ_{U89} (Eq. 4.1) for each mode in the PSP. We see that only the deep, narrow dips have most of their kinetic energy in the outer g-mode cavity ($\Delta_{U89} < 1$). Following the discourse from Sect. 4.3.2, these are the dips caused by mode coupling between inner- and outer-cavity g-modes. The more regular, quasi-periodic variation in the PSP involves only modes with most of their kinetic energy in the inner g-mode cavity ($\Delta_{U89} \approx 1$). This confirms that the quasi-periodic variation of these modes in the PSP is caused by mode trapping in the inner g-mode cavity (see e.g. Michielsen et al. 2021 for details on mode trapping).

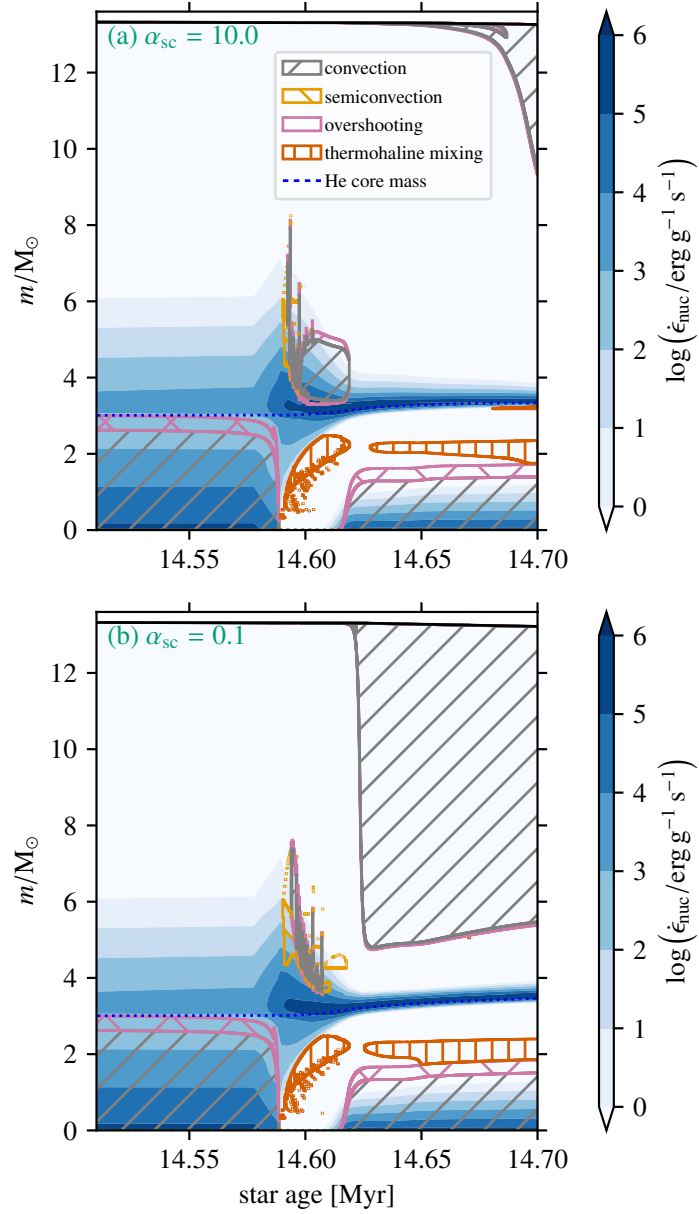


Figure C.4: Kippenhahn diagram for a $13.6 M_{\odot}$ genuine single star with an intermediate convection zone for $\alpha_{\text{sc}} = 10.0$ (a) and $\alpha_{\text{sc}} = 0.1$ (b).

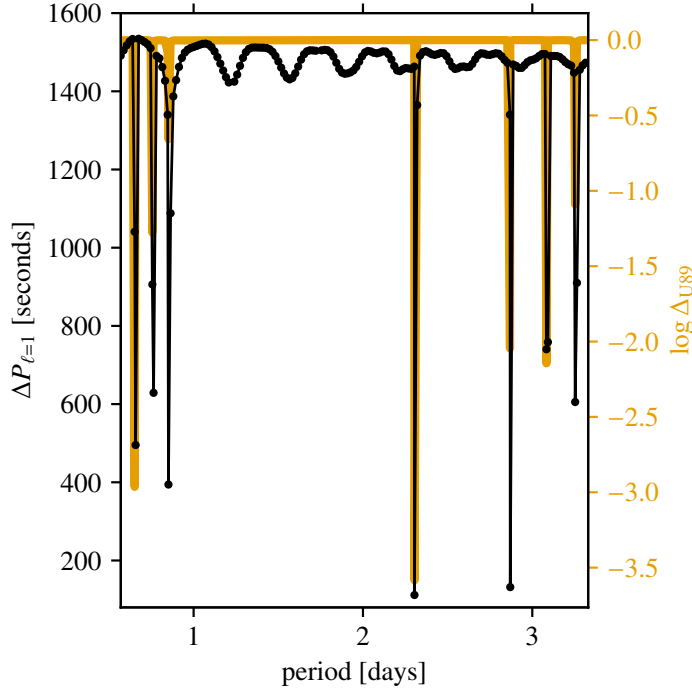


Figure C.5: Same as Fig. 4.8 but for the $13.6 M_{\odot}$ genuine single star and $(\ell, m) = (1, 0)$ modes.

C.5. Wave displacements and differential mode inertia for a selection of modes

Figures C.6 and C.7 show the wave displacements $\xi_r(r)$, $\xi_h(r)$ and the differential mode inertia dE/dr (see Eq. 3.139 in Aerts et al. 2010a) for a selection of long-period (high-frequency) pure g modes of the merger product and genuine single-star models described in Sects. 4.3.1.1 and 4.3.1.2. We computed these mode properties with GYRE’s non-adiabatic setting to include non-adiabatic effects such as damping. Since we used the boundary conditions from Unno et al. (1989), the wave displacements at the surface behave as

$$\frac{\xi_h(r = R_{\star})}{\xi_r(r = R_{\star})} \simeq \frac{GM_{\star}}{R_{\star}^3 \omega^2}. \quad (\text{C.1})$$

Using this relation, we normalised the wave displacements such that $\xi_r(r = R_{\star}) \equiv 1$. In Fig. C.8, we show the equivalent plots for p-g mixed modes (shorter period, higher frequencies) for the $6.0 + 2.4 M_{\odot}$ merger product and $7.8 M_{\odot}$ genuine single star.

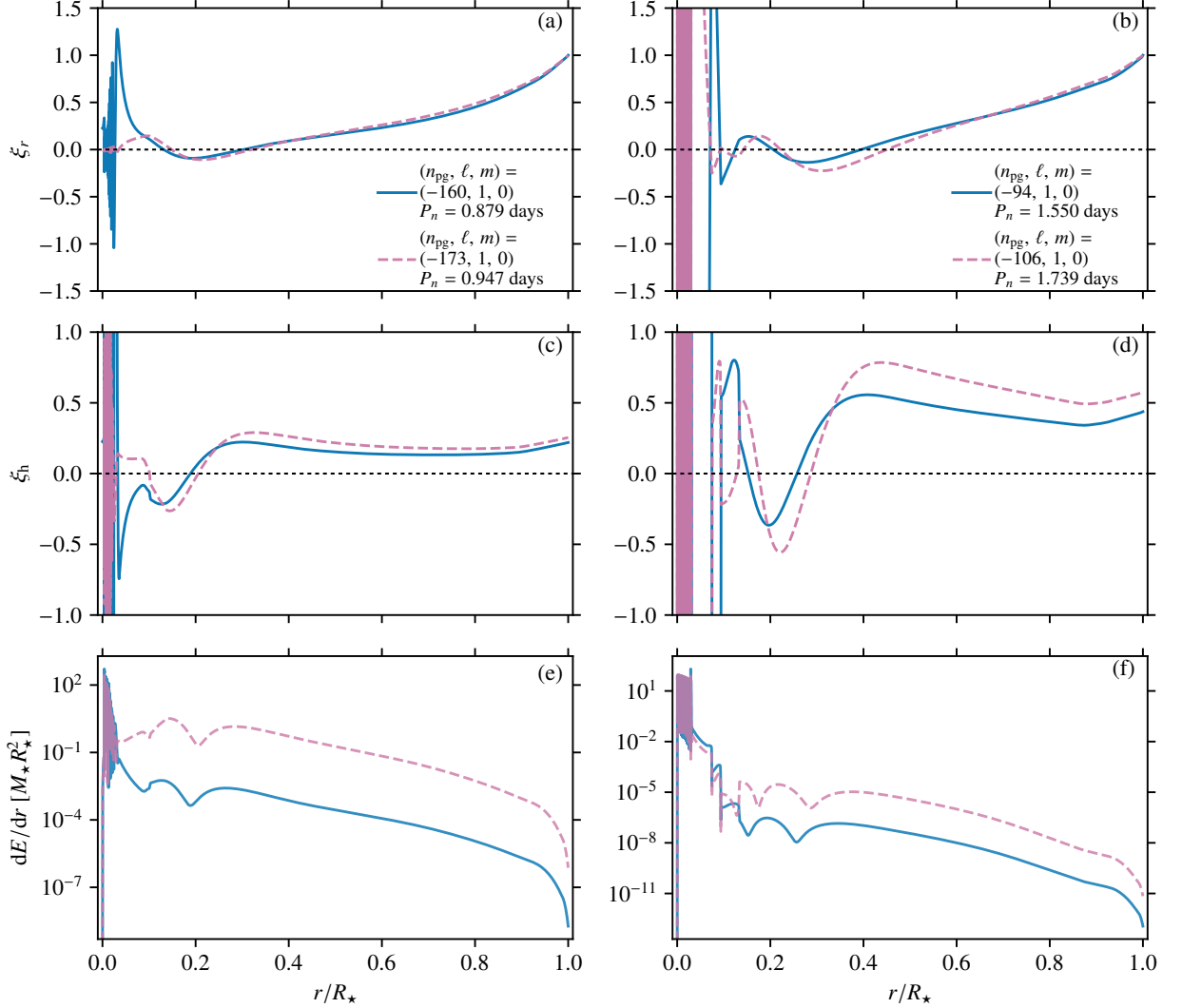


Figure C.6: Wave displacement and differential mode inertia profiles for the $6.0 + 2.4 M_\odot$ merger product (left column) and $7.8 M_\odot$ genuine single star (right column) from non-adiabatic GYRE calculations for pure g modes in the long-period (low-frequency) regime. Panel (a)–(b) show the radial wave displacement $\xi_r(r)$, Panel (c)–(d) the horizontal wave displacement $\xi_h(r)$, and Panel (e)–(f) the differential mode inertia dE/dr . The dashed pink lines in Panel (a), (c), and (e) show the aforementioned quantities for a mode in a deep PSP dip. The solid blue lines show those for a mode outside of a deep PSP dip, that is, for an inner-cavity g mode.

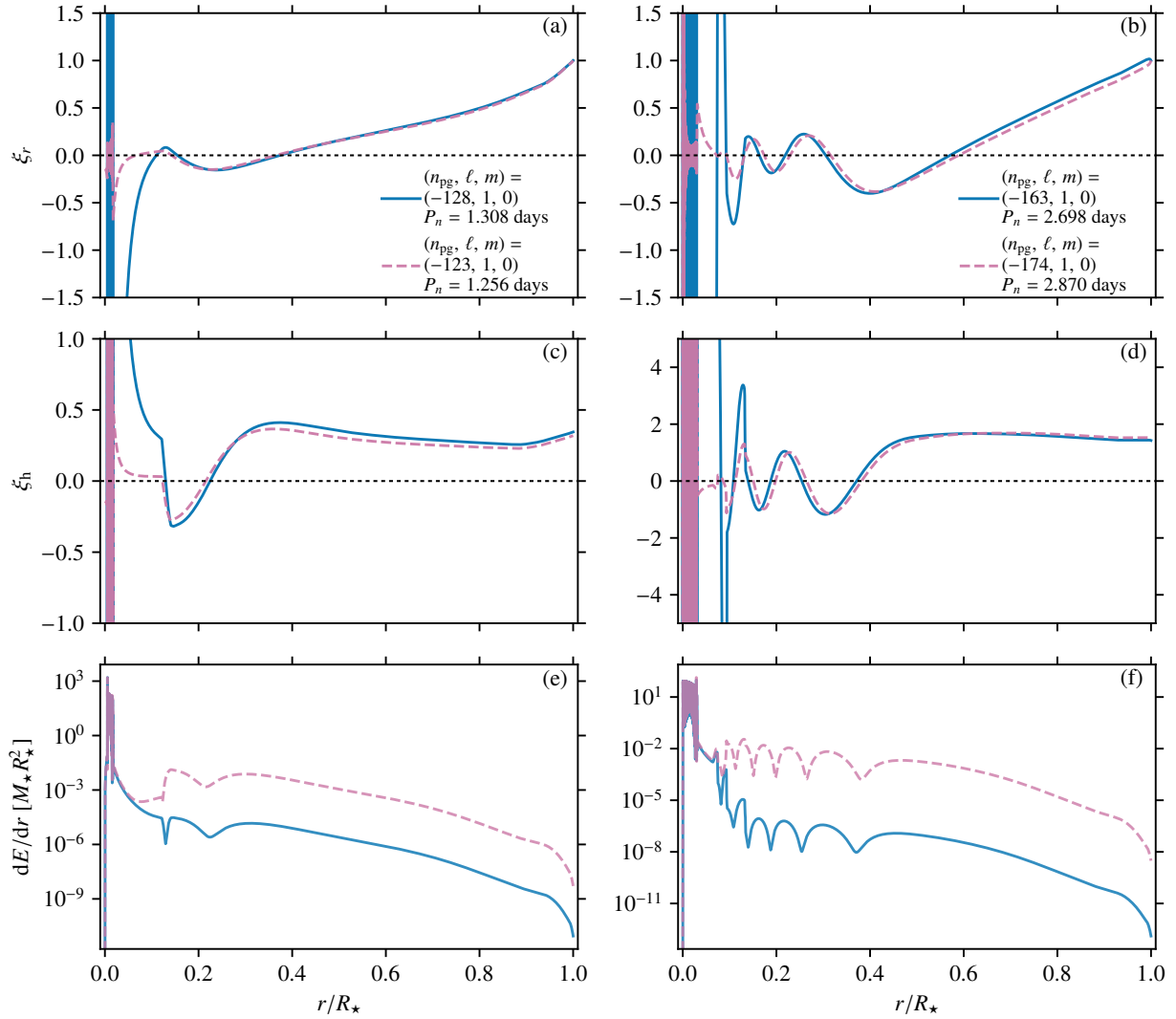


Figure C.7: Same as Fig. C.6 but for the $9.0 + 6.3 M_\odot$ merger product (left column) and $13.6 M_\odot$ genuine single star (right column). The dashed pink lines in all panels show the aforementioned quantities for a mode in a deep PSP dip. The solid blue lines show those for a mode outside of a deep PSP dip, that is, for an inner-cavity g mode.

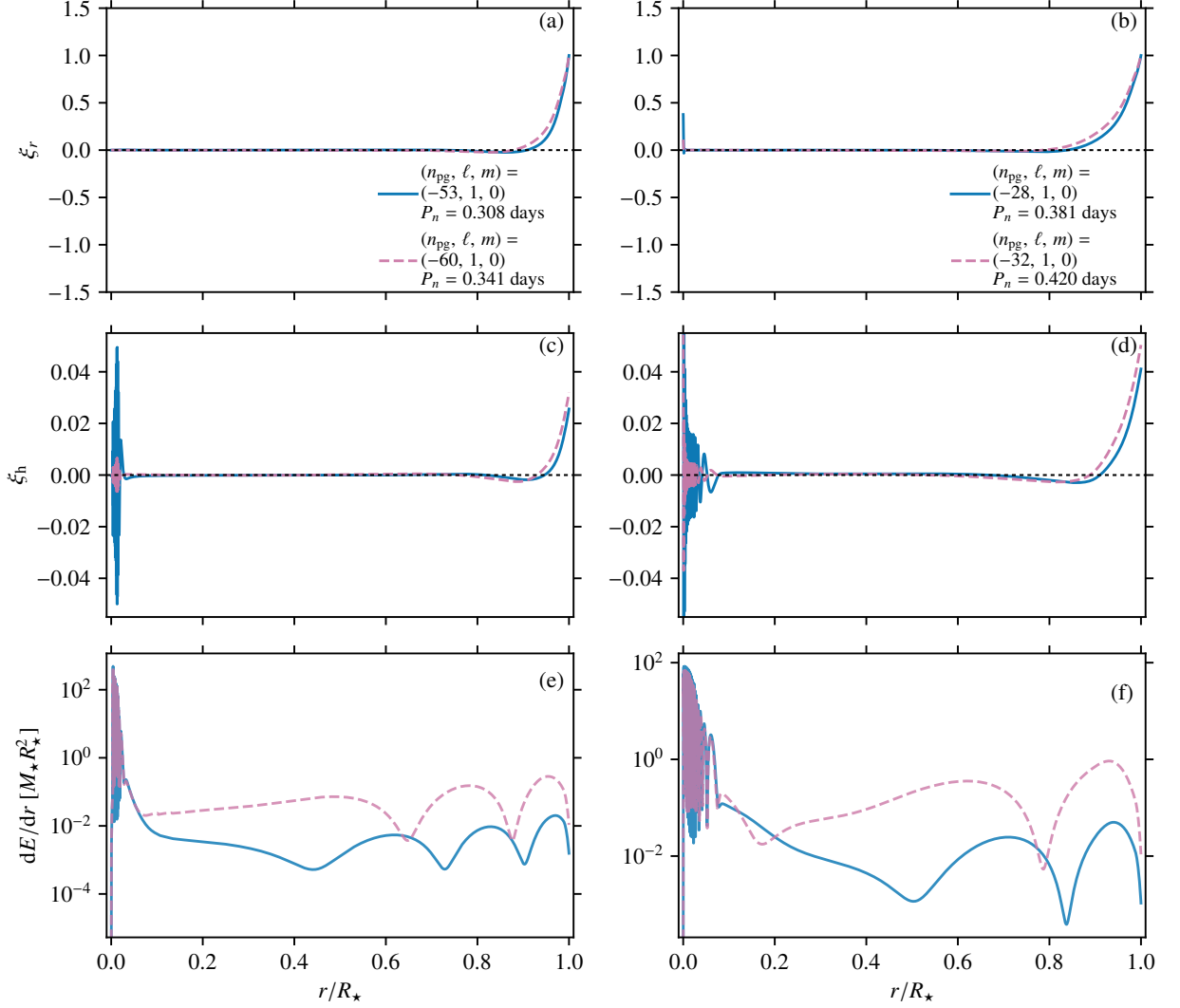


Figure C.8: Same as Fig. C.6 but for p-g mixed modes predicted for the 6.0 + 2.4 M_{\odot} merger product (left column) and 7.8 M_{\odot} genuine single star (right column). The dashed pink lines in all panels show the aforementioned quantities for a mode in a deep PSP dip. The solid blue lines show those for a mode outside of a deep PSP dip, that is, for an inner-cavity g mode. The radial orders $n_{pg} = n_p - n_g$ of the p-g mixed modes in these plots are as follows: $n_{pg} = -53 = 3 - 56$, $n_{pg} = -60 = 2 - 62$, $n_{pg} = -28 = 2 - 30$, and $n_{pg} = -32 = 1 - 33$.

Appendices for Chapter 5: ‘Astero-seismic predictions for a massive main-sequence merger product’

D.1. Period spacing patterns for $\ell = 2$ modes of 3D MHD merger product

Figure D.1 shows the PSPs for the $(\ell, m) = (2, 0)$ modes of the $16.9 M_{\odot}$ 3D MHD merger product and its corresponding $17.4 M_{\odot}$ genuine single star.

D.2. Mean envelope density and sound speed comparison

In Fig. D.2, we compare the mean values of the density ρ and sound speed c_s in the respective envelopes of the $16.9 M_{\odot}$ 3D MHD merger product and $17.4 M_{\odot}$ genuine single star. The bottom of the envelope is taken as the location where the mass coordinate $m = M_{cc}$. We interpolated the density and sound speed on a grid of equal-sized (in radius) cells to arrive at weighted means.

D.3. Comparison of p modes with rotation

Figures D.3 and D.4 show the results of the GYRE calculations for p modes with the inclusion of rotation in the first-order Ledoux perturbative approach (see Sect. 5.2.3). We only show the results for the models at the point where $X_{c, \text{merger}} = 0.50$. Figure D.3 only shows the results for $\Omega/\Omega_c = 0.30$.

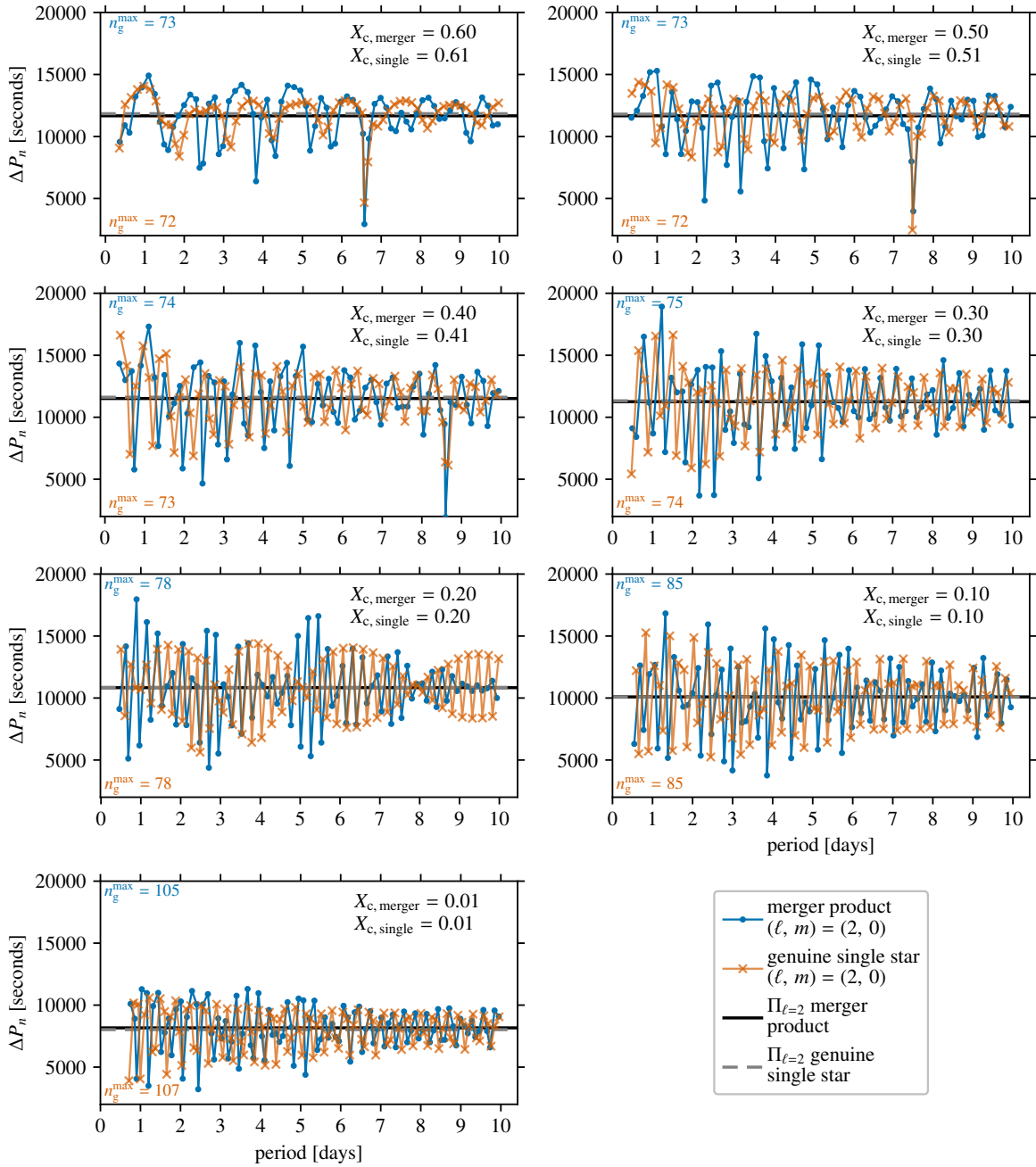


Figure D.1: Same as Fig. 5.6, now for $\ell = 2$ modes.

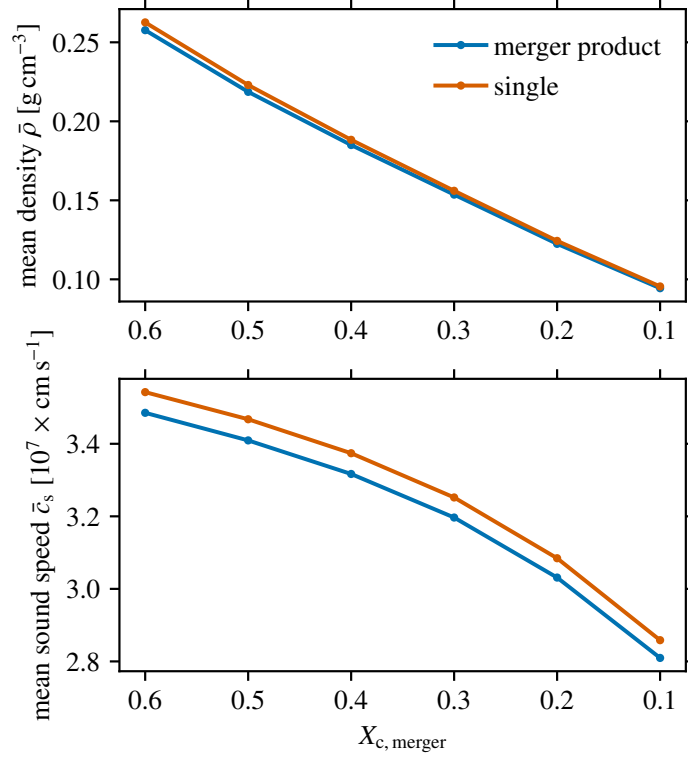


Figure D.2: Mean envelope density (top panel) and sound speed (bottom panel) for the $16.9 M_{\odot}$ 3D MHD merger product (blue line) and $17.4 M_{\odot}$ genuine single star (red line) at different MS ages.

D.4. Composition profiles and propagation diagrams for 1D merger methods

Figures D.5–D.7 and D.8–D.10 show the evolution of the composition profiles and propagation diagrams with X_c for the $16.9 M_{\odot}$ entropy-sorted, PyMMAMS, and fast accretion merger product models and their genuine single star counterparts, respectively.

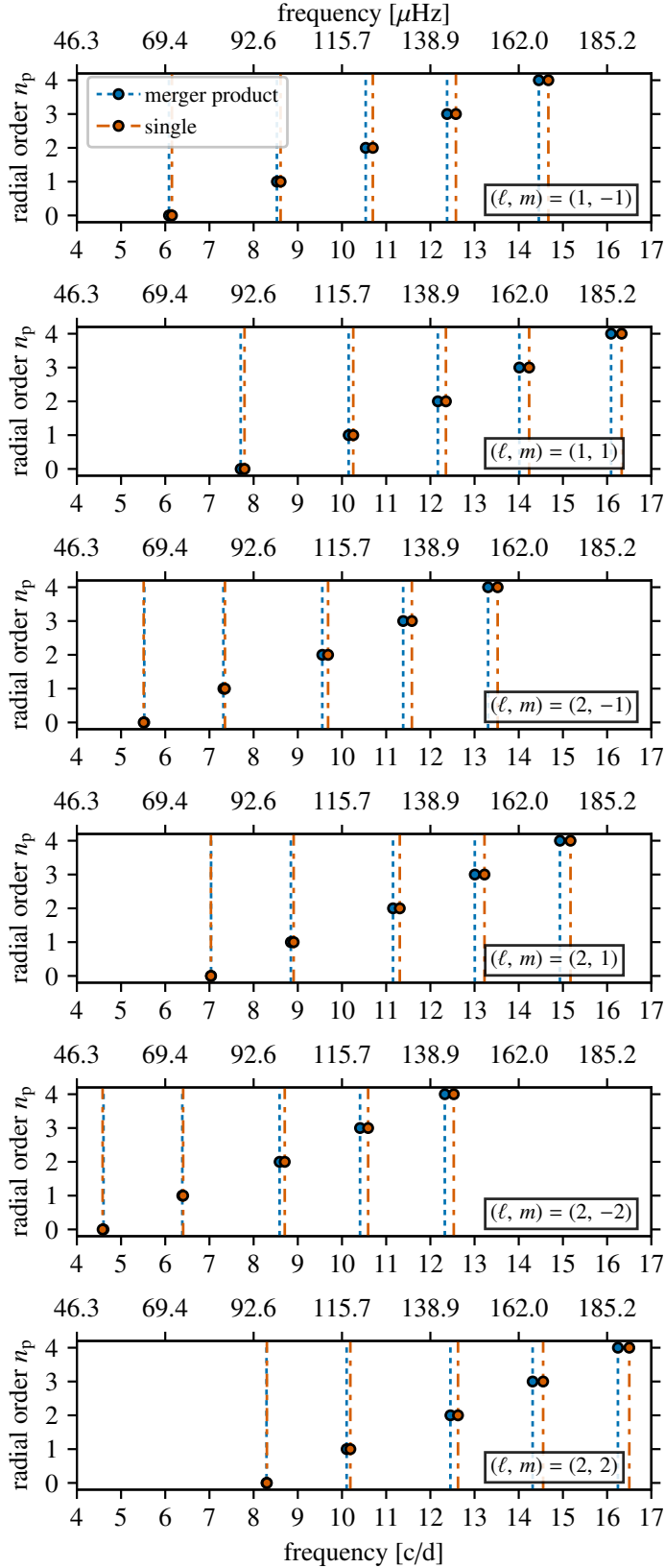


Figure D.3: Frequencies and radial orders n_p of $(\ell, m) = (1, \pm 1)$, $(2, \pm 1)$, and $(2, \pm 2)$ p modes for the $16.9 M_\odot$ 3D MHD merger product (blue dot markers) and the $17.4 M_\odot$ genuine single star (red dot markers) at $X_c = 0.50$ and with $\Omega/\Omega_c = 0.30$. The dotted and dash-dotted lines are drawn to accentuate the frequency differences and improve the legibility of the frequency values. The modes are shown in the inertial (observer’s) frame.

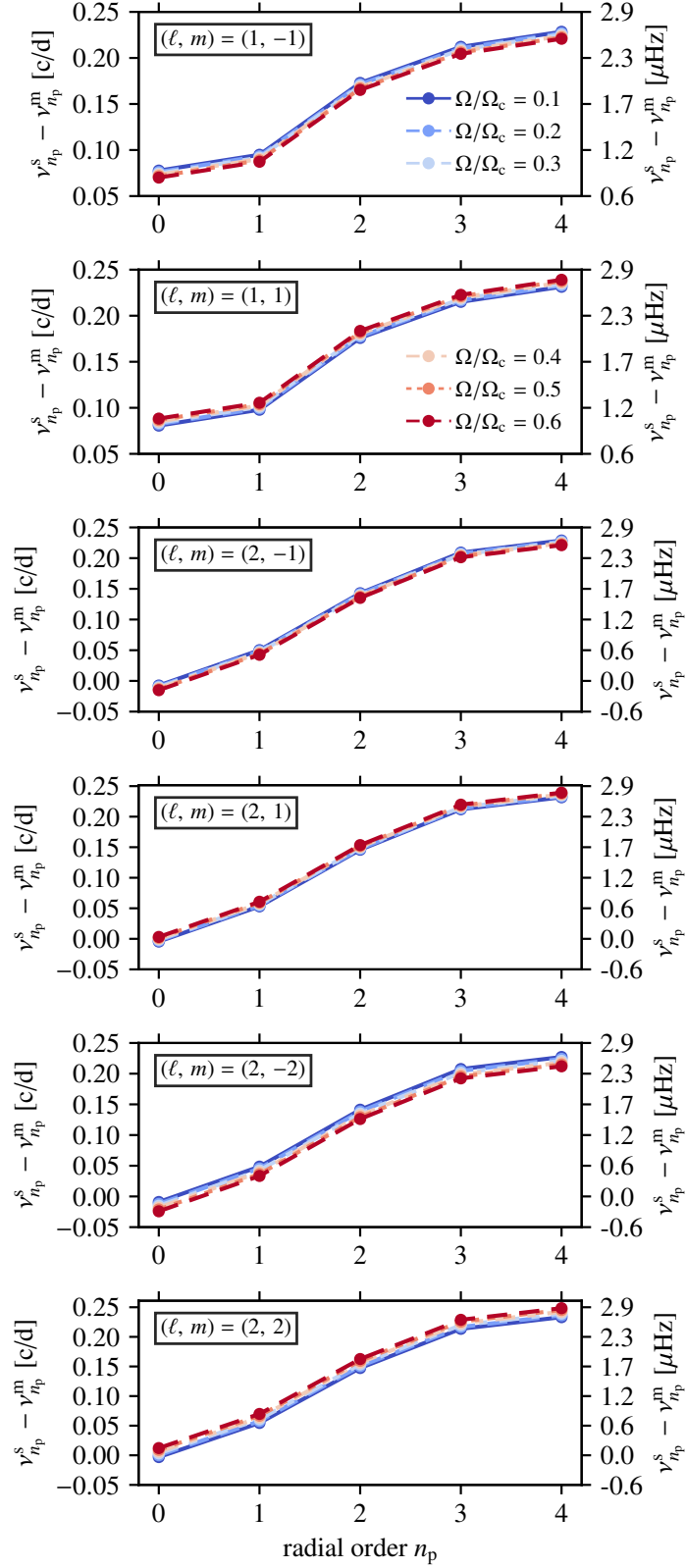


Figure D.4: Absolute differences between the $17.4 M_{\odot}$ genuine single star's p-mode frequencies $\nu_{n_p}^s$ and the $16.9 M_{\odot}$ 3D MHD merger product's p-mode frequencies $\nu_{n_p}^m$ per radial order n_p , with rotation rates of $\Omega/\Omega_c = 0.10, 0.20, 0.30, 0.40, 0.50,$ and 0.60 , at $X_c = 0.50$. The lines are colour-coded according to the rotation rate. The modes are shown in the inertial (observer's) frame.

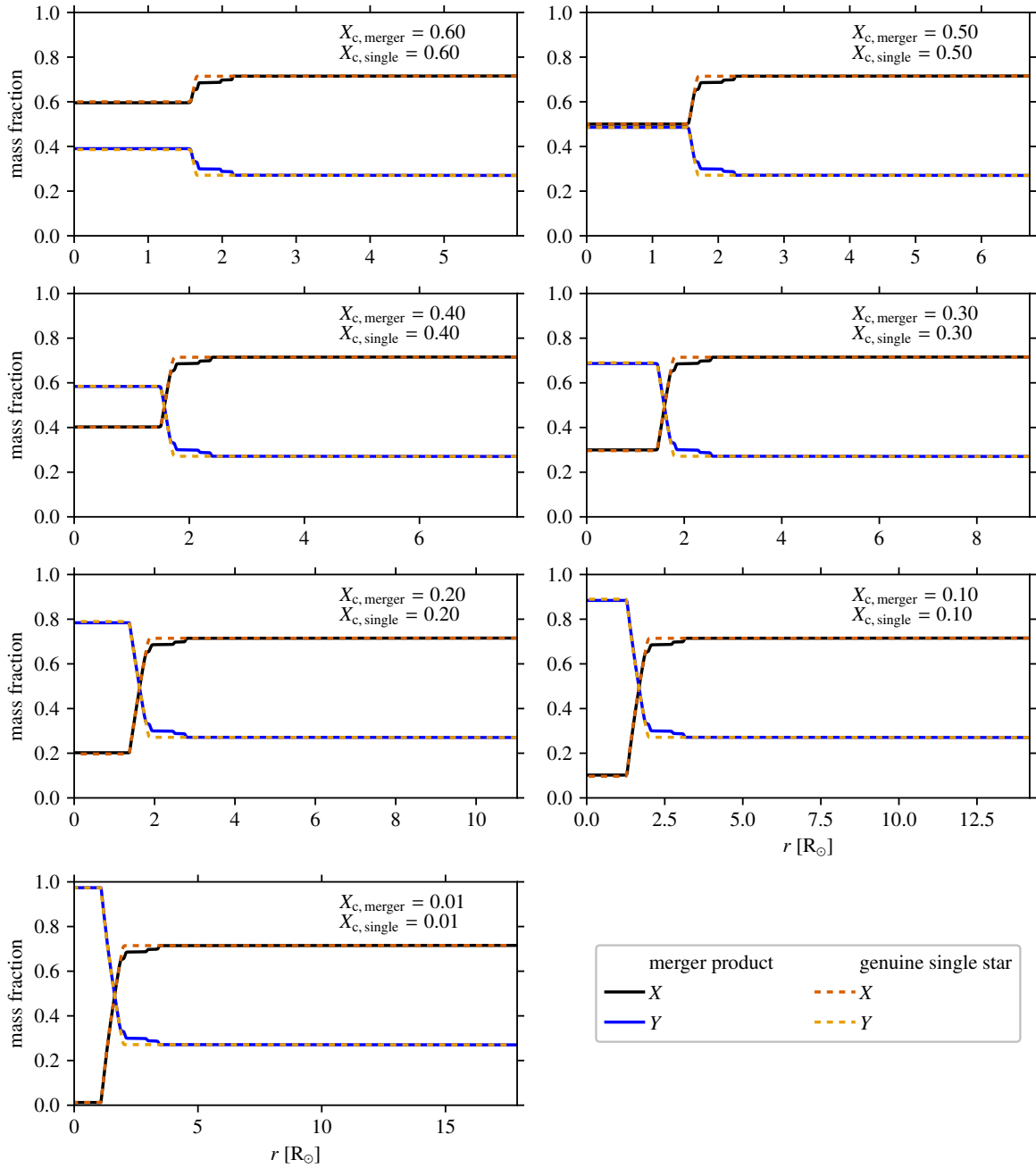


Figure D.5: Same as Fig. 5.2, now for the $16.9 M_{\odot}$ entropy-sorted merger product (solid lines) and the $17.15 M_{\odot}$ genuine single star (dashed lines).

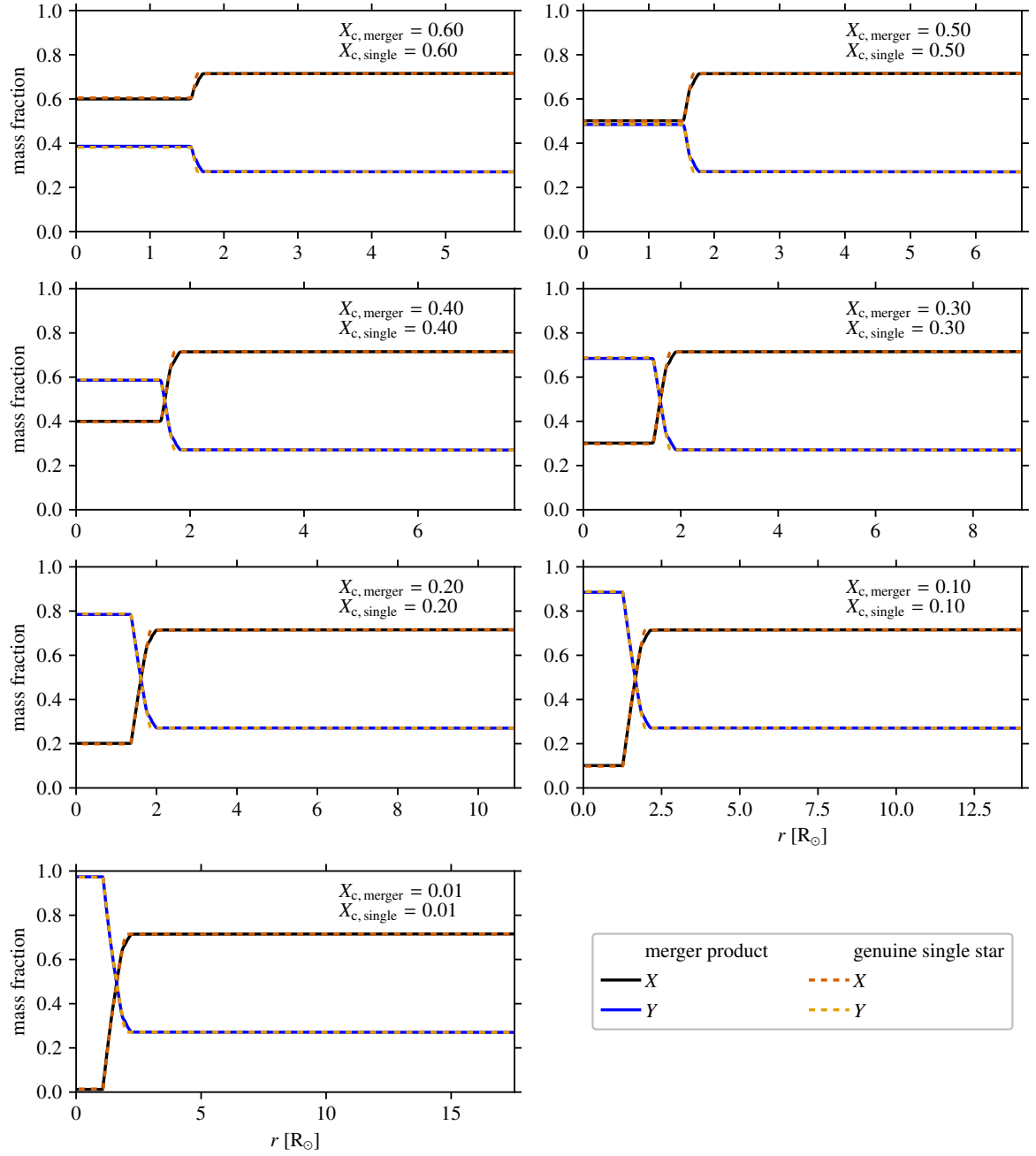


Figure D.6: Same as Fig. 5.2, now for the $16.9 M_{\odot}$ PyMMAMS merger product (solid lines) and the $17.0 M_{\odot}$ genuine single star (dashed lines).

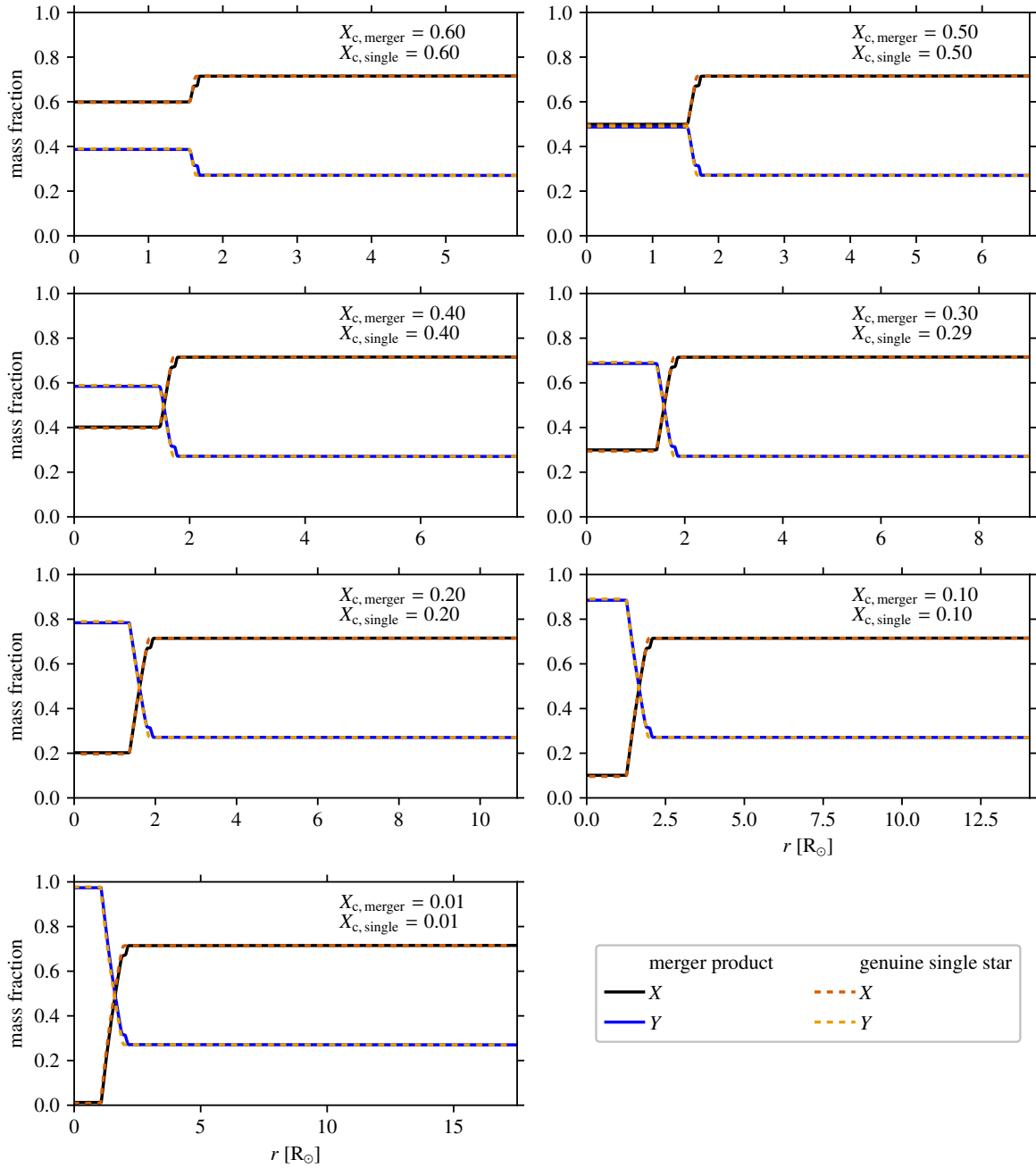


Figure D.7: Same as Fig. 5.2, now for the $16.9 M_{\odot}$ fast accretion merger product (solid lines) and the $16.9 M_{\odot}$ genuine single star (dashed lines).

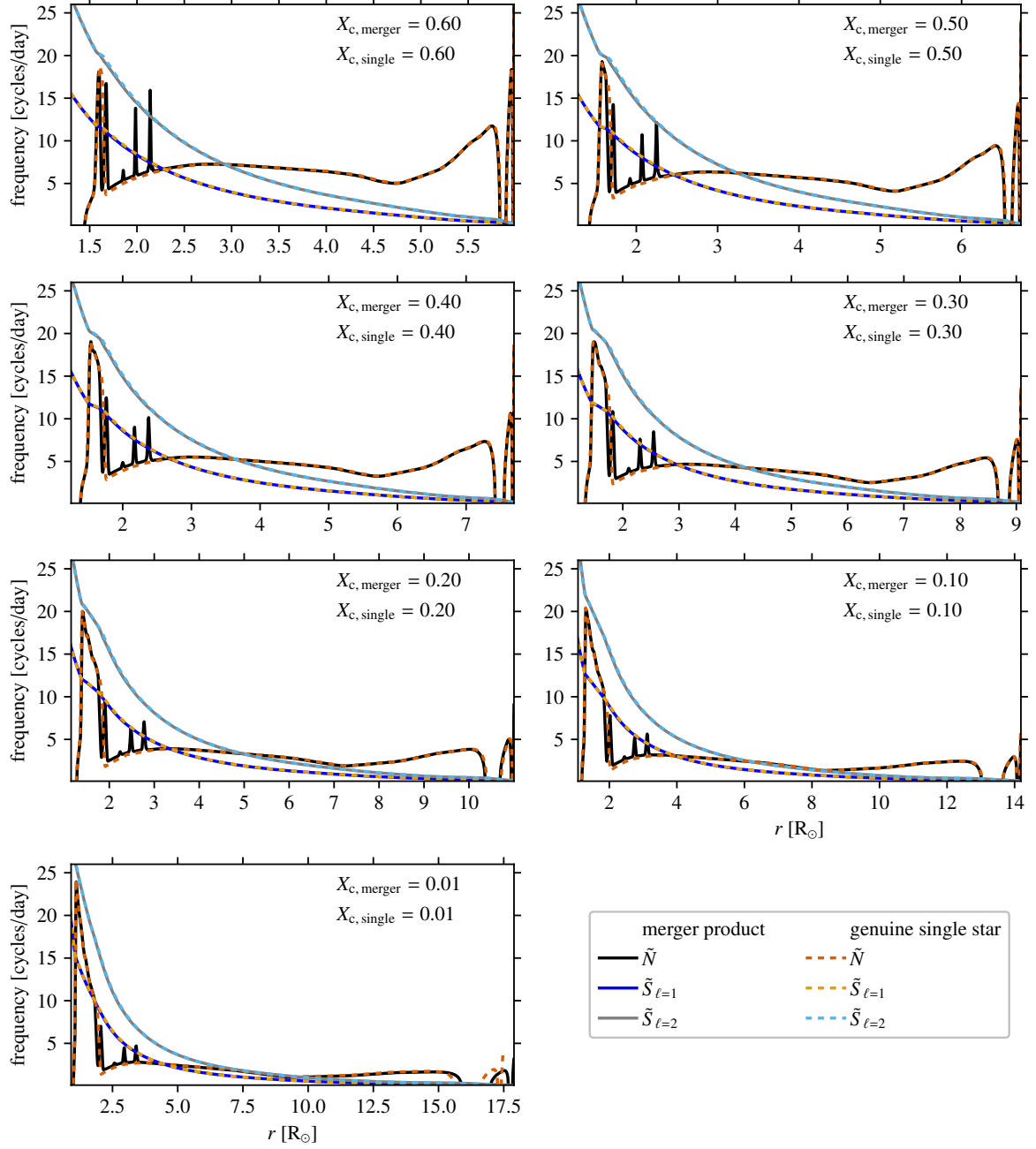


Figure D.8: Same as Fig. 5.5, now for the $16.9 M_{\odot}$ entropy-sorted merger product (solid lines) and the $17.15 M_{\odot}$ genuine single star (dashed lines).

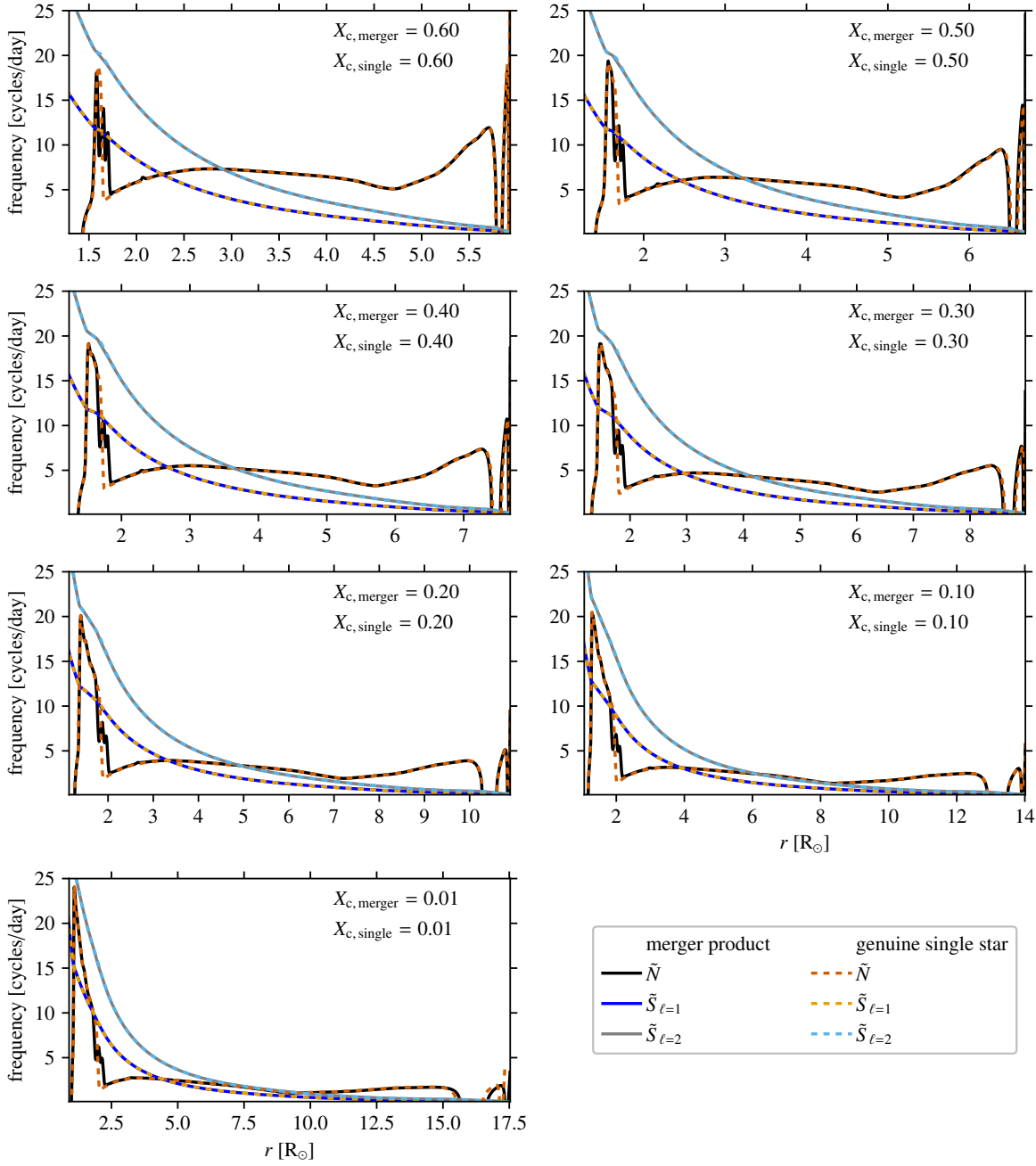


Figure D.9: Same as Fig. 5.5, now for the $16.9 M_{\odot}$ PyMMAMS merger product (solid lines) and the $17.0 M_{\odot}$ genuine single star (dashed lines).

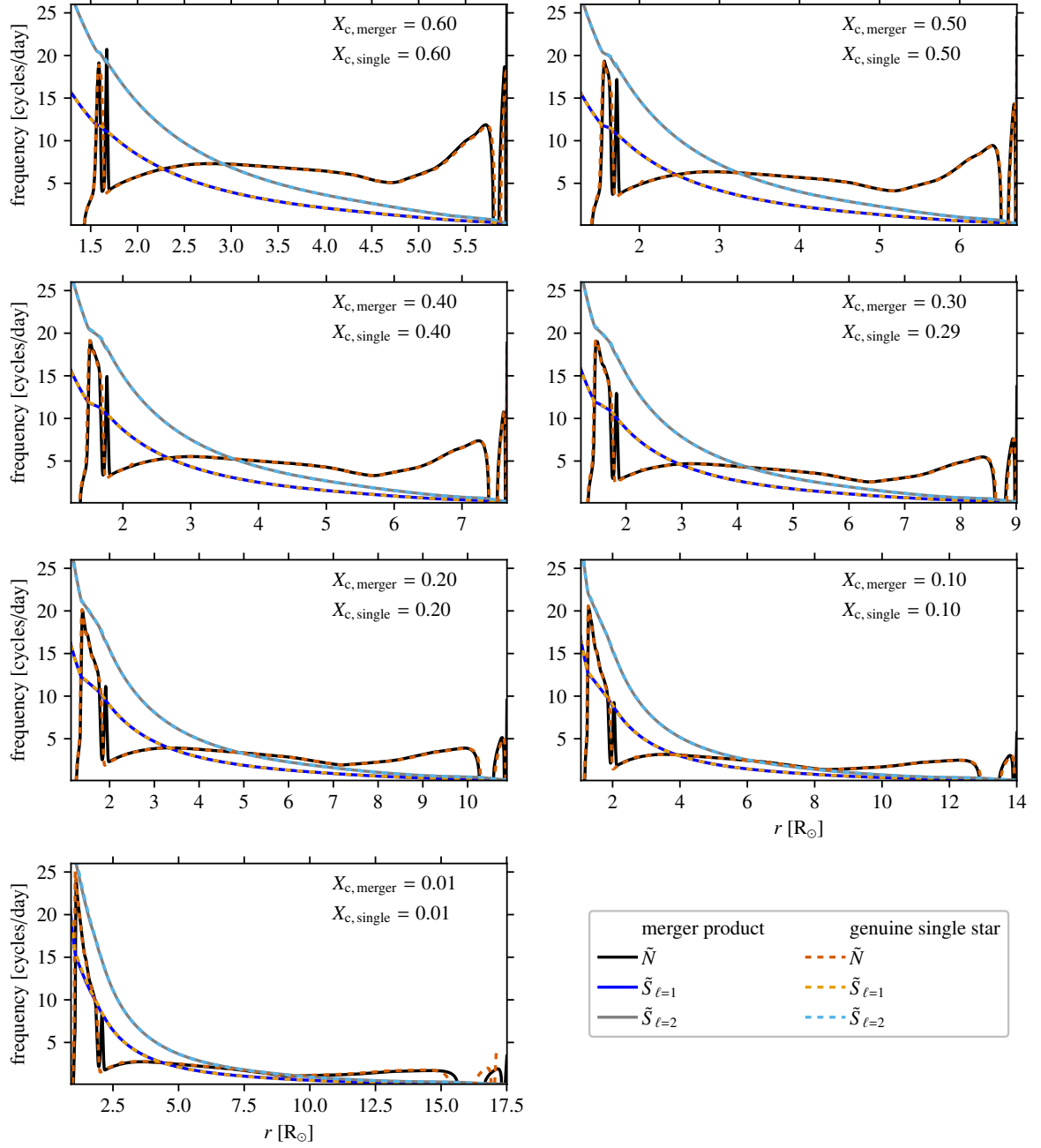


Figure D.10: Same as Fig. 5.5, now for the $16.9 M_{\odot}$ fast accretion merger product (solid lines) and the $16.9 M_{\odot}$ genuine single star (dashed lines).

List of publications

Papers used in this thesis:

- [1] **Henneco, J.**; Schneider, F. R. N.; Heller, M.; Hekker, S.; Aerts, C.; soon to be submitted; *Asteroseismic predictions for a massive main-sequence merger product*
- [2] **Henneco, J.**; Schneider, F. R. N.; Laplace, L.; 2024; **A&A**, **690** **A65**; *Merger seismology: Distinguishing massive merger products from genuine single stars using asteroseismology*
- [3] **Henneco, J.**; Schneider, F. R. N.; Hekker, S.; Aerts, C.; 2024; **A&A**, **682** **A169**; *Contact tracing of binary stars: Pathways to stellar mergers*

Papers not used in this thesis:

- [1] Gull, M.; Weisz, D. R.; El-Badry, K.; **Henneco, J.**; Savino, A.; Durbin, M.; Choi, Y.; Cohen, R. E.; Cole, A. A.; Correnti, M.; Dalcanton, J. J.; Gilbert, K. M.; Goldman, S. R.; Guhathakurta, P.; McQuinn, K. B. W.; Newman, M. J. B.; Skillman, E. D.; Williams, B. F.; 2024; **submitted to ApJ**; *A Low Metallicity Massive Contact Binary Star System Candidate in WLM identified by Hubble and James Webb Space Telescope imaging*
- [2] **Henneco, J.**; Van Reeth, T.; Prat, V.; Mathis, S.; Mombarg, J. S. G.; Aerts, C.; 2021; **A&A**, **648** **A97**; *The effect of the centrifugal acceleration on period spacings of gravito-inertial modes in intermediate-mass stars*

Bibliography

- Abdul-Masih, M., Escorza, A., Menon, A., Mahy, L., and Marchant, P., “Constraining the overcontact phase in massive binary evolution. II. Period stability of known O+O overcontact systems,” *Astronomy & Astrophysics*, vol. 666, p. A18, 2022, doi:10.1051/0004-6361/202244148, aDS Bibcode: 2022A&A...666A..18A.
- Aerts, C., “Probing the interior physics of stars through asteroseismology,” *Reviews of Modern Physics*, vol. 93, no. 1, 015001, 2021, doi:10.1103/RevModPhys.93.015001.
- Aerts, C., Bowman, D. M., S imon-D iaz, S., Buyschaert, B., Johnston, C., Moravveji, E., Beck, P. G., De Cat, P., Triana, S., Aigrain, S., et al., “K2 photometry and HERMES spectroscopy of the blue supergiant ρ Leo: rotational wind modulation and low-frequency waves,” *Monthly Notices of the Royal Astronomical Society*, vol. 476, no. 1, pp. 1234–1241, 2018a, doi:10.1093/mnras/sty308.
- Aerts, C., Christensen-Dalsgaard, J., and Kurtz, D. W., *Asteroseismology*, Springer Dordrecht, 2010a, doi:10.1007/978-1-4020-5803-5.
- Aerts, C., Lefever, K., Baglin, A., Degroote, P., Oreiro, R., Vučkovi c, M., Smolders, K., Acke, B., Verhoelst, T., Desmet, M., et al., “Periodic mass-loss episodes due to an oscillation mode with variable amplitude in the hot supergiant HD 50064,” *Astronomy & Astrophysics*, vol. 513, L11, 2010b, doi:10.1051/0004-6361/201014124.
- Aerts, C. and Mathis, S., “Mode coupling coefficients between the convective core and radiative envelope of γ Doradus and slowly pulsating B stars,” *Astronomy & Astrophysics*, vol. 677, A68, 2023, doi:10.1051/0004-6361/202347196.
- Aerts, C., Mathis, S., and Rogers, T. M., “Angular Momentum Transport in Stellar Interiors,” *Annual Review of Astronomy and Astrophysics*, vol. 57, pp. 35–78, 2019, doi:10.1146/annurev-astro-091918-104359.
- Aerts, C., Molenberghs, G., Michielsen, M., Pedersen, M. G., Bj orklund, R., Johnston, C., Mombarg, J. S. G., Bowman, D. M., Buyschaert, B., P apics, P. I., et al., “Forward Asteroseismic Modeling of Stars with a Convective Core from Gravity-mode Oscillations: Parameter Estimation and Stellar Model Selection,” *The Astrophysical Journal Supplement Series*, vol. 237, no. 1, 15, 2018b, doi:10.3847/1538-4365/aaccfb.

- Aerts, C., S imon-D iaz, S., Bloemen, S., Debosscher, J., Papics, P. I., Bryson, S., Still, M., Moravveji, E., Williamson, M. H., Grundahl, F., et al., “Kepler sheds new and unprecedented light on the variability of a blue supergiant: Gravity waves in the O9.5Iab star HD 188209,” *Astronomy & Astrophysics*, vol. 602, A32, 2017, doi:10.1051/0004-6361/201730571.
- Aerts, C., Thoul, A., Daszyńska, J., Scuflaire, R., Waelkens, C., Dupret, M. A., Niemczura, E., and Noels, A., “Asteroseismology of HD 129929: Core Overshooting and Nonrigid Rotation,” *Science*, vol. 300, no. 5627, pp. 1926–1928, 2003, doi:10.1126/science.1084993.
- Aerts, C. and Tkachenko, A., “Asteroseismic Modelling of Fast Rotators and its Opportunities for Astrophysics,” *arXiv e-prints*, arXiv:2311.08453, 2023, doi:10.48550/arXiv.2311.08453.
- Aerts, C., Waelkens, C., Daszyńska-Daszkiewicz, J., Dupret, M. A., Thoul, A., Scuflaire, R., Uytterhoeven, K., Niemczura, E., and Noels, A., “Asteroseismology of the β Cep star HD 129929. I. Observations, oscillation frequencies and stellar parameters,” *Astronomy & Astrophysics*, vol. 415, pp. 241–249, 2004, doi:10.1051/0004-6361:20034142.
- Aerts, C., Waelkens, C., De Cat, P., Kolenberg, K., Kestens, E., Grenon, M., and Eyer, L., “Pulsating B Stars Discovered by HIPPARCOS,” *The Journal of the American Association of Variable Star Observers*, vol. 35, no. 1, p. 58, 2006.
- Andersen, M. F., Grundahl, F., Beck, A. H., and Pall e, P., “The SONG prototype: Efficiency of a robotic telescope,” in “Revista Mexicana de Astronom a y Astrof sica Conference Series,” *Revista Mexicana de Astronom a y Astrof sica Conference Series*, vol. 48, pp. 54–58, 2016, doi:10.48550/arXiv.1901.08293.
- Andrassy, R., Leidi, G., Higl, J., Edelmann, P. V. F., Schneider, F. R. N., and R opke, F. K., “Towards a self-consistent model of the convective core boundary in upper main sequence stars. I. 2.5D and 3D simulations,” *Astronomy & Astrophysics*, vol. 683, A97, 2024, doi:10.1051/0004-6361/202347407.
- Angelou, G. C., Bellinger, E. P., Hekker, S., Mints, A., Elsworth, Y., Basu, S., and Weiss, A., “Convective boundary mixing in low- and intermediate-mass stars - I. Core properties from pressure-mode asteroseismology,” *Monthly Notices of the Royal Astronomical Society*, vol. 493, no. 4, pp. 4987–5004, 2020, doi:10.1093/mnras/staa390.
- Antonini, F., Lombardi, J., James C., and Merritt, D., “Tidal Breakup of Binary Stars at the Galactic Center. II. Hydrodynamic Simulations,” *Astrophysical Journal*, vol. 731, no. 2, 128, 2011, doi:10.1088/0004-637X/731/2/128.
- Asplund, M., Grevesse, N., Sauval, A. J., and Scott, P., “The Chemical Composition of the Sun,” *Annual Review of Astronomy and Astrophysics*, vol. 47, no. 1, pp. 481–522, 2009, doi:10.1146/annurev.astro.46.060407.145222.
- Astropy Collaboration, Price-Whelan, A. M., Lim, P. L., Earl, N., Starkman, N., Bradley, L., Shupe, D. L., Patil, A. A., Corrales, L., Brasseur, C. E., et al., “The Astropy Project: Sustaining and Growing a Community-oriented Open-source Project and the Latest Major Release (v5.0) of the Core Package,” *Astrophysical Journal*, vol. 935, no. 2, 167, 2022, doi:10.3847/1538-4357/ac7c74.

- Astropy Collaboration, Price-Whelan, A. M., Sipőcz, B. M., Günther, H. M., Lim, P. L., Crawford, S. M., Conseil, S., Shupe, D. L., Craig, M. W., Dencheva, N., et al., “The Astropy Project: Building an Open-science Project and Status of the v2.0 Core Package,” *The Astronomical Journal*, vol. 156, no. 3, 123, 2018, doi:10.3847/1538-3881/aabc4f.
- Astropy Collaboration, Robitaille, T. P., Tollerud, E. J., Greenfield, P., Droettboom, M., Bray, E., Aldcroft, T., Davis, M., Ginsburg, A., Price-Whelan, A. M., et al., “Astropy: A community Python package for astronomy,” *Astronomy & Astrophysics*, vol. 558, A33, 2013, doi:10.1051/0004-6361/201322068.
- Auvergne, M., Bodin, P., Boissard, L., Buey, J. T., Chaintreuil, S., Epstein, G., Jouret, M., Lam-Trong, T., Levacher, P., Magnan, A., et al., “The CoRoT satellite in flight: description and performance,” *Astronomy & Astrophysics*, vol. 506, no. 1, pp. 411–424, 2009, doi:10.1051/0004-6361/200810860.
- Ballone, A., Costa, G., Mapelli, M., MacLeod, M., Tornamenti, S., and Pacheco-Arias, J. M., “Formation of black holes in the pair-instability mass gap: hydrodynamical simulations of a head-on massive star collision,” *Monthly Notices of the Royal Astronomical Society*, vol. 519, no. 4, pp. 5191–5201, 2023, doi:10.1093/mnras/stac3752.
- Balona, L. A., “Pulsation in hot main sequence stars: comparison of observations with models,” *Astrophysical Journal*, submitted, arXiv:2310.09805, 2024, doi:10.48550/arXiv.2310.09805.
- Banerjee, S., Kroupa, P., and Oh, S., “The emergence of super-canonical stars in R136-type starburst clusters,” *Monthly Notices of the Royal Astronomical Society*, vol. 426, no. 2, pp. 1416–1426, 2012, doi:10.1111/j.1365-2966.2012.21672.x.
- Bellinger, E. P., de Mink, S. E., van Rossem, W. E., and Justham, S., “The Potential of Asteroseismology to Resolve the Blue Supergiant Problem,” *The Astrophysical Journal Letters*, vol. 967, no. 2, L39, 2024, doi:10.3847/2041-8213/ad4990.
- Bernini-Peron, M., Marcolino, W. L. F., Sander, A. A. C., Bouret, J. C., Ramachandran, V., Saling, J., Schneider, F. R. N., Oskinova, L. M., and Najarro, F., “Clumping and X-rays in cooler B supergiant stars,” *Astronomy & Astrophysics*, vol. 677, A50, 2023, doi:10.1051/0004-6361/202346469.
- Berthomieu, G., Gonczi, G., Graff, P., Provost, J., and Rocca, A., “Low-frequency Gravity Modes of a Rotating Star,” *Astronomy & Astrophysics*, vol. 70, p. 597, 1978.
- Bessila, L. and Mathis, S., “Stochastic excitation of waves in magnetic stars: I. Scaling laws for the mode amplitudes,” *Astronomy & Astrophysics*, vol. 690, A270, 2024, doi:10.1051/0004-6361/202450802.
- Bhattacharya, S., Das, S. B., Bugnet, L., Panda, S., and Hanasoge, S. M., “Detectability of Axisymmetric Magnetic Fields from the Core to the Surface of Oscillating Post-main-sequence Stars,” *Astrophysical Journal*, vol. 970, no. 1, 42, 2024, doi:10.3847/1538-4357/ad4708.
- Bloecker, T., “Stellar evolution of low and intermediate-mass stars. I. Mass loss on the AGB and its consequences for stellar evolution.” *Astronomy & Astrophysics*, vol. 297, p. 727, 1995.

- Bodensteiner, J., Sana, H., Wang, C., Langer, N., Mahy, L., Banyard, G., de Koter, A., de Mink, S. E., Evans, C. J., Götberg, Y., et al., “The young massive SMC cluster NGC 330 seen by MUSE. II. Multiplicity properties of the massive-star population,” *Astronomy & Astrophysics*, vol. 652, A70, 2021, doi:10.1051/0004-6361/202140507.
- Boekholt, T. C. N., Schleicher, D. R. G., Fellhauer, M., Klessen, R. S., Reinoso, B., Stutz, A. M., and Haemmerlé, L., “Formation of massive seed black holes via collisions and accretion,” *Monthly Notices of the Royal Astronomical Society*, vol. 476, no. 1, pp. 366–380, 2018, doi:10.1093/mnras/sty208.
- Boffin, H. M. J. and Jones, D., *The Importance of Binaries in the Formation and Evolution of Planetary Nebulae*, Springer Cham, 2019, doi:10.1007/978-3-030-25059-1.
- Böhm-Vitense, E., “Über die Wasserstoffkonvektionszone in Sternen verschiedener Effektivtemperaturen und Leuchtkräfte. Mit 5 Textabbildungen,” *Zeitschrift für Astrophysik*, vol. 46, p. 108, 1958.
- Bossini, D., Miglio, A., Salaris, M., Vrad, M., Cassisi, S., Mosser, B., Montalbán, J., Girardi, L., Noels, A., Bressan, A., et al., “Kepler red-clump stars in the field and in open clusters: constraints on core mixing,” *Monthly Notices of the Royal Astronomical Society*, vol. 469, no. 4, pp. 4718–4725, 2017, doi:10.1093/mnras/stx1135.
- Bouabid, M. P., Dupret, M. A., Salmon, S., Montalbán, J., Miglio, A., and Noels, A., “Effects of the Coriolis force on high-order g modes in γ Doradus stars,” *Monthly Notices of the Royal Astronomical Society*, vol. 429, no. 3, pp. 2500–2514, 2013, doi:10.1093/mnras/sts517.
- Bowman, D. M., “Making waves in massive star asteroseismology,” *Astrophysics and Space Science*, vol. 368, no. 12, 107, 2023, doi:10.1007/s10509-023-04262-7.
- Bowman, D. M., Burssens, S., Pedersen, M. G., Johnston, C., Aerts, C., Buyschaert, B., Michielsen, M., Tkachenko, A., Rogers, T. M., Edelmann, P. V. F., et al., “Low-frequency gravity waves in blue supergiants revealed by high-precision space photometry,” *Nature Astronomy*, vol. 3, pp. 760–765, 2019, doi:10.1038/s41550-019-0768-1.
- Bowman, D. M., Burssens, S., Simón-Díaz, S., Edelmann, P. V. F., Rogers, T. M., Horst, L., Röpke, F. K., and Aerts, C., “Photometric detection of internal gravity waves in upper main-sequence stars. II. Combined TESS photometry and high-resolution spectroscopy,” *Astronomy & Astrophysics*, vol. 640, A36, 2020, doi:10.1051/0004-6361/202038224.
- Braithwaite, J. and Spruit, H. C., “Magnetic fields in non-convective regions of stars,” *Royal Society Open Science*, vol. 4, no. 2, 160271, 2017, doi:10.1098/rsos.160271.
- Braun, H. and Langer, N., “Effects of accretion onto massive main sequence stars.” *Astronomy & Astrophysics*, vol. 297, p. 483, 1995.
- Bressan, A., Marigo, P., Girardi, L., Salasnich, B., Dal Cero, C., Rubele, S., and Nanni, A., “PARSEC: stellar tracks and isochrones with the PAdova and TRieste Stellar Evolution Code,” *Monthly Notices of the Royal Astronomical Society*, vol. 427, no. 1, pp. 127–145, 2012, doi:10.1111/j.1365-2966.2012.21948.x.

- Brinkman, H. E., Roberti, L., Kemp, A., Michielsen, M., Tkachenko, A., and Aerts, C., “The impact of asteroseismically calibrated internal mixing on nucleosynthetic wind yields of massive stars,” *arXiv e-prints*, arXiv:2406.02404, 2024, doi:10.48550/arXiv.2406.02404.
- Britavskiy, N., Lennon, D. J., Patrick, L. R., Evans, C. J., Herrero, A., Langer, N., van Loon, J. T., Clark, J. S., Schneider, F. R. N., Almeida, L. A., et al., “The VLT-FLAMES Tarantula Survey. XXX. Red stragglers in the clusters Hodge 301 and SL 639,” *Astronomy & Astrophysics*, vol. 624, A128, 2019, doi:10.1051/0004-6361/201834564.
- Brott, I., de Mink, S. E., Cantiello, M., Langer, N., de Koter, A., Evans, C. J., Hunter, I., Trundle, C., and Vink, J. S., “Rotating massive main-sequence stars. I. Grids of evolutionary models and isochrones,” *Astronomy & Astrophysics*, vol. 530, A115, 2011, doi:10.1051/0004-6361/201016113.
- Burssens, S., Bowman, D. M., Michielsen, M., Simón-Díaz, S., Aerts, C., Vanlaer, V., Bannard, G., Nardetto, N., Townsend, R. H. D., Handler, G., et al., “A calibration point for stellar evolution from massive star asteroseismology,” *Nature Astronomy*, vol. 7, pp. 913–930, 2023, doi:10.1038/s41550-023-01978-y.
- Buzasi, D., “Platforms of opportunity: asteroseismology by Piggyback,” in Pallavicini, R., Micela, G., and Sciortino, S. (editors), “Stellar Clusters and Associations: Convection, Rotation, and Dynamos,” *Astronomical Society of the Pacific Conference Series*, vol. 198, p. 557, 2000.
- Cadiou, C., “Matplotlib label lines,” Zenodo, 2022, doi:10.5281/zenodo.7428071.
- Cantiello, M., Lecoanet, D., Jermyn, A. S., and Grassitelli, L., “On the Origin of Stochastic, Low-Frequency Photometric Variability in Massive Stars,” *Astrophysical Journal*, vol. 915, no. 2, 112, 2021, doi:10.3847/1538-4357/ac03b0.
- Castro, N., Fossati, L., Langer, N., Simón-Díaz, S., Schneider, F. R. N., and Izzard, R. G., “The spectroscopic Hertzsprung-Russell diagram of Galactic massive stars,” *Astronomy & Astrophysics*, vol. 570, L13, 2014, doi:10.1051/0004-6361/201425028.
- Castro, N., Oey, M. S., Fossati, L., and Langer, N., “The Spectroscopic Hertzsprung-Russell Diagram of Hot Massive Stars in the Small Magellanic Cloud,” *Astrophysical Journal*, vol. 868, no. 1, 57, 2018, doi:10.3847/1538-4357/aae6d0.
- Cehula, J. and Pejcha, O., “A theory of mass transfer in binary stars,” *Monthly Notices of the Royal Astronomical Society*, vol. 524, no. 1, pp. 471–490, 2023, doi:10.1093/mnras/stad1862.
- Chen, X. and Han, Z., “Mass transfer from a giant star to a main-sequence companion and its contribution to long-orbital-period blue stragglers,” *Monthly Notices of the Royal Astronomical Society*, vol. 387, no. 4, pp. 1416–1430, 2008, doi:10.1111/j.1365-2966.2008.13334.x.
- Chiappini, C., Anders, F., Rodrigues, T. S., Miglio, A., Montalbán, J., Mosser, B., Girardi, L., Valentini, M., Noels, A., Morel, T., et al., “Young $[\alpha/\text{Fe}]$ -enhanced stars discovered by CoRoT and APOGEE: What is their origin?” *Astronomy & Astrophysics*, vol. 576, L12, 2015, doi:10.1051/0004-6361/201525865.

- Choi, J., Dotter, A., Conroy, C., Cantiello, M., Paxton, B., and Johnson, B. D., “Mesa Isochrones and Stellar Tracks (MIST). I. Solar-scaled Models,” *Astrophysical Journal*, vol. 823, no. 2, 102, 2016, doi:10.3847/0004-637X/823/2/102.
- Christensen-Dalsgaard, J., “ADIPLS—the Aarhus adiabatic oscillation package,” *Astrophysics and Space Science*, vol. 316, no. 1-4, pp. 113–120, 2008, doi:10.1007/s10509-007-9689-z.
- Christensen-Dalsgaard, J. and Gough, D. O., “Towards a heliological inverse problem,” *Nature*, vol. 259, no. 5539, pp. 89–92, 1976, doi:10.1038/259089a0.
- Claeys, J. S. W., de Mink, S. E., Pols, O. R., Eldridge, J. J., and Baes, M., “Binary progenitor models of type IIb supernovae,” *Astronomy & Astrophysics*, vol. 528, A131, 2011, doi:10.1051/0004-6361/201015410.
- Constantino, T., Campbell, S. W., Lattanzio, J. C., and van Duijneveldt, A., “The treatment of mixing in core helium burning models - II. Constraints from cluster star counts,” *Monthly Notices of the Royal Astronomical Society*, vol. 456, no. 4, pp. 3866–3885, 2016, doi:10.1093/mnras/stv2939.
- Costa, G., Ballone, A., Mapelli, M., and Bressan, A., “Formation of black holes in the pair-instability mass gap: Evolution of a post-collision star,” *Monthly Notices of the Royal Astronomical Society*, vol. 516, no. 1, pp. 1072–1080, 2022, doi:10.1093/mnras/stac2222.
- Cox, J. P. and Giuli, R. T., *Principles of stellar structure*, Gordon and Breach, 1968.
- Crawford, J. A., “On the Subgiant Components of Eclipsing Binary Systems.” *Astrophysical Journal*, vol. 121, p. 71, 1955, doi:10.1086/145965.
- Cunha, M. S., Avelino, P. P., Christensen-Dalsgaard, J., Stello, D., Vrad, M., Jiang, C., and Mosser, B., “Analytical modelling of period spacings across the HR diagram,” *Monthly Notices of the Royal Astronomical Society*, vol. 490, no. 1, pp. 909–926, 2019, doi:10.1093/mnras/stz2582.
- Cunha, M. S., Damasceno, Y. C., Amaral, J., Falorca, A., Christensen-Dalsgaard, J., and Avelino, P. P., “Buoyancy glitches in pulsating stars revisited,” *Astronomy & Astrophysics*, vol. 687, A100, 2024, doi:10.1051/0004-6361/202348681.
- Cunha, M. S., Stello, D., Avelino, P. P., Christensen-Dalsgaard, J., and Townsend, R. H. D., “Structural Glitches near the Cores of Red Giants Revealed by Oscillations in g-mode Period Spacings from Stellar Models,” *Astrophysical Journal*, vol. 805, no. 2, 127, 2015, doi:10.1088/0004-637X/805/2/127.
- Dalcin, L. and Fang, Y.-L. L., “mpi4py: Status Update After 12 Years of Development,” *Computing in Science & Engineering*, vol. 23, no. 4, pp. 47–54, 2021, doi:10.1109/MCSE.2021.3083216.
- Dalcín, L., Paz, R., and Storti, M., “MPI for Python,” *Journal of Parallel and Distributed Computing*, vol. 65, no. 9, pp. 1108–1115, 2005, doi:10.1016/j.jpdc.2005.03.010.
- Dale, J. E. and Davies, M. B., “Collisions and close encounters involving massive main-sequence stars,” *Monthly Notices of the Royal Astronomical Society*, vol. 366, no. 4, pp. 1424–1436, 2006, doi:10.1111/j.1365-2966.2005.09937.x.

- Darwin, G. H., “The Determination of the Secular Effects of Tidal Friction by a Graphical Method,” *Proceedings of the Royal Society of London Series I*, vol. 29, pp. 168–181, 1879.
- Daszyńska-Daszkiewicz, J., Pamyatnykh, A. A., Walczak, P., Colgan, J., Fontes, C. J., and Kilcrease, D. P., “Interpretation of the BRITE oscillation data of the hybrid pulsator ν Eridani: a call for the modification of stellar opacities,” *Monthly Notices of the Royal Astronomical Society*, vol. 466, no. 2, pp. 2284–2293, 2017, doi:10.1093/mnras/stw3315.
- de Burgos, A., Simón-Díaz, S., Urbaneja, M. A., and Negueruela, I., “The IACOB project. IX. Building a modern empirical database of Galactic O9 - B9 supergiants: Sample selection, description, and completeness,” *Astronomy & Astrophysics*, vol. 674, A212, 2023, doi:10.1051/0004-6361/202346179.
- de Mink, S. E., Pols, O. R., and Hilditch, R. W., “Efficiency of mass transfer in massive close binaries. Tests from double-lined eclipsing binaries in the SMC,” *Astronomy & Astrophysics*, vol. 467, no. 3, pp. 1181–1196, 2007, doi:10.1051/0004-6361:20067007.
- de Mink, S. E., Sana, H., Langer, N., Izzard, R. G., and Schneider, F. R. N., “The Incidence of Stellar Mergers and Mass Gainers among Massive Stars,” *Astrophysical Journal*, vol. 782, no. 1, 7, 2014, doi:10.1088/0004-637X/782/1/7.
- Degroote, P., Aerts, C., Baglin, A., Miglio, A., Briquet, M., Noels, A., Niemczura, E., Montalbán, J., Bloemen, S., Oreiro, R., et al., “Deviations from a uniform period spacing of gravity modes in a massive star,” *Nature*, vol. 464, no. 7286, pp. 259–261, 2010, doi:10.1038/nature08864.
- Deheuvels, S., Ballot, J., Gehan, C., and Mosser, B., “Seismic signature of electron degeneracy in the core of red giants: Hints for mass transfer between close red-giant companions,” *Astronomy & Astrophysics*, vol. 659, A106, 2022, doi:10.1051/0004-6361/202142094.
- Deloye, C. J. and Taam, R. E., “Adiabatic Mass Loss and the Outcome of the Common Envelope Phase of Binary Evolution,” *The Astrophysical Journal Letters*, vol. 719, no. 1, pp. L28–L31, 2010, doi:10.1088/2041-8205/719/1/L28.
- Derişoğlu, A., Pavlovski, K., Lehmann, H., Southworth, J., and Bewsher, D., “Evidence for conservative mass transfer in the classical Algol system δ Librae from its surface carbon-to-nitrogen abundance ratio,” *Monthly Notices of the Royal Astronomical Society*, vol. 481, no. 4, pp. 5660–5674, 2018, doi:10.1093/mnras/sty2684.
- Dhouib, H., Mathis, S., Bugnet, L., Van Reeth, T., and Aerts, C., “Detecting deep axisymmetric toroidal magnetic fields in stars. The traditional approximation of rotation for differentially rotating deep spherical shells with a general azimuthal magnetic field,” *Astronomy & Astrophysics*, vol. 661, A133, 2022, doi:10.1051/0004-6361/202142956.
- Dhouib, H., Prat, V., Van Reeth, T., and Mathis, S., “The traditional approximation of rotation for rapidly rotating stars and planets. I. The impact of strong deformation,” *Astronomy & Astrophysics*, vol. 652, A154, 2021, doi:10.1051/0004-6361/202140615.
- Donati, J. F. and Landstreet, J. D., “Magnetic Fields of Nondegenerate Stars,” *Annual Review of Astronomy and Astrophysics*, vol. 47, no. 1, pp. 333–370, 2009, doi:10.1146/annurev-astro-082708-101833.

- Drout, M. R., Götberg, Y., Ludwig, B. A., Groh, J. H., de Mink, S. E., O’Grady, A. J. G., and Smith, N., “An observed population of intermediate-mass helium stars that have been stripped in binaries,” *Science*, vol. 382, no. 6676, pp. 1287–1291, 2023, doi:10.1126/science.ade4970.
- Eckart, C., “Variation Principles of Hydrodynamics,” *Physics of Fluids*, vol. 3, no. 3, pp. 421–427, 1960, doi:10.1063/1.1706053.
- Eggenberger, P., Meynet, G., Maeder, A., Hirschi, R., Charbonnel, C., Talon, S., and Ekström, S., “The Geneva stellar evolution code,” *Astrophysics and Space Science*, vol. 316, no. 1-4, pp. 43–54, 2008, doi:10.1007/s10509-007-9511-y.
- Eggleton, P. P., “The evolution of low mass stars,” *Monthly Notices of the Royal Astronomical Society*, vol. 151, p. 351, 1971, doi:10.1093/mnras/151.3.351.
- Eggleton, P. P., “Composition changes during stellar evolution,” *Monthly Notices of the Royal Astronomical Society*, vol. 156, p. 361, 1972, doi:10.1093/mnras/156.3.361.
- Eggleton, P. P., “A numerical treatment of double shell source stars,” *Monthly Notices of the Royal Astronomical Society*, vol. 163, p. 279, 1973, doi:10.1093/mnras/163.3.279.
- Eggleton, P. P., “Aproximations to the radii of Roche lobes,” *Astrophysical Journal*, vol. 268, pp. 368–369, 1983, doi:10.1086/160960.
- Eggleton, P. P., Faulkner, J., and Flannery, B. P., “An Approximate Equation of State for Stellar Material,” *Astronomy & Astrophysics*, vol. 23, p. 325, 1973.
- El-Badry, K. and Burdge, K. B., “NGC 1850 BH1 is another stripped-star binary masquerading as a black hole,” *Monthly Notices of the Royal Astronomical Society*, vol. 511, no. 1, pp. 24–29, 2022, doi:10.1093/mnras/511.1.24.
- El-Badry, K., Burdge, K. B., and Mróz, P., “NGC 2004 #115: a black hole imposter containing three luminous stars,” *Monthly Notices of the Royal Astronomical Society*, vol. 511, no. 2, pp. 3089–3100, 2022, doi:10.1093/mnras/stac274.
- El-Badry, K. and Quataert, E., “A stripped-companion origin for Be stars: clues from the putative black holes HR 6819 and LB-1,” *Monthly Notices of the Royal Astronomical Society*, vol. 502, no. 3, pp. 3436–3455, 2021, doi:10.1093/mnras/stab285.
- Ercolino, A., Jin, H., Langer, N., and Dessart, L., “Interacting supernovae from wide massive binary systems,” *arXiv e-prints*, arXiv:2308.01819, 2023, doi:10.48550/arXiv.2308.01819.
- Fabry, M., Marchant, P., Langer, N., and Sana, H., “Modeling contact binaries. II. Effects of energy transfer,” *Astronomy & Astrophysics*, vol. 672, A175, 2023, doi:10.1051/0004-6361/202346277.
- Fabry, M., Marchant, P., and Sana, H., “Modeling overcontact binaries. I. The effect of tidal deformation,” *Astronomy & Astrophysics*, vol. 661, A123, 2022, doi:10.1051/0004-6361/202243094.

- Ferguson, J. W., Alexander, D. R., Allard, F., Barman, T., Bodnarik, J. G., Hauschildt, P. H., Hefner-Wong, A., and Tamanai, A., “Low-Temperature Opacities,” *Astrophysical Journal*, vol. 623, no. 1, pp. 585–596, 2005, doi:10.1086/428642.
- Ferrario, L., Pringle, J. E., Tout, C. A., and Wickramasinghe, D. T., “The origin of magnetism on the upper main sequence,” *Monthly Notices of the Royal Astronomical Society*, vol. 400, no. 1, pp. L71–L74, 2009, doi:10.1111/j.1745-3933.2009.00765.x.
- Ferrario, L. and Wickramasinghe, D. T., “Magnetic fields and rotation in white dwarfs and neutron stars,” *Monthly Notices of the Royal Astronomical Society*, vol. 356, no. 2, pp. 615–620, 2005, doi:10.1111/j.1365-2966.2004.08474.x.
- Ferraro, F. R., Lanzoni, B., Dalessandro, E., Beccari, G., Pasquato, M., Miocchi, P., Rood, R. T., Sigurdsson, S., Sills, A., Vesperini, E., et al., “Dynamical age differences among coeval star clusters as revealed by blue stragglers,” *Nature*, vol. 492, no. 7429, pp. 393–395, 2012, doi:10.1038/nature11686.
- Fitzpatrick, B. J. R., *Binary hypotheses for bipolar mass loss in transients*, Ph.D. thesis, University of Oxford, UK, 2012.
- Flannery, B. P., “A Cyclic Thermal Instability in Contact Binary Stars,” *Astrophysical Journal*, vol. 205, pp. 217–225, 1976, doi:10.1086/154266.
- Forestini, M., Arnould, M., and Paulus, G., “On the production of Al-26 in AGB stars,” *Astronomy & Astrophysics*, vol. 252, no. 2, pp. 597–604, 1991.
- Fossati, L., Castro, N., Schöller, M., Hubrig, S., Langer, N., Morel, T., Briquet, M., Herrero, A., Przybilla, N., Sana, H., et al., “B fields in OB stars (BOB): Low-resolution FORS2 spectropolarimetry of the first sample of 50 massive stars,” *Astronomy & Astrophysics*, vol. 582, A45, 2015, doi:10.1051/0004-6361/201526725.
- Fossati, L., Schneider, F. R. N., Castro, N., Langer, N., Simón-Díaz, S., Müller, A., de Koter, A., Morel, T., Petit, V., Sana, H., et al., “Evidence of magnetic field decay in massive main-sequence stars,” *Astronomy & Astrophysics*, vol. 592, A84, 2016, doi:10.1051/0004-6361/201628259.
- Fragos, T., Andrews, J. J., Bavera, S. S., Berry, C. P. L., Coughlin, S., Dotter, A., Giri, P., Kalogera, V., Katsaggelos, A., Kovelakas, K., et al., “POSYDON: A General-purpose Population Synthesis Code with Detailed Binary-evolution Simulations,” *The Astrophysical Journal Supplement Series*, vol. 264, no. 2, 45, 2023, doi:10.3847/1538-4365/ac90c1.
- Freitag, M. and Benz, W., “A comprehensive set of simulations of high-velocity collisions between main-sequence stars,” *Monthly Notices of the Royal Astronomical Society*, vol. 358, no. 4, pp. 1133–1158, 2005, doi:10.1111/j.1365-2966.2005.08770.x.
- Frew, D. J., “The Historical Record of η Carinae I. The Visual Light Curve, 1595-2000,” *Journal of Astronomical Data*, vol. 10, p. 6, 2004.
- Fritzewski, D. J., Aerts, C., Mombarg, J. S. G., Gossage, S., and Van Reeth, T., “Age uncertainties of red giants due to cumulative rotational mixing of progenitors calibrated by asteroseismology,” *Astronomy & Astrophysics*, vol. 684, A112, 2024a, doi:10.1051/0004-6361/202449300.

- Fritzewski, D. J., Vanrespaille, M., Aerts, C., Hey, D., and De Ridder, J., “Mode identification and ensemble asteroseismology of 164 β Cep stars discovered from Gaia light curves and monitored by TESS,” *arXiv e-prints*, arXiv:2408.06097, 2024b, doi:10.48550/arXiv.2408.06097.
- Frost, A. J., Bodensteiner, J., Rivinius, T., Baade, D., Merand, A., Selman, F., Abdul-Masih, M., Banyard, G., Bordier, E., Dsilva, K., et al., “HR 6819 is a binary system with no black hole. Revisiting the source with infrared interferometry and optical integral field spectroscopy,” *Astronomy & Astrophysics*, vol. 659, L3, 2022, doi:10.1051/0004-6361/202143004.
- Frost, A. J., Sana, H., Mahy, L., Wade, G., Barron, J., Bouquin, J.-B. L., Mérand, A., Schneider, F. R. N., Shenar, T., Barbá, R. H., et al., “A magnetic massive star has experienced a stellar merger,” *Science*, vol. 384, no. 6692, pp. 214–217, 2024, doi:10.1126/science.adg7700.
- Fuller, J., Cantiello, M., Stello, D., Garcia, R. A., and Bildsten, L., “Asteroseismology can reveal strong internal magnetic fields in red giant stars,” *Science*, vol. 350, no. 6259, pp. 423–426, 2015, doi:10.1126/science.aac6933.
- Gaburov, E., Gualandris, A., and Portegies Zwart, S., “On the onset of runaway stellar collisions in dense star clusters - I. Dynamics of the first collision,” *Monthly Notices of the Royal Astronomical Society*, vol. 384, no. 1, pp. 376–385, 2008a, doi:10.1111/j.1365-2966.2007.12731.x.
- Gaburov, E., Lombardi, J. C., and Portegies Zwart, S., “Mixing in massive stellar mergers,” *Monthly Notices of the Royal Astronomical Society*, vol. 383, no. 1, pp. L5–L9, 2008b, doi:10.1111/j.1745-3933.2007.00399.x.
- Gaia Collaboration, De Ridder, J., Ripepi, V., Aerts, C., Palaversa, L., and Eyer, L. e. a., “Gaia Data Release 3. Pulsations in main sequence OBAF-type stars,” *Astronomy & Astrophysics*, vol. 674, A36, 2023a, doi:10.1051/0004-6361/202243767.
- Gaia Collaboration, Prusti, T., de Bruijne, J. H. J., Brown, A. G. A., Vallenari, A., Babusiaux, C., Bailer-Jones, C. A. L., Bastian, U., Biermann, M., Evans, D. W., et al., “The Gaia mission,” *Astronomy & Astrophysics*, vol. 595, A1, 2016, doi:10.1051/0004-6361/201629272.
- Gaia Collaboration, Vallenari, A., Brown, A. G. A., Prusti, T., de Bruijne, J. H. J., Arenou, F., Babusiaux, C., Biermann, M., Creevey, O. L., Ducourant, C., et al., “Gaia Data Release 3. Summary of the content and survey properties,” *Astronomy & Astrophysics*, vol. 674, A1, 2023b, doi:10.1051/0004-6361/202243940.
- Gallagher, J. S., “Close Binary Models for Luminous Blue Variables Stars,” in Davidson, K., Moffat, A. F. J., and Lamers, H. J. G. L. M. (editors), “IAU Colloq. 113: Physics of Luminous Blue Variables,” *Astrophysics and Space Science Library*, vol. 157, p. 185, 1989, doi:10.1007/978-94-009-1031-7_22.
- Garcia, S., Van Reeth, T., De Ridder, J., and Aerts, C., “Internal rotation and buoyancy travel time of 60 γ Doradus stars from uninterrupted TESS light curves spanning 352 days,” *Astronomy & Astrophysics*, vol. 668, A137, 2022a, doi:10.1051/0004-6361/202244365.

- Garcia, S., Van Reeth, T., De Ridder, J., Tkachenko, A., IIspeert, L., and Aerts, C., “Detection of period-spacing patterns due to the gravity modes of rotating dwarfs in the TESS southern continuous viewing zone,” *Astronomy & Astrophysics*, vol. 662, A82, 2022b, doi:10.1051/0004-6361/202141926.
- Ge, H., Hjellming, M. S., Webbink, R. F., Chen, X., and Han, Z., “Adiabatic Mass Loss in Binary Stars. I. Computational Method,” *Astrophysical Journal*, vol. 717, pp. 724–738, 2010a, doi:10.1088/0004-637X/717/2/724, aDS Bibcode: 2010ApJ...717..724G.
- Ge, H., Tout, C. A., Chen, X., Sarkar, A., Walton, D. J., and Han, Z., “Criteria for Dynamical Timescale Mass Transfer of Metal-poor Intermediate-mass Stars,” *Astrophysical Journal*, vol. 945, no. 1, 7, 2023, doi:10.3847/1538-4357/acb7e9.
- Ge, H., Tout, C. A., Chen, X., Wang, S., Xiong, J., Zhang, L., Liu, Q., and Han, Z., “Adiabatic Mass Loss in Binary Stars. V. Effects of Metallicity and Nonconservative Mass Transfer – Application in High Mass X-ray Binaries,” *arXiv e-prints*, arXiv:2408.16350, 2024, doi:10.48550/arXiv.2408.16350.
- Ge, H., Webbink, R. F., Chen, X., and Han, Z., “ADIABATIC MASS LOSS IN BINARY STARS. II. FROM ZERO-AGE MAIN SEQUENCE TO THE BASE OF THE GIANT BRANCH,” *Astrophysical Journal*, vol. 812, no. 1, p. 40, 2015, doi:10.1088/0004-637X/812/1/40.
- Ge, H., Webbink, R. F., Chen, X., and Han, Z., “Adiabatic Mass Loss in Binary Stars. III. From the Base of the Red Giant Branch to the Tip of the Asymptotic Giant Branch,” *Astrophysical Journal*, vol. 899, p. 132, 2020, doi:10.3847/1538-4357/aba7b7, aDS Bibcode: 2020ApJ...899..132G.
- Ge, H., Webbink, R. F., and Han, Z., “The Thermal Equilibrium Mass-loss Model and Its Applications in Binary Evolution,” *The Astrophysical Journal Supplement Series*, vol. 249, no. 1, 9, 2020, doi:10.3847/1538-4365/ab98f6.
- Ge, H., Webbink, R. F., Han, Z., and Chen, X., “Stellar adiabatic mass loss model and applications,” *Astrophysics and Space Science*, vol. 329, no. 1-2, pp. 243–248, 2010b, doi:10.1007/s10509-010-0286-1.
- Ghodla, S., Eldridge, J. J., Stanway, E. R., and Stevance, H. F., “Evaluating chemically homogeneous evolution in stellar binaries: electromagnetic implications - ionizing photons, SLSN-I, GRB, Ic-BL,” *Monthly Notices of the Royal Astronomical Society*, vol. 518, no. 1, pp. 860–877, 2023, doi:10.1093/mnras/stac3177.
- Gilkis, A. and Shenar, T., “Ups!... I did it again: unveiling the hidden companion in Upsilon Sagittarii, a unique binary system at a second mass transfer stage,” *Monthly Notices of the Royal Astronomical Society*, vol. 518, no. 3, pp. 3541–3555, 2023, doi:10.1093/mnras/stac3375.
- Giuricin, G., Mardirossian, F., and Mezzetti, M., “Orbital circulation in early-type detached close binaries,” *Astronomy & Astrophysics*, vol. 134, pp. 365–367, 1984.
- Glebbeek, E., Gaburov, E., Portegies Zwart, S., and Pols, O. R., “Structure and evolution of high-mass stellar mergers,” *Monthly Notices of the Royal Astronomical Society*, vol. 434, pp. 3497–3510, 2013, doi:10.1093/mnras/stt1268.

- Glebbeeck, E., Pols, O. R., and Hurley, J. R., “Evolution of stellar collision products in open clusters. I. Blue stragglers in N-body models of M 67,” *Astronomy & Astrophysics*, vol. 488, no. 3, pp. 1007–1015, 2008, doi:10.1051/0004-6361:200809930.
- Götberg, Y., Drout, M. R., Ji, A. P., Groh, J. H., Ludwig, B. A., Crowther, P. A., Smith, N., de Koter, A., and de Mink, S. E., “Stellar Properties of Observed Stars Stripped in Binaries in the Magellanic Clouds,” *Astrophysical Journal*, vol. 959, no. 2, 125, 2023, doi:10.3847/1538-4357/ace5a3.
- Grundahl, F., Kjeldsen, H., Frandsen, S., Andersen, M., Bedding, T., Arentoft, T., and Christensen-Dalsgaard, J., “SONG: Stellar Oscillations Network Group . A global network of small telescopes for asteroseismology and planet searches.” *Memorie della Societa Astronomica Italiana*, vol. 77, p. 458, 2006.
- Grunhut, J. H., Wade, G. A., Neiner, C., Oksala, M. E., Petit, V., Alecian, E., Bohlender, D. A., Bouret, J. C., Henrichs, H. F., Hussain, G. A. J., et al., “The MiMeS survey of Magnetism in Massive Stars: magnetic analysis of the O-type stars,” *Monthly Notices of the Royal Astronomical Society*, vol. 465, no. 2, pp. 2432–2470, 2017, doi:10.1093/mnras/stw2743.
- Guo, Z., “Asteroseismology of Close Binary Stars: Tides and Mass Transfer,” *Frontiers in Astronomy and Space Sciences*, vol. 8, 67, 2021, doi:10.3389/fspas.2021.663026.
- Guo, Z., Ogilvie, G. I., Li, G., Townsend, R. H. D., and Sun, M., “A new window to tidal asteroseismology: non-linearly excited stellar eigenmodes and the period spacing pattern in KOI-54,” *Monthly Notices of the Royal Astronomical Society*, vol. 517, no. 1, pp. 437–446, 2022, doi:10.1093/mnras/stac2611.
- Guo, Z., Shporer, A., Hambleton, K., and Isaacson, H., “Tidally Excited Oscillations in Heartbeat Binary Stars: Pulsation Phases and Mode Identification,” *Astrophysical Journal*, vol. 888, no. 2, 95, 2020, doi:10.3847/1538-4357/ab58c2.
- Gutenberg, B. and Richter, C. F., *Seismicity of the Earth*, Geological Society of America, 1941, doi:10.1130/SPE34-p1.
- Han, Z. and Podsiadlowski, P., “A single-degenerate model for the progenitor of the Type Ia supernova 2002ic,” *Monthly Notices of the Royal Astronomical Society*, vol. 368, no. 3, pp. 1095–1100, 2006, doi:10.1111/j.1365-2966.2006.10185.x.
- Harries, T. J., Hilditch, R. W., and Howarth, I. D., “Ten eclipsing binaries in the Small Magellanic Cloud: fundamental parameters and Cloud distance,” *Monthly Notices of the Royal Astronomical Society*, vol. 339, no. 1, pp. 157–172, 2003, doi:10.1046/j.1365-8711.2003.06169.x.
- Harris, C. R., Millman, K. J., van der Walt, S. J., Gommers, R., Virtanen, P., Cournapeau, D., Wieser, E., Taylor, J., Berg, S., Smith, N. J., et al., “Array programming with NumPy,” *Nature*, vol. 585, no. 7825, pp. 357–362, 2020, doi:10.1038/s41586-020-2649-2.
- Hatt, E. J., Ong, J. M. J., Nielsen, M. B., Chaplin, W. J., Davies, G. R., Deheuvels, S., Ballot, J., Li, G., and Bugnet, L., “Asteroseismic signatures of core magnetism and rotation in hundreds of low-luminosity red giants,” *Monthly Notices of the Royal Astronomical Society*, p. stae2053, 2024, doi:10.1093/mnras/stae2053.

- Hazlehurst, J., “The dissipation factor in contact binaries.” *Astronomy & Astrophysics*, vol. 145, pp. 25–40, 1985.
- Heger, A., Langer, N., and Woosley, S. E., “Presupernova Evolution of Rotating Massive Stars. I. Numerical Method and Evolution of the Internal Stellar Structure,” *Astrophysical Journal*, vol. 528, no. 1, pp. 368–396, 2000, doi:10.1086/308158.
- Hekker, S. and Christensen-Dalsgaard, J., “Giant star seismology,” *The Astronomy and Astrophysics Review*, vol. 25, no. 1, 1, 2017, doi:10.1007/s00159-017-0101-x.
- Hekker, S. and Johnson, J. A., “Origin of α -rich young stars: clues from C, N, and O,” *Monthly Notices of the Royal Astronomical Society*, vol. 487, pp. 4343–4354, 2019, doi:10.1093/mnras/stz1554, aDS Bibcode: 2019MNRAS.487.4343H.
- Hellings, P., “Phenomenological Study of Massive Accretion Stars,” *Astrophysics and Space Science*, vol. 96, no. 1, pp. 37–54, 1983, doi:10.1007/BF00661941.
- Hellings, P., “The post-RLOF structure of the secondary components in close binary systems, with an application to masses of Wolf-Rayet stars,” *Astrophysics and Space Science*, vol. 104, no. 1, pp. 83–109, 1984, doi:10.1007/BF00653994.
- Henneco, J., Schneider, F. R. N., Hekker, S., and Aerts, C., “Merger seismology: Distinguishing massive merger products from genuine single stars using asteroseismology,” *Astronomy & Astrophysics*, vol. 690, A65, 2024a, doi:10.1051/0004-6361/202450508.
- Henneco, J., Schneider, F. R. N., and Laplace, E., “Contact tracing of binary stars: Pathways to stellar mergers,” *Astronomy & Astrophysics*, vol. 682, A169, 2024b, doi:10.1051/0004-6361/202347893.
- Henneco, J., Van Reeth, T., Prat, V., Mathis, S., Mombarg, J. S. G., and Aerts, C., “The effect of the centrifugal acceleration on period spacings of gravito-inertial modes in intermediate-mass stars,” *Astronomy & Astrophysics*, vol. 648, A97, 2021, doi:10.1051/0004-6361/202039464.
- Heney, L. G., Forbes, J. E., and Gould, N. L., “A New Method of Automatic Computation of Stellar Evolution.” *Astrophysical Journal*, vol. 139, p. 306, 1964, doi:10.1086/147754.
- Herwig, F., “The evolution of AGB stars with convective overshoot,” *Astronomy & Astrophysics*, vol. 360, pp. 952–968, 2000.
- Hey, D. and Aerts, C., “Confronting sparse Gaia DR3 photometry with TESS for a sample of around 60 000 OBAF-type pulsators,” *Astronomy & Astrophysics*, vol. 688, A93, 2024, doi:10.1051/0004-6361/202450489.
- Hilditch, R. W., Howarth, I. D., and Harries, T. J., “Forty eclipsing binaries in the Small Magellanic Cloud: fundamental parameters and Cloud distance,” *Monthly Notices of the Royal Astronomical Society*, vol. 357, no. 1, pp. 304–324, 2005, doi:10.1111/j.1365-2966.2005.08653.x.
- Hills, J. G. and Day, C. A., “Stellar Collisions in Globular Clusters,” *Astrophysical Letters*, vol. 17, p. 87, 1976.

- Hirai, R., Podsiadlowski, P., Owocki, S. P., Schneider, F. R. N., and Smith, N., “Simulating the formation of η Carinae’s surrounding nebula through unstable triple evolution and stellar merger-induced eruption,” *Monthly Notices of the Royal Astronomical Society*, vol. 503, no. 3, pp. 4276–4296, 2021, doi:10.1093/mnras/stab571.
- Hjellming, M. S., “ALGOLS as Limits on Binary Evolution Scenarios,” *Space Science Reviews*, vol. 50, no. 1-2, pp. 155–164, 1989a, doi:10.1007/BF00215927.
- Hjellming, M. S., *Rapid Mass Transfer in Binary Systems.*, Ph.D. thesis, University of Illinois, Urbana-Champaign, 1989b.
- Hjellming, M. S. and Webbink, R. F., “Thresholds for Rapid Mass Transfer in Binary System. I. Polytropic Models,” *Astrophysical Journal*, vol. 318, p. 794, 1987, doi:10.1086/165412, aDS Bibcode: 1987ApJ...318..794H.
- Hofmeister, E., Kippenhahn, R., and Weigert, A., “Sternentwicklung I. Ein Programm zur Lösung der zeitabhängigen Aufbaugleichungen. Mit 3 Textabbildungen,” *Zeitschrift für Astrophysik*, vol. 59, p. 215, 1964.
- Howell, S. B., Sobek, C., Haas, M., Still, M., Barclay, T., Mullally, F., Troeltzsch, J., Aigrain, S., Bryson, S. T., Caldwell, D., et al., “The K2 Mission: Characterization and Early Results,” *Publications of the Astronomical Society of the Pacific*, vol. 126, no. 938, p. 398, 2014, doi:10.1086/676406.
- Hunter, J. D., “Matplotlib: A 2D graphics environment,” *Computing in Science & Engineering*, vol. 9, no. 3, pp. 90–95, 2007, doi:10.1109/MCSE.2007.55.
- Hurley, J. R., Tout, C. A., and Pols, O. R., “Evolution of binary stars and the effect of tides on binary populations,” *Monthly Notices of the Royal Astronomical Society*, vol. 329, pp. 897–928, 2002, doi:10.1046/j.1365-8711.2002.05038.x.
- Hut, P., “Tidal evolution in close binary systems.” *Astronomy & Astrophysics*, vol. 99, pp. 126–140, 1981.
- Iben, J., I., “The Effects of Possible Binary and Tertiary Companions on the Behavior of Eta Carinae,” in Morse, J. A., Humphreys, R. M., and Daminieli, A. (editors), “Eta Carinae at The Millennium,” *Astronomical Society of the Pacific Conference Series*, vol. 179, p. 367, 1999.
- Iben, J., Icko and Ehrman, J. R., “The Internal Structure of Middle Main-Sequence Stars.” *Astrophysical Journal*, vol. 135, p. 770, 1962, doi:10.1086/147320.
- Iglesias, C. A. and Rogers, F. J., “Radiative Opacities for Carbon- and Oxygen-rich Mixtures,” *Astrophysical Journal*, vol. 412, p. 752, 1993, doi:10.1086/172958.
- Iglesias, C. A. and Rogers, F. J., “Updated Opal Opacities,” *Astrophysical Journal*, vol. 464, p. 943, 1996, doi:10.1086/177381.
- Irrgang, A., Przybilla, N., and Meynet, G., “ γ Columbae as a recently stripped pulsating core of a massive star,” *Nature Astronomy*, vol. 6, pp. 1414–1420, 2022, doi:10.1038/s41550-022-01809-6.

- Ivanova, N., Justham, S., Chen, X., De Marco, O., Fryer, C. L., Gaburov, E., Ge, H., Glebbeek, E., Han, Z., Li, X. D., et al., “Common envelope evolution: where we stand and how we can move forward,” *The Astronomy and Astrophysics Review*, vol. 21, 59, 2013, doi:10.1007/s00159-013-0059-2.
- Ivanova, N., Kundu, S., and Pourmand, A., “Unified Rapid Mass Transfer,” *Astrophysical Journal*, vol. 971, no. 1, 64, 2024, doi:10.3847/1538-4357/ad583e.
- Ivanova, N., Podsiadlowski, P., and Spruit, H., “Hydrodynamical simulations of the stream-core interaction in the slow merger of massive stars,” *Monthly Notices of the Royal Astronomical Society*, vol. 334, no. 4, pp. 819–832, 2002, doi:10.1046/j.1365-8711.2002.05543.x.
- Izzard, R. G., Preece, H., Jofre, P., Halabi, G. M., Masseron, T., and Tout, C. A., “Binary stars in the Galactic thick disc,” *Monthly Notices of the Royal Astronomical Society*, vol. 473, no. 3, pp. 2984–2999, 2018, doi:10.1093/mnras/stx2355.
- Janssens, S., Shenar, T., Mahy, L., Marchant, P., Sana, H., and Bodensteiner, J., “BAT99 126: A multiple Wolf-Rayet system in the Large Magellanic Cloud with a massive near-contact binary,” *Astronomy & Astrophysics*, vol. 646, A33, 2021, doi:10.1051/0004-6361/202039305.
- Jermyn, A. S., Bauer, E. B., Schwab, J., Farmer, R., Ball, W. H., Bellinger, E. P., Dotter, A., Joyce, M., Marchant, P., Mombarg, J. S. G., et al., “Modules for Experiments in Stellar Astrophysics (MESA): Time-dependent Convection, Energy Conservation, Automatic Differentiation, and Infrastructure,” *The Astrophysical Journal Supplement Series*, vol. 265, no. 1, 15, 2023, doi:10.3847/1538-4365/acae8d.
- Johnston, C., “One size does not fit all: Evidence for a range of mixing efficiencies in stellar evolution calculations,” *Astronomy & Astrophysics*, vol. 655, A29, 2021, doi:10.1051/0004-6361/202141080.
- Johnston, C., Aerts, C., Pedersen, M. G., and Bastian, N., “Isochrone-cloud fitting of the extended main-sequence turn-off of young clusters,” *Astronomy & Astrophysics*, vol. 632, A74, 2019, doi:10.1051/0004-6361/201936549.
- Justham, S., Podsiadlowski, P., and Vink, J. S., “Luminous Blue Variables and Superluminous Supernovae from Binary Mergers,” *Astrophysical Journal*, vol. 796, no. 2, 121, 2014, doi:10.1088/0004-637X/796/2/121.
- Kaehler, H., “The structure equations of contact binaries and the light curve paradox,” *Astronomy & Astrophysics*, vol. 209, no. 1-2, pp. 67–84, 1989.
- Kaiser, E. A., Hirschi, R., Arnett, W. D., Georgy, C., Scott, L. J. A., and Cristini, A., “Relative importance of convective uncertainties in massive stars,” *Monthly Notices of the Royal Astronomical Society*, vol. 496, no. 2, pp. 1967–1989, 2020, doi:10.1093/mnras/staa1595.
- Kippenhahn, R. and Meyer-Hofmeister, E., “On the radii of accreting main sequence stars,” *Astronomy & Astrophysics*, vol. 54, pp. 539–542, 1977, aDS Bibcode: 1977A&A....54..539K.

- Kippenhahn, R. and Weigert, A., “Entwicklung in engen Doppelsternsystemen I. Masse-
naustausch vor und nach Beendigung des zentralen Wasserstoff-Brennens,” *Zeitschrift für
Astrophysik*, vol. 65, p. 251, 1967.
- Kippenhahn, R., Weigert, A., and Hofmeister, E., “Methods in computational physics,” *New
York: Academic Press*, vol. 7, p. 129, 1967.
- Kippenhahn, R., Weigert, A., and Weiss, A., *Stellar Structure and Evolution*, Springer
Berlin, Heidelberg, 2013, doi:10.1007/978-3-642-30304-3.
- Kobulnicky, H. A., Molnar, L. A., Cook, E. M., and Henderson, L. E., “A Bayesian Analysis
of Physical Parameters for 783 Kepler Close Binaries: Extreme-mass-ratio Systems and
a New Mass Ratio versus Period Lower Limit,” *The Astrophysical Journal Supplement
Series*, vol. 262, no. 1, 12, 2022, doi:10.3847/1538-4365/ac75bd.
- Koch, D. G., Borucki, W. J., Basri, G., Batalha, N. M., Brown, T. M., Caldwell,
D., Christensen-Dalsgaard, J., Cochran, W. D., DeVore, E., Dunham, E. W., et al.,
“KEPLER MISSION DESIGN, REALIZED PHOTOMETRIC PERFORMANCE, AND
EARLY SCIENCE,” *The Astrophysical Journal Letters*, vol. 713, no. 2, p. L79, 2010,
doi:10.1088/2041-8205/713/2/L79.
- Koen, C. and Eyer, L., “New periodic variables from the Hipparcos epoch photometry,”
Monthly Notices of the Royal Astronomical Society, vol. 331, no. 1, pp. 45–59, 2002,
doi:10.1046/j.1365-8711.2002.05150.x.
- Kolb, U. and Ritter, H., “A comparative study of the evolution of a close binary using a stan-
dard and an improved technique for computing mass transfer.” *Astronomy & Astrophysics*,
vol. 236, pp. 385–392, 1990.
- Kozai, Y., “Secular perturbations of asteroids with high inclination and eccentricity,” *The
Astronomical Journal*, vol. 67, pp. 591–598, 1962, doi:10.1086/108790.
- Kroupa, P., “On the variation of the initial mass function,” *Monthly Notices of the Royal As-
tronomical Society*, vol. 322, pp. 231–246, 2001, doi:10.1046/j.1365-8711.2001.04022.x,
aDS Bibcode: 2001MNRAS.322..231K.
- Krtićka, J. and Feldmeier, A., “Light variations due to the line-driven wind instability
and wind blanketing in O stars,” *Astronomy & Astrophysics*, vol. 617, A121, 2018,
doi:10.1051/0004-6361/201731614.
- Kuiper, G. P., “On the Interpretation of β Lyrae and Other Close Binaries.” *Astrophysical
Journal*, vol. 93, p. 133, 1941, doi:10.1086/144252.
- Kurtz, D. W., “Asteroseismology Across the Hertzsprung-Russell Diagram,” *Annual Review
of Astronomy and Astrophysics*, vol. 60, pp. 31–71, 2022, doi:10.1146/annurev-astro-
052920-094232.
- Landstreet, J. D., Bagnulo, S., Andretta, V., Fossati, L., Mason, E., Silaj, J., and Wade, G. A.,
“Searching for links between magnetic fields and stellar evolution: II. The evolution of
magnetic fields as revealed by observations of Ap stars in open clusters and associa-
tions,” *Astronomy & Astrophysics*, vol. 470, no. 2, pp. 685–698, 2007, doi:10.1051/0004-
6361:20077343.

- Landstreet, J. D., Silaj, J., Andretta, V., Bagnulo, S., Berdyugina, S. V., Donati, J. F., Fossati, L., Petit, P., Silvester, J., and Wade, G. A., “Searching for links between magnetic fields and stellar evolution. III. Measurement of magnetic fields in open cluster Ap stars with ESPaDOnS,” *Astronomy & Astrophysics*, vol. 481, no. 2, pp. 465–480, 2008, doi:10.1051/0004-6361:20078884.
- Langer, N., “Presupernova Evolution of Massive Single and Binary Stars,” *Annual Review of Astronomy and Astrophysics*, vol. 50, pp. 107–164, 2012, doi:10.1146/annurev-astro-081811-125534.
- Langer, N. and Kudritzki, R. P., “The spectroscopic Hertzsprung-Russell diagram,” *Astronomy & Astrophysics*, vol. 564, A52, 2014, doi:10.1051/0004-6361/201423374.
- Laplace, E., Justham, S., Renzo, M., Göteborg, Y., Farmer, R., Vartanyan, D., and de Mink, S. E., “Different to the core: The pre-supernova structures of massive single and binary-stripped stars,” *Astronomy & Astrophysics*, vol. 656, A58, 2021, doi:10.1051/0004-6361/202140506.
- Laplace, P. S., *Traité de Mécanique Céleste*, Imprimerie de Crapelet (Paris), 1799.
- Lau, H. H. B., Gil-Pons, P., Doherty, C., and Lattanzio, J., “The end of super AGB and massive AGB stars. I. The instabilities that determine the final mass of AGB stars,” *Astronomy & Astrophysics*, vol. 542, A1, 2012, doi:10.1051/0004-6361/201218826.
- Lau, M. Y. M., Hirai, R., González-Bolívar, M., Price, D. J., De Marco, O., and Mandel, I., “Common envelopes in massive stars: towards the role of radiation pressure and recombination energy in ejecting red supergiant envelopes,” *Monthly Notices of the Royal Astronomical Society*, vol. 512, no. 4, pp. 5462–5480, 2022a, doi:10.1093/mnras/stac049.
- Lau, M. Y. M., Hirai, R., Mandel, I., and Tout, C. A., “Expansion of Accreting Main-sequence Stars during Rapid Mass Transfer,” *The Astrophysical Journal Letters*, vol. 966, no. 1, L7, 2024, doi:10.3847/2041-8213/ad3d50.
- Lau, M. Y. M., Hirai, R., Price, D. J., and Mandel, I., “Common envelopes in massive stars II: The distinct roles of hydrogen and helium recombination,” *Monthly Notices of the Royal Astronomical Society*, vol. 516, no. 4, pp. 4669–4678, 2022b, doi:10.1093/mnras/stac2490.
- Lecoanet, D., Bowman, D. M., and Van Reeth, T., “Asteroseismic inference of the near-core magnetic field strength in the main-sequence B star HD 43317,” *Monthly Notices of the Royal Astronomical Society*, vol. 512, no. 1, pp. L16–L20, 2022, doi:10.1093/mnras/slac013.
- Lee, U. and Saio, H., “Low-frequency oscillations of uniformly rotating stars,” *Monthly Notices of the Royal Astronomical Society*, vol. 224, pp. 513–526, 1987, doi:10.1093/mnras/224.3.513.
- Lefever, K., Puls, J., and Aerts, C., “Statistical properties of a sample of periodically variable B-type supergiants. Evidence for opacity-driven gravity-mode oscillations,” *Astronomy & Astrophysics*, vol. 463, no. 3, pp. 1093–1109, 2007, doi:10.1051/0004-6361:20066038.

- Lefèvre, L., Marchenko, S. V., Moffat, A. F. J., and Acker, A., “A systematic study of variability among OB-stars based on HIPPARCOS photometry,” *Astronomy & Astrophysics*, vol. 507, no. 2, pp. 1141–1201, 2009, doi:10.1051/0004-6361/200912304.
- Lehmann, I., *P’ as read from the records of the earthquake of June 16th 1929*, Akademische Verlagsgesellschaft, 1930.
- Lennon, D. J., Dufton, P. L., Villaseñor, J. I., Langer, N., Evans, C. J., Sana, H., and Taylor, W. D., “Rotational synchronisation of B-type binaries in 30 Doradus,” *Astronomy & Astrophysics*, vol. 688, A141, 2024, doi:10.1051/0004-6361/202450583.
- Li, G., Bedding, T. R., Murphy, S. J., Van Reeth, T., Antoci, V., and Ouazzani, R.-M., “Period spacings of γ Doradus pulsators in the Kepler field: detection methods and application to 22 slow rotators,” *Monthly Notices of the Royal Astronomical Society*, vol. 482, no. 2, pp. 1757–1785, 2019, doi:10.1093/mnras/sty2743.
- Li, G., Van Reeth, T., Bedding, T. R., Murphy, S. J., Antoci, V., Ouazzani, R.-M., and Barbara, N. H., “Gravity-mode period spacings and near-core rotation rates of 611 γ Doradus stars with Kepler,” *Monthly Notices of the Royal Astronomical Society*, vol. 491, no. 3, pp. 3586–3605, 2020, doi:10.1093/mnras/stz2906.
- Li, Y., Bedding, T. R., Murphy, S. J., Stello, D., Chen, Y., Huber, D., Joyce, M., Marks, D., Zhang, X., Bi, S., et al., “Discovery of post-mass-transfer helium-burning red giants using asteroseismology,” *Nature Astronomy*, vol. 6, pp. 673–680, 2022, doi:10.1038/s41550-022-01648-5.
- Li, Z., Chen, X., Ge, H., Chen, H.-L., and Han, Z., “Influence of a mass transfer stability criterion on double white dwarf populations,” *Astronomy & Astrophysics*, vol. 669, A82, 2023, doi:10.1051/0004-6361/202243893.
- Lidov, M. L., “The evolution of orbits of artificial satellites of planets under the action of gravitational perturbations of external bodies,” *Planetary and Space Science*, vol. 9, no. 10, pp. 719–759, 1962, doi:10.1016/0032-0633(62)90129-0.
- Lin, J., Rappaport, S., Podsiadlowski, P., Nelson, L., Paxton, B., and Todorov, P., “LMXB and IMXB Evolution: I. The Binary Radio Pulsar PSR J1614-2230,” *Astrophysical Journal*, vol. 732, no. 2, 70, 2011, doi:10.1088/0004-637X/732/2/70.
- Lombardi, J., James C., Rasio, F. A., and Shapiro, S. L., “Collisions of Main-Sequence Stars and the Formation of Blue Stragglers in Globular Clusters,” *Astrophysical Journal*, vol. 468, p. 797, 1996, doi:10.1086/177736.
- Lombardi, J., James C., Warren, J. S., Rasio, F. A., Sills, A., and Warren, A. R., “Stellar Collisions and the Interior Structure of Blue Stragglers,” *Astrophysical Journal*, vol. 568, no. 2, pp. 939–953, 2002, doi:10.1086/339060.
- Longair, M. S., *High Energy Astrophysics*, Cambridge University Press, 2011.
- Lubow, S. H. and Artymowicz, P., “Interactions of Young Binaries with Disks,” in Mannings, V., Boss, A. P., and Russell, S. S. (editors), “Protostars and Planets IV,” p. 731, 2000, doi:10.48550/arXiv.2111.07411.

- Lubow, S. H. and Shu, F. H., “Gas dynamics of semidetached binaries.” *Astrophysical Journal*, vol. 198, pp. 383–405, 1975, doi:10.1086/153614, aDS Bibcode: 1975ApJ...198..383L.
- Lubow, S. H. and Shu, F. H., “On the structure of contact binaries. II. Zero-age models.” *Astrophysical Journal*, vol. 216, pp. 517–525, 1977, doi:10.1086/155493.
- Lubow, S. H. and Shu, F. H., “On the structure of contact binaries. IV. High-mass models.” *Astrophysical Journal*, vol. 229, pp. 657–660, 1979, doi:10.1086/156999.
- Lucy, L. B., “The Structure of Contact Binaries,” *Astrophysical Journal*, vol. 151, p. 1123, 1968, doi:10.1086/149510.
- Lucy, L. B., “W Ursae Majoris systems with marginal contact.” *Astrophysical Journal*, vol. 205, pp. 208–216, 1976, doi:10.1086/154265.
- Ma, L., Johnston, C., Bellinger, E. P., and de Mink, S. E., “Variability of Blue Supergiants in the LMC with TESS,” *Astrophysical Journal*, vol. 966, no. 2, 196, 2024, doi:10.3847/1538-4357/ad38bc.
- Madhusudhan, N., Justham, S., Nelson, L., Paxton, B., Pfahl, E., Podsiadlowski, P., and Rappaport, S., “Models of Ultraluminous X-Ray Sources with Intermediate-Mass Black Holes,” *Astrophysical Journal*, vol. 640, no. 2, pp. 918–922, 2006, doi:10.1086/500238.
- Maeder, A., *Physics, Formation and Evolution of Rotating Stars*, Springer Berlin, Heidelberg, 2009, doi:10.1007/978-3-540-76949-1.
- Mahy, L., Almeida, L. A., Sana, H., Clark, J. S., de Koter, A., de Mink, S. E., Evans, C. J., Grin, N. J., Langer, N., Moffat, A. F. J., et al., “The Tarantula Massive Binary Monitoring. IV. Double-lined photometric binaries,” *Astronomy & Astrophysics*, vol. 634, A119, 2020, doi:10.1051/0004-6361/201936152.
- Mapelli, M., Sigurdsson, S., Ferraro, F. R., Colpi, M., Possenti, A., and Lanzoni, B., “The radial distribution of blue straggler stars and the nature of their progenitors,” *Monthly Notices of the Royal Astronomical Society*, vol. 373, no. 1, pp. 361–368, 2006, doi:10.1111/j.1365-2966.2006.11038.x.
- Marchant, P., *The impact of tides and mass transfer on the evolution of metal-poor massive binary stars*, Ph.D. thesis, Rheinischen Friedrich-Wilhelms-Universität Bonn, 2017.
- Marchant, P., “mkippp,” GitHub, 2020, <https://github.com/orlox/mkippp>.
- Marchant, P. and Bodensteiner, J., “The Evolution of Massive Binary Stars,” *Annual Review of Astronomy and Astrophysics*, vol. 62, no. 1, pp. 21–61, 2024, doi:10.1146/annurev-astro-052722-105936.
- Marchant, P., Langer, N., Podsiadlowski, P., Tauris, T. M., and Moriya, T. J., “A new route towards merging massive black holes,” *Astronomy & Astrophysics*, vol. 588, A50, 2016, doi:10.1051/0004-6361/201628133.

- Marchant, P., Pappas, K. M. W., Gallegos-Garcia, M., Berry, C. P. L., Taam, R. E., Kalogera, V., and Podsiadlowski, P., “The role of mass transfer and common envelope evolution in the formation of merging binary black holes,” *Astronomy & Astrophysics*, vol. 650, A107, 2021, doi:10.1051/0004-6361/202039992.
- Martig, M., Rix, H.-W., Silva Aguirre, V., Hekker, S., Mosser, B., Elsworth, Y., Bovy, J., Stello, D., Anders, F., García, R. A., et al., “Young α -enriched giant stars in the solar neighbourhood,” *Monthly Notices of the Royal Astronomical Society*, vol. 451, pp. 2230–2243, 2015, doi:10.1093/mnras/stv1071, aDS Bibcode: 2015MNRAS.451.2230M.
- Martinet, S., Meynet, G., Ekström, S., Simón-Díaz, S., Holgado, G., Castro, N., Georgy, C., Eggenberger, P., Buldgen, G., Salmon, S., et al., “Convective core sizes in rotating massive stars. I. Constraints from solar metallicity OB field stars,” *Astronomy & Astrophysics*, vol. 648, A126, 2021, doi:10.1051/0004-6361/202039426.
- Mathis, S., “Transport by gravito-inertial waves in differentially rotating stellar radiation zones. I - Theoretical formulation,” *Astronomy & Astrophysics*, vol. 506, no. 2, pp. 811–828, 2009, doi:10.1051/0004-6361/200810544.
- Mathis, S., Bugnet, L., Prat, V., Augustson, K., Mathur, S., and Garcia, R. A., “Probing the internal magnetism of stars using asymptotic magneto-asteroseismology,” *Astronomy & Astrophysics*, vol. 647, A122, 2021, doi:10.1051/0004-6361/202039180.
- Mennekens, N. and Vanbeveren, D., “A comparison between observed Algol-type double stars in the solar neighborhood and evolutionary computations of galactic case A binaries with a B-type primary at birth,” *Astronomy & Astrophysics*, vol. 599, A84, 2017, doi:10.1051/0004-6361/201630131.
- Menon, A., Ercolino, A., Urbaneja, M. A., Lennon, D. J., Herrero, A., Hirai, R., Langer, N., Schootemeijer, A., Chatzopoulos, E., Frank, J., et al., “Evidence for Evolved Stellar Binary Mergers in Observed B-type Blue Supergiants,” *The Astrophysical Journal Letters*, vol. 963, no. 2, L42, 2024, doi:10.3847/2041-8213/ad2074.
- Menon, A. and Heger, A., “The quest for blue supergiants: binary merger models for the evolution of the progenitor of SN 1987A,” *Monthly Notices of the Royal Astronomical Society*, vol. 469, pp. 4649–4664, 2017, doi:10.1093/mnras/stx818.
- Menon, A., Langer, N., de Mink, S. E., Justham, S., Sen, K., Szécsi, D., de Koter, A., Abdul-Masih, M., Sana, H., Mahy, L., et al., “Detailed evolutionary models of massive contact binaries - I. Model grids and synthetic populations for the Magellanic Clouds,” *Monthly Notices of the Royal Astronomical Society*, vol. 507, pp. 5013–5033, 2021, doi:10.1093/mnras/stab2276, aDS Bibcode: 2021MNRAS.507.5013M.
- Meyer, F. and Meyer-Hofmeister, E., “A model for the standstill of the Z Camelopardalis variables,” *Astronomy & Astrophysics*, vol. 121, pp. 29–34, 1983.
- Michielsen, M., Aerts, C., and Bowman, D. M., “Probing the temperature gradient in the core boundary layer of stars with gravito-inertial modes. The case of KIC 7760680,” *Astronomy & Astrophysics*, vol. 650, A175, 2021, doi:10.1051/0004-6361/202039926.

- Michielsen, M., Pedersen, M. G., Augustson, K. C., Mathis, S., and Aerts, C., “Probing the shape of the mixing profile and of the thermal structure at the convective core boundary through asteroseismology,” *Astronomy & Astrophysics*, vol. 628, A76, 2019, doi:10.1051/0004-6361/201935754.
- Michielsen, M., Van Reeth, T., Tkachenko, A., and Aerts, C., “Probing the physics in the core boundary layers of the double-lined B-type binary KIC 4930889 from its gravito-inertial modes,” *Astronomy & Astrophysics*, vol. 679, A6, 2023, doi:10.1051/0004-6361/202244192.
- Miglio, A., Montalbán, J., Noels, A., and Eggenberger, P., “Probing the properties of convective cores through g modes: high-order g modes in SPB and γ Doradus stars,” *Monthly Notices of the Royal Astronomical Society*, vol. 386, no. 3, pp. 1487–1502, 2008, doi:10.1111/j.1365-2966.2008.13112.x.
- Milone, A. P., Marino, A. F., Di Criscienzo, M., D’Antona, F., Bedin, L. R., Da Costa, G., Piotto, G., Tailo, M., Dotter, A., Angeloni, R., et al., “Multiple stellar populations in Magellanic Cloud clusters - VI. A survey of multiple sequences and Be stars in young clusters,” *Monthly Notices of the Royal Astronomical Society*, vol. 477, no. 2, pp. 2640–2663, 2018, doi:10.1093/mnras/sty661.
- Misra, D., Fragos, T., Tauris, T. M., Zapartas, E., and Aguilera-Dena, D. R., “The origin of pulsating ultra-luminous X-ray sources: Low- and intermediate-mass X-ray binaries containing neutron star accretors,” *Astronomy & Astrophysics*, vol. 642, A174, 2020, doi:10.1051/0004-6361/202038070.
- Moe, M. and Di Stefano, R., “Mind Your Ps and Qs: The Interrelation between Period (P) and Mass-ratio (Q) Distributions of Binary Stars,” *The Astrophysical Journal Supplement Series*, vol. 230, no. 2, 15, 2017, doi:10.3847/1538-4365/aa6fb6.
- Mohorovičić, A., “Earthquake of 8 october 1909,” *Geofizika*, vol. 9, no. 1, pp. 3–55, 1910.
- Mombarg, J. S. G., Aerts, C., Van Reeth, T., and Hey, D., “Estimates of (convective core) masses, radii, and relative ages for $\sim 14,000$ Gaia-discovered gravity-mode pulsators monitored by TESS,” *arXiv e-prints*, arXiv:2410.05367, 2024a, doi:10.48550/arXiv.2410.05367.
- Mombarg, J. S. G., Rieutord, M., and Espinosa Lara, F., “The first two-dimensional stellar structure and evolution models of rotating stars. Calibration to β Cephei pulsator HD 192575,” *Astronomy & Astrophysics*, vol. 677, L5, 2023, doi:10.1051/0004-6361/202347454.
- Mombarg, J. S. G., Rieutord, M., and Espinosa Lara, F., “A two-dimensional perspective of the rotational evolution of rapidly rotating intermediate-mass stars. Implications for the formation of single Be stars,” *Astronomy & Astrophysics*, vol. 683, A94, 2024b, doi:10.1051/0004-6361/202348466.
- Mombarg, J. S. G., Van Reeth, T., and Aerts, C., “Constraining stellar evolution theory with asteroseismology of γ Doradus stars using deep learning. Stellar masses, ages, and core-boundary mixing,” *Astronomy & Astrophysics*, vol. 650, A58, 2021, doi:10.1051/0004-6361/202039543.

- Mombarg, J. S. G., Van Reeth, T., Pedersen, M. G., Molenberghs, G., Bowman, D. M., Johnston, C., Tkachenko, A., and Aerts, C., “Astero seismic masses, ages, and core properties of γ Doradus stars using gravito-inertial dipole modes and spectroscopy,” *Monthly Notices of the Royal Astronomical Society*, vol. 485, no. 3, pp. 3248–3263, 2019, doi:10.1093/mnras/stz501.
- Monteiro, M. J. P. F. G., “Porto Oscillation Code (posc),” *Astrophysics and Space Science*, vol. 316, no. 1-4, pp. 121–127, 2008, doi:10.1007/s10509-008-9802-y.
- Morán-Fraile, J., Schneider, F. R. N., Röpke, F. K., Ohlmann, S. T., Pakmor, R., Soutanis, T., and Bauswein, A., “Gravitational wave emission from dynamical stellar interactions,” *Astronomy & Astrophysics*, vol. 672, A9, 2023, doi:10.1051/0004-6361/202245109.
- Moravveji, E., “The impact of enhanced iron opacity on massive star pulsations: updated instability strips,” *Monthly Notices of the Royal Astronomical Society*, vol. 455, no. 1, pp. L67–L71, 2016, doi:10.1093/mnrasl/slv142.
- Moravveji, E., Aerts, C., Pápics, P. I., Triana, S. A., and Vandoren, B., “Tight asteroseismic constraints on core overshooting and diffusive mixing in the slowly rotating pulsating B8.3V star KIC 10526294,” *Astronomy & Astrophysics*, vol. 580, A27, 2015, doi:10.1051/0004-6361/201425290.
- Moravveji, E., Guinan, E. F., Shultz, M., Williamson, M. H., and Moya, A., “Astero seismology of the nearby SN-II Progenitor: Rigel. I. The MOST High-precision Photometry and Radial Velocity Monitoring,” *Astrophysical Journal*, vol. 747, no. 2, 108, 2012a, doi:10.1088/0004-637X/747/2/108.
- Moravveji, E., Moya, A., and Guinan, E. F., “Astero seismology of the nearby SN II Progenitor Rigel. II. epsilon-mechanism Triggering Gravity-mode Pulsations?” *Astrophysical Journal*, vol. 749, no. 1, 74, 2012b, doi:10.1088/0004-637X/749/1/74.
- Moravveji, E., Townsend, R. H. D., Aerts, C., and Mathis, S., “Sub-inertial Gravity Modes in the B8V Star KIC 7760680 Reveal Moderate Core Overshooting and Low Vertical Diffusive Mixing,” *Astrophysical Journal*, vol. 823, no. 2, 130, 2016, doi:10.3847/0004-637X/823/2/130.
- Moreno, M. M., Schneider, F. R. N., Röpke, F. K., Ohlmann, S. T., Pakmor, R., Podsiadlowski, P., and Sand, C., “From 3D hydrodynamic simulations of common-envelope interaction to gravitational-wave mergers,” *Astronomy & Astrophysics*, vol. 667, A72, 2022, doi:10.1051/0004-6361/202142731.
- Morris, T. and Podsiadlowski, P., “Anisotropic mass ejection in binary mergers,” *Monthly Notices of the Royal Astronomical Society*, vol. 365, no. 1, pp. 2–10, 2006, doi:10.1111/j.1365-2966.2005.09645.x.
- Morris, T. and Podsiadlowski, P., “The Triple-Ring Nebula Around SN 1987A: Fingerprint of a Binary Merger,” *Science*, vol. 315, no. 5815, p. 1103, 2007, doi:10.1126/science.1136351.
- Mosser, B., Goupil, M. J., Belkacem, K., Michel, E., Stello, D., Marques, J. P., Elsworth, Y., Barban, C., Beck, P. G., Bedding, T. R., et al., “Probing the core structure and evolution

- of red giants using gravity-dominated mixed modes observed with Kepler,” *Astronomy & Astrophysics*, vol. 540, A143, 2012, doi:10.1051/0004-6361/201118519.
- Moya, A. and Garrido, R., “Granada oscillation code (GraCo),” *Astrophysics and Space Science*, vol. 316, no. 1-4, pp. 129–133, 2008, doi:10.1007/s10509-007-9694-2.
- Naoz, S., “The Eccentric Kozai-Lidov Effect and Its Applications,” *Annual Review of Astronomy and Astrophysics*, vol. 54, pp. 441–489, 2016, doi:10.1146/annurev-astro-081915-023315.
- Neo, S., Miyaji, S., Nomoto, K., and Sugimoto, D., “Effect of Rapid Mass Accretion onto the Main-Sequence Stars,” *Publications of the Astronomical Society of Japan*, vol. 29, pp. 249–262, 1977, aDS Bibcode: 1977PASJ...29..249N.
- Nieuwenhuijzen, H. and de Jager, C., “Parametrization of stellar rates of mass loss as functions of the fundamental stellar parameters M , L , and R ,” *Astronomy & Astrophysics*, vol. 231, pp. 134–136, 1990.
- Offner, S. S. R., Moe, M., Kratter, K. M., Sadavoy, S. I., Jensen, E. L. N., and Tobin, J. J., “The Origin and Evolution of Multiple Star Systems,” in Inutsuka, S., Aikawa, Y., Muto, T., Tomida, K., and Tamura, M. (editors), “Protostars and Planets VII,” *Astronomical Society of the Pacific Conference Series*, vol. 534, p. 275, 2023, doi:10.48550/arXiv.2203.10066.
- Oldham, R. D., “The Constitution of the Interior of the Earth, as Revealed by Earthquakes,” *Quarterly Journal of the Geological Society of London*, vol. 62, no. 1-4, pp. 456–475, 1906, doi:10.1144/GSL.JGS.1906.062.01-04.21.
- Ondratschek, P. A., Röpkke, F. K., Schneider, F. R. N., Fendt, C., Sand, C., Ohlmann, S. T., Pakmor, R., and Springel, V., “Bipolar planetary nebulae from common-envelope evolution of binary stars,” *Astronomy & Astrophysics*, vol. 660, L8, 2022, doi:10.1051/0004-6361/202142478.
- Ostrov, P. G., “Orbital solution for the MACHO*05:34:41.3-69:31:39 O3If*+O6:V eclipsing binary system in the Large Magellanic Cloud,” *Monthly Notices of the Royal Astronomical Society*, vol. 321, no. 1, pp. L25–L28, 2001, doi:10.1046/j.1365-8711.2001.04267.x.
- Ostrowski, J., Baran, A. S., Sanjayan, S., and Sahoo, S. K., “Evolutionary modelling of subdwarf B stars using MESA with the predictive mixing and convective pre-mixing schemes,” *Monthly Notices of the Royal Astronomical Society*, vol. 503, no. 3, pp. 4646–4661, 2021, doi:10.1093/mnras/staa3751.
- Ostrowski, J. and Daszyńska-Daszkiewicz, J., “Pulsations in B-type supergiants with masses $M_{\text{J}} \geq 20 M_{\odot}$ before and after core helium ignition,” *Monthly Notices of the Royal Astronomical Society*, vol. 447, no. 3, pp. 2378–2386, 2015, doi:10.1093/mnras/stu2605.
- Ouazzani, R.-M., Salmon, S. J. A. J., Antoci, V., Bedding, T. R., Murphy, S. J., and Roxburgh, I. W., “A new asteroseismic diagnostic for internal rotation in γ Doradus stars,” *Monthly Notices of the Royal Astronomical Society*, vol. 465, no. 2, pp. 2294–2309, 2017, doi:10.1093/mnras/stw2717.

- Owocki, S. P., Hirai, R., Podsiadlowski, P., and Schneider, F. R. N., “Hydrodynamical simulations and similarity relations for eruptive mass-loss from massive stars,” *Monthly Notices of the Royal Astronomical Society*, vol. 485, no. 1, pp. 988–1000, 2019, doi:10.1093/mnras/stz461.
- Packet, W., “On the spin-up of the mass accreting component in a close binary system,” *Astronomy & Astrophysics*, vol. 102, no. 1, pp. 17–19, 1981.
- Paczyński, B., “Evolutionary Processes in Close Binary Systems,” *Annual Review of Astronomy and Astrophysics*, vol. 9, p. 183, 1971, doi:10.1146/annurev.aa.09.090171.001151.
- Paczynski, B., “Common Envelope Binaries,” in Eggleton, P., Mitton, S., and Whelan, J. (editors), “Structure and Evolution of Close Binary Systems,” *IAU Symposium*, vol. 73, p. 75, 1976.
- Paczynski, B., “A Polytropic Model of an Accretion Disk, a Boundary Layer, and a Star,” *Astrophysical Journal*, vol. 370, p. 597, 1991, doi:10.1086/169846, aDS Bibcode: 1991ApJ...370..597P.
- Paczyński, B., Szczygieł, D. M., Pilecki, B., and Pojmański, G., “Eclipsing binaries in the All Sky Automated Survey catalogue,” *Monthly Notices of the Royal Astronomical Society*, vol. 368, no. 3, pp. 1311–1318, 2006, doi:10.1111/j.1365-2966.2006.10223.x.
- Pápics, P. I., Moravveji, E., Aerts, C., Tkachenko, A., Triana, S. A., Bloemen, S., and Southworth, J., “KIC 10526294: a slowly rotating B star with rotationally split, quasi-equally spaced gravity modes,” *Astronomy & Astrophysics*, vol. 570, A8, 2014, doi:10.1051/0004-6361/201424094.
- Pápics, P. I., Tkachenko, A., Aerts, C., Van Reeth, T., De Smedt, K., Hillen, M., Østensen, R., and Moravveji, E., “Astero seismic Fingerprints of Rotation and Mixing in the Slowly Pulsating B8 V Star KIC 7760680,” *The Astrophysical Journal Letters*, vol. 803, no. 2, L25, 2015, doi:10.1088/2041-8205/803/2/L25.
- Pápics, P. I., Tkachenko, A., Van Reeth, T., Aerts, C., Moravveji, E., Van de Sande, M., De Smedt, K., Bloemen, S., Southworth, J., Debosscher, J., et al., “Signatures of internal rotation discovered in the Kepler data of five slowly pulsating B stars,” *Astronomy & Astrophysics*, vol. 598, A74, 2017, doi:10.1051/0004-6361/201629814.
- Pavlovskii, K. and Ivanova, N., “Mass transfer from giant donors,” *Monthly Notices of the Royal Astronomical Society*, vol. 449, no. 4, pp. 4415–4427, 2015, doi:10.1093/mnras/stv619.
- Pawlak, M., Soszyński, I., Udalski, A., Szymański, M. K., Wyrzykowski, Ł., Ulaczyk, K., Poleski, R., Pietrukowicz, P., Kozłowski, S., Skowron, D. M., et al., “The OGLE Collection of Variable Stars. Eclipsing Binaries in the Magellanic System,” *Acta Astronomica*, vol. 66, no. 4, pp. 421–432, 2016, doi:10.48550/arXiv.1612.06394.
- Paxton, B., “EZ to Evolve ZAMS Stars: A Program Derived from Eggleton’s Stellar Evolution Code,” *Publications of the Astronomical Society of the Pacific*, vol. 116, no. 821, pp. 699–701, 2004, doi:10.1086/422345.

- Paxton, B., Bildsten, L., Dotter, A., Herwig, F., Lesaffre, P., and Timmes, F., “Modules for Experiments in Stellar Astrophysics (MESA),” *The Astrophysical Journal Supplement Series*, vol. 192, no. 1, 3, 2011, doi:10.1088/0067-0049/192/1/3.
- Paxton, B., Cantiello, M., Arras, P., Bildsten, L., Brown, E. F., Dotter, A., Mankovich, C., Montgomery, M. H., Stello, D., Timmes, F. X., et al., “Modules for Experiments in Stellar Astrophysics (MESA): Planets, Oscillations, Rotation, and Massive Stars,” *The Astrophysical Journal Supplement Series*, vol. 208, no. 1, 4, 2013, doi:10.1088/0067-0049/208/1/4.
- Paxton, B., Marchant, P., Schwab, J., Bauer, E. B., Bildsten, L., Cantiello, M., Dessart, L., Farmer, R., Hu, H., Langer, N., et al., “Modules for Experiments in Stellar Astrophysics (MESA): Binaries, Pulsations, and Explosions,” *The Astrophysical Journal Supplement Series*, vol. 220, no. 1, 15, 2015, doi:10.1088/0067-0049/220/1/15.
- Paxton, B., Schwab, J., Bauer, E. B., Bildsten, L., Blinnikov, S., Duffell, P., Farmer, R., Goldberg, J. A., Marchant, P., Sorokina, E., et al., “Modules for Experiments in Stellar Astrophysics (MESA): Convective Boundaries, Element Diffusion, and Massive Star Explosions,” *The Astrophysical Journal Supplement Series*, vol. 234, no. 2, 34, 2018, doi:10.3847/1538-4365/aaa5a8.
- Paxton, B., Smolec, R., Schwab, J., Gautschy, A., Bildsten, L., Cantiello, M., Dotter, A., Farmer, R., Goldberg, J. A., Jermyn, A. S., et al., “Modules for Experiments in Stellar Astrophysics (MESA): Pulsating Variable Stars, Rotation, Convective Boundaries, and Energy Conservation,” *The Astrophysical Journal Supplement Series*, vol. 243, no. 1, 10, 2019, doi:10.3847/1538-4365/ab2241.
- Pedersen, M. G., Aerts, C., Pápics, P. I., Michielsen, M., Gebruers, S., Rogers, T. M., Molénberghs, G., Burssens, S., Garcia, S., and Bowman, D. M., “Internal mixing of rotating stars inferred from dipole gravity modes,” *Nature Astronomy*, 2021, doi:10.1038/s41550-021-01351-x.
- Pedersen, M. G., Aerts, C., Pápics, P. I., and Rogers, T. M., “The shape of convective core overshooting from gravity-mode period spacings,” *Astronomy & Astrophysics*, vol. 614, A128, 2018, doi:10.1051/0004-6361/201732317.
- Pelupessy, F. I., van Elteren, A., de Vries, N., McMillan, S. L. W., Drost, N., and Portegies Zwart, S. F., “The Astrophysical Multipurpose Software Environment,” *Astronomy & Astrophysics*, vol. 557, A84, 2013, doi:10.1051/0004-6361/201321252.
- Perets, H. B. and Fabrycky, D. C., “ON THE TRIPLE ORIGIN OF BLUE STRAGGLERS,” *Astrophysical Journal*, vol. 697, no. 2, p. 1048, 2009, doi:10.1088/0004-637X/697/2/1048.
- Picco, A., Marchant, P., Sana, H., and Nelemans, G., “Forming merging double compact objects with stable mass transfer,” *Astronomy & Astrophysics*, vol. 681, A31, 2024, doi:10.1051/0004-6361/202347090.
- Pietrukowicz, P., Mróz, P., Soszyński, I., Udalski, A., Poleski, R., Szymański, M. K., Kubiak, M., Pietrzyński, G., Wyrzykowski, Ł., Ulaczyk, K., et al., “Eclipsing Binary Stars in the OGLE-III Galactic Disk Fields,” *Acta Astronomica*, vol. 63, no. 2, pp. 115–133, 2013, doi:10.48550/arXiv.1306.6324.

- Pinsonneault, M. H., Kawaler, S. D., Sofia, S., and Demarque, P., “Evolutionary Models of the Rotating Sun,” *Astrophysical Journal*, vol. 338, p. 424, 1989, doi:10.1086/167210.
- Podsiadlowski, P., “The Progenitor of SN 1987A,” *Publications of the Astronomical Society of the Pacific*, vol. 104, p. 717, 1992, doi:10.1086/133043, aDS Bibcode: 1992PASP..104..717P.
- Podsiadlowski, P., “Massive binary evolution,” *New Astronomy Reviews*, vol. 54, no. 3-6, pp. 39–44, 2010, doi:10.1016/j.newar.2010.09.023.
- Podsiadlowski, P., Joss, P. C., and Hsu, J. J. L., “Presupernova Evolution in Massive Interacting Binaries,” *Astrophysical Journal*, vol. 391, p. 246, 1992, doi:10.1086/171341.
- Podsiadlowski, P., Joss, P. C., and Rappaport, S., “A merger model for SN 1987A.” *Astronomy & Astrophysics*, vol. 227, pp. L9–L12, 1990.
- Podsiadlowski, P., Morris, T. S., and Ivanova, N., “Massive Binary Mergers: A Unique Scenario for the sgB[e] Phenomenon?” in Kraus, M. and Miroshnichenko, A. S. (editors), “Stars with the B[e] Phenomenon,” *Astronomical Society of the Pacific Conference Series*, vol. 355, p. 259, 2006.
- Pols, O. R., “Case A evolution of massive close binaries: formation of contact systems and possible reversal of the supernova order,” *Astronomy & Astrophysics*, vol. 290, pp. 119–128, 1994.
- Pols, O. R., Tout, C. A., Eggleton, P. P., and Han, Z., “Approximate input physics for stellar modelling,” *Monthly Notices of the Royal Astronomical Society*, vol. 274, no. 3, pp. 964–974, 1995, doi:10.1093/mnras/274.3.964.
- Popham, R. and Narayan, R., “Does Accretion Cease When a Star Approaches Breakup?” *Astrophysical Journal*, vol. 370, p. 604, 1991, doi:10.1086/169847, aDS Bibcode: 1991ApJ...370..604P.
- Portegies Zwart, S. and McMillan, S., *Astrophysical Recipes; The art of AMUSE*, 2514–3433, IOP Publishing, 2018, ISBN 978-0-7503-1320-9, doi:10.1088/978-0-7503-1320-9.
- Portegies Zwart, S., McMillan, S., Harfst, S., Groen, D., Fujii, M., Nualláin, B. Ó., Glebbeek, E., Hoggie, D., Lombardi, J., Hut, P., et al., “A multiphysics and multiscale software environment for modeling astrophysical systems,” *New Astronomy*, vol. 14, no. 4, pp. 369–378, 2009, doi:10.1016/j.newast.2008.10.006.
- Portegies Zwart, S., McMillan, S. L. W., van Elteren, E., Pelupessy, I., and de Vries, N., “Multi-physics simulations using a hierarchical interchangeable software interface,” *Computer Physics Communications*, vol. 184, no. 3, pp. 456–468, 2013, doi:10.1016/j.cpc.2012.09.024.
- Portegies Zwart, S., van Elteren, A., Pelupessy, I., McMillan, S., Rieder, S., de Vries, N., Marosvolgyi, M., Whitehead, A., Wall, J., Drost, N., et al., “AMUSE: the Astrophysical Multipurpose Software Environment,” Zenodo, 2019, doi:10.5281/zenodo.1435860.
- Portegies Zwart, S. F., Baumgardt, H., Hut, P., Makino, J., and McMillan, S. L. W., “Formation of massive black holes through runaway collisions in dense young star clusters,” *Nature*, vol. 428, no. 6984, pp. 724–726, 2004, doi:10.1038/nature02448.

- Portegies Zwart, S. F., Hut, P., McMillan, S. L. W., and Verbunt, F., “Star cluster ecology. II. Binary evolution with single-star encounters,” *Astronomy & Astrophysics*, vol. 328, pp. 143–157, 1997, doi:10.48550/arXiv.astro-ph/9706090.
- Portegies Zwart, S. F., Makino, J., McMillan, S. L. W., and Hut, P., “Star cluster ecology. III. Runaway collisions in young compact star clusters,” *Astronomy & Astrophysics*, vol. 348, pp. 117–126, 1999, doi:10.48550/arXiv.astro-ph/9812006.
- Portegies Zwart, S. F. and van den Heuvel, E. P. J., “Was the nineteenth century giant eruption of Eta Carinae a merger event in a triple system?” *Monthly Notices of the Royal Astronomical Society*, vol. 456, no. 4, pp. 3401–3412, 2016, doi:10.1093/mnras/stv2787.
- Prat, V., Mathis, S., Buysschaert, B., Van Beeck, J., Bowman, D. M., Aerts, C., and Neiner, C., “Period spacings of gravity modes in rapidly rotating magnetic stars. I. Axisymmetric fossil field with poloidal and toroidal components,” *Astronomy & Astrophysics*, vol. 627, A64, 2019, doi:10.1051/0004-6361/201935462.
- Provost, J., “NOSC: Nice Oscillations Code,” *Astrophysics and Space Science*, vol. 316, no. 1-4, pp. 135–140, 2008, doi:10.1007/s10509-007-9654-x.
- Prša, A., Batalha, N., Slawson, R. W., Doyle, L. R., Welsh, W. F., Orosz, J. A., Seager, S., Rucker, M., Mjaseth, K., Engle, S. G., et al., “Kepler Eclipsing Binary Stars. I. Catalog and Principal Characterization of 1879 Eclipsing Binaries in the First Data Release,” *The Astronomical Journal*, vol. 141, no. 3, 83, 2011, doi:10.1088/0004-6256/141/3/83.
- Quentin, L. G. and Tout, C. A., “Rotation and magnetism in intermediate-mass stars,” *Monthly Notices of the Royal Astronomical Society*, vol. 477, no. 2, pp. 2298–2309, 2018, doi:10.1093/mnras/sty770.
- Ramachandran, V., Klencki, J., Sander, A. A. C., Pauli, D., Shenar, T., Oskinova, L. M., and Hamann, W. R., “A partially stripped massive star in a Be binary at low metallicity. A missing link towards Be X-ray binaries and double neutron star mergers,” *Astronomy & Astrophysics*, vol. 674, L12, 2023, doi:10.1051/0004-6361/202346818.
- Rasio, F. A., “The Minimum Mass Ratio of W Ursae Majoris Binaries,” *Astrophysical Journal*, vol. 444, p. L41, 1995, doi:10.1086/187855, aDS Bibcode: 1995ApJ...444L..41R.
- Rauer, H., Aerts, C., Cabrera, J., Deleuil, M., Erikson, A., Gizon, L., Goupil, M., Heras, A., Lorenzo-Alvarez, J., Marliani, F., et al., “The PLATO Mission,” *arXiv e-prints*, arXiv:2406.05447, 2024, doi:10.48550/arXiv.2406.05447.
- Rehm, R., Mombarg, J. S. G., Aerts, C., Michielsen, M., Burssens, S., and Townsend, R. H. D., “The impact of radiative levitation on mode excitation of main-sequence B-type pulsators,” *Astronomy & Astrophysics*, vol. 687, A175, 2024, doi:10.1051/0004-6361/202449624.
- Reimers, D., “Circumstellar absorption lines and mass loss from red giants.” *Memoires of the Societe Royale des Sciences de Liege*, vol. 8, pp. 369–382, 1975.
- Ricker, G. R., Vanderspek, R., Winn, J., Seager, S., Berta-Thompson, Z., Levine, A., Villaseñor, J., Latham, D., Charbonneau, D., Holman, M., et al., “The Transiting Exoplanet

- Survey Satellite,” in MacEwen, H. A., Fazio, G. G., Lystrup, M., Batalha, N., Siegler, N., and Tong, E. C. (editors), “Space Telescopes and Instrumentation 2016: Optical, Infrared, and Millimeter Wave,” *Society of Photo-Optical Instrumentation Engineers (SPIE) Conference Series*, vol. 9904, p. 99042B, 2016, doi:10.1117/12.2232071.
- Ricker, G. R., Winn, J. N., Vanderspek, R., Latham, D. W., Bakos, G. Á., Bean, J. L., Bert-Thompson, Z. K., Brown, T. M., Buchhave, L., Butler, N. R., et al., “Transiting Exoplanet Survey Satellite (TESS),” *Journal of Astronomical Telescopes, Instruments, and Systems*, vol. 1, 014003, 2015, doi:10.1117/1.JATIS.1.1.014003.
- Ritter, H., “Turning on and off mass transfer in cataclysmic binaries.” *Astronomy & Astrophysics*, vol. 202, pp. 93–100, 1988.
- Röpke, F. K. and De Marco, O., “Simulations of common-envelope evolution in binary stellar systems: physical models and numerical techniques,” *Living Reviews in Computational Astrophysics*, vol. 9, no. 1, 2, 2023, doi:10.1007/s41115-023-00017-x.
- Roxburgh, I. W., “The OSCROX stellar oscillation code,” *Astrophysics and Space Science*, vol. 316, no. 1–4, pp. 141–147, 2008, doi:10.1007/s10509-007-9607-4.
- Rucinski, S. M., “The short-period end of the contact binary period distribution based on the All-Sky Automated Survey,” *Monthly Notices of the Royal Astronomical Society*, vol. 382, no. 1, pp. 393–396, 2007, doi:10.1111/j.1365-2966.2007.12377.x.
- Rui, N. Z. and Fuller, J., “Asteroseismic fingerprints of stellar mergers,” *Monthly Notices of the Royal Astronomical Society*, vol. 508, no. 2, pp. 1618–1631, 2021, doi:10.1093/mnras/stab2528.
- Rui, N. Z., Ong, J. M. J., and Mathis, S., “Asteroseismic g-mode period spacings in strongly magnetic rotating stars,” *Monthly Notices of the Royal Astronomical Society*, vol. 527, no. 3, pp. 6346–6362, 2024, doi:10.1093/mnras/stad3461.
- Ryu, T., Sills, A., Pakmor, R., de Mink, S., and Mathieu, R., “Magnetic Field Amplification during Stellar Collisions between Low-Mass Stars,” *arXiv e-prints*, arXiv:2410.00148, 2024, doi:10.48550/arXiv.2410.00148.
- Saio, H., Bedding, T. R., Kurtz, D. W., Murphy, S. J., Antoci, V., Shibahashi, H., Li, G., and Takata, M., “An astrophysical interpretation of the remarkable g-mode frequency groups of the rapidly rotating γ Dor star, KIC 5608334,” *Monthly Notices of the Royal Astronomical Society*, vol. 477, no. 2, pp. 2183–2195, 2018, doi:10.1093/mnras/sty784.
- Saio, H., Georgy, C., and Meynet, G., “Evolution of blue supergiants and α Cygni variables: puzzling CNO surface abundances,” *Monthly Notices of the Royal Astronomical Society*, vol. 433, no. 2, pp. 1246–1257, 2013, doi:10.1093/mnras/stt796.
- Saio, H., Kuschnig, R., Gautschy, A., Cameron, C., Walker, G. A. H., Matthews, J. M., Guenther, D. B., Moffat, A. F. J., Rucinski, S. M., Sasselov, D., et al., “MOST Detects g- and p-Modes in the B Supergiant HD 163899 (B2 Ib/II),” *Astrophysical Journal*, vol. 650, no. 2, pp. 1111–1118, 2006, doi:10.1086/507409.

- Sana, H., de Mink, S. E., de Koter, A., Langer, N., Evans, C. J., Gieles, M., Gosset, E., Izzard, R. G., Le Bouquin, J. B., and Schneider, F. R. N., “Binary Interaction Dominates the Evolution of Massive Stars,” *Science*, vol. 337, p. 444, 2012, doi:10.1126/science.1223344.
- Sánchez Arias, J. P., Németh, P., de Almeida, E. S. d. G., Ruiz Diaz, M. A., Kraus, M., and Haucke, M., “Unveiling the Evolutionary State of Three B Supergiant Stars: PU Gem, ϵ CMa, and η CMa,” *Galaxies*, vol. 11, no. 5, 93, 2023, doi:10.3390/galaxies11050093.
- Sander, A. A. C. and Vink, J. S., “On the nature of massive helium star winds and Wolf-Rayet-type mass-loss,” *Monthly Notices of the Royal Astronomical Society*, vol. 499, no. 1, pp. 873–892, 2020, doi:10.1093/mnras/staa2712.
- Sandquist, E. L., Bolte, M., and Hernquist, L., “Composition Mixing during Blue Straggler Formation and Evolution,” *Astrophysical Journal*, vol. 477, no. 1, pp. 335–345, 1997, doi:10.1086/303709.
- Savonije, G. J., “Roche-lobe overflow and massive X-ray binary systems.” *Astronomy & Astrophysics*, vol. 71, pp. 352–358, 1979.
- Scherer, P. O., *Computational physics: simulation of classical and quantum systems*, Springer, 2017.
- Schneider, F. R. N., Izzard, R. G., de Mink, S. E., Langer, N., Stolte, A., de Koter, A., Gvaramadze, V. V., Hußmann, B., Liermann, A., and Sana, H., “Ages of Young Star Clusters, Massive Blue Stragglers, and the Upper Mass Limit of Stars: Analyzing Age-dependent Stellar Mass Functions,” *Astrophysical Journal*, vol. 780, no. 2, 117, 2014, doi:10.1088/0004-637X/780/2/117.
- Schneider, F. R. N., Izzard, R. G., Langer, N., and de Mink, S. E., “Evolution of Mass Functions of Coeval Stars through Wind Mass Loss and Binary Interactions,” *Astrophysical Journal*, vol. 805, no. 1, 20, 2015, doi:10.1088/0004-637X/805/1/20.
- Schneider, F. R. N., Ohlmann, S. T., Podsiadlowski, P., Röpke, F. K., Balbus, S. A., and Pakmor, R., “Long-term evolution of a magnetic massive merger product,” *Monthly Notices of the Royal Astronomical Society*, vol. 495, no. 3, pp. 2796–2812, 2020, doi:10.1093/mnras/staa1326.
- Schneider, F. R. N., Ohlmann, S. T., Podsiadlowski, P., Röpke, F. K., Balbus, S. A., Pakmor, R., and Springel, V., “Stellar mergers as the origin of magnetic massive stars,” *Nature*, vol. 574, no. 7777, pp. 211–214, 2019, doi:10.1038/s41586-019-1621-5.
- Schneider, F. R. N., Podsiadlowski, P., Langer, N., Castro, N., and Fossati, L., “Rejuvenation of stellar mergers and the origin of magnetic fields in massive stars,” *Monthly Notices of the Royal Astronomical Society*, vol. 457, no. 3, pp. 2355–2365, 2016, doi:10.1093/mnras/stw148.
- Schneider, F. R. N., Podsiadlowski, P., and Laplace, E., “Pre-supernova evolution and final fate of stellar mergers and accretors of binary mass transfer,” *Astronomy & Astrophysics*, vol. 686, A45, 2024, doi:10.1051/0004-6361/202347854.

- Schootemeijer, A., Götberg, Y., de Mink, S. E., Gies, D., and Zapartas, E., “Clues about the scarcity of stripped-envelope stars from the evolutionary state of the sdO+Be binary system φ Persei,” *Astronomy & Astrophysics*, vol. 615, A30, 2018, doi:10.1051/0004-6361/201731194.
- Schootemeijer, A., Langer, N., Grin, N. J., and Wang, C., “Constraining mixing in massive stars in the Small Magellanic Cloud,” *Astronomy & Astrophysics*, vol. 625, A132, 2019, doi:10.1051/0004-6361/201935046.
- Schürmann, C. and Langer, N., “Exploring the borderline between stable mass transfer and mergers in close binary evolution,” *arXiv e-prints*, arXiv:2404.08615, 2024, doi:10.48550/arXiv.2404.08615.
- Sen, K., Langer, N., Marchant, P., Menon, A., de Mink, S. E., Schootemeijer, A., Schürmann, C., Mahy, L., Hastings, B., Nathaniel, K., et al., “Detailed models of interacting short-period massive binary stars,” *Astronomy & Astrophysics*, vol. 659, A98, 2022, doi:10.1051/0004-6361/202142574.
- Shenar, T., Bodensteiner, J., Sana, H., Crowther, P. A., Lennon, D. J., Abdul-Masih, M., Almeida, L. A., Backs, F., Berlanas, S. R., Bernini-Peron, M., et al., “Binarity at LOW Metallicity (BLOeM): A spectroscopic VLT monitoring survey of massive stars in the SMC,” *Astronomy & Astrophysics*, vol. 690, A289, 2024, doi:10.1051/0004-6361/202451586.
- Shenar, T., Wade, G. A., Marchant, P., Bagnulo, S., Bodensteiner, J., Bowman, D. M., Gilkis, A., Langer, N., Nicolas-Chené, A., Oskinova, L., et al., “A massive helium star with a sufficiently strong magnetic field to form a magnetar,” *Science*, vol. 381, no. 6659, pp. 761–765, 2023, doi:10.1126/science.ade3293.
- Shu, F. H., Lubow, S. H., and Anderson, L., “On the structure of contact binaries. I. The contact discontinuity,” *Astrophysical Journal*, vol. 209, pp. 536–546, 1976, doi:10.1086/154748.
- Shu, F. H., Lubow, S. H., and Anderson, L., “On the structure of contact binaries. III. Mass and energy flow,” *Astrophysical Journal*, vol. 229, pp. 223–241, 1979, doi:10.1086/156948.
- Sibony, Y., Georgy, C., Ekström, S., and Meynet, G., “The impact of convective criteria on the properties of massive stars,” *Astronomy & Astrophysics*, vol. 680, A101, 2023, doi:10.1051/0004-6361/202346638.
- Siess, L., “Evolution of massive AGB stars. I. Carbon burning phase,” *Astronomy & Astrophysics*, vol. 448, no. 2, pp. 717–729, 2006, doi:10.1051/0004-6361:20053043.
- Siess, L., Dufour, E., and Forestini, M., “An internet server for pre-main sequence tracks of low- and intermediate-mass stars,” *Astronomy & Astrophysics*, vol. 358, pp. 593–599, 2000, doi:10.48550/arXiv.astro-ph/0003477.
- Sills, A., Faber, J. A., Lombardi, J., James C., Rasio, F. A., and Warren, A. R., “Evolution of Stellar Collision Products in Globular Clusters. II. Off-Axis Collisions,” *Astrophysical Journal*, vol. 548, no. 1, pp. 323–334, 2001, doi:10.1086/318689.

- Sills, A., Lombardi, J., James C., Baily, C. D., Demarque, P., Rasio, F. A., and Shapiro, S. L., “Evolution of Stellar Collision Products in Globular Clusters. I. Head-on Collisions,” *Astrophysical Journal*, vol. 487, no. 1, pp. 290–303, 1997, doi:10.1086/304588.
- Smeyers, P. and van Hoolst, T., *Linear Isentropic Oscillations of Stars: Theoretical Foundations*, vol. 371, Springer Berlin, Heidelberg, 2010, doi:10.1007/978-3-642-13030-4.
- Smith, N., Rest, A., Andrews, J. E., Matheson, T., Bianco, F. B., Prieto, J. L., James, D. J., Smith, R. C., Strampelli, G. M., and Zenteno, A., “Exceptionally fast ejecta seen in light echoes of Eta Carinae’s Great Eruption,” *Monthly Notices of the Royal Astronomical Society*, vol. 480, no. 2, pp. 1457–1465, 2018, doi:10.1093/mnras/sty1479.
- Soberman, G. E., Phinney, E. S., and van den Heuvel, E. P. J., “Stability criteria for mass transfer in binary stellar evolution.” *Astronomy & Astrophysics*, vol. 327, pp. 620–635, 1997.
- Soker, N. and Tylenda, R., “Modelling V838 Monocerotis as a Mergeburst Object,” in Corradi, R. L. M. and Munari, U. (editors), “The Nature of V838 Mon and its Light Echo,” *Astronomical Society of the Pacific Conference Series*, vol. 363, p. 280, 2007, doi:10.48550/arXiv.astro-ph/0606371.
- Soszyński, I., Pawlak, M., Pietrukowicz, P., Udalski, A., Szymański, M. K., Wyrzykowski, Ł., Ulaczyk, K., Poleski, R., Kozłowski, S., Skowron, D. M., et al., “The OGLE Collection of Variable Stars. Over 450 000 Eclipsing and Ellipsoidal Binary Systems Toward the Galactic Bulge,” *Acta Astronomica*, vol. 66, no. 4, pp. 405–420, 2016, doi:10.48550/arXiv.1701.03105.
- Stępień, K., “Evolution of the progenitor binary of V1309 Scorpii before merger,” *Astronomy & Astrophysics*, vol. 531, A18, 2011, doi:10.1051/0004-6361/201116689.
- Suran, M. D., “LNAWENR—linear nonadiabatic nonradial waves,” *Astrophysics and Space Science*, vol. 316, no. 1-4, pp. 163–166, 2008, doi:10.1007/s10509-007-9714-2.
- Suzuki, T. K., Nakasato, N., Baumgardt, H., Ibukiyama, A., Makino, J., and Ebisuzaki, T., “Evolution of Collisionally Merged Massive Stars,” *Astrophysical Journal*, vol. 668, no. 1, pp. 435–448, 2007, doi:10.1086/521214.
- Szewczuk, W. and Daszyńska-Daszkiewicz, J., “Domains of pulsational instability of low-frequency modes in rotating upper main sequence stars,” *Monthly Notices of the Royal Astronomical Society*, vol. 469, no. 1, pp. 13–46, 2017, doi:10.1093/mnras/stx738.
- Szewczuk, W. and Daszyńska-Daszkiewicz, J., “KIC 3240411 - the hottest known SPB star with the asymptotic g-mode period spacing,” *Monthly Notices of the Royal Astronomical Society*, vol. 478, no. 2, pp. 2243–2256, 2018, doi:10.1093/mnras/sty1126.
- Szewczuk, W., Walczak, P., and Daszyńska-Daszkiewicz, J., “Variability of newly identified B-type stars observed by Kepler,” *Monthly Notices of the Royal Astronomical Society*, vol. 503, no. 4, pp. 5894–5928, 2021, doi:10.1093/mnras/stab683.
- Takata, M., “Analysis of Adiabatic Dipolar Oscillations of Stars,” *Publications of the Astronomical Society of Japan*, vol. 58, pp. 893–908, 2006, doi:10.1093/pasj/58.5.893.

- Takata, M., “Mode Classification of Linear Adiabatic Oscillations of Spherically Symmetric Stars,” *Publications of the Astronomical Society of Japan*, vol. 64, 66, 2012, doi:10.1093/pasj/64.4.66.
- Tassoul, M., “Asymptotic approximations for stellar nonradial pulsations.” *The Astrophysical Journal Supplement Series*, vol. 43, pp. 469–490, 1980, doi:10.1086/190678.
- Tauris, T. M. and van den Heuvel, E. P. J., “Formation and evolution of compact stellar X-ray sources,” in Lewin, W. H. G. and van der Klis, M. (editors), “Compact stellar X-ray sources,” vol. 39, pp. 623–665, Cambridge University Press, 2006, doi:10.48550/arXiv.astro-ph/0303456.
- Tauris, T. M. and van den Heuvel, E. P. J., *Physics of Binary Star Evolution. From Stars to X-ray Binaries and Gravitational Wave Sources*, Princeton University Press, 2023, doi:10.48550/arXiv.2305.09388.
- Temaj, D., Schneider, F. R. N., Laplace, E., Wei, D., and Podsiadlowski, P., “Convective-core overshooting and the final fate of massive stars,” *Astronomy & Astrophysics*, vol. 682, A123, 2024, doi:10.1051/0004-6361/202347434.
- Temmink, K. D., Pols, O. R., Justham, S., Istrate, A. G., and Toonen, S., “Coping with loss. Stability of mass transfer from post-main-sequence donor stars,” *Astronomy & Astrophysics*, vol. 669, A45, 2023, doi:10.1051/0004-6361/202244137.
- Tokuno, T. and Takata, M., “Asteroseismology of the dip structure in period-spacings of rapidly rotating γ Doradus stars caused by the coupling between core and envelope oscillations,” *Monthly Notices of the Royal Astronomical Society*, vol. 514, no. 3, pp. 4140–4159, 2022, doi:10.1093/mnras/stac1492.
- Toonen, S., Boekholt, T. C. N., and Portegies Zwart, S., “Stellar triples on the edge. Comprehensive overview of the evolution of destabilised triples leading to stellar and binary exotica,” *Astronomy & Astrophysics*, vol. 661, A61, 2022, doi:10.1051/0004-6361/202141991.
- Toonen, S., Portegies Zwart, S., Hamers, A. S., and Bandopadhyay, D., “The evolution of stellar triples. The most common evolutionary pathways,” *Astronomy & Astrophysics*, vol. 640, A16, 2020, doi:10.1051/0004-6361/201936835.
- Tout, C. A., Wickramasinghe, D. T., and Ferrario, L., “Magnetic fields in white dwarfs and stellar evolution,” *Monthly Notices of the Royal Astronomical Society*, vol. 355, no. 3, pp. L13–L16, 2004, doi:10.1111/j.1365-2966.2004.08482.x.
- Townsend, R. and Rosenberg, J., “PyGYRE,” Python Package Index, 2020, <https://pygyre.readthedocs.io/en/stable/>.
- Townsend, R. H. D., “Asymptotic expressions for the angular dependence of low-frequency pulsation modes in rotating stars,” *Monthly Notices of the Royal Astronomical Society*, vol. 340, no. 3, pp. 1020–1030, 2003, doi:10.1046/j.1365-8711.2003.06379.x.
- Townsend, R. H. D., “Influence of the Coriolis force on the instability of slowly pulsating B stars,” *Monthly Notices of the Royal Astronomical Society*, vol. 360, no. 2, pp. 465–476, 2005, doi:10.1111/j.1365-2966.2005.09002.x.

- Townsend, R. H. D., Goldstein, J., and Zweibel, E. G., “Angular momentum transport by heat-driven g-modes in slowly pulsating B stars,” *Monthly Notices of the Royal Astronomical Society*, vol. 475, no. 1, pp. 879–893, 2018, doi:10.1093/mnras/stx3142.
- Townsend, R. H. D. and Teitler, S. A., “GYRE: an open-source stellar oscillation code based on a new Magnus Multiple Shooting scheme,” *Monthly Notices of the Royal Astronomical Society*, vol. 435, pp. 3406–3418, 2013, doi:10.1093/mnras/stt1533.
- Tylenda, R., Crause, L. A., Górny, S. K., and Schmidt, M. R., “V4332 Sagittarii revisited,” *Astronomy & Astrophysics*, vol. 439, no. 2, pp. 651–661, 2005, doi:10.1051/0004-6361:20041581.
- Tylenda, R., Hajduk, M., Kamiński, T., Udalski, A., Soszyński, I., Szymański, M. K., Kubiak, M., Pietrzyński, G., Poleski, R., Wyrzykowski, Ł., et al., “V1309 Scorpii: merger of a contact binary,” *Astronomy & Astrophysics*, vol. 528, A114, 2011, doi:10.1051/0004-6361/201016221.
- Ulrich, R. K. and Burger, H. L., “The accreting component of mass-exchange binaries.” *Astrophysical Journal*, vol. 206, pp. 509–514, 1976, doi:10.1086/154406, aDS Bibcode: 1976ApJ...206..509U.
- Unno, W., Osaki, Y., Ando, H., Saio, H., and Shibahashi, H., *Nonradial oscillations of stars*, University of Tokyo Press, 1989.
- Urbaneja, M. A., Kudritzki, R. P., Gieren, W., Pietrzyński, G., Bresolin, F., and Przybilla, N., “LMC Blue Supergiant Stars and the Calibration of the Flux-weighted Gravity-Luminosity Relationship,” *The Astronomical Journal*, vol. 154, no. 3, 102, 2017, doi:10.3847/1538-3881/aa79a8.
- Van Beeck, J., Bowman, D. M., Pedersen, M. G., Van Reeth, T., Van Hoolst, T., and Aerts, C., “Detection of non-linear resonances among gravity modes of slowly pulsating B stars: Results from five iterative pre-whitening strategies,” *Astronomy & Astrophysics*, vol. 655, A59, 2021, doi:10.1051/0004-6361/202141572.
- Van Beeck, J., Prat, V., Van Reeth, T., Mathis, S., Bowman, D. M., Neiner, C., and Aerts, C., “Detecting axisymmetric magnetic fields using gravity modes in intermediate-mass stars,” *Astronomy & Astrophysics*, vol. 638, A149, 2020, doi:10.1051/0004-6361/201937363.
- Van Beeck, J., Van Hoolst, T., Aerts, C., and Fuller, J., “Non-linear three-mode coupling of gravity modes in rotating slowly pulsating B stars. Stationary solutions and modeling potential,” *Astronomy & Astrophysics*, vol. 687, A265, 2024, doi:10.1051/0004-6361/202348369.
- van Leeuwen, F., Evans, D. W., Grenon, M., Grossmann, V., Mignard, F., and Perryman, M. A. C., “The HIPPARCOS mission: photometric data.” *Astronomy & Astrophysics*, vol. 323, pp. L61–L64, 1997.
- Van Reeth, T., De Cat, P., Van Beeck, J., Prat, V., Wright, D. J., Lehmann, H., Chené, A. N., Kambe, E., Yang, S. L. S., Gentile, G., et al., “The near-core rotation of HD 112429. A γ Doradus star with TESS photometry and legacy spectroscopy,” *Astronomy & Astrophysics*, vol. 662, A58, 2022, doi:10.1051/0004-6361/202142921.

- Van Reeth, T., Mombarg, J. S. G., Mathis, S., Tkachenko, A., Fuller, J., Bowman, D. M., Buyschaert, B., Johnston, C., García Hernández, A., Goldstein, J., et al., “Sensitivity of gravito-inertial modes to differential rotation in intermediate-mass main-sequence stars,” *Astronomy & Astrophysics*, vol. 618, A24, 2018, doi:10.1051/0004-6361/201832718.
- Van Reeth, T., Tkachenko, A., and Aerts, C., “Interior rotation of a sample of γ Doradus stars from ensemble modelling of their gravity-mode period spacings,” *Astronomy & Astrophysics*, vol. 593, A120, 2016, doi:10.1051/0004-6361/201628616.
- Van Reeth, T., Tkachenko, A., Aerts, C., Pápics, P. I., Degroote, P., Deboscher, J., Zwintz, K., Bloemen, S., De Smedt, K., Hrudkova, M., et al., “Detecting non-uniform period spacings in the Kepler photometry of γ Doradus stars: methodology and case studies,” *Astronomy & Astrophysics*, vol. 574, A17, 2015a, doi:10.1051/0004-6361/201424585.
- Van Reeth, T., Tkachenko, A., Aerts, C., Pápics, P. I., Triana, S. A., Zwintz, K., Degroote, P., Deboscher, J., Bloemen, S., Schmid, V. S., et al., “Gravity-mode Period Spacings as a Seismic Diagnostic for a Sample of γ Doradus Stars from Kepler Space Photometry and High-resolution Ground-based Spectroscopy,” *The Astrophysical Journal Supplement Series*, vol. 218, no. 2, 27, 2015b, doi:10.1088/0067-0049/218/2/27.
- Vanbeveren, D., Mennekens, N., Van Rensbergen, W., and De Loore, C., “Blue supergiant progenitor models of type II supernovae,” *Astronomy & Astrophysics*, vol. 552, A105, 2013, doi:10.1051/0004-6361/201321072.
- Vanlaer, V., Aerts, C., Bellinger, E. P., and Christensen-Dalsgaard, J., “Feasibility of structure inversions for gravity-mode pulsators,” *Astronomy & Astrophysics*, vol. 675, A17, 2023, doi:10.1051/0004-6361/202245597.
- Vetter, M., Roepke, F. K., Schneider, F. R. N., Pakmor, R., Ohlmann, S. T., Lau, M. Y. M., and Andrassy, R., “From spherical stars to disk-like structures: 3D common-envelope evolution of massive binaries beyond inspiral,” *arXiv e-prints*, arXiv:2410.07841, 2024, doi:10.48550/arXiv.2410.07841.
- Vigna-Gómez, A., Neijssel, C. J., Stevenson, S., Barrett, J. W., Belczynski, K., Justham, S., de Mink, S. E., Müller, B., Podsiadlowski, P., Renzo, M., et al., “On the formation history of Galactic double neutron stars,” *Monthly Notices of the Royal Astronomical Society*, vol. 481, no. 3, pp. 4009–4029, 2018, doi:10.1093/mnras/sty2463.
- Vinciguerra, S., Neijssel, C. J., Vigna-Gómez, A., Mandel, I., Podsiadlowski, P., Maccarone, T. J., Nicholl, M., Kingdon, S., Perry, A., and Salemi, F., “Be X-ray binaries in the SMC as indicators of mass-transfer efficiency,” *Monthly Notices of the Royal Astronomical Society*, vol. 498, pp. 4705–4720, 2020, doi:10.1093/mnras/staa2177, aDS Bibcode: 2020MNRAS.498.4705V.
- Vink, J. S., “Winds from stripped low-mass helium stars and Wolf-Rayet stars,” *Astronomy & Astrophysics*, vol. 607, L8, 2017, doi:10.1051/0004-6361/201731902.
- Vink, J. S., de Koter, A., and Lamers, H. J. G. L. M., “New theoretical mass-loss rates of O and B stars,” *Astronomy & Astrophysics*, vol. 362, pp. 295–309, 2000.

- Vink, J. S., de Koter, A., and Lamers, H. J. G. L. M., “Mass-loss predictions for O and B stars as a function of metallicity,” *Astronomy & Astrophysics*, vol. 369, pp. 574–588, 2001, doi:10.1051/0004-6361:20010127.
- Virtanen, P., Gommers, R., Oliphant, T. E., Haberland, M., Reddy, T., Cournapeau, D., Burovski, E., Peterson, P., Weckesser, W., Bright, J., et al., “SciPy 1.0: Fundamental Algorithms for Scientific Computing in Python,” *Nature Methods*, vol. 17, pp. 261–272, 2020, doi:10.1038/s41592-019-0686-2.
- von Zeipel, H., “Sur l’application des séries de M. Lindstedt à l’étude du mouvement des comètes périodiques,” *Astronomische Nachrichten*, vol. 183, no. 22, p. 345, 1910, doi:10.1002/asna.19091832202.
- Waelkens, C., Aerts, C., Kestens, E., Grenon, M., and Eyer, L., “Study of an unbiased sample of B stars observed with Hipparcos: the discovery of a large amount of new slowly pulsating B stars,” *Astronomy & Astrophysics*, vol. 330, pp. 215–221, 1998.
- Wagenhuber, J. and Weiss, A., “Termination of AGB-evolution by hydrogen recombination.” *Astronomy & Astrophysics*, vol. 290, pp. 807–814, 1994.
- Wagg, T., Johnston, C., Bellinger, E. P., Renzo, M., Townsend, R., and de Mink, S. E., “The asteroseismic imprints of mass transfer. A case study of a binary mass-gainer in the SPB instability strip,” *Astronomy & Astrophysics*, vol. 687, A222, 2024, doi:10.1051/0004-6361/202449912.
- Walker, G., Matthews, J., Kuschnig, R., Johnson, R., Rucinski, S., Pazder, J., Burley, G., Walker, A., Skaret, K., Zee, R., et al., “The MOST Asteroseismology Mission: Ultraprecise Photometry from Space,” *Publications of the Astronomical Society of the Pacific*, vol. 115, no. 811, pp. 1023–1035, 2003, doi:10.1086/377358.
- Wang, C., Langer, N., Schootemeijer, A., Milone, A., Hastings, B., Xu, X.-T., Bodensteiner, J., Sana, H., Castro, N., Lennon, D. J., et al., “Stellar mergers as the origin of the blue main-sequence band in young star clusters,” *Nature Astronomy*, vol. 6, pp. 480–487, 2022, doi:10.1038/s41550-021-01597-5.
- Wang, L., Gies, D. R., Peters, G. J., Götberg, Y., Chojnowski, S. D., Lester, K. V., and Howell, S. B., “The Detection and Characterization of Be+sdO Binaries from HST/STIS FUV Spectroscopy,” *The Astronomical Journal*, vol. 161, no. 5, 248, 2021, doi:10.3847/1538-3881/abf144.
- Webbink, R. F., “The evolution of low-mass close binary systems. I. The evolutionary fate of contact binaries.” *Astrophysical Journal*, vol. 209, pp. 829–845, 1976, doi:10.1086/154781, aDS Bibcode: 1976ApJ...209..829W.
- Webbink, R. F., “Double white dwarfs as progenitors of R Coronae Borealis stars and type I supernovae.” *Astrophysical Journal*, vol. 277, pp. 355–360, 1984, doi:10.1086/161701.
- Wei, D., Schneider, F. R. N., Podsiadlowski, P., Laplace, E., Röpke, F. K., and Vetter, M., “Evolution and final fate of massive post-common-envelope binaries,” *Astronomy & Astrophysics*, vol. 688, A87, 2024, doi:10.1051/0004-6361/202348560.

- Weiss, A. and Schlattl, H., “GARSTEC—the Garching Stellar Evolution Code. The direct descendant of the legendary Kippenhahn code,” *Astrophysics and Space Science*, vol. 316, no. 1-4, pp. 99–106, 2008, doi:10.1007/s10509-007-9606-5.
- Weiss, W. W., Rucinski, S. M., Moffat, A. F. J., Schwarzenberg-Czerny, A., Koudelka, O. F., Grant, C. C., Zee, R. E., Kuschnig, R., Mochacki, S., Matthews, J. M., et al., “BRITe-Constellation: Nanosatellites for Precision Photometry of Bright Stars,” *Publications of the Astronomical Society of the Pacific*, vol. 126, no. 940, p. 573, 2014, doi:10.1086/677236.
- Wellstein, S., Langer, N., and Braun, H., “Formation of contact in massive close binaries,” *Astronomy & Astrophysics*, vol. 369, pp. 939–959, 2001, doi:10.1051/0004-6361:20010151.
- Wickramasinghe, D. T. and Ferrario, L., “The origin of the magnetic fields in white dwarfs,” *Monthly Notices of the Royal Astronomical Society*, vol. 356, no. 4, pp. 1576–1582, 2005, doi:10.1111/j.1365-2966.2004.08603.x.
- Wickramasinghe, D. T., Tout, C. A., and Ferrario, L., “The most magnetic stars,” *Monthly Notices of the Royal Astronomical Society*, vol. 437, no. 1, pp. 675–681, 2014, doi:10.1093/mnras/stt1910.
- Wolf, W. and Schwab, J., “py_mesa_reader,” Python Package Index, 2017, https://billwolf.space/py_mesa_reader/.
- Woods, T. E. and Ivanova, N., “Can We Trust Models for Adiabatic Mass Loss?” *The Astrophysical Journal Letters*, vol. 739, no. 2, L48, 2011, doi:10.1088/2041-8205/739/2/L48.
- Wu, S., Everson, R. W., Schneider, F. R. N., Podsiadlowski, P., and Ramirez-Ruiz, E., “The Art of Modeling Stellar Mergers and the Case of the B[e] Supergiant R4 in the Small Magellanic Cloud,” *Astrophysical Journal*, vol. 901, no. 1, 44, 2020a, doi:10.3847/1538-4357/abaf48.
- Wu, T. and Li, Y., “High-precision Asteroseismology in a Slowly Pulsating B Star: HD 50230,” *Astrophysical Journal*, vol. 881, no. 1, 86, 2019, doi:10.3847/1538-4357/ab2ad8.
- Wu, T., Li, Y., Deng, Z.-m., Lin, G.-f., Song, H.-f., and Jiang, C., “Asteroseismic Analyses of Slowly Pulsating B Star KIC 8324482: Ultraweak Element Mixing beyond the Central Convective Core,” *Astrophysical Journal*, vol. 899, no. 1, 38, 2020b, doi:10.3847/1538-4357/aba430.
- Yoon, S. C. and Langer, N., “The first binary star evolution model producing a Chandrasekhar mass white dwarf,” *Astronomy & Astrophysics*, vol. 412, pp. L53–L56, 2003, doi:10.1051/0004-6361:20034607.
- Zahn, J. P., “Tidal dissipation in binary systems,” in Goupil, M. J. and Zahn, J. P. (editors), “EAS Publications Series,” *EAS Publications Series*, vol. 29, pp. 67–90, 2008, doi:10.1051/eas:0829002.
- Zhao, Z.-Q., Li, Z.-W., Xiao, L., Ge, H.-W., and Han, Z.-W., “The radius variations of accreting main-sequence stars and mass transfer instability,” *Monthly Notices of the Royal Astronomical Society*, vol. 531, no. 1, pp. L45–L51, 2024, doi:10.1093/mnras/slae029.

Acknowledgments

I moved to Heidelberg in the winter of 2021 during one of Germany's first major COVID-19 waves. As you can imagine, this was not the ideal time to move to a new country for the first time and leave my family, friends, and partner behind. However, I was excited to start my PhD, and since we had no idea how this pandemic would evolve further (despite people's best attempts), I decided to go ahead with it. The reason I am bringing up this not-so-ideal start of an otherwise great PhD time, is that I want to begin by thanking the people at HITS, such as Frauke, Christina, Silvia, Rémy, and Isabel, for creating a welcoming environment in what was, at the time, an (almost) empty institute.

As time passed on and more things became possible again, I was able to experience more and more of life as a PhD student and life in Heidelberg. Now, almost four years have passed, and I have learned a lot about astrophysics and academia, but also about myself. In this part of my thesis, I would like to take the space and time (spacetime?) to thank the people who have contributed to making this such a wonderful adventure.

I want to thank my first supervisor, Fabian Schneider, for giving me the opportunity to start my doctoral journey into the world of binary physics and asteroseismology, and for successfully guiding me through it. Fabian, it has been an honour to be your first official doctoral student. I appreciate that, when I started almost four years ago, you were open about still figuring out some of the intricacies of being a PhD supervisor, since this immediately showed me how much you care about these things. I will say this: I counted myself lucky with you as a supervisor back then, and I still do to this day. Thank you for being a great mentor on all the different aspects of doing a PhD and on being a scientist in general, for gradually giving me the freedom and trust to take my PhD project into my own hands, and for not only being there for me as my supervisor but also as a person. I wish you all the best for the future and am confident we will stay in touch—whether to collaborate on an exciting new project or simply to catch up.

Next, I want to thank Saskia Hekker, my second supervisor during my doctoral studies. Saskia, thank you for all the scientific and academic advice you have given me over the past years. I am glad that, after two years of me focussing mainly on binary physics, we finally got to work together more closely on the second part of my doctoral project about asteroseismology. I really appreciate that you have always made it very clear that your door is always open, even if I just wanted to have a chat. Many times when I knocked on your

door for a quick question or update, it would turn into a slightly longer-than-planned but always enjoyable conversation about stars, academia, or life in general. I also want to thank you for explicitly including me in your Theory and Observations of Stars group despite the administrative barriers.

There is someone else who deserves a spot on this list of mentors during my doctoral studies, and that is Conny Aerts. Conny, I want to thank you for joining me on the ‘merger seismology’ adventure, for regularly opening my eyes to the bigger picture of the work we were doing, for the nice dinners during your visits to Heidelberg, and for all the opportunities you have given me—from helping me publish my first paper after finishing my master’s, to highlighting my work by letting me produce a figure for your review, and introducing me to many people in the asteroseismology community.

During one of the first meetings between Fabian, Saskia, and myself, Saskia referred to herself and Fabian and my PhD Mother and Father. About half a year into my doctoral studies, this academic family saw the addition of a new member who became very important to me: my PhD Aunt Eva Laplace. Dear Eva, as I said when you left Heidelberg, there was a before and after Eva at HITS, and you have made a big impact on my PhD time and the kind of scientist I am now and will strive to be in the future. I wish every PhD student could have a PhD Aunt like yourself. Thank you for all the encouragement, advice, and help, and for being a fantastic friend and colleague.

In your doctoral studies, you often work on some very specific topics, which, in a way, can make you feel somewhat isolated. A good remedy for this feeling is having great colleagues and friends (some people would call them ‘frolleagues’) around you. I want to give a big thank you to all the people (past and present) of the two research groups I was part of, the Stellar Evolution Theory and Theory and Observations of Stars groups, and to the people of the Physics of Stellar Objects and Computational Carbon Chemistry groups, for all the nice coffee breaks, dinners, group outings, meetings, and discussions (both scientific and non-scientific).

I want to thank a few of these people specifically because they have become good friends over the past few years. Javier, Lynn, Quentin (we have been friends for a while longer, of course), Anna, Marco, Lukrécia, Fran, Bea, and Alex, thank you for being the amazing people you are, and for letting me be myself. Sometimes, life—or your PhD project—slaps you in the face. When I had these moments, it was a relief knowing I could always turn to each of you for support or take my mind off things by doing something fun. And fun when had! I will never forget all the parties, hikes, bouldering sessions, runs, times we hung out at Neckarwiese, dinners... No matter where our lives take us, I hope—no, I am sure—that our paths will continue to cross in the future.

I also want to thank all my friends back in Belgium. It has not always been easy to keep in touch with everyone and plan my times in Belgium so that I could see all of you regularly, but despite this, you have never held this against me and always made me feel like I never left. To my fellow ‘IvS fanclub’ members, Silke, Aaron, Cis, and Quentin: we all went our separate ways geographically (kind of, at least), but that did not stop us from staying good friends and supporting each other in work and life, and I am really grateful for that!

Mama, papa, bedankt om zulke fantastische ouders te zijn en me altijd de vrijheid en steun te geven om te doen wat ik graag doe. Al van toen ik klein was hebben jullie steeds mijn interesse in de ruimte, techniek, en wetenschap in het algemeen aangewakkerd. Van mijn eigen werkbank in ‘het kot’, naar boeken over de planeten, een bezoek aan het Euro Space Center en tal van andere musea, een ingenieurskamp, en ondersteuning bij schoolprojecten over wetenschap, tot het duwtje in de rug om de sprong te wagen die me tot hier in Heidelberg heeft gebracht. Een welgemeende dankjewel en heel veel liefs!

Lena, ik wil je graag bedanken om de beste zus te zijn die ik me kan inbeelden. Ondanks het feit dat we elkaar minder zagen de voorbije jaren, heb ik het gevoel dat we nog dichter bij elkaar zijn gegroeid. Ik heb je vanuit Heidelberg zien ontpoppen tot een gedreven en zelfzekere bijna-arts (ik moet nog even wachten totdat ik je dokter mag noemen) en ik wil dat je weet dat ik ongelofelijk trots op je ben!

Louise, lange-afstandsrelaties zijn niet gemakkelijk, maar ik ben fier op het feit dat we het ondanks alles toch hebben kunnen laten werken. Bedankt om er steeds voor mij te zijn het voorbije anderhalf jaar, zelfs vanop afstand. Je wist me de voorbije maanden geregeld ‘uit mijn kot’ te trekken voor wat broodnodige ontspanning, maar je had er ook steeds begrip voor als ik even wat extra hard moest doorwerken, waarvoor bedankt. Ik zie je graag en kijk er naar uit om samen een plekje te zoeken op de wereld waar we verder van ons werk en leven kunnen genieten.

Lastly, I want to acknowledge the financial support from the Heidelberg Institute for Theoretical Studies (HITS) and the International Max Planck Research School for Astronomy and Cosmic Physics at the University of Heidelberg (IMPRS-HD) for the financial support I received during my doctoral studies.

